

STUDIES OF THE SAFETY OF MATERIALS FOR METAL-ION BATTERIES

by

Xin Xia

Submitted in partial fulfilment of the requirements  
for the degree of Doctor of Philosophy

at

Dalhousie University  
Halifax, Nova Scotia  
April 2013

© Copyright by Xin Xia, 2013

DALHOUSIE UNIVERSITY

DEPARTMENT OF PHYSICS AND ATMOSPHERIC SCIENCE

The undersigned hereby certify that they have read and recommend to the Faculty of Graduate Studies for acceptance a thesis entitled “STUDIES OF THE SAFETY OF MATERIALS FOR METAL-ION BATTERIES” by Xin Xia in partial fulfillment of the requirements for the degree of Doctor of Philosophy.

Dated: April 3, 2013

External Examiner: \_\_\_\_\_

Research Supervisor: \_\_\_\_\_

Examining Committee: \_\_\_\_\_

\_\_\_\_\_

\_\_\_\_\_

Departmental Representative: \_\_\_\_\_

DALHOUSIE UNIVERSITY

DATE: April 3, 2013

AUTHOR: Xin Xia

TITLE: STUDIES OF THE SAFETY OF MATERIALS FOR METAL-ION  
BATTERIES

DEPARTMENT OR SCHOOL: Department of Physics and Atmospheric Science

DEGREE: PhD CONVOCATION: October YEAR: 2013

Permission is herewith granted to Dalhousie University to circulate and to have copied for non-commercial purposes, at its discretion, the above title upon the request of individuals or institutions. I understand that my thesis will be electronically available to the public.

The author reserves other publication rights, and neither the thesis nor extensive extracts from it may be printed or otherwise reproduced without the author's written permission.

The author attests that permission has been obtained for the use of any copyrighted material appearing in the thesis (other than the brief excerpts requiring only proper acknowledgement in scholarly writing), and that all such use is clearly acknowledged.

---

Signature of Author

致 爸爸， 妈妈及所有我爱和爱我的人

## TABLE OF CONTENTS

LIST OF TABLES .....	x
LIST OF FIGURES .....	xi
ABSTRACT.....	xvii
LIST OF ABBREVIATIONS AND SYMBOLS USED.....	xviii
ACKNOWLEDGMENTS .....	xxi
CHAPTER 1 INTRODUCTION .....	1
1.1 Introduction to the safety of metal-ion batteries.....	1
1.1.1 Introduction to the reactivity of battery materials .....	1
1.1.2 Introduction to fire-related safety concerns of lithium-ion batteries .....	2
1.2 Introduction to sodium-ion batteries.....	4
1.2.1 Positive electrode materials for sodium-ion batteries.....	6
1.2.1.1 $\text{Na}_x\text{CoO}_2$ .....	6
1.2.1.2 $\text{NaCrO}_2$ .....	8
1.2.1.3 $\text{NaNi}_{0.5}\text{Mn}_{0.5}\text{O}_2$ .....	11
1.2.1.4 $\text{Na}_x\text{Fe}_{0.5}\text{Mn}_{0.5}\text{O}_2$ .....	12
1.2.1.5 $\text{NaMnO}_2$ , $\text{Na}_{0.44}\text{MnO}_2$ , $\text{Na}_{2/3}\text{Ni}_{1/3}\text{Mn}_{2/3}\text{O}_2$ .....	13
1.2.1.6 Other positive electrode materials for Na-ion batteries .....	14
1.2.2 Negative electrode materials.....	15
1.2.2.1 Hard carbon .....	15
1.2.2.2 Other compounds.....	16
1.2.3 Electrolyte.....	17
1.3 Flame retardants as electrolyte additives for lithium-ion batteries.....	17
1.3.1 Organophosphorus flame retardant additives .....	20
1.3.2 Non-phosphorus flame retardant additives.....	34
1.4 Scope of this thesis .....	35
CHAPTER 2 EXPERIMENTAL TECHNIQUES .....	37

2.1 Synthesis of electrode materials .....	37
2.1.1 Hard carbon .....	37
2.1.2 Transition metal hydroxide precursor .....	39
2.1.3 Sodium transition metal oxides .....	41
2.1.4 Sodium foil .....	41
2.2 X-ray diffraction .....	42
2.3 Electrode preparation for ARC or electrochemical testing .....	44
2.3.1 Thin film electrodes for electrochemical tests .....	44
2.3.2 Pellet electrodes for ARC .....	45
2.3.3 Cell construction for thin-film electrodes .....	45
2.3.4 Cell construction for pellet electrodes .....	47
2.3.5 Cell testing .....	47
2.4 Theory of accelerating rate calorimetry (ARC) .....	48
2.4.1 Introduction to reaction kinetics .....	48
2.4.2 Accelerating rate calorimetry .....	50
2.5 Introduction to the ARC machine .....	52
2.5 Scanning electron microscopy .....	55
2.6 Surface area measurement .....	55
2.7. Measurement of the solubility of NaPF <sub>6</sub> or NaF in different solvents .....	56
2.8 Automatic storage system .....	56
2.9 Symmetric cells .....	58
2.10 Electrochemical impedance spectroscopy measurement .....	59
2.11 Self-extinguishing time (SET) tests .....	59
CHAPTER 3 STUDIES OF THE REACTIVITY OF NEGATIVE ELECTRODE MATERIALS FOR SODIUM-ION BATTERIES IN SOLVENTS AND ELECTROLYTES. ....	61
3.1 Hard carbon .....	61
3.1.1 Sample preparation .....	61

3.1.2 Electrochemical performance of hard carbon.....	61
3.1.3 Reactivity of sodium-inserted hard carbon (Na:HC) in different solvents and electrolytes .....	63
3.1.4 Summary.....	76
3.2. Comparison of the reactivity of $\text{Na}_x\text{C}_6$ and $\text{Li}_x\text{C}_6$ with non-aqueous solvents and electrolytes .....	76
3.2.1 Summary.....	78
CHAPTER 4 STUDIES OF THE REACTIVITY OF POSITIVE ELECTRODE MATERIALS FOR SODIUM-ION BATTERIES IN SOLVENTS AND ELECTROLYTES. ....	79
4.1 $\text{NaCrO}_2$ .....	79
4.1.1 Synthesis of samples.....	79
4.1.2 XRD and SEM.....	79
4.1.3 Electrochemical performance of Na/ $\text{NaCrO}_2$ half cells.....	80
4.1.4 Reactivity of deintercalated $\text{NaCrO}_2$ ( $\sim\text{Na}_{0.5}\text{CrO}_2$ ) in solvents and electrolytes .....	82
4.1.5 Calculations of the XRD pattern $\text{P3-CrO}_2$ with different type of stacking faults .....	88
4.1.6 Summary.....	92
4.2 $\text{Na}_{0.65}\text{CoO}_2$ .....	93
4.2.1 Synthesis of samples.....	93
4.2.2 XRD and SEM.....	93
4.2.3 Electrochemical performance of $\text{Na}_{0.65}\text{CoO}_2/\text{Na}$ half cells .....	95
4.2.4 Reactivity of deintercalated $\text{Na}_{0.65}\text{CoO}_2$ ( $\sim\text{Na}_{0.3}\text{CoO}_2$ ) in solvents and electrolytes .....	96
4.2.5 Summary.....	103
4.3 $\text{NaNi}_{0.5}\text{Mn}_{0.5}\text{O}_2$ .....	104
4.3.1 Synthesis of the sample. ....	104
4.3.2 XRD and SEM.....	104
4.3.3 Electrochemical performance of Na/ $\text{NaNi}_{0.5}\text{Mn}_{0.5}\text{O}_2$ half cells .....	106

4.3.4 Reactivity of deintercalated $\text{NaNi}_{0.5}\text{Mn}_{0.5}\text{O}_2$ ( $\sim\text{Na}_{0.5}\text{Ni}_{0.5}\text{Mn}_{0.5}\text{O}_2$ ) in solvents and electrolytes .....	107
4.3.5 Summary .....	115
CHAPTER 5 THE REACTIVITY OF CHARGED ELECTRODE MATERIALS WITH SODIUM BIS(TRIFLUOROMETHANESULFONYL)IMIDE (NaTFSI) BASED-ELECTROLYTE AT ELEVATED TEMPERATURES .....	116
5.1 Thermal stability of NaTFSI.....	116
5.2 Electrochemical performance of $\text{NaCrO}_2$ and hard carbon in NaTFSI based-electrolyte .....	117
5.3 The reactivity of charged electrode materials with NaTFSI-based electrolyte...	119
5.4 Al-corrosion of NaTFSI.....	122
5.5 Summary .....	124
CHAPTER 6 TRIPHENYL PHOSPHATE AS A FLAME RETARDANT ADDITIVE FOR LITHIUM-ION BATTERIES .....	125
6.1 The impact of TPP on electrochemical performance of negative electrode materials.....	125
6.1.1 Electrochemical performance of petroleum coke/Li cells with different electrolytes .....	125
6.1.2 Electrochemical performance of graphite/graphite symmetric cells with different electrolytes .....	132
6.1.3 Summary.....	138
6.2 The reactivity of charged electrode materials with electrolytes containing TPP	139
6.2.1 Impact of TPP on the electrochemical performance of NMC/NMC and graphite/graphite symmetric cells.....	140
6.2.2 Impact of TPP on the reactivity of NMC and graphite in electrolytes .....	141
6.2.3 Impact of TPP on the flammability of electrolyte .....	145
6.2.4 Summary .....	147
CHAPTER 7 CONCLUSIONS AND FUTURE WORK .....	148
7.1 Conclusions.....	148
7.1.1 Thermal Stability of sodium-ion battery materials .....	148



7.2.2 Triphenyl phosphate (TPP) as a flame retardant additive for lithium-ion battery .....	150
7.2 Future work.....	151
7.2.1 Study of the reactivity of new sodium intercalated compounds for sodium-ion batteries.....	151
7.2.2 Improvement of the performance of TPP-based electrolytes for lithium-ion batteries.....	152
7.2.3 Study of other flame retardants as additives for lithium-ion batteries.....	154
7.2.4 Fundamental understanding of function of additives on the electrochemical performance of lithium-ion batteries.....	155
7.2.5 Studies the reactivity of other layered-structure sodium transition metal oxides as positive electrode materials for Na-ion batteries.....	155
7.2.6 Can Na-ion batteries work in aqueous electrolytes?.....	156
REFERENCES .....	157
APPENDIX A: Structure of some organic molecules in this thesis .....	163
APPENDIX B: Copyright Information.....	164

## LIST OF TABLES

Table 1.1 Some physical properties of organic solvents.....	3
Table 1.2 Some physical properties of different flame retardants .....	29
Table 2.1 Synthesis conditions and properties of hard carbon from different sources. ....	37
Table 2.2 Reaction models typically applied to describe the thermal decomposition of solids . .....	49
Table 2.3 Parameters used to calculate ARC profiles for the chosen reaction models of Table 2.2.....	51
Table 3.1 Solubility of NaPF <sub>6</sub> in DMC, DEC, PC and EC .....	73
Table 4.1 Layer stacking probabilities and stacking vectors .....	90
Table 4.2 Atomic coordinates of the CrO <sub>2</sub> layer used for the calculation.....	91
Table 4.3 Reaction products between Na <sub>0.65</sub> CoO <sub>2</sub> or Na <sub>0.35</sub> CoO <sub>2</sub> and solvent or electrolytes heated in ARC experiments to different temperatures. ....	103
Table 4.4 Reactants and reaction products found after the ARC experiments of Figure 4.16 as described by Figure 4.17. Products of the reaction of Na <sub>x</sub> Ni <sub>0.5</sub> Mn <sub>0.5</sub> O <sub>2</sub> with PVDF as detailed in Figure 4.18 are also listed .....	112
Table 6.1 First discharge specific capacity, first charge specific capacity and irreversible capacity for coke/Li cells tested at 30°C with different amounts of TPP in the electrolyte. ....	127
Table 6.2 First discharge specific capacity, first charge specific capacity and irreversible capacity for coke/Li cells tested at 60°C with different amounts of TPP in the electrolyte. ....	128
Table 6.3 Measured impedance results for graphite/graphite symmetric cells with different concentration of TPP after 40 cycles. ....	137

## LIST OF FIGURES

Figure 1.1 A picture of the Chevrolet Volt before and after a fire .....	3
Figure 1.2 Abundance of elements in the earth’s crust .....	5
Figure 1.3 A schematic of a sodium-ion battery .....	6
Figure 1.4 Crystal structure of P2-Na <sub>2/3</sub> CoO <sub>2</sub> in a [110] projection .....	7
Figure 1.5 Potential versus specific capacity of a Na <sub>0.74</sub> CoO <sub>2</sub> electrode in a Na/Na <sub>0.74</sub> CoO <sub>2</sub> cell.....	8
Figure 1.6 Crystal structure of O3-NaCrO <sub>2</sub> in a [110] projection .....	9
Figure 1.7 First cycle of NaCrO <sub>2</sub> vs. Na in NaClO <sub>4</sub> /PC electrolyte .....	9
Figure 1.8 Charge/discharge curve of NaCrO <sub>2</sub> /Na cells cycled between 2.0 and 3.6 V in NaClO <sub>4</sub> /PC electrolyte using a current density of 25 mA/g .....	10
Figure 1.9 Charge/discharge curves of NaNi <sub>0.5</sub> Mn <sub>0.5</sub> O <sub>2</sub> /Na cells cycled between 2.0 and 3.8 V, and the cycle performance of the cells. ....	11
Figure 1.10 Charge/discharge curve and cycle performance of NaNi <sub>0.5</sub> Mn <sub>0.5</sub> O <sub>2</sub> /hard carbon Na-ion cells cycled between 1.0 and 3.8 V. ....	12
Figure 1.11. Charge/discharge curves and cycle performance of Na <sub>2/3</sub> Fe <sub>0.5</sub> Mn <sub>0.5</sub> O <sub>2</sub> /Na half cells cycled between 1.5 and 4.3 V .....	13
Figure 1.12 (Left) Charge/discharge curve of hard carbon vs. Li and hard carbon vs. Na. (Right) A schematic of alkali metal insert into hard carbon.. ....	16
Figure 1.13 (a) DSC results of lithiated graphite in electrolytes with/without HMPN; (b) ARC results of lithium metal in electrolytes with/without HMPN.....	21
Figure 1.14 The lowest TMP content needed to ensure nonflammability of various electrolytes using different solvents.....	23
Figure 1.15 The relationship of nonflammability index and the lowest TMP content needed to ensure nonflammability .....	24
Figure 1.16 The thermal stability of natural graphite/LiCoO <sub>2</sub> (LiMn <sub>2</sub> O <sub>4</sub> ) cells with different electrolytes .....	25
Figure 1.17 Normalized SET thus obtained vs. the weight percentage of TMP, TEP and HMPN in electrolytes .....	26

Figure 1.18 Differential capacity of the graphite anode and the cathode in various TMP, TEP and HMPN-containing electrolytes. The first cycles are shown and FR concentrations are indicated followed by the columbic efficiency of the cathodic cycling.....	27
Figure 1.19 Trade-off between the flammability and electrochemical performance of the electrolytes .....	28
Figure 1.20 Normalized SET thus obtained vs. the weight percentage of TMP, TEP and HMPN, TFP, BMP and TDP in electrolytes.....	30
Figure 1.21 Capacity retention of cells with different electrolytes containing different amount of FRs.....	32
Figure 2.1 Process of making hard carbon pellet electrodes from pyrolysed oak .....	38
Figure 2.2 Photograph of the continuously-stirred tank reactor (CSTR).....	39
Figure 2.3 Process of making sodium foil .....	42
Figure 2.4 Siemens D5000 diffractometer.....	43
Figure 2.5 Air sensitive XRD holder .....	44
Figure 2.6 Construction of a 2325 size sodium coin cell.....	46
Figure 2.7 Calculated ARC profiles for zero order kinetics. ....	51
Figure 2.8 Calculated ARC profiles for first order kinetics.....	52
Figure 2.9 Schematic of the Accelerating Rate Calorimeter (ARC).....	53
Figure 2.10 A picture of the ARC when the blast shell is open .....	53
Figure 2.11 An ARC sample tube hooked on the tip of the sample thermocouple.....	54
Figure 2.12 ARC tubes for ARC experiments at various stages of sample preparation. ..	55
Figure 2.13. A picture of the 190-channel automated cell storage system .....	57
Figure 2.14 Illustration of the two different SET test methods. ....	60
Figure 3.1 Potential versus specific capacity of Na/HC and Li/HC cells measured during the first discharge.....	62
Figure 3.2 Self heating rate (SHR) vs. temperature of 70 mg Li:HC or 70 mg Na:HC reacting with 70 mg of electrolyte or solvent. ....	64
Figure 3.3 Self heating rate (SHR) vs. temperature of 70mg Na:HC in 70mg EC, 70mg DEC, 70mg DMC and the XRD patterns of the products after ARC tests, respectively. .	65

Figure 3.4 Reference, calculated and experimental XRD patterns of sodium methyl carbonate. The experimental pattern is the product of the reaction of Na:HC and DMC after the ARC experiment.....	67
Figure 3.5 Self heating rate (SHR) vs. temperature of 70 mg Na:HC in 70 mg EC, 70 mg DEC or 70 mg EC:DEC (1:2 v/v) and the XRD patterns of the products after ARC tests, respectively. ....	69
Figure 3.6 Expanded version of the XRD patterns (from 10° to 40°) of the products of Na:HC reacting with EC, DEC and EC:DEC, respectively. ....	69
Figure 3.7 Self heating rate (SHR) vs. temperature of 70 mg Na:HC in 70 mg EC, 70 mg DEC or 70 mg 1M NaPF <sub>6</sub> in EC:DEC (1:2 v/v) and the XRD patterns of the products after ARC tests, respectively. ....	70
Figure 3.8 Expanded view of the XRD patterns (from 10° to 40°) of the ARC products, of Na:HC reacting with EC, DEC and 1M NaPF <sub>6</sub> in EC:DEC (1:2 v/v), respectively. ....	71
Figure 3.9 TGA experiments on NaPF <sub>6</sub> and LiPF <sub>6</sub> . The samples were heated at 5°C/min in argon gas. ....	72
Figure 3.10 Self heating rate (SHR) vs. temperature of 70 mg Na:HC in 70 mg EC:DEC (1:2 v/v), 70 mg EC:DMC (1:2 v/v), 70 mg 1M NaPF <sub>6</sub> in EC:DEC (1:2 v/v) or 70 mg 1M NaPF <sub>6</sub> in EC:DMC (1:2 v/v).....	74
Figure 3.11 Self heating rate (SHR) vs. temperature of 96 mg Na:HC in 40 mg 1 M, 0.5 M, 0.25 M or 0 M (solvent only) NaPF <sub>6</sub> in EC:DEC (1:2 v/v). ....	75
Figure 3.12 Self heating rate (SHR) vs. temperature of 70 mg LiC <sub>6</sub> or 70 mg Na:HC in 70 mg EC:DEC (1:2 v/v) or 70 mg 1M LiPF <sub>6</sub> in EC:DEC (1:2 v/v) or 1M NaPF <sub>6</sub> in EC:DEC (1:2 v/v) .....	77
Figure 4.1 Diffraction pattern of synthesized NaCrO <sub>2</sub> and Rietveld profile refinement. .	80
Figure 4.2 Potential versus specific capacity of a NaCrO <sub>2</sub> electrode in a Na/NaCrO <sub>2</sub> coin-type cell.....	81
Figure 4.3 Self heating rate (SHR) vs. temperature of 100 mg Na <sub>0.5</sub> CrO <sub>2</sub> , Li <sub>0.5</sub> CoO <sub>2</sub> or Li <sub>0</sub> FePO <sub>4</sub> in the same mass of EC: DEC (1:2 v/v) or 1M NaPF <sub>6</sub> in EC: DEC (1:2 v/v), and the electrolyte itself.....	83
Figure 4.4 TGA experiments on Na <sub>0.5</sub> CrO <sub>2</sub> .....	84
Figure 4.5 XRD patterns of a) pristine NaCrO <sub>2</sub> , b) Na <sub>0.5</sub> CrO <sub>2</sub> prepared by charging an Na/NaCrO <sub>2</sub> cell to 3.6 V, c) the product of Na <sub>0.5</sub> CrO <sub>2</sub> after a TGA experiment in argon, d) the product of Na <sub>0.5</sub> CrO <sub>2</sub> reacting with solvent in an ARC experiment to 300°C. (right column) XRD patterns of e) same as (a) with the NaCrO <sub>2</sub> subtracted showing only the	

P3-CrO <sub>2-δ</sub> f) calculated pattern of P3-CrO <sub>2</sub> , g) calculated pattern of O3-CrO <sub>2</sub> and h) calculated pattern of O1- CrO <sub>2</sub> . .....	86
Figure 4.6 Crystal structure of P3 and O3 type layered-CrO <sub>2</sub> viewed in 110 projection .	89
Figure 4.7 Simulations showing the effect of O3-P3 inter-growth. The calculations were made for 0 < x < 1.0.....	91
Figure 4.8 Calculated XRD pattern of P3-type CrO <sub>2</sub> with 10% O3-type stacking faults and the experimental result from Figure 4.5 (e). .....	92
Figure 4.9 Diffraction pattern of synthesized Na <sub>0.65</sub> CoO <sub>2</sub> and Rietveld profile refinement. ....	94
Figure 4.10 Potential versus specific capacity of a Na <sub>0.65</sub> CoO <sub>2</sub> electrode in a Na/Na <sub>0.65</sub> CoO <sub>2</sub> coin-type cell.....	95
Figure 4.11 Self heating rate (SHR) vs. temperature of 100 mg Na <sub>0.35</sub> CoO <sub>2</sub> in the same mass of EC: DEC (1:2 v/v), 0.5M NaPF <sub>6</sub> in EC: DEC (1:2 v/v) or 1M NaPF <sub>6</sub> in EC: DEC (1:2 v/v).....	97
Figure 4.12 XRD patterns of a) Na <sub>0.35</sub> CoO <sub>2</sub> in solvent heated to 180°C, b) Na <sub>0.35</sub> CoO <sub>2</sub> in solvent heated to 230°C, c) Na <sub>0.35</sub> CoO <sub>2</sub> in solvent heated to 300°C; (right column) XRD patterns of d) Na <sub>0.35</sub> CoO <sub>2</sub> in 1M NaPF <sub>6</sub> based electrolyte heated to 180°C, e) Na <sub>0.35</sub> CoO <sub>2</sub> in 0.5 M NaPF <sub>6</sub> -based electrolyte heated to 300°C, f) Na <sub>0.35</sub> CoO <sub>2</sub> in 1M NaPF <sub>6</sub> -based electrolyte heated to 300°C .....	99
Figure 4.13 (left panel) Self heating rate (SHR) vs. temperature of a)100 mg Na <sub>0.35</sub> CoO <sub>2</sub> in 100 mg EC: DEC (1:2 v/v) heated to 300°C, b) Na <sub>0.65</sub> CoO <sub>2</sub> in the 100 mg EC: DEC (1:2 v/v) heated to 230°C, c) Na <sub>0.65</sub> CoO <sub>2</sub> in the 100 mg EC: DEC (1:2 v/v) heated to 300°C. (right panel) XRD patterns of d) Na <sub>0.35</sub> CoO <sub>2</sub> in solvent heated to 300°C, e) Na <sub>0.65</sub> CoO <sub>2</sub> in solvent heated to 230°C, f) Na <sub>0.65</sub> CoO <sub>2</sub> in solvent heated to 300°C. ....	100
Figure 4.14 Diffraction pattern of synthesized NaNi <sub>0.5</sub> Mn <sub>0.5</sub> O <sub>2</sub> and Rietveld profile refinement. ....	105
Figure 4.15 Potential versus specific capacity of a NaNi <sub>0.5</sub> Mn <sub>0.5</sub> O <sub>2</sub> electrode in a Na/NaNi <sub>0.5</sub> Mn <sub>0.5</sub> O <sub>2</sub> coin-type cell.....	106
Figure 4.16 Self heating rate (SHR) vs. temperature of 100 mg Na <sub>0.5</sub> Ni <sub>0.5</sub> Mn <sub>0.5</sub> O <sub>2</sub> in the same mass of EC: DEC (1:2 v/v), 1M NaPF <sub>6</sub> in EC: DEC (1:2 v/v) and 1M NaPF <sub>6</sub> in PC.. ..	108
Figure 4.17 XRD patterns of a) dry, unheated Na <sub>0.5</sub> Ni <sub>0.5</sub> Mn <sub>0.5</sub> O <sub>2</sub> , b) Na <sub>0.5</sub> Ni <sub>0.5</sub> Mn <sub>0.5</sub> O <sub>2</sub> heated to 175°C in electrolyte, c) Na <sub>0.5</sub> Ni <sub>0.5</sub> Mn <sub>0.5</sub> O <sub>2</sub> heated to 300°C in electrolyte and d) Na <sub>0.5</sub> Ni <sub>0.5</sub> Mn <sub>0.5</sub> O <sub>2</sub> heated to 300°C in solvent after the ARC tests.....	110

Figure 4.18 XRD patterns of a) $\text{Na}_{0.5}\text{Ni}_{0.5}\text{Mn}_{0.5}\text{O}_2$ electrode powder (containing PVDF), b) dry $\text{NaNi}_{0.5}\text{Mn}_{0.5}\text{O}_2$ electrode powder (containing PVDF), c) $\text{Na}_{0.5}\text{Ni}_{0.5}\text{Mn}_{0.5}\text{O}_2$ with solvent and d) fresh $\text{NaNi}_{0.5}\text{Mn}_{0.5}\text{O}_2$ after heating to $300^\circ\text{C}$ in the ARC.....	114
Figure 5.1 Fractional remaining weight versus temperature in TGA experiments on $\text{NaPF}_6$ and $\text{NaTFSI}$ .....	116
Figure 5.2 Potential versus specific capacity of a $\text{NaCrO}_2$ electrode in a $\text{Na}/\text{NaCrO}_2$ coin-type cell using $\text{NaTFSI}/\text{PC}$ electrolyte .....	118
Figure 5.3 Potential versus specific capacity of a hard carbon electrode in a hard carbon/ $\text{Na}$ coin-type cell.t.....	119
Figure 5.4 Self heating rate (SHR) vs. temperature for 100 mg $\text{Na}_{0.5}\text{CrO}_2$ in the same mass of EC:DEC, PC, $\text{NaPF}_6/\text{EC}:\text{EDC}$ and $\text{NaTFSI}/\text{PC}$ .....	120
Figure 5.5 Self heating rate (SHR) vs. temperature of 70 mg sodium inserted hard carbon ( $\text{Na}:\text{HC}$ ) in the same mass of EC:DEC, PC, $\text{NaPF}_6/\text{EC}:\text{EDC}$ , $\text{NaPF}_6/\text{PC}$ , $\text{NaClO}_4/\text{PC}$ or $\text{NaTFSI}/\text{PC}$ .....	122
Figure 5.6 Cyclic voltammogram of an $\text{Al}/\text{Na}$ cell using $\text{NaTFSI}/\text{PC}$ electrolyte at a sweep rate of 10 mV/s.....	123
Figure 6.1 Potential versus specific capacity for the first discharge-charge cycle of coke/ $\text{Li}$ half cells using control electrolyte and electrolyte with 40% TPP .....	126
Figure 6.2 The irreversible capacity measured during the first cycle of coke/ $\text{Li}$ cells with different concentrations of TPP at $30^\circ\text{C}$ and $60^\circ\text{C}$ .....	127
Figure 6.3 The open-circuit voltage (OCV) versus time of coke/ $\text{Li}$ cells at $30^\circ\text{C}$ and $60^\circ\text{C}$ stored at 0.005 V (left panel) and 0.4 V (right panel) with different concentrations of TPP as indicated in the Figure.. ..	129
Figure 6.4 Amount of $\text{Li}$ in $\text{mAh/g}$ removed from $\text{Li}_x\text{C}_6$ during storage at $30^\circ\text{C}$ plotted as a function of the storage potential and the amount of TPP in the electrolyte.....	131
Figure 6.5 Amount of $\text{Li}$ in $\text{mAh/g}$ removed from $\text{Li}_x\text{C}_6$ during storage at $60^\circ\text{C}$ plotted as a function of the storage potential and the amount of TPP in the electrolyte. ....	131
Figure 6.6 Voltage versus specific capacity for a graphite/graphite symmetric cells with different concentrations of TPP cycled at $C/10$ and at a temperature of $30.0 \pm 0.1^\circ\text{C}$ ... ..	132
Figure 6.7 The specific capacity versus cycle number of graphite/graphite symmetric cells with different concentrations of TPP cycled at $C/10$ at a temperature of $30.0 \pm 0.1^\circ\text{C}$ .. ..	134
Figure 6.8 Charge-discharge potential polarizations, $\Delta V$ , in units of volts, plotted versus cycle number for graphite/graphite cells .....	135

Figure 6.9 The negative imaginary impedance plotted versus the real impedance for graphite/graphite symmetric cells with different concentrations of TPP. ....	137
Figure 6.10 The specific capacity versus cycle number of NMC/NMC symmetric cells with different concentrations of TPP in their electrolytes as indicated. The cells were cycled at C/10 at a temperature of $30.0 \pm 0.1^\circ\text{C}$ . ....	141
Figure 6.11 Self heating rate (SHR) vs. temperature for 70 mg lithiated graphite ( $\text{LiC}_6$ ), in the same mass of electrolytes containing different amounts of TPP. ....	142
Figure 6.12 Self heating rate (SHR) vs. temperature of 94 mg of charged NMC (4.2 V vs. $\text{Li}/\text{Li}^+$ ), in 30 mg of electrolytes containing different amounts of TPP. ....	143
Figure 6.13 Self heating rate (SHR) vs. temperature of 94 mg of charged NCA (4.2 V vs. $\text{Li}/\text{Li}^+$ ), in 30 mg of electrolyte containing different amounts of TPP. ....	144
Figure 6.14 Self-extinguishing time (SET) for electrolytes containing various concentrations of TPP. Results using the two test methods are shown. ....	146
Figure 7.1 The negative imaginary impedance plotted versus the real impedance for coke/coke symmetric cells with different electrolytes. ....	153



## ABSTRACT

In order for battery manufacturers to have a sustainable business, the batteries they produce must be as safe as possible. For lithium-ion batteries, reducing the flammability of the electrolyte is considered to be one way to improve safety, which might be achieved by adding flame retardants to the electrolyte. On the other hand, sodium-ion batteries are attracting attention from academic researchers due to the abundance of sodium reserves compared to lithium reserves. However, there are virtually no studies about the safety of sodium-ion batteries. In this thesis, studies of these two issues will be reported.

The reactivity of charged/discharged electrode materials for sodium-ion batteries in different solvents and electrolytes at elevated temperature was studied using Accelerating Rate Calorimetry (ARC). Hard carbon was studied as a negative electrode material for sodium-ion batteries. The reactivity of sodium-inserted hard carbon in solvents and electrolytes was investigated. Then, the reactivity of sodium-inserted hard carbon was compared to lithiated graphite.  $\text{NaCrO}_2$ ,  $\text{Na}_x\text{CoO}_2$  and  $\text{NaNi}_{0.5}\text{Mn}_{0.5}\text{O}_2$  were studied as positive electrode materials for sodium-ion batteries. The electrochemical performance of these materials was investigated. The reactivity of charged  $\text{NaCrO}_2$ ,  $\text{Na}_x\text{CoO}_2$  and  $\text{NaNi}_{0.5}\text{Mn}_{0.5}\text{O}_2$  in solvents and electrolytes was studied using ARC. Sodium bis(trifluoromethanesulfonyl)imide (NaTFSI) was studied as an electrolyte salt for sodium-ion batteries. The electrochemical performance of hard carbon and  $\text{NaCrO}_2$  in NaTFSI/PC electrolyte was studied. The reactivity of sodium-inserted hard carbon and deintercalated  $\text{NaCrO}_2$  in NaTFSI/PC electrolyte was also investigated.

Triphenyl phosphate (TPP) was studied as a flame retardant additive for lithium-ion batteries. Its impact on electrochemical performance of negative electrode materials (petroleum coke and graphite) and positive electrode materials ( $\text{LiNi}_{1/3}\text{Mn}_{1/3}\text{Co}_{1/3}\text{O}_2$  (NMC) and  $\text{LiNi}_{0.8}\text{Co}_{0.15}\text{Al}_{0.05}\text{O}_2$  (NCA)) was studied using an automated storage test, symmetric cells and Electrochemical Impedance Spectroscopy (EIS). The reactivity of lithiated graphite, deintercalated NMC and NCA in electrolyte containing TPP was investigated using ARC. Finally, the flammability of electrolytes containing TPP was studied using a Self-Extinguishing Time (SET) test.

## LIST OF ABBREVIATIONS AND SYMBOLS USED

$\alpha$	Fractional degree of conversion of reactants
ARC	Accelerating rate calorimetry
AND	Adiponitrile
BET	Brunauer-Emmett-Teller
BMP	Bis (2, 2, 2- trifluoroethyl) methylphosphate
$C_{tot}$	Heat capacity
CSTR	Continuously-stirred tank reactor
DEC	Diethyl carbonate
DEMMPA	Bis(N,N-diethyl)(2-methoxyethoxy)methylphosphonamidate
DMC	Dimethyl carbonate
DME	Dimethoxyethane
DMMP	Dimethyl methylphosphonate
DSC	Differential scanning calorimetry
$E_a$	Activation energy
EC	Ethylene carbonate
EMC	Ethylmethyl carbonate
FRs	Flame retardants
GBL	Gamma-butyrolactone
h	Total heat

HMPN	Hexamethoxycyclotriphosphazene
$K_B$	Boltzmann's constant
MFE	Methy nonafluorobutyl ether
NaTFSI	Sodium bis(trifluoromethanesulfonyl)imide
Na:HC	Sodium-inserted hard carbon
NMC	$\text{LiNi}_{1/3}\text{Mn}_{1/3}\text{Co}_{1/3}\text{O}_2$
NMP	N-methyl pyrrolidinone
O	Octahedral
P	Prismatic
PC	Propylene carbonate
PVDF	Polyvinylidene difluoride
$\gamma$	Frequency factor
SEI	Solid Electrolyte Interface
SEM	Scanning electron microscopy
SET	Self-extinguishing time
$T_b$	Boiling point
$T_f$	Flash point
$T_m$	Melting point
TDP	(2, 2, 2-trifluoroethyl)diethyl phosphate
TEP	Triethyl phosphate
TFP	Tris(2, 2, 2-trifluoroethyl) phosphate

THF	Tetrahydrofuran
TMP	Trimethyl phosphate
TPP	Triphenyl phosphate
XRD	X-ray diffraction

## ACKNOWLEDGMENTS

I would like to first thank my supervisor, Dr. Jeff. Dahn, for his invaluable guidance and constant encouragement. His great intelligence and profound knowledge inspires me all the time. Thanks for his patience for all my mistakes and “laziness”. Without his support, I could not finish this work. He provides the best environment for students to study and research. He is creating the best lab and research group for lithium-ion batteries.

I would like to thank my committee members, Dr. Mark Obrovac and Dr. Harm Rotermund. Mark has great knowledge and research experience in metal-ion batteries. Thanks for his valuable discussions about my sodium-ion battery projects and generously sharing the resources in his lab. Harm is very kind and helpful. He always gives valuable suggestion about my course studies and research.

I would like to thank all Dahn Lab members. Thanks David for my everyday life in the lab. Thanks Robbie for help with the problems/questions of facilities in the lab. Thanks Chris Burns for very useful discussions about study, research and sports. Thanks Remi and Eric for the time we spend together in the gym. Thanks John C. for all the “fights” we had. Thanks Aaron, Nupur, Laura, Tim, Ramesh, Patrick, Jennifer, and people have left, such as Aaron and Mark. Thanks for the time we spent together. I would like to thank all my Chinese friends here. Thanks Fu and Xuemei for great help in my research and life. Thanks Deijun for the meaningful talks we had. Thanks Ping, Sirong and Lin for all the great moments we experienced together.

Finally, I want to thank to my parents who give me the best all the time

## CHAPTER 1 INTRODUCTION

### 1.1 Introduction to the safety of metal-ion batteries.

#### 1.1.1 Introduction to the reactivity of battery materials

In order for battery manufacturers to have a sustainable business, the batteries they produce must be as safe as possible. The safety record of Li-ion batteries has been excellent because there are strict safety guidelines and battery manufacturers have paid close attention to potential hazards in battery systems [1]. Manufacturers and scientists have developed various test methods to measure the safety performance of lithium-ion batteries, such as the oven test, short circuit test, overcharge test and so on [2]. One of the most important considerations for battery safety is the relative reactivities of charged/discharged electrode materials with electrolytes or solvents at elevated temperatures. Finding materials having lower reactivity generally leads to a safer cell [2].

For university researchers, fundamental studies of the reactivities of electrode materials with electrolytes or solvents can be made using calorimetry. Accelerating Rate Calorimetry (ARC) can be used for such studies. Richard and Dahn studied the reactivity of lithium intercalated graphite with 1M LiPF<sub>6</sub>/EC:DEC electrolyte using Accelerating Rate Calorimetry (ARC), and proposed a reaction mechanism [3, 4]. MacNeil *et al.* studied the reactivity of various carbonaceous negative electrode materials and pointed out that the reactivity was strongly dependent on the surface area of graphitic samples [5]. Jiang *et al.*

studied the effects of additions of the salts ( $\text{LiPF}_6$  and  $\text{LiBOB}$ ) to solvents on the thermal reactivity of lithiated graphite. They showed that additions of  $\text{LiPF}_6$  reduced the reactivity of lithiated graphite due to the incorporation of thermally stable  $\text{LiF}$  in the solid electrolyte interface (SEI) [6].

MacNeil and Dahn also studied the reaction of  $\text{Li}_{0.5}\text{CoO}_2$  with nonaqueous solvents, and they showed that  $\text{Li}_{0.5}\text{CoO}_2$  decomposed to  $\text{LiCoO}_2$  and  $\text{CoO}$  or  $\text{Co}_3\text{O}_4$ , and that  $\text{O}_2$  was released in these reactions. The majority of the heat detected in these reactions came from the combustion of solvent with released  $\text{O}_2$  [7]. Jiang *et al.* studied the reactivity of the series of  $\text{LiNi}_x\text{Co}_{1-2x}\text{Mn}_x\text{O}_2$  ( $x=0.1, 0.2, 0.35, 0.45$ ) in non-aqueous solvents and electrolytes using ARC [8]. Zhou *et al.* studied the effect of Al-substitution on the reactivity of  $\text{LiNi}_{1/3}\text{Mn}_{1/3}\text{Co}_{1/3}\text{O}_2$  (NMC) with non-aqueous electrolytes, and they found that Al-substitution greatly reduced the reactivity of NMC without significantly impacting the electrochemical performance of the material [9].

### **1.1.2 Introduction to fire-related safety concerns of lithium-ion batteries**

In most commercial lithium-ion batteries, carbonate solvents are used in the electrolytes. Co-solvents, such as dimethyl carbonate (DMC), ethylmethyl carbonate (EMC) and diethyl carbonate (DEC), have relatively low flash points as shown in Table 1.1. This creates potential fire hazards in various types of accidents and abuse. These organic solvents serve as fuel for combustion processes in open air when cells are ruptured and the electrolytes are ignited by accidental sparks, or by thermal runaway of

lithium-ion batteries caused by electrical or mechanical abuse.

Table 1.1 Some physical properties of organic solvents

Solvent	$T_{\text{melting}}/^{\circ}\text{C}$	$T_{\text{boiling}}/^{\circ}\text{C}$	$T_{\text{flash pointing}}/^{\circ}\text{C}$
Ethylene Carbonate	36.4	248	160
Propylene Carbonate	-48.8	242	132
Dimethyl Carbonate	4.6	91	18
Diethyl Carbonate	-74.3	126	31
Ethylmethyl Carbonate	-53	110	26.7

(Please refer to Appendix A for the structure of these solvents)

Recently, lithium-ion batteries have been used in electric vehicles. The Chevrolet Volt is a plug-in hybrid electric vehicle that has received many awards. However, in June 2011 a Volt that had been intentionally subjected to a 20 mph (32 km/h) side pole impact crash test followed by a post-impact rollover, caught fire three weeks later in the test center parking lot, burning nearby vehicles. The battery was found to be the source of the fire [10]. Figure 1.1 shows the picture of the Chevrolet Volt before and after the fire.



Figure 1.1 A picture of the Chevrolet Volt before and after a fire



There are other reports related to fires in lithium-ion battery powered electric vehicles. One accident happened in Shenzhen, China in May, 2012. An electric-powered taxi caught fire 4 seconds after a crash with a car speeding at 180km/h. Three passengers were killed in this accident. The lithium-ion batteries used in the electric taxi were made using  $\text{LiFePO}_4$  as the positive electrode material. Charged  $\text{LiFePO}_4$  does not show any significant reactivity in solvents or electrolytes until  $300^\circ\text{C}$  [11]. This result indicates that any large lithium-ion battery can create a fire situation if temperatures are high enough, just like a tank of gasoline.

Reducing the flammability of the electrolytes/solvents in lithium-ion batteries would be one way to reduce the fire related safety concerns. Ionic liquids are currently heavily studied due to their non-flammability; however, they are still far away from practical applications [2]. For the present non-aqueous organic electrolyte systems, adding flame retardants to the electrolyte is one way of reducing the flammability [12], which will be discussed in section 1.3.

## **1.2 Introduction to sodium-ion batteries.**

The first commercial lithium-ion battery was produced by Sony Corp. in 1991. Since then, this safe, low-cost, environment-friendly device has been a "hot-spot" of scientific study and industrial manufacture. Li-ion cells have been widely used in various portable electronic devices, such as cell-phones, cameras, laptop computers, medical devices, satellites, space vehicles and submarines. Lithium-ion batteries are presently

considered the best electrochemical storage device for powering electric vehicles based on their high energy density and long cycle life [2]. Based on the amount of annual mine production of 2012, the known lithium reserves could be used for 382 years [13]. However, such calculation does not consider the potentially increasing demand for lithium reserves annually to support a possible world-wide adoption of electric vehicles. Additionally, lithium is not as abundant as other elements, like Fe, Al and Na. It is also concentrated non-uniformly on the planet. For example, 50% of the known reserves of Li are in Bolivia [14].

Another battery system---the sodium-ion battery, has gained popularity recently [15-27]. Compared to lithium, sodium is much more abundant and widely distributed as indicated in Figure 1.2. Therefore, sodium-ion batteries could be more sustainable than lithium-ion batteries.

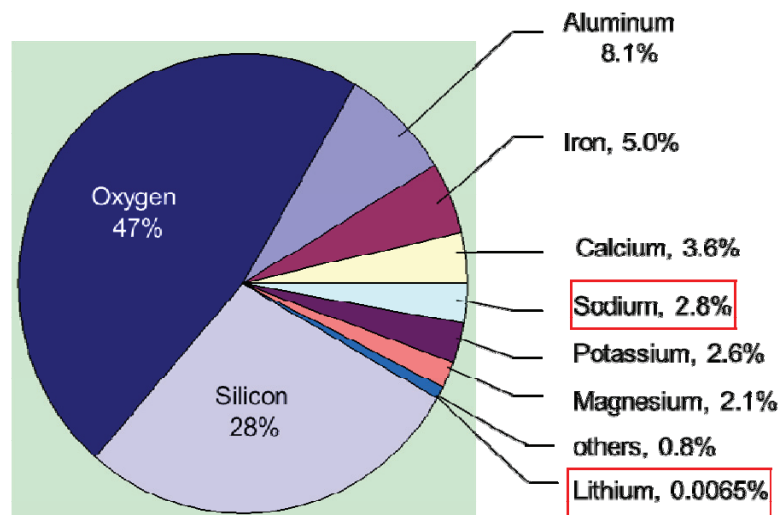


Figure 1.2 Abundance of elements by weight in the earth's crust [28]

A sodium-ion cell is analogous to a Li-ion cell except Na replaces Li. A Na-ion cell includes: a positive electrode, a negative electrode, and an electrolyte (as shown in Figure 1.3). On paper, a Na-ion cell can be made in the same way as a Li-ion cell by simply “replacing” “Li” with “Na” in the electrode materials and electrolyte. In reality, it is not so simple because the negative electrode, lithiated graphite of a Li-ion cell does not have an analogous sodium counterpart. Additionally, there are more concerns and potential issues with sodium-ion cells, which motivate more study.

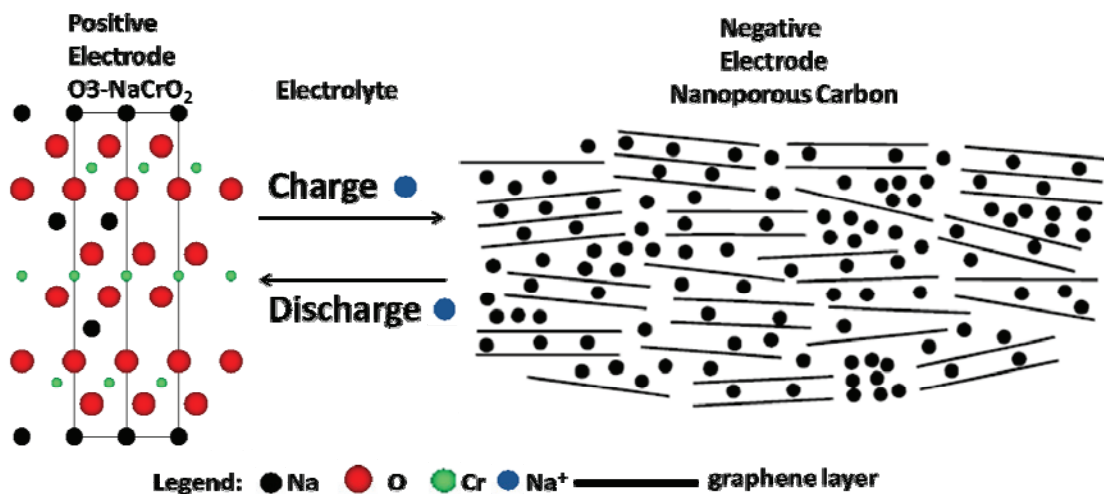


Figure 1.3 A schematic of a sodium-ion battery

## 1.2.1 Positive electrode materials for sodium-ion batteries

### 1.2.1.1 $\text{Na}_x\text{CoO}_2$

$\text{Na}_x\text{CoO}_2$  was studied as the first positive electrode material for sodium-ion batteries. In the 1980s, Delmas *et al.* reported the electrochemical properties of P2-type

$\text{Na}_{0.70}\text{CoO}_2$  for sodium cells [15]. The designation “P2” means Na atoms in prismatic sites and a unit cell containing two  $\text{CoO}_2$  slabs. Figure 1.4 shows the crystal structure of  $\text{P2-Na}_{2/3}\text{CoO}_2$  in a [110] projection. Recently, the same group published a detailed study of the electrochemical properties of  $\text{Na}_x\text{CoO}_2$  having a P2-structure [16]. Figure 1.5 shows the potential versus specific capacity of a  $\text{Na}/\text{Na}_{0.74}\text{CoO}_2$  cell. Several plateaus and steps, which are related to several  $\text{Na}_x\text{CoO}_2$  two-phase and single-phase domains during intercalation and deintercalation, could be observed. They also pointed out that electrochemical intercalation/deintercalation could be the best way to control the accurate sodium content when synthesizing  $\text{Na}_x\text{CoO}_2$ .

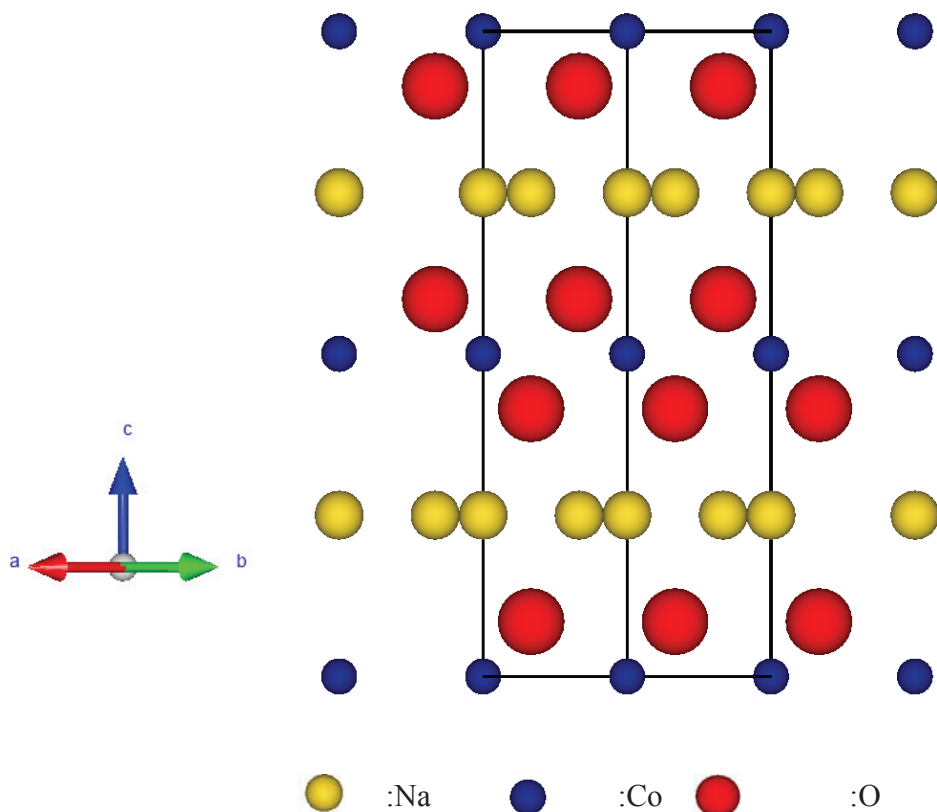


Figure 1.4 Crystal structure of  $\text{P2-Na}_{2/3}\text{CoO}_2$  in a [110] projection (Na sites are filled with a probability of 1/3)

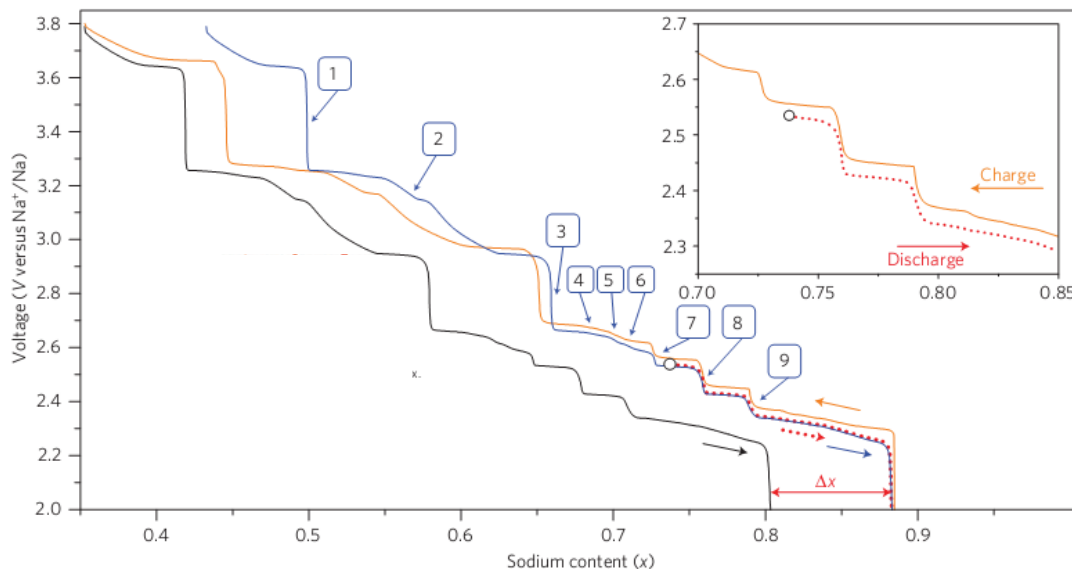


Figure 1.5 Potential versus specific capacity of a  $\text{Na}_{0.74}\text{CoO}_2$  electrode in a  $\text{Na}/\text{Na}_{0.74}\text{CoO}_2$  cell as reported in ref. [16]. Reprinted by permission from Macmillan Publishers Ltd: Nature Materials. Copyright 2010.

### 1.2.1.2 $\text{NaCrO}_2$

The electrochemical properties of O3-type  $\text{NaCrO}_2$  as a positive electrode material for sodium-ion batteries were first studied by Delmas *et al.* in 1982 [17]. Figure 1.6 shows a view of the crystal structure of O3- $\text{NaCrO}_2$  in a [110] projection. Figure 1.7 shows the first cycle of their  $\text{NaCrO}_2$  vs. Na cell in  $\text{NaClO}_4/\text{PC}$  electrolyte.  $\text{NaCrO}_2$  showed very low capacity which corresponds to a deintercalated compound of  $\text{Na}_{0.85}\text{CrO}_2$ . This poor electrochemical performance suggested that  $\text{NaCrO}_2$  was not satisfactory as a battery material.

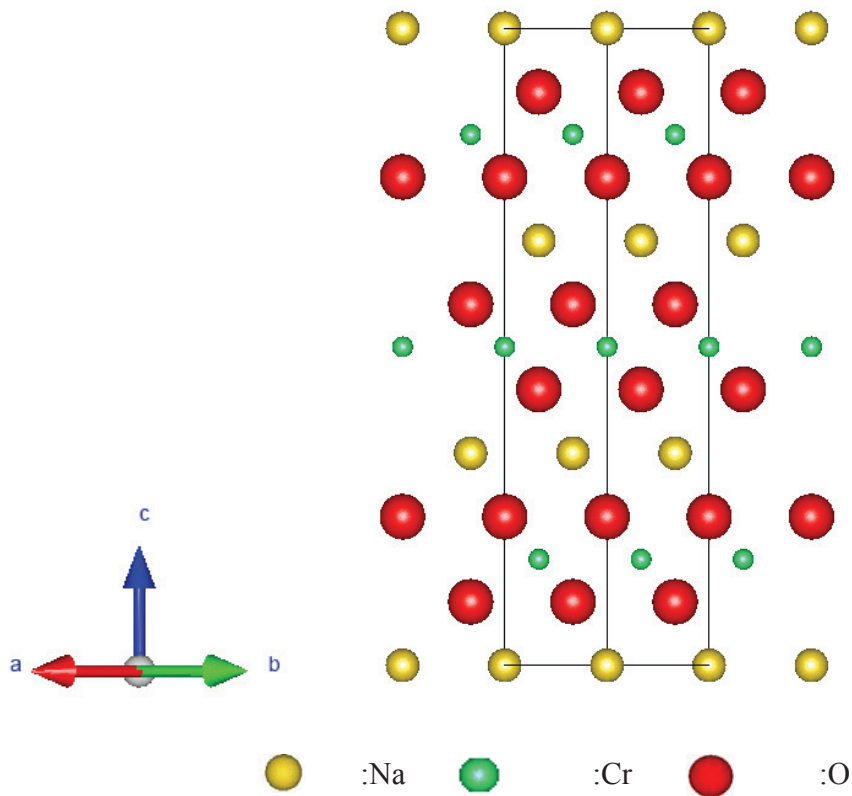


Figure 1.6 Crystal structure of O3-NaCrO<sub>2</sub> in a [110] projection

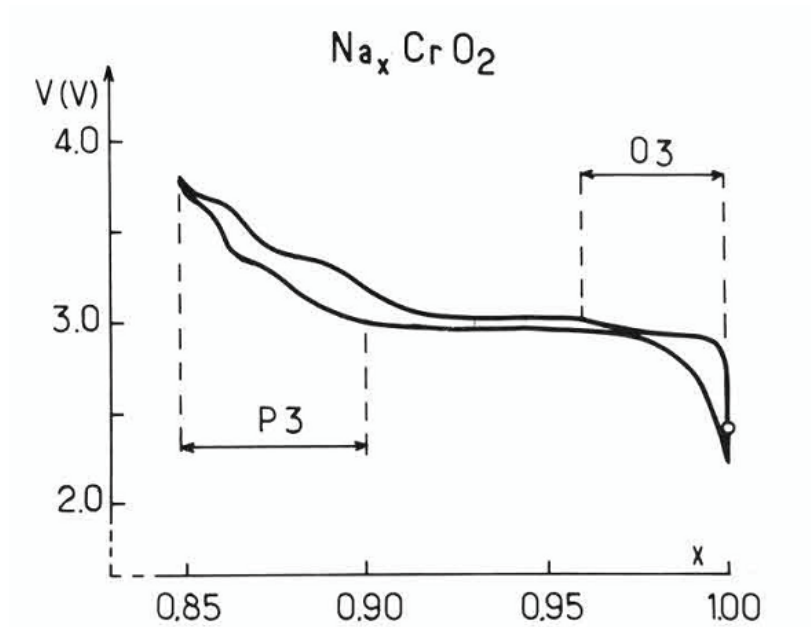


Figure 1.7 First cycle of NaCrO<sub>2</sub> vs. Na in NaClO<sub>4</sub>/PC electrolyte as reported in ref. [17]. Reprinted from Materials Research Bulletin, with permission from Elsevier. Copyright 1982

Recently, Komaba *et al.* reported promising electrochemical performance of O3-type NaCrO<sub>2</sub> through optimization of the synthesis route [18]. Figure 1.8 shows the potential versus specific capacity of NaCrO<sub>2</sub>/Na cells cycled between 2.0 and 3.6 V in NaClO<sub>4</sub>/PC electrolyte using a current density of 25 mA/g. The material delivered a capacity of about 120 mAh/g during the first charge and showed good capacity retention after 20 cycles. NaCrO<sub>2</sub> is one of the best candidate positive electrode materials for sodium-ion batteries from the view of electrochemical performance. In fact, in March, 2011, Sumitomo Electric Industries announced a commercial secondary sodium-ion battery using NaCrO<sub>2</sub> as the positive electrode material, a Na alloy as the negative electrode material and sodium bis (fluoro sulfonyl) amide (NaFSA) as the molten salt electrolyte. This battery is expected to be commercialized in 2015.

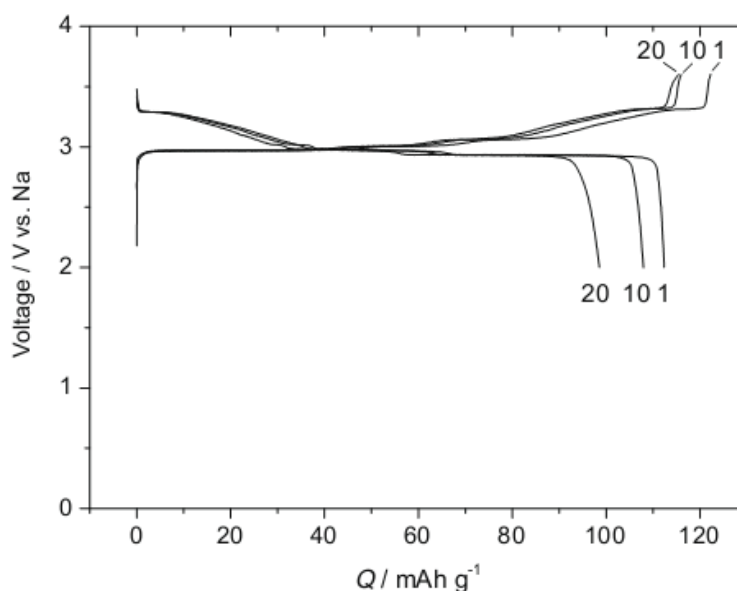


Figure 1.8 Charge/discharge curve of NaCrO<sub>2</sub>/Na cells cycled between 2.0 and 3.6 V in NaClO<sub>4</sub>/PC electrolyte using a current density of 25 mA/g as reported in Ref [18]. Reprinted from Electrochemistry Communications, with permission from Elsevier. Copyright 2010

### 1.2.1.3 $\text{NaNi}_{0.5}\text{Mn}_{0.5}\text{O}_2$

O3-type  $\text{NaNi}_{0.5}\text{Mn}_{0.5}\text{O}_2$  was studied as a positive electrode material for sodium-ion batteries by Komaba *et al.* [19]. Figure 1.9 shows the potential versus specific capacity for a  $\text{NaNi}_{0.5}\text{Mn}_{0.5}\text{O}_2/\text{Na}$  cell cycled between 2.0 and 3.8 V, and the capacity versus cycle number for the cell. A couple of potential-capacity plateaus can be observed, which are related to the phase transitions: Hex. O3  $\rightarrow$  Mon. O3  $\rightarrow$  Hex. P3  $\rightarrow$  Mon. P3.  $\text{NaNi}_{0.5}\text{Mn}_{0.5}\text{O}_2$  could deliver a capacity of 150 mAh/g during the first charge and cycle well for at least 20 cycles. The same group also reported the electrochemical performance of  $\text{NaNi}_{0.5}\text{Mn}_{0.5}\text{O}_2/\text{hard carbon Na-ion}$  cells, which is shown in Figure 1.10. The cell has a voltage of 2.8 V. Assuming the capacity of  $\text{NaNi}_{0.5}\text{Mn}_{0.5}\text{O}_2$  ( $\sim 120$  mAh/g)/hard carbon ( $\sim 240$  mAh/g), the sodium ion cells could achieve about 60% of the practical energy density of a conventional lithium-ion battery (3.7 V) using  $\text{LiCoO}_2$  ( $\sim 140$  mAh/g) and graphite ( $\sim 350$  mAh/g) [20]. These promising results indicate that it is possible to make a sodium-ion battery.

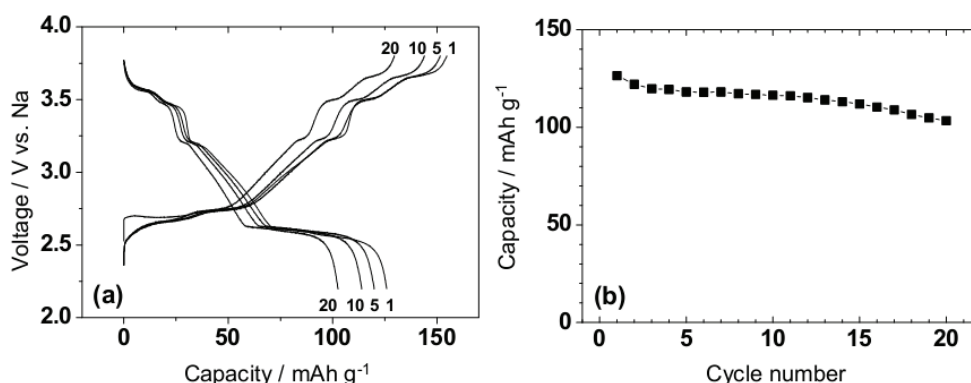


Figure 1.9 Charge/discharge curves of  $\text{NaNi}_{0.5}\text{Mn}_{0.5}\text{O}_2/\text{Na}$  cells cycled between 2.0 and 3.8 V, and the cycle performance of the cells as reported in ref. [19]. Reprinted with permission from The Electrochemical Society. Copyright 2009.



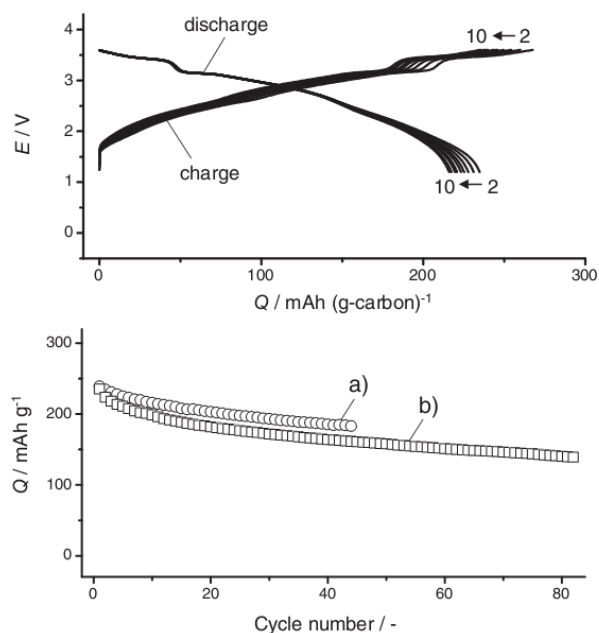


Figure 1.10 Charge/discharge curve and cycle performance of  $\text{NaNi}_{0.5}\text{Mn}_{0.5}\text{O}_2$ /hard carbon Na-ion cells cycled between 1.0 and 3.8 V as reported in ref. [20]. Reprinted with permission from John Wiley and Sons. Copyright 2011.

#### 1.2.1.4 $\text{Na}_x\text{Fe}_{0.5}\text{Mn}_{0.5}\text{O}_2$

Researchers and manufacturers have tried to lower the cost of positive electrode materials in lithium-ion batteries using cheaper metal elements, such as Mn and Fe, to substitute for the more expensive ones, like Co and Ni. The same efforts have been tried in sodium-ion battery materials. Recently, Komaba *et al.* reported the electrochemical performance of P2-type  $\text{Na}_x\text{Fe}_{0.5}\text{Mn}_{0.5}\text{O}_2$  as a positive electrode material for sodium-ion batteries [21]. Figure 1.11 shows the electrochemical performance of  $\text{Na}_x\text{Fe}_{0.5}\text{Mn}_{0.5}\text{O}_2$ /Na half cells cycled between 1.5 and 4.3 V. P2-type  $\text{Na}_x\text{Fe}_{0.5}\text{Mn}_{0.5}\text{O}_2$  could deliver a capacity of about 190 mAh/g, which is one of the largest ever reported, and has good capacity retention as well. Assuming the average voltage of  $\text{Na}_x\text{Fe}_{0.5}\text{Mn}_{0.5}\text{O}_2$  vs. Na is 2.75 V, the

energy density of  $\text{Na}_x\text{Fe}_{0.5}\text{Mn}_{0.5}\text{O}_2$  is estimated to be 520 mWh/g, which is competitive to that of  $\text{LiFePO}_4$  (about 530 mWh/g) and slightly higher than that of  $\text{LiMn}_2\text{O}_4$  (about 450 mWh/g) [21].

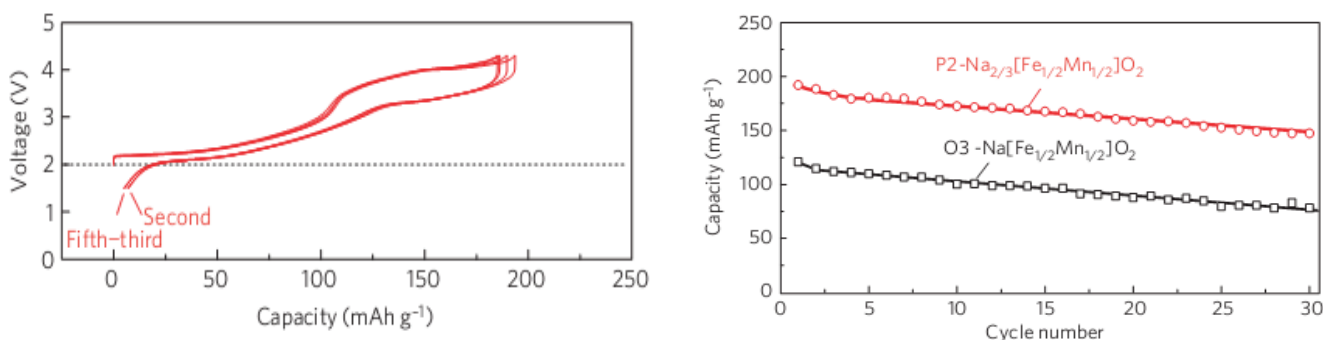


Figure 1.11. Charge/discharge curves and cycle performance of  $\text{Na}_{2/3}\text{Fe}_{0.5}\text{Mn}_{0.5}\text{O}_2/\text{Na}$  half cells cycled between 1.5 and 4.3 V as reported in ref. [21]. Reprinted by permission from Macmillan Publishers Ltd: Nature Materials. Copyright 2012

### 1.2.1.5 $\text{NaMnO}_2$ , $\text{Na}_{0.44}\text{MnO}_2$ , $\text{Na}_{2/3}\text{Ni}_{1/3}\text{Mn}_{2/3}\text{O}_2$

$\text{O3}$  type monoclinic  $\text{NaMnO}_2$  was studied as a positive electrode material for sodium-ion batteries by Ma et al. [22]. About 0.85 mol Na can be deintercalated and 0.8 mol Na can be reversibly intercalated when  $\text{NaMnO}_2//\text{Na}$  cells were cycled between 2.0 and 3.8 V. The cycling performance of the cells was good and no obvious structural changes could be observed. This result indicates the difference between Na and Li manganese layered compounds, since layered  $\text{LiMnO}_2$  converts to spinel  $\text{LiMn}_2\text{O}_4$  during electrochemical cycling and this process causes a large loss of capacity [22].

Doeff et al. reported the structure and electrochemical performance of another Na manganese compound, which is  $\text{Na}_{0.44}\text{MnO}_2$  [23].  $\text{Na}_{0.44}\text{MnO}_2$  crystallizes in an

orthorhombic lattice (*Pbam* space group). Mn is located in five types of sites and Na is located in two types of sites. In a Na//P(EO)<sub>8</sub>NaCF<sub>3</sub>SO<sub>3</sub>//Na<sub>0.44</sub>MnO<sub>2</sub> polymer cell, Na<sub>0.44</sub>MnO<sub>2</sub> delivered a capacity of about 160 mAh/g when charged to 3.5 V [23]. The electrochemical performance of Na<sub>0.44</sub>MnO<sub>2</sub> in a sodium-ion battery needs to be investigated in the future.

Lu *et al.* reported the structural changes and electrochemical performance of P2-Na<sub>2/3</sub>Mn<sub>2/3</sub>Ni<sub>1/3</sub>O<sub>2</sub> as a function of Na content [24]. The material achieved capacity of 160 mAh/g when charged to 4.5 V and showed good cycling performance. An *in situ* XRD study showed that when x in Na<sub>x</sub>Mn<sub>2/3</sub>Ni<sub>1/3</sub>O<sub>2</sub> was greater than 1/3, the compound adopted the P2 structure. When x ≈ 1/3, some O2-type stacking faults develop. When x < 1/3, a mixture of Na<sub>1/3</sub>Mn<sub>2/3</sub>Ni<sub>1/3</sub>O<sub>2</sub> and Mn<sub>2/3</sub>Ni<sub>1/3</sub>O<sub>2</sub> phases exists.

#### **1.2.1.6 Other positive electrode materials for Na-ion batteries**

Some new types of sodium intercalation compounds have been studied as positive electrodes in sodium-ion batteries. Ellis *et al.* first synthesized the new compounds, Na<sub>2</sub>MPO<sub>4</sub>F (M= Fe, Mn, Co, Ni) with space group *Pbcn*, and then studied their structural properties and electrochemical performance vs. Li in test cells [25]. Recently, Komaba *et al.* studied the electrochemical performance of carbon-coated Na<sub>2</sub>FePO<sub>4</sub>F for sodium-ion batteries. They found that Na<sub>2</sub>FePO<sub>4</sub>F synthesized with 2% ascorbic acid delivered about 110 mAh/g of reversible capacity and that the rate capability was acceptable [26]. Tripathi *et al.* also reported structural and electrochemical properties of a new sodium

intercalation compound  $\text{NaFeSO}_4\text{F}$  [27]. However, all these new compounds have not received as much attention as the layered-structure compounds due to their relatively poor electrochemical performance and complicated synthesis conditions.

## **1.2.2 Negative electrode materials**

### **1.2.2.1 Hard carbon**

Compared with positive electrode materials, there are far fewer scientific reports on negative electrode materials for sodium-ion batteries. Only a very small amount of sodium can intercalate into graphitized carbon, which is used as the negative electrode material for lithium-ion batteries. Presently, nanoporous or hard carbon is the most attractive negative electrode material for sodium-ion batteries. In this document, "hard carbon" means carbon synthesized from certain carbonaceous precursors (such as wood, sugar or phenolic resin) by pyrolysis in inert atmosphere at elevated temperature. Such a synthesis does not allow the formed graphene sheets to stack in a parallel manner. As a result, nanopores are formed in the carbon structure. Stevens *et al.* studied the mechanism of sodium insertion in hard carbon by SAXS (small angle X-ray scattering), and they explained that the insertion of Na into hard carbon could be divided into two parts: sodium inserting between the parallel graphene layers and sodium inserting into the nanopores [29, 30]. Figure 1.12 shows a schematic of the hard carbon structure and the mechanism for sodium/lithium insertion into hard carbon.

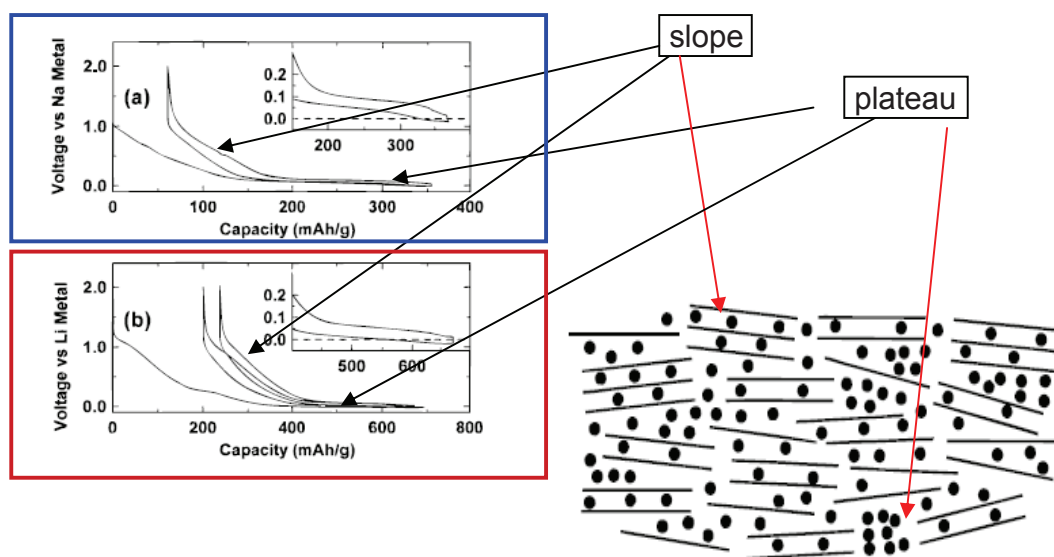


Figure 1.12 (Left) Charge/discharge curve of hard carbon vs. Li and hard carbon vs. Na. (Right) A schematic of alkali metal insert into hard carbon. Taken from ref. [30]. Reprinted with permission from The Electrochemical Society. Copyright 2001.

Komaba *et al.* recently reported sodium/hard carbon cells with a stable capacity of 250 mAh/g for 50 cycles. The cells used hard carbon and sodium metal as the working electrodes [20]. They also reported similar electrochemical performance for full cells using  $\text{NaNi}_{0.5}\text{Mn}_{0.5}\text{O}_2$  as the positive electrode and hard carbon as the negative electrode [20].

### 1.2.2.2 Other compounds

Nanocrystalline  $\text{Fe}_3\text{O}_4$  and  $\alpha\text{-Fe}_2\text{O}_3$  were also reported to have a capacity of 190 mAh/g in sodium cells with a voltage range between 1.2-4.0 V [31].

Senguttuvan *et al.* reported that  $\text{Na}_2\text{Ti}_3\text{O}_7$  has the lowest voltage ever reported for sodium insertion, which had a capacity of around 200 mAh/g at an average voltage of 0.3

V [32].

Recently, some alloy negative electrode materials for sodium-ion batteries have been studied [33, 34]. Ellis et al. reported the electrochemistry and structural changes that occurred during sodium insertion and removal from Tin [33]. The alloy formed at full sodiation was found to be  $\text{Na}_{15}\text{Sn}_4$ . Three unknown intermediate Na-Sn phases were found during sodiation [33].

### **1.2.3 Electrolyte**

So far, there are few reports on electrolytes for sodium-ion batteries. There is a recent report by Ponrouch *et al.* [35]. They finished a comparative study on electrolytes with different salts ( $\text{NaClO}_4$ ,  $\text{NaPF}_6$  and  $\text{NaTFSI}$ ) and different solvents (PC, EC, DEC, DMC, and THF) or solvent mixtures (EC:DMC, EC: PC and EC: DME). They studied the viscosity, ionic conductivity and electrochemical and thermal stability of these electrolytes. They found  $\text{NaPF}_6$  in EC:PC electrolyte showed the best properties over all [35].

### **1.3 Flame retardants as electrolyte additives for lithium-ion batteries**

Flame retardants are chemicals used widely in thermoplastics, thermosets, textiles and coatings that inhibit or resist the spread of fire. They can be divided in to several different classed of chemicals:

1. Minerals such as aluminum hydroxide, magnesium hydroxide, various hydrates, red phosphorus and boron compounds [36].

2. Organohalogen compounds: These include organochlorines such as, chlorendic acid derivatives and chlorinated paraffins; organobromines such as decabromodiphenyl ether, decabromodiphenyl ethane, polymeric brominated compounds such as brominated polystyrenes, brominated carbonate oligomers , brominated epoxy oligomers (BEOs), tetrabromophthalic anyhydride, tetrabromobisphenol A and hexabromocyclododecane . Most, but not all, halogenated flame retardants are used in conjunction with a synergist to enhance their efficiency. Antimony trioxide is widely used but other forms of antimony such as the pentoxide and sodium antimonate are also used [36].

3. Organophosphorus compounds such as organophosphates, tris(2,3-dibromopropyl) phosphate, triphenyl phosphate, resorcinol bis- (diphenyl phosphate), bisphenol a bis- (diphenyl phosphate), tri-o-cresyl phosphate, phosphonates such as dimethyl methylphosphonate and phosphinates. There is also an important class of flame retardants that contain both phosphorus and halogen, examples of such are the chlorophosphates like tris(2-chloroisopropyl) phosphate and tris(1,3-dichloroisopropyl) phosphate [36].

Mineral flame retardants are typically additives while organohalogen and organophosphorus can be either reactive or additive. Additives are compounds that are

added into materials with high flammability to reduce the flammability. Reactives are compounds that react with the easily-flammable material through chemical reaction to reduce the flammability. The basic mechanisms of flame retardancy vary dependent on the specific flame retardant and the substrate. Additive and reactive flame-retardant chemicals can function in the vapor or condensed phase [36].

There are several mechanisms that have been proposed for the function of flame retardants.

1. Endothermic degradation.

Some compounds break down endothermically when subjected to high temperatures. Magnesium and aluminum hydroxides are an example, together with various carbonates and hydrates such as mixtures of huntite and hydromagnesite [36]. The decomposition removes heat from the substrate, thereby cooling the material. The use of hydroxides and hydrates is limited by their relatively low decomposition temperature, which limits the maximum processing temperature of polymers which they are added to (typically used in polyolefins for wire and cable applications) [36].

2. Thermal shielding

A way to stop the spreading of flame over a solid material is to create a thermal insulating barrier between the burning and unburned parts. Intumescent additives are often employed; their role is to turn a polymer into a char, which separates the flame from the material and slows the heat transfer to the unburned fuel [36].



### 3. Dilution of gas phase

Inert gases (most often carbon dioxide and water) produced by thermal degradation of some materials act as diluents of the combustible gases, lowering their partial pressures and the partial pressure of oxygen, and slowing the reaction rate [37].

### 4. Gas phase radical quenching

Chlorinated and brominated materials undergo thermal degradation and release hydrogen chloride and hydrogen bromide, or if used in the presence of a synergist like antimony trioxide, release antimony halides. These react with the highly reactive  $H\cdot$  and  $OH\cdot$  radicals in the flame, resulting in an inactive molecule and a  $Cl\cdot$  or  $Br\cdot$  radical. The halogen radical has much lower energy than  $H\cdot$  or  $OH\cdot$ , and therefore has much lower potential to propagate the radical oxidation reactions of combustion [38].

#### 1.3.1 Organophosphorus flame retardant additives

The first report of a flame retardant additive in the electrolyte of a lithium-ion battery was described by Prakash *et al* [39]. Figure 1.13 (a) shows DSC results of lithiated graphite in different electrolytes. Prakash *et al.* found that adding a flame retardant additive- Hexamethoxycyclotriphosphazene (HMPN) (1.68%) could significantly reduce the overall heat produced due to the exothermic reactions. In addition, for the electrolyte containing the flame retardant additive, the exothermic peak also shifted to higher temperature. Figure 1.13 (b) shows ARC results for lithium metal reacting with different electrolytes. For lithium metal in electrolyte without the flame

retardant additive, the onset temperature of the exothermic reaction was 177.6°C, and the maximum self-heating rate reached 0.68°C/min. As a comparison, the maximum self-heating rate for the reaction between lithium metal and electrolyte with 10% HMPN was 0.196°C/min at T=170.2°C. Figure 1.13b shows that the exothermic peak was suppressed in the presence of flame retardant. This may be attributed to the passivation layer on the surface of the lithium metal formed by the flame retardant additive. While Li/electrolyte reactivity decreased, the electrochemical performance of LiNi<sub>0.8</sub>Co<sub>0.2</sub>O<sub>2</sub>//Li half cells was not impacted negatively, which may due to the small amount of flame retardant additive used (~ 1.5 wt%).

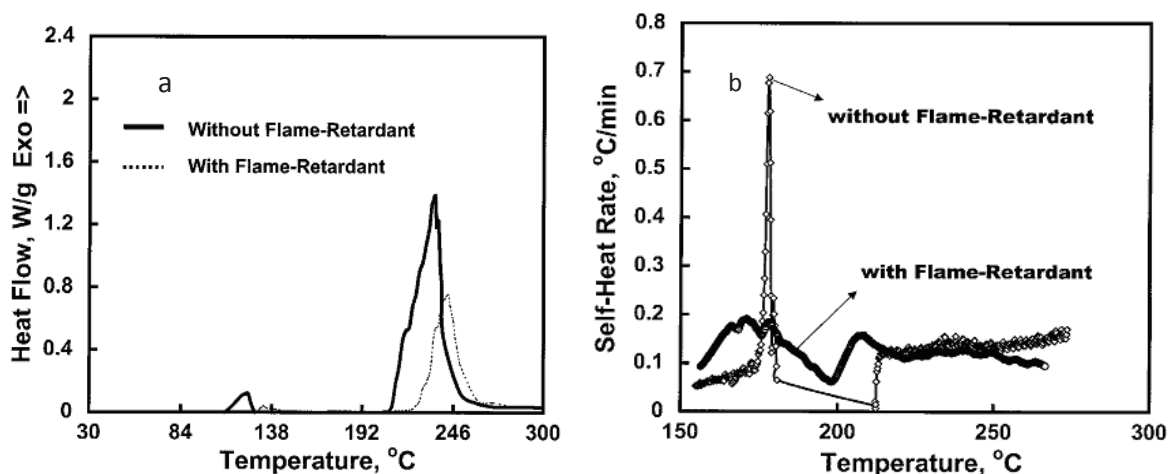


Figure 1.13 (a) DSC results of lithiated graphite in electrolytes with/without HMPN; (b) ARC results of lithium metal in electrolytes with/without HMPN as reported in ref. [39]. Reprinted with permission from The Electrochemical Society. Copyright 2000

Since the report by Prakash *et al.*, organophosphorus compounds have been studied as flame retardant additives for lithium-ion batteries. Organophosphorus

compounds were chosen mainly due to their great success as flame retardants in polymers, and the deeper understanding of combustion of organic materials. Organophosphorus compounds provide flame retardation by two mechanisms: (1) char-formation, which is similar to mechanism “2” discussed in last section; and (2) radical-scavenging, which is similar to mechanism “4” discussed in last section [38].

Wang *et al.* studied trimethyl phosphate (TMP) as a flame retardant additive for lithium-ion batteries [40]. When the TMP content exceeded a critical value, which depended on the flammability of the co-solvents used, nonflammability of the electrolytes was achieved. Figure 1.14 shows the lowest TMP content needed to ensure nonflammability of various electrolytes containing TMP. The needed TMP content increased in the following order: EC < PC < GBL < DEC < EMC < DME. Based on previous work showing that radical species containing phosphate were detected in mass spectroscopy experiments, they proposed that the radical containing phosphorus acted like a trap to scavenge the main active agent for flame propagation,  $H\cdot$  radicals [38]. They also derived an empirical equation to estimate the minimum amount ( $N_{\text{limit}}$ ) of TMP needed to achieve nonflammability in any binary electrolyte composition:

$$\log N_{\text{limit}} = 2.6 - 9.3(C_p T_H^* / C_H T_p^*) \quad (\text{Equation 1.1})$$

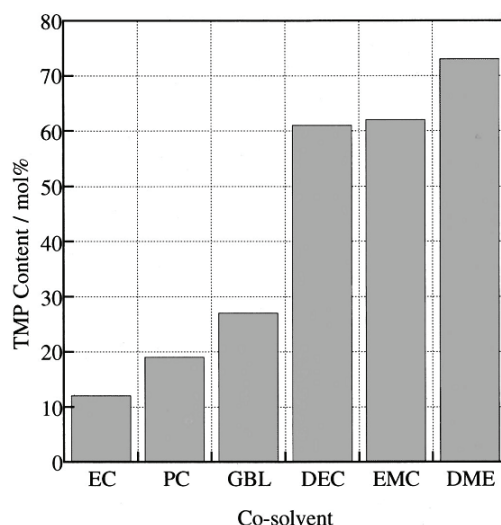


Figure 1.14 The lowest TMP content needed to ensure nonflammability of various electrolytes using different solvents from ref.[40]. Reprinted with permission from The Electrochemical Society. Copyright 2001.

The quantity  $C_P T_H / C_H T_P$  is called “non-flammability index”, which is defined by the atoms content of H or P (numbers of atoms) in the two electrolyte components and their boiling points.  $C_H$  in Equation 1.1 is the number of H atoms in each molecule of the solvent.  $C_P$  in Equation 1.1 is the number of P atoms in each molecule of the flame retardant.  $T_H$  and  $T_P$  are the boiling points of the solvent and the FR respectively. Figure 1.15 shows the relationship between the nonflammability index and the lowest TMP content needed to ensure nonflammability based on the result of Figure 1.14. The higher the boiling point and the lower the H content of the co-solvent, the lower the flammability that could be achieved. Hence, cyclic carbonates with higher boiling points and lower H content, such as EC and PC, should be chosen as co-solvents to reduce electrolyte flammability. At the same time, the effectiveness of a certain flame retardant is proportional to its P content and inversely proportional to its boiling point. This result

could guide the search for flame retardants with higher effectiveness.

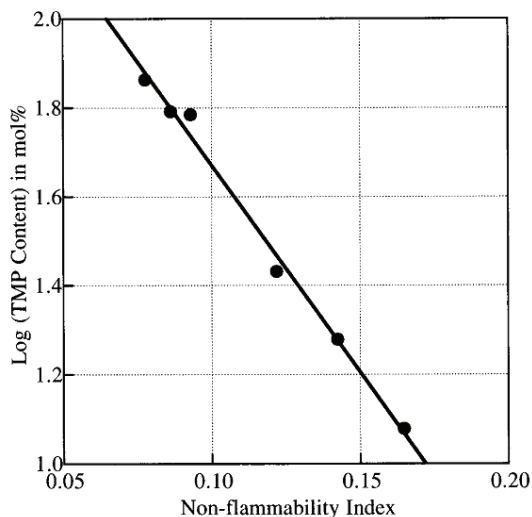


Figure 1.15 The relationship of nonflammability index and the lowest TMP content needed to ensure nonflammability from ref. [40]. Reprinted with permission from The Electrochemical Society. Copyright 2001

Figure 1.16 shows the thermal stability of natural graphite/LiCoO<sub>2</sub> (LiMn<sub>2</sub>O<sub>4</sub>) cells with different electrolytes measured using a Calvet-type calorimeter (Setaram C80) [40]. The authors claimed that thermal stability of the cells was significantly improved when 20% TMP was added to the electrolyte. The electrochemical performance of the Li/LiCoO<sub>2</sub> cells was not impacted negatively by the presence of TMP [40]. However, TMP shows poor reductive stability on a graphitic anode surface. It also cointercalated into the graphite structure at 1.2 V, similar to PC. TMP also increased the impedance of cells and caused poor capacity retention [40].

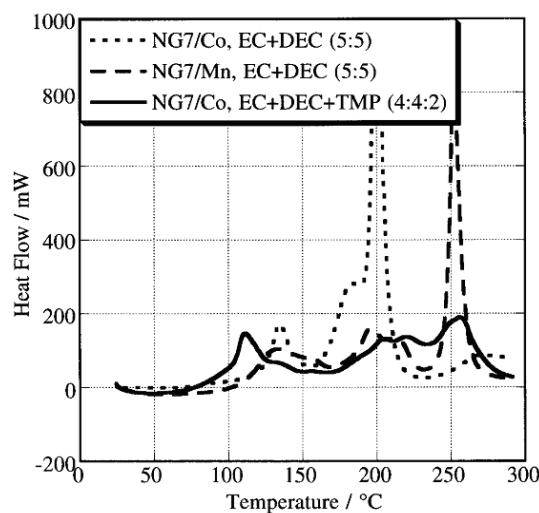


Figure 1.16 The thermal stability of natural graphite/LiCoO<sub>2</sub> (LiMn<sub>2</sub>O<sub>4</sub>) cells with different electrolytes as reported in ref. [40]. Reprinted with permission from The Electrochemical Society. Copyright 2001

Following these two reports about HMPN and TMP, Xu *et al.* systematically characterized these two compounds along with triethyl phosphate (TEP) and tried to establish a correlation between the flame-retarding ability and cell performance of these already known flame retardants (FRs) [41]. In order to characterize the flammability of the electrolyte system quantitatively, a new test called the self-extinguishing time (SET) test based on the standard test UL 94 HB (intended for polymeric or other solid samples), was proposed. The new method normalized the extinguishing time to the amount of electrolyte, which significantly improved the reproducibility of the test. It was also found to be more suitable for samples of low flammability. The SET test will be discussed further in section 2.10.

Figure 1.17 shows the normalized SET obtained vs. the weight percentage of TMP, TEP and HMPN in various electrolytes. In all cases the FRs were tested up to 40%.

The flammability of EC/EMC based electrolytes was reduced dramatically as the FR content increased from 5%. However, the electrolytes were not totally nonflammable even when 40% FR was added. The efficiency of TMP and TEP in reducing flammability was nearly equivalent, and apparently better than HMPN [41].

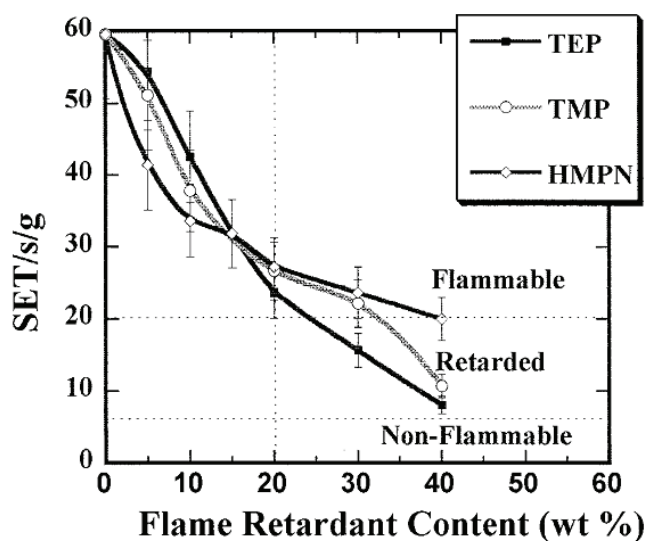


Figure 1.17 Normalized SET thus obtained vs. the weight percentage of TMP, TEP and HMPN in electrolytes as reported in ref [41]. Reprinted with permission from The Electrochemical Society. Copyright 2002

Figure 1.18 shows the effect of these three FRs on the cathodic stability of the electrolyte vs. a carbonaceous anode. It was found that when over 10% TMP was added, the decomposition of TMP on the anode surface, which occurred at 0.5 V and intensified with TMP concentration, made it impossible to use in a lithium-ion cell [41]. This result agrees well with the conclusion of Wang *et al.* [40]. However, TEP and HMPN showed very good stability on the anode material even when the concentration of FR was as large as 50%, without detection of any decomposition of TEP or HMPN.

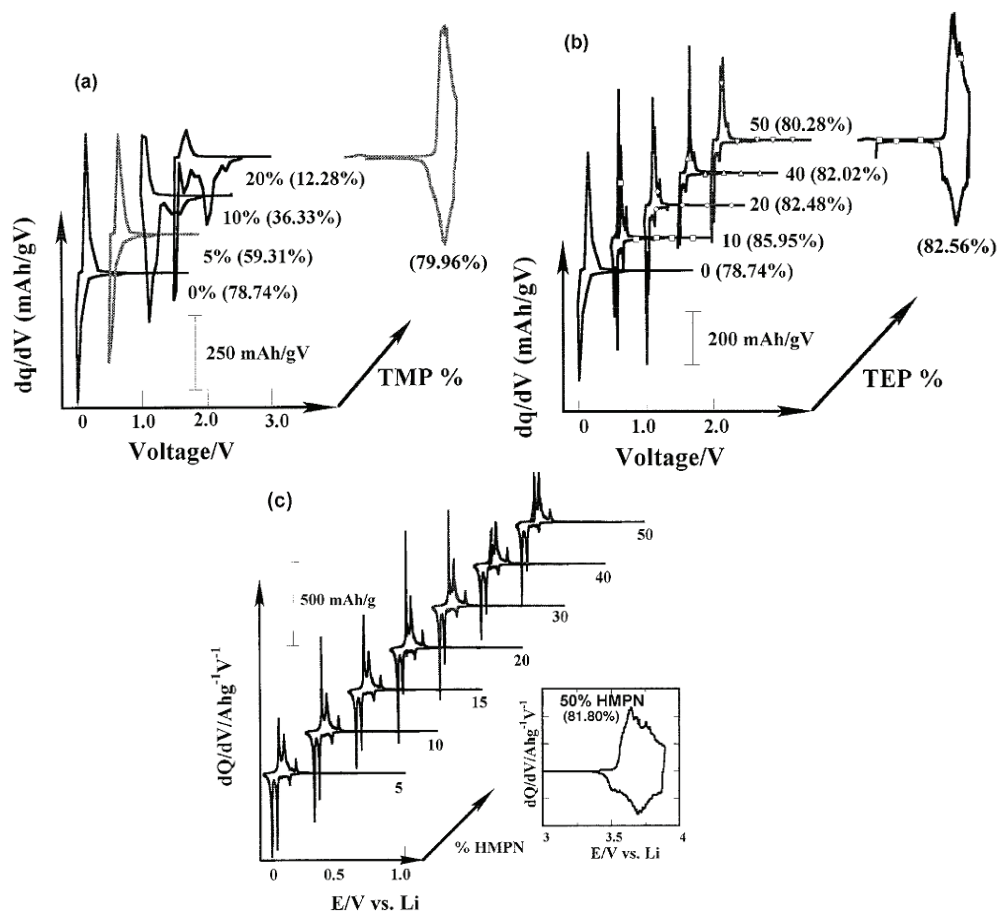


Figure 1.18 Differential capacity of the graphite anode and the cathode in various TMP, TEP and HMPN-containing electrolytes. The first cycles are shown and FR concentrations are indicated followed by the columbic efficiency of the cathodic cycling. Take from ref. [41]. Reprinted with permission from The Electrochemical Society. Copyright 2002

Figure 1.19 summarizes the dependence of full cell performance (both flammability and electrochemical performance) on FR concentration [41]. A relationship between the flammability, the capacity utilization and the capacity retention ( $R_{100/1}$  for TMP and TEP,  $R_{50/1}$  for HMPN) was established. Before the electrolyte flammability could be reduced significantly by the addition of TMP (<15%), the capacity utilization and capacity retention suffered. The presence of TEP seems to have little impact on the



initial capacity of the cells even up to 50%. However, TEP addition degraded the capacity retention,  $R_{100/1}$ . HMPN showed good capacity utilization and capacity retention due to its high stability on the surface of both the anode and cathode. However, considering its insufficient flame-retarding ability, it was not possible to achieve a balance between electrolyte flammability and electrochemical performance.

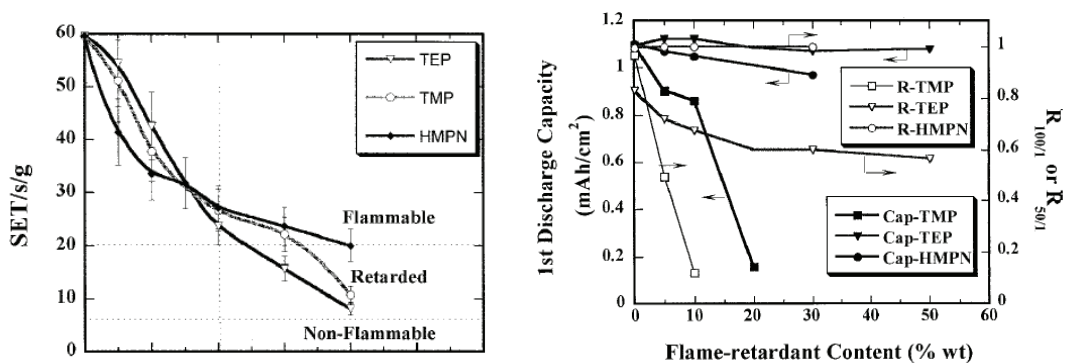


Figure 1.19 Trade-off between the flammability and electrochemical performance of the electrolytes as reported in ref. [41]. Reprinted with permission from The Electrochemical Society. Copyright 2002

Based on the study of the three phosphorous-containing FRs discussed above, Xu *et al.* modified the structure of alkyl phosphates by fluorination and characterized the effect of the fluorinated phosphates on the flammability of electrolytes and the electrochemical performance of the cells [42, 43]. They believed that F was one element with low flammability which was similar to P, and that organofluorides could help to form a stable SEI on the anode surface which could improve the electrochemical stability of the FRs.

Three fluorinated phosphates, tris(2, 2, 2-trifluoroethyl) phosphate (TFP), bis (2,

2, 2- trifluoroethyl) methylphosphate (BMP), and (2, 2, 2-trifluoroethyl)diethyl phosphate (TDP), were synthesized. Some of the physical properties of these fluorinated phosphates and their non-fluorinated counterparts are shown in Table 1.2. All fluorinated alkyl phosphates show a lower boiling point and a higher melting point than the non-fluorinated phosphates, as well as a lower dielectric constant.

Table 1.2 Some physical properties of different flame retardants from ref. [42]

FRs	TFP	BMP	TDP	TMP	TEP	HMPN
bp (°C)	178	203	210	197	215	>250(dec.)
mp (°C)	-19.6	-22.5		-46	-56.4	50
$\epsilon_{20^\circ\text{C}}$	10.5	12	15	20.7	12	
$C_{\text{set}}$ (wt%)	20	20	40	>40	>40	>40
1 <sup>st</sup> CE <sub>A</sub>	0.911	0.884	0.734	0.825	0.825	0.915
1 <sup>st</sup> CE <sub>C</sub>	0.770	0.790	0.760	0.801	0.801	0.801

( $C_{\text{set}}$ : Concentration of the FRs needed to ensure nonflammability of the electrolytes.

1<sup>st</sup> CE<sub>A</sub>: 1st cycle coulombic efficiency of control electrolyte (1M LiPF<sub>6</sub> in EC:EMC (1:1 w/w)) containing 20% FR at graphitic anode.

1<sup>st</sup> CE<sub>C</sub>: 1st cycle coulombic efficiency of control electrolyte containing 20% FR at nickel-based cathode.)

Figure 1.20 shows the self-extinguishing time (SET) of different electrolytes vs. the percentage of FRs added to the electrolytes. The results for TMP, TEP and HMPN were shown before in Figure 1.17. Electrolytes containing 20% TFP and BMP were completely nonflammable (SET < 6 s/g); while up to 40% TDP was required to achieve this goal [42]. TFP and BMP are better at reducing the flammability of electrolyte than TMP, TEP and HMPN. TDP is not as effective as TFP and BMP, which could be due to

insufficient fluorination. In addition to the intrinsic flame retarding ability of the phosphate structure, fluorination of the alkyls appears to add extra flame retarding properties to the molecules. Since the required FR concentration drops to 20%, it may be possible to make a nonflammable electrolyte without sacrificing the electrochemical performance of the cells [42].

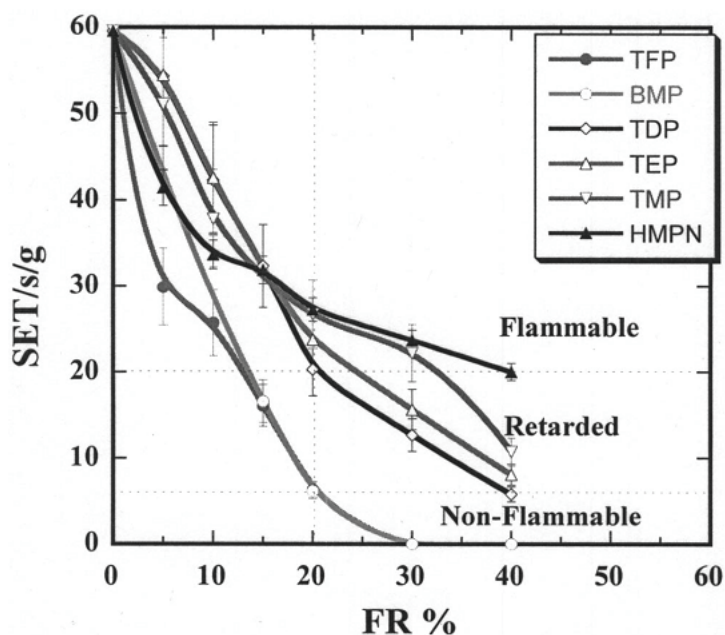


Figure 1.20 Normalized SET thus obtained vs. the weight percentage of TMP, TEP and HMPN, TFP, BMP and TDP in electrolytes as reported in ref. [42]. Reprinted with permission from The Electrochemical Society. Copyright 2003

The fluorinated phosphates showed generally improved cathodic stability except for TDP [42]. Both TEP and BMP showed reductive decomposition at a potential of  $\sim 1.0$  V, which is higher than the potential of lithium intercalation and for the reduction of carbonate solvents. Hence, it is reasonable to believe that the SEI will contain some fluorine-containing organic compounds that might protect the graphite structure due to

the absence of sustained decomposition of the FRs. Long term storage tests probed the stability of electrolytes containing such FRs in fully charged lithium ion cells at 70°C. However, TDP decomposes reductively at 0.5 V and the decomposition continues to lower potential where lithiation of the graphite occurs. The SEI in this case is not as protective as that which forms when TEP or BMP are present. Continuous decomposition of co-solvent could lead to a thicker SEI film, which may increase the impedance of cells. Such unstable cathodic performance disqualifies TDP as a FR for lithium-ion batteries.

Figure 1.21 shows the capacity retention of cells (after 100 cycles, defined as  $C_{100}$ ) with different electrolytes containing different amount of FRs [43]. Both TDP and HMPN cause a decrease in cell capacity, especially TDP, which causes severe deterioration in cell performance due to its poor cathodic stability on graphitic carbon as mentioned above. HMPN has good stability on both anode and cathode materials. The drop in capacity as the HMPN concentration increases is believed to be the result of its high viscosity or the high impedance of the SEI formed upon the decomposition of electrolyte containing HMPN. On the other hand, both TFP and BMP showed a maximum in capacity at concentrations lower than 20%; at higher concentrations the high cell impedance is eventually overwhelming and subsequently cell capacity decreases, but the rate of decrease is still less severe than HMPN-based electrolytes.

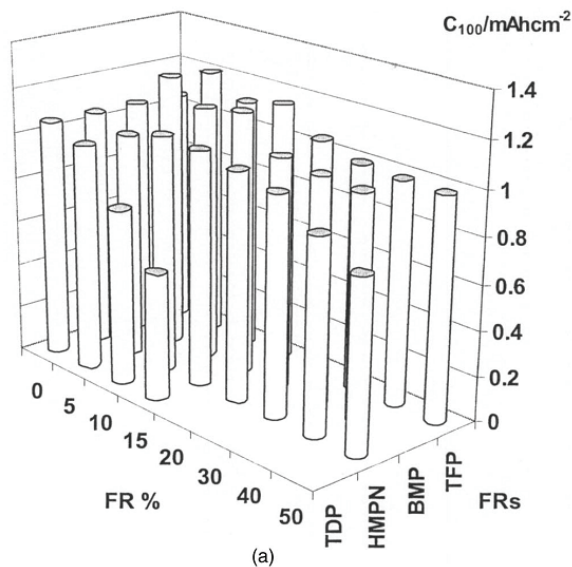


Figure 1.21 Capacity retention of cells with different electrolytes containing different amount of FRs as reported in ref. [43]. Reprinted with permission from The Electrochemical Society. Copyright 2003

The stable performance of cells containing TFP and BMP suggests their feasibility to be used in lithium ion cells. Overall, considering the electrochemical performance of the cells and the flammability of the electrolytes, 20 % TFP or BMP could be used to make a safer cell without negative impact on the cell's performance. However, in a following study, Xu *et al.* found that TFP reduced the rate capability and low-temperature performance of the cells, due to high impedance introduced by TFP [43]. Finally, they proposed a compromised electrolyte which could be between 15 and 20% TFP/BMP in 1.0 M LiPF<sub>6</sub>/EC/EMC(1: 1 v/v) or 30% TFP/BMP in 1.0 M LiPF<sub>6</sub>/PC/EC/EMC (1:1:3 v/v/v) . They considered the nonflammability and SEI stability of the electrolytes, as well as the capacity utilization, rate capabilities, and low-temperature operation of cells. Such electrolytes are completely or at least nearly nonflammable, thus effectively reducing the

potential for safety hazards.

Since the pioneering work by Prakash *et al.* and Xu *et al.*, little research on flame retardant systems for lithium-ion batteries was performed. However, recently flame retardants are receiving more attention due to the perceived need in EV batteries. Triphenyl phosphate (TPP) is now one of the most popular FRs for lithium-ion batteries, and has been studied by Smart *et al* [44]. In fact, TPP was first studied as a flame retardant additive by Amine *et al.* in 2003 [45]. They only studied the concentration range from 0 to 10%. They found that TPP-containing electrolyte showed very good anodic stability up to 5 V in a cell with a glassy carbon electrode as the working electrode. Such good anodic stability was also confirmed by good cycling performance of  $\text{LiNi}_{0.8}\text{Co}_{0.2}\text{O}_2/\text{graphite}$  full cells using an electrolyte with 5% TPP. UL 94 was used by the authors to characterize the flammability of electrolytes containing different amounts of TPP. They found that only 1% TPP significantly reduced the flammability of the electrolyte and that 5% TPP gave the best flame retardant ability. They also used ARC to study the reactivity of fully-lithiated graphite in electrolyte with/without TPP at elevated temperature. A significant reduction of the exothermic heat generation was found in electrolyte with 5% TPP, which was believed to be due to a protective coating formed on the surface of graphite. However, based on the standard of “non-flammability” proposed by Xu *et al* [41], Amine *et al.* failed to make a truly non-flammable electrolyte with only 5 % TPP.

There are also several other organophosphorus flame retardant additives that have been studied. Xiang *et al.* [46] studied dimethyl methylphosphonate (DMMP) as a flame retardant additive for lithium-ion batteries. They found that 10 wt. % DMMP created a non-flammable electrolyte and that the cell performance was not strongly affected by the addition of DMMP [46].

Hu *et al.* [47] studied bis(N,N-diethyl)(2-methoxyethoxy)methylphosphonamidate (DEMEMP) as a flame retardant additive for lithium-ion batteries. They found that adding 10% DEMEMP could make a non-flammable electrolyte but the compatibility between the electrolyte and natural graphite became worse [47].

### **1.3.2 Non-phosphorus flame retardant additives**

Some non-phosphorus compounds with high flash point have been investigated as co-solvents to achieve non-flammable electrolytes. Arai *et al.* used methylnonafluorobutyl ether (MFE) as a co-solvent for lithium-ion batteries [48]. They found LiCoO<sub>2</sub>/graphite 18650 cells with 1M LiBETI (lithium bis[pentafluoroethylsulfonyl]imide) in MFE: EMC (2:8 v/v) showed the same electrochemical performance as the baseline electrolyte 1M LiPF<sub>6</sub> in EC: EMC (3:7 v/v) at a low rate. The cells using such electrolyte did not show any thermal runaway in a nail test which indicated a remarkable improvement in safety. However, the rate capability of cells using MFE-based electrolyte was really poor due to high impedance caused by MFE. In a following study, they found that adding 0.5 M EC and 0.1 M LiPF<sub>6</sub> in a MFE-based electrolyte significantly improved

the rate capability of the cells [49]. The authors believed that such electrolyte systems based on MFE are candidates for safer lithium-ion batteries.

Isken *et al.* studied adiponitrile (ADN) as a co-solvent to achieve a non-flammable electrolyte [50]. They used  $\text{LiBF}_4$  as the salt and ADN to replace DEC to form an electrolyte with a flash point of  $149^\circ\text{C}$ , an increase of  $110^\circ\text{C}$  over the flash point of the EC: DEC system. Graphite/Li and NCM/Li half cells showed very good rate capability and capacity retention using such an electrolyte.

#### **1.4 Scope of this thesis**

There are only a few reports of the reactivity of charged/discharged electrode materials with solvents and electrolytes for sodium-ion batteries. The first part of this thesis concentrates on a sweeping study of the reactivity of various charged positive electrode materials and discharged negative electrode materials for Na-ion batteries. Reactivity with non-aqueous solvents and non-aqueous electrolytes containing various electrolyte salts will be reported.

Flame retardant additives are thought to be the most efficient method to reduce fire-related safety concerns of lithium-ion batteries. However, there is a lack of systematic studies of flame retardant additives since the reports of Xu *et al* [41, 42, 43]. The second part of this thesis will focus on a systematic study of the impact of triphenyl phosphate, which is one of most popular flame retardant additives, on the electrochemical



performance of both negative and positive electrode materials and on safety related properties (reactivity of the electrode materials and the flame retarding ability).

Chapter 2 describes the experimental techniques used in this thesis. Chapter 3 starts with the study of the reactivity of negative electrode materials for sodium-ion batteries in non-aqueous solvents and electrolytes. Chapter 4 then describes the reactivity of positive electrode materials. Chapter 5 gives the experimental results about of the properties of NaTFSI as a salt for sodium-ion battery. Chapter 6 shows the impact of triphenyl phosphate on the electrochemical performance of both negative and positive electrode materials for lithium-ion batteries as well as the impact of TPP on cell safety. Conclusions and suggestions for future work are given in Chapter 7.

## CHAPTER 2 EXPERIMENTAL TECHNIQUES

### 2.1 Synthesis of electrode materials

#### 2.1.1 Hard carbon

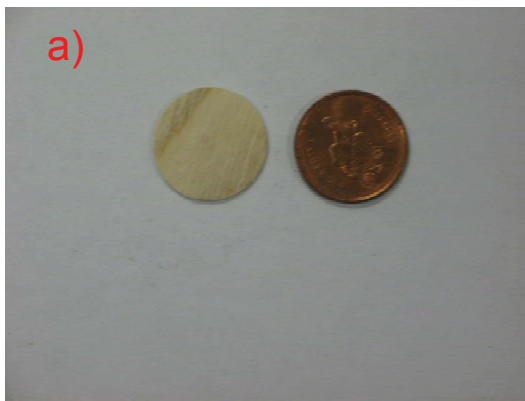
Table 2.1 describes different hard carbon samples synthesized from different precursors [51]. Hard carbon made from oak at 1100°C delivered the highest reversible capacity,  $C_{rev}$ , and the second smallest irreversible capacity,  $C_{irr}$ , (bigger than maple at 1100°C). It is also very easy to make wood into a pellet, which can be used as a pellet electrode in coin-type cells directly after pyrolysis.

Table 2.1 Synthesis conditions and properties of hard carbon from different sources [51]. Reprinted with permission from The Electrochemical Society. Copyright 1997.

sample	Sample	$T_{pyr}$ (°C)	Heating rate (°C/min)	Ar flow rate (cc/min)	$R_g$ (Å)	R	Surf. area (m <sup>2</sup> /g)	$C_{irr}$ (mAh/g)	$C_{rev}$ (mAh/g)	Remak
sx126i14	oak1	1600	25	150	6.58	2.66	4.6	30	193	
sx126i18	oak2	1400	25	150	6.11	2.26	4.7	34	265	
sx126i22	oak3	1200	25	150	5.94	2.02	4.8	49	332	
sx126i26	oak4	1100	25	150	5.47	1.78	12.1	118	562	
sx126i6	oak5	1000	25	150	5.53	1.85	13.4	152	517	
sx126i10	oak6	900	25	150	5.25	1.85	124.2	141	536	
sx126i1	filbert	1000	25	150	5.72	1.95	179	191	406	
sx126i3	walnut1	1000	25	150	5.97	1.85	60.1	142	476	
sx126i24	walnut2	1100	25	150	5.69	1.87	11.2	131	508	
sx126i4	almond	1000	25	150	5.93	2.00	46.4	176	383	
sx126i5	b sugar	1000	25	150	5.84	2.02	12.3	125	447	brown sugar
sx126i0	maple1	1000	25	150	5.58	1.98	62.7	134	500	
sx126i25	maple2	1100	25	150	5.54	1.86	10.7	52	535	

Figure 2.1 shows the synthesis of nanoporous or hard carbon. First, 1.8 cm diameter by 1mm thick discs of oak or maple (Piercy's Lumber Yard, Halifax, N. S., Canada) were heated at 1°C/min to 700°C where they were held for 1 hour under an

argon flow of  $150 \text{ cm}^3/\text{min}$  for a preliminary pyrolysis to remove the majority of the decomposition products. During this step, the oak or maple was carbonized; the discs shrunk, remained a single sturdy piece and lost about 80% of their initial mass. Then these discs were heated under vacuum at  $1100^\circ\text{C}$  and transferred directly to a glove box for cell assembly according to the procedures in [52]. This step minimizes irreversible capacity, as shown by the work of Xing *et al.* [52].



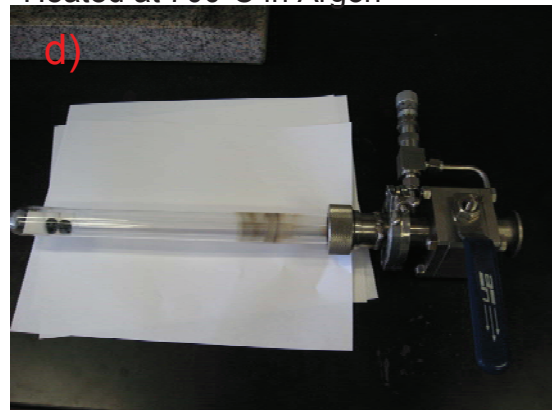
Original pellet from oak



Heated at  $700^\circ\text{C}$  in Argon



Vacuum heating at  $1100^\circ\text{C}$



Transfer to glove box without contacting air

Figure 2.1 Process of making hard carbon pellet electrodes from pyrolysed oak

### 2.1.2 Transition metal hydroxide precursor.

A transition metal hydroxide precursor  $\text{Ni}_{0.5}\text{Mn}_{0.5}(\text{OH})_2$  was made using a continuously-stirred tank reactor (CSTR). Figure 2.2 shows the CSTR.

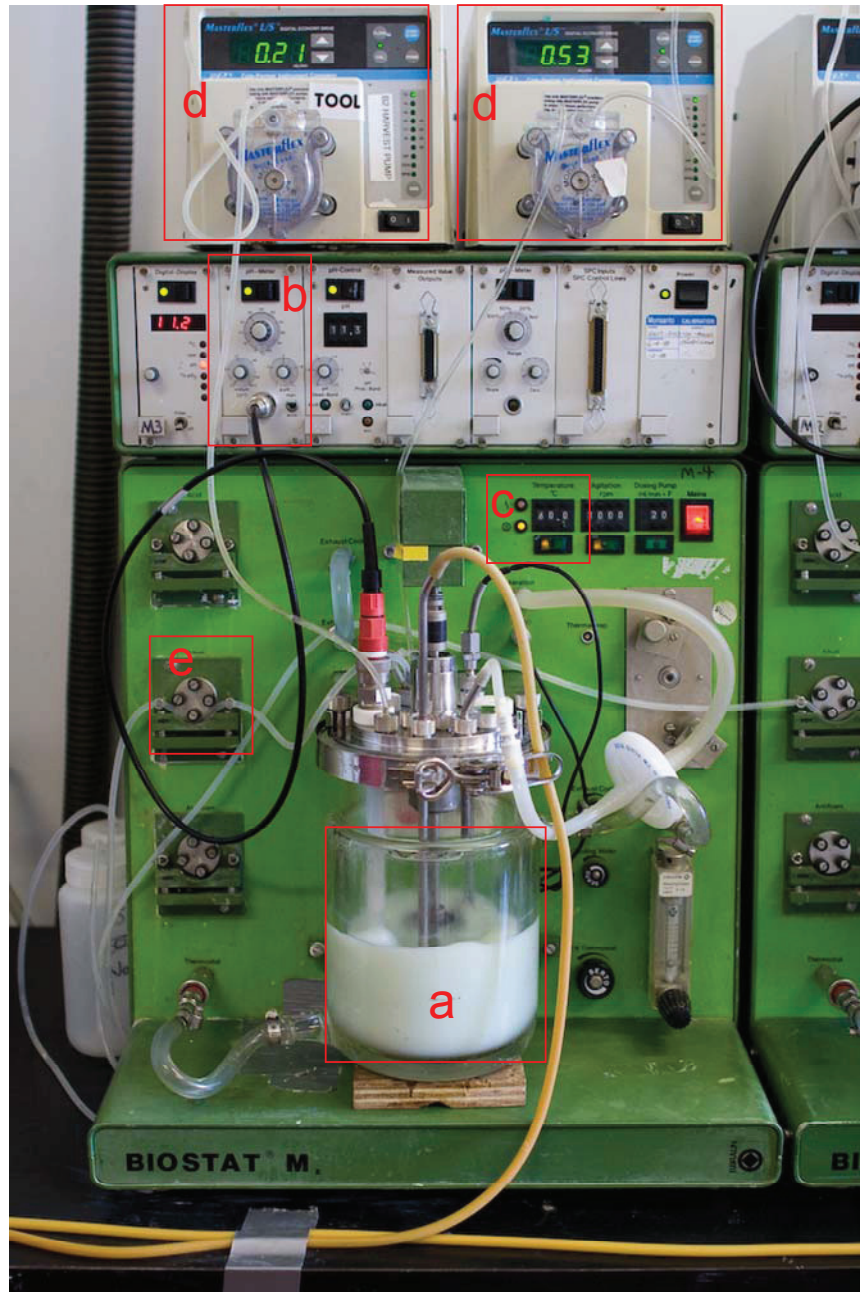


Figure 2.2 Photograph of the continuously-stirred tank reactor (CSTR) [53].

Nickel (II) sulfate hexahydrate (98%, Alfa Aesar), manganese sulfate monohydrate (Alfa Aesar, 98%), sodium hydroxide (Alfa Aesar), and ammonium hydroxide (28.0-30.0%, Sigma-Aldrich) were used to prepare solutions with deionized water which was deaerated by boiling for 10 minutes.

A coprecipitation reactor with a 2 L jacketed reaction vessel (a in Figure 2.2) equipped with pH (b in Figure 2.2) and temperature controllers (c in Figure 2.2) was used. Reagents were added using digital peristaltic pumps (Masterflex L/S 07524, d in Figure 2.2) and sodium hydroxide addition was automatically controlled by the pH controller and added as required by a peristaltic pump (e in Figure 2.2) on the reactor. Reaction contents were maintained at a temperature of 60°C and the contents of the reactor were stirred by an overhead stirrer at 1000 rpm. Nitrogen was bubbled (60 sccm) into the reactor throughout the reaction [53].

A volume of 1 L of a 1 M  $\text{NH}_3(\text{aq})$  solution made in de-aerated water was added to the reactor vessel and was heated to 60°C. The reaction proceeded with the addition of 10.0 M  $\text{NH}_3(\text{aq})$  at 0.005 L/h and 2.0 M  $\text{MSO}_4$  (M = Ni, and Mn in equimolar ratios, Aldrich, 98%) at 0.025 L/h. A concentration of 5.0 M NaOH (Aldrich, 98%) was automatically added to the reaction contents to maintain the desired pH. The reaction vessel was fitted with an overflow pipe and the reaction contents were pressurized with nitrogen to ensure a constant volume during the reaction. The residence time, given by the total flow rate of the reagents and the reactor volume, was set to be 20 h. After

reaction, the solid material was filtered and washed with 3 L deaerated deionized water in several rinses.

### **2.1.3 Sodium transition metal oxides**

Sodium transition metal oxides were synthesized using solid state reaction.  $\text{NaCrO}_2$  was made by heating stoichiometric ratios of  $\text{Na}_2\text{CO}_3$  (Aldrich, 99.5%) and  $\text{Cr}_2\text{O}_3$  (Aldrich, 98%) at  $900^\circ\text{C}$  in argon for 5h.  $\text{Na}_x\text{CoO}_2$  was synthesized by heating stoichiometric ratios of  $\text{Na}_2\text{CO}_3$  (Aldrich, 99.5%) and  $\text{CoCO}_3$  (Alfa, 99%) at  $950^\circ\text{C}$  in air for 24h.  $\text{NaNi}_{0.5}\text{Mn}_{0.5}\text{O}_2$  was made by heating stoichiometric ratios of  $\text{Na}_2\text{CO}_3$  (Aldrich, 99.5%) and  $\text{Ni}_{0.5}\text{Mn}_{0.5}(\text{OH})_2$  at  $850^\circ\text{C}$  in air for 24h and then quenching into liquid nitrogen. After quenching,  $\text{NaNi}_{0.5}\text{Mn}_{0.5}\text{O}_2$  sample was transferred into a glove box quickly for future use.

### **2.1.4 Sodium foil**

A method to make good sodium foils for coin cells was also developed based on a home-made furnace because of the lack of commercial sodium foil. Figure 2.3 shows the method used to make sodium foils. All the operations in this process were made in an argon-filled glove box. First, a homemade temperature-controlled furnace was set to  $135^\circ\text{C}$ , which was higher than the melting point of sodium metal (melting point:  $97.72^\circ\text{C}$ ). Then about 0.1g of commercial sodium rods (Sigma Adrich) was put into the furnace for 10 min. After liquid sodium formed, it was poured into a mold made from two

polypropylene plates and hand pressed for one minute. In this way, a sodium foil was formed and was then punched for use in coin cells.



Figure 2.3 Process of making sodium foil. a). A home-made temperature-controlled furnace; b). Liquid (molten) sodium in a stainless vessel; c) a piece of sodium foil on the polypropylene plate; d) a punched sodium foil that is ready for coin-cell assembling

## 2.2 X-ray diffraction

X-ray diffraction (XRD) is the most widely applied technique to identify crystal structure, phase composition and grain size. A Siemens D5000 diffractometer equipped with a copper target X-ray tube and a diffracted beam monochromator was used for the diffraction measurements (Figure 2.4).



Figure 2.4 Siemens D5000 diffractometer.

Two different kinds of samples were prepared for XRD measurements: (1) newly synthesized electrode materials to identify their structure and lattice constants and (2) samples before and after ARC measurements in order to study the reaction between the electrode materials and electrolytes or solvents. Different sample holders were used for these two different types of samples.

The holder for the new electrode material samples was made from a stainless steel plate. The sample was tightly packed in a well in the center of the plate. The second type of samples are air sensitive materials that cannot be studied in air. The sample holder shown in Figure 2.5 was used to prevent air exposure during the diffraction measurement. An aluminized mylar shroud was sealed to the semi-circular frame using Torr-seal vacuum epoxy (Varian) [54]. A small amount of sample was placed on a



zero-background silicon wafer. During an XRD measurement, X-rays can pass through the mylar layer to reach the sample but air cannot. The XRD sample holder is then placed into the diffractometer mount to ensure that the surface of the sample holder is coincident with the goniometer center.

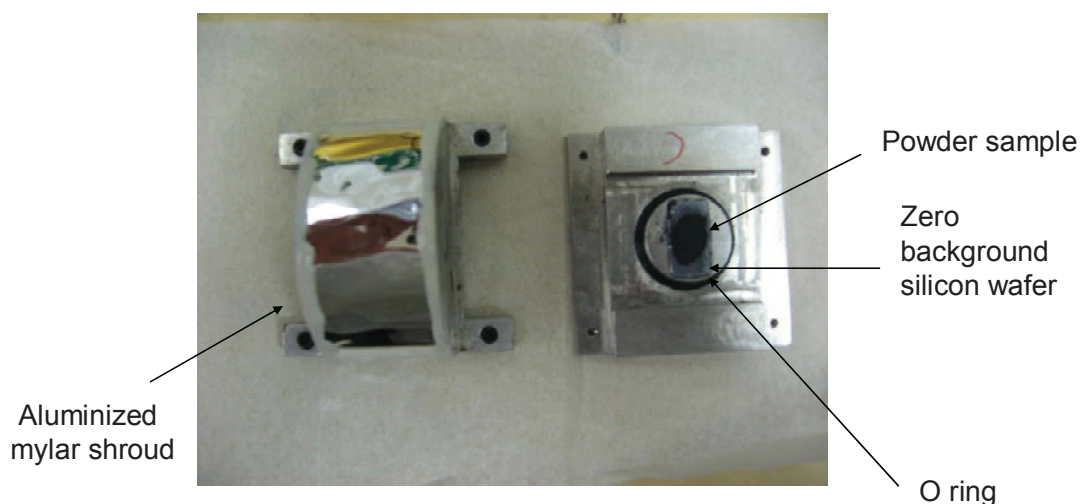


Figure 2.5 Air sensitive XRD holder

## 2.3 Electrode preparation for ARC or electrochemical testing

### 2.3.1 Thin film electrodes for electrochemical tests.

Thin film electrodes were made to test the electrochemical properties of the materials prepared. About 0.8 g of the active electrode material, such as  $\text{NaCrO}_2$  or hard carbon, was mixed with 0.1 g Super-S carbon black (MMM Carbon, Belgium), 0.1 g polyvinylidene difluoride (PVDF) (Arkema Inc.) and about 1 g N-methyl pyrrolidone (NMP) (Aldrich) in a 30 ml vial. The slurry was spread on an aluminum foil (positive) or copper foil (negative) after stirring in a planetary mixer (Mazerustar KK50S) for 5 minutes, and then the electrode was dried in an oven overnight at  $100^\circ\text{C}$ .

### **2.3.2 Pellet electrodes for ARC**

One ARC experiment requires approximately 100 mg of active electrode material. In order to prepare enough material all at once, about 4 g of electrode material, with the same ratio of PVDF, Super-S carbon black and NMP as for the thin film electrode was used. The mixture was put into a stainless steel vial with four stainless steel beads. The vial was put onto a low-energy ball milling machine for milling for about 1h. Then the slurry was put into an oven at 100°C for drying. When the slurry was dry, the powder was lightly ground in a mortar and then passed through a 300 µm sieve. About 250 mg electrode powder was then placed in a stainless steel die and pressed with 13.8 MPa to produce an approximately 1 mm thick pellet electrode. When studying the reactivity of sodium intercalated hard carbon, discs made from wood were used as the pellet electrodes (see section 2.1.1).

### **2.3.3 Cell construction for thin-film electrodes**

The electrochemical cells were assembled from the parts shown in Figure 2.6 in an argon-filled glove box. The 2325 type coin cell has stainless steel top and bottom casings. The prepared electrode was placed in the center of the bottom casing and the desired electrolyte was added. A polypropylene separator was placed above the electrode. Celgard 2502 type separator was used for EC/DEC based electrolyte and Celgard 3501 type separator was used for PC based electrolyte. Then the negative film electrode was

put on the top of the separator. The negative film electrode, depending on the particular cell type, was normally made of a piece of lithium or sodium foil. A stainless steel spacer and spring were added to maintain pressure on the electrode stack. The cell top, on which there was a polypropylene gasket, was then placed on the top of the spring and the cell was crimped shut, which sealed the electrodes from the environment. When the electrochemical cells were removed from the argon-filled glove box, stainless steel tabs were welded onto the two sides of the cells for electrical contact. 1M LiPF<sub>6</sub> in EC:DEC (1:2, v/v) was used as the control electrolyte for the lithium cells described in this thesis.

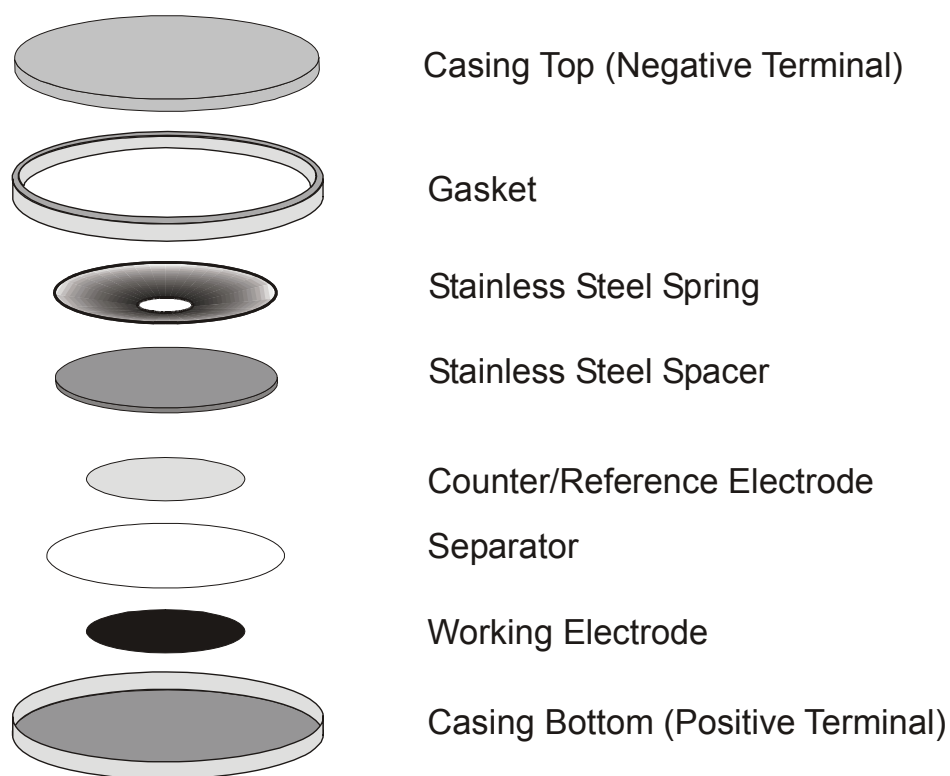


Figure 2.6 Construction of a 2325 size sodium coin cell

### **2.3.4 Cell construction for pellet electrodes**

The construction of cells with pellet negative or positive electrodes was slightly different from the thin film cells. The pellet electrode was placed in the center of the bottom casing with enough electrolyte to wet the pellet electrode completely. Then three pieces of separator were put onto the pellet, to cover it completely in order to avoid a short circuit. Then a stainless steel spacer was added on top of the lithium or sodium foil, which was used as the counter electrode, and no spring was needed here because of the large thickness of the pellet. The crimping step was the same as for the thin film cell.

### **2.3.5 Cell testing**

All assembled cells were tested on a charger provided by E-One Moli Energy (Maple Ridge, BC, Canada). The thin film cells were cycled between certain voltage ranges, for example, NaCrO<sub>2</sub>/Na cells were cycled between 2.0 V and 3.6 V using a current density of 25 mA/g. The pellet cells were charged or discharged using special test procedures, called signature charge (Rsig) or signature discharge (Disg), which were equivalent to constant voltage charging or discharging [55]. These special test procedures stabilized the electrode to a desired potential, such as 3.6 V for NaCrO<sub>2</sub> or 0 V for hard carbon.

## 2.4 Theory of accelerating rate calorimetry (ARC)

### 2.4.1 Introduction to reaction kinetics

When a reactant is converted to products by a single-step thermally induced reaction, it is common to write

$$\frac{d\alpha}{dt} = k(T)f(\alpha) \quad (\text{Equation 2.1})$$

where  $t$  is the time,  $T$  is the temperature and  $\alpha$  is the fractional degree of conversion of reactants ( $0 \leq \alpha \leq 1$ ) to products. It is common to assume that the temperature dependence of the rate of constant,  $k(T)$ , can be separated from the reaction model,  $f(\alpha)$ , and that

$$k(T) = \gamma e^{-\frac{E_a}{k_B T}} \quad (\text{Equation 2.2})$$

where  $E_a$  is the activation energy,  $k_B$  is Boltzmann's constant and  $\gamma$  is the frequency factor [56]. The reaction model,  $f(\alpha)$ , can be derived from a number of physical situations and examples are given in Table 2.2 [57]. Table 2.2 contains a column for the reaction model type, a column for the differential equation describing the extent of conversion and columns used to describe exponents in a “universal” equation for the thermal decomposition of solids [57],

$$\frac{d\alpha}{dt} = k\alpha^m(1-\alpha)^n(-\ln(1-\alpha))^p \quad (\text{Equation 2.3})$$

Table 2.2 Reaction models typically applied to describe the thermal decomposition of solids [57].

Reaction model		$\frac{d\alpha}{dt} = k\alpha^m(1-\alpha)^n(-\ln(1-\alpha))^p$	m	n	p
1	One-dimensional diffusion	$k\alpha^{-1}$	-1	0	0
2		$k\alpha$	1	0	0
3	Power law	$k\alpha^{1/2}$	0.5	0	0
4	Power law	$k\alpha^{2/3}$	0.6667	0	0
5	Power law	$k\alpha^{3/4}$	0.75	0	0
6	Zero order	$k$	0	0	0
7	Contracting sphere	$k(1-\alpha)^{2/3}$	0	0.6667	0
8	Contracting cylinder	$k(1-\alpha)^{1/2}$	0	0.5	0
9	First order	$k(1-\alpha)$	0	1	0
10	Second order	$k(1-\alpha)^2$	0	2	0
11	Avrami-Erofeev	$k(1-\alpha)(-\ln(1-\alpha))^{1/2}$	0	1	0.5
12	Avrami-Erofeev	$k(1-\alpha)(-\ln(1-\alpha))^{2/3}$	0	1	0.6667
13	Avrami-Erofeev	$k(1-\alpha)(-\ln(1-\alpha))^{3/4}$	0	1	0.75

The variables in Equation 2.3 can be chosen to describe most solid thermal decomposition mechanisms from simple  $n^{\text{th}}$  – order to diffusion-controlled reactions. In order to describe the reaction kinetics accurately, it is necessary to determine  $f(\alpha)$ ,  $E_a$  and  $\gamma$ .

## 2.4.2 Accelerating rate calorimetry

Accelerating Rate Calorimetry is one kind of adiabatic calorimetry, and it has been typically used as a method to determine reaction kinetic information, such as  $f(\alpha)$ ,  $E_a$  and  $\gamma$  as discussed in the last section.

In an ARC experiment, the self-heating rate is given by

$$\frac{dT}{dt} = \frac{h}{C_{tot}} * \frac{d\alpha}{dt} \quad (\text{Equation 2.4})$$

where  $h$  is the total heat which can be evolved by the sample due to the reaction (Joules) and  $C_{tot}$  is the total heat capacity of the reactants and the sample bomb ( $\text{JK}^{-1}$ ).  $h/C_{tot}$  corresponds to the temperature rise,  $\Delta T$ , from the onset of the exothermic reaction to the end of it.

Combining Eqn. 2-1 and Eqn. 2-4, the following equation is obtained and used for the initial self-heating rate.

$$\frac{dT}{dt} = \Delta T k(T) f(\alpha_0) \quad (\text{Equation 2.5})$$

Taking the natural logarithm of both sides, gives

$$\ln\left(\frac{dT}{dt}\right) = \ln(\gamma \Delta T f(\alpha_0)) - \frac{E_a}{k_B T} \quad (\text{Equation 2.6})$$

where the substitution for the rate constant,  $k(T)$ , (Eqn. 2-2) has been made here. Hence, a plot of the natural logarithm of the initial self-heating rate versus  $1/T$  has a slope related to the activation energy,  $E_a$ , and an intercept related to the frequency factor,  $\gamma$ .

Simulations of ARC profiles for typical zero-order and first-order reactions are shown in Figure 2.7 and Figure 2.8. Four starting temperatures 140°C, 150°C, 160°C and 170°C were used.  $E_a$  was selected to be 1.6 eV, which is close to that found in experiments on  $\text{Li}_{0.5}\text{CoO}_2$  in electrolyte [7].  $\Delta T$  was set to be 60°C.  $\gamma$  was selected so that the ARC simulation would produce a measurable self-heating at 140°C.  $\alpha_0$  was selected to be 0.001. Table 2.3 lists the values of the parameters used for the simulations of the reaction models given in Table 2.2

Table 2.3 Parameters used to calculate ARC profiles for the chosen reaction models of Table 2.2

Reaction Model	$E_a$ (eV)	$\gamma$	$\alpha$
6	1.6	$5 \times 10^{16}$	0.001
9	1.6	$5 \times 10^{16}$	0.001

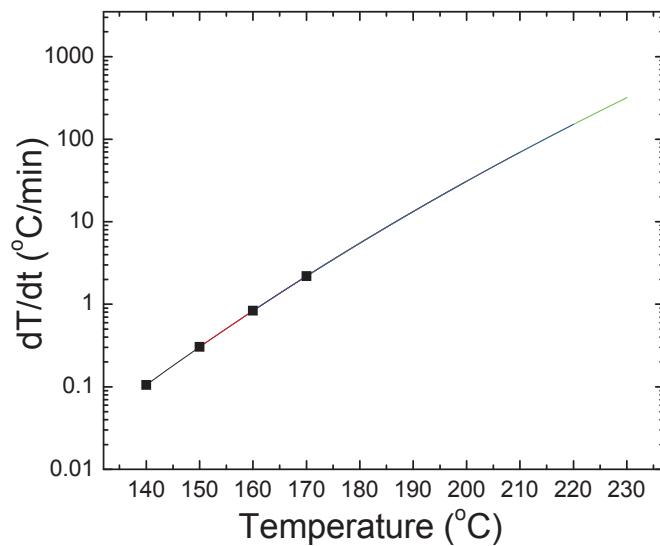


Figure 2.7 Calculated ARC profiles for zero order kinetics (model 6 in Table 2.2) using the parameters for model 6 in Table 2.3.



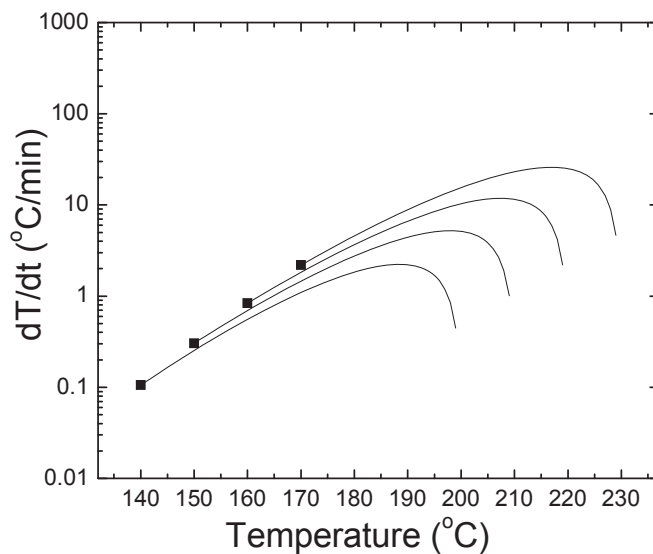


Figure 2.8 Calculated ARC profiles for first order kinetics (model 9 in Table 2.2) using the parameters for model 9 in Table 2.3.

## 2.5 Introduction to the ARC machine

A simple schematic diagram of an Accelerating Rate Calorimeter is shown in Figure 2.9. A temperature sensor (a thermocouple) is attached to the surface of the sample holder to monitor the temperature of the sample. If the sample holder is heated by an exothermic reaction, a difference between the sample and jacket temperatures is detected. The heaters then heat the jacket so it has the same temperature as the sample. Hence, there is no heat flow between the sample holder and the jacket. The sample holder is therefore maintained under adiabatic conditions and it self-heats due to the exothermic reactions occurring within it. The temperature of the sample ( $T$ ) is measured versus time ( $t$ ) and the self-heating rate ( $dT/dt$ ) vs.  $T$  is usually plotted.

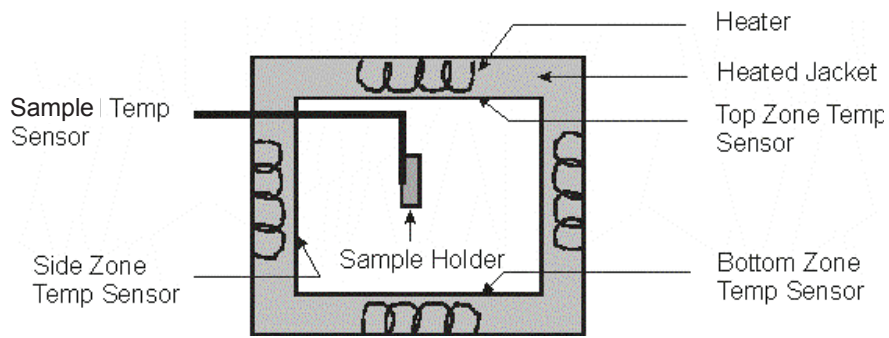


Figure 2.9 Schematic of the Accelerating Rate Calorimeter (ARC)

Figure 2.10 shows a picture of an ARC with its outside blast shell open. The blast shell is added mainly for safety concerns as the ARC can be used to study the thermal instability of explosives. When the cover is lifted up, there is a thermocouple (type N) suspended in the center of the jacket and an ARC sample tube is hooked on the tip of the thermocouple as shown in Figure 2.11. There are also heaters and thermocouples located in the top, bottom, and side zones around the jacket, which cannot be seen in this picture.

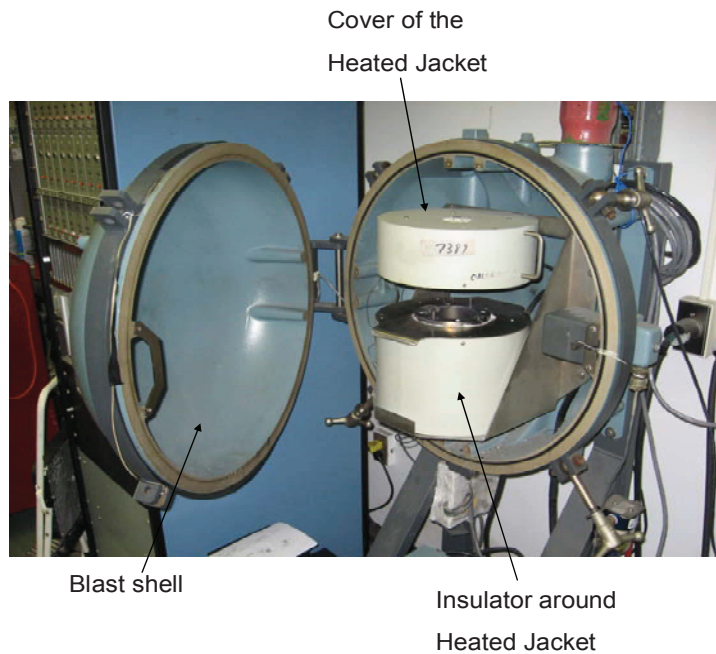


Figure 2.10 A picture of the ARC when the blast shell is open

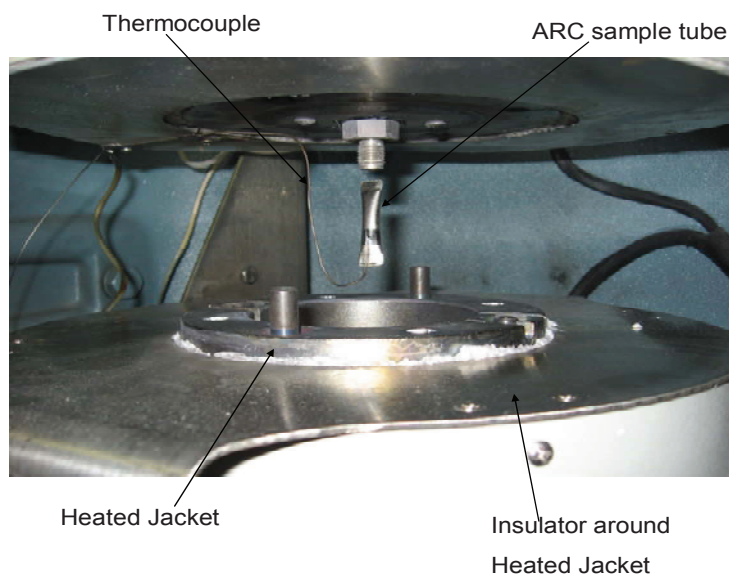


Figure 2.11 An ARC sample tube hooked on the tip of the sample thermocouple

The ARC sample holder was made from a 6.35 mm (0.250'') outer diameter stainless steel (type 304) seamless tube with a wall thickness of 0.015 mm (0.006'') (MicroGroup, Medway, Mass.). The stainless steel tubing was cut into 39.1 mm (1.540'') long pieces shown in Figure 2.12a. A dime is shown in Figure 2.12 to indicate the size of the stainless steel tubing. The sample tubing was sonicated twice in acetone for cleaning. One end of the tubing was flattened and then welded inside an argon-filled glove box using Tungsten Inert Gas (TIG) welding with a Miller Maxstar 91 ARC welder, equipped with a Snap Start II high frequency ARC starter. A small piece of stainless steel foil was attached to the surface of the tubing for hooking the thermal sensor in the ARC experiment. The sample holder is shown in Figure 2.12b. A certain amount of electrode material, such as  $\text{Na}_{0.5}\text{CrO}_2$ , and solvent or electrolyte was then added to the tube in an argon-filled glove box. The other end of the tube was clamped and welded shut with the

sample held in a large copper block as a heat sink [58]. TIG welding was performed under a flow of argon and essentially melted the end of the tube together. Then the sample holder in Figure 2.12c was ready for the ARC experiment.

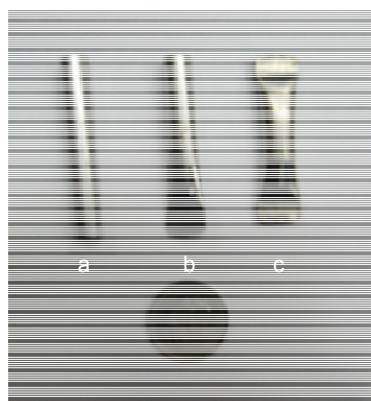


Figure 2.12 ARC tubes for ARC experiments at various stages of sample preparation.

## 2.5 Scanning electron microscopy

Scanning electron microscope (SEM) was used to image materials with micron and submicron-sized particles. All SEM images were obtained with a Hitachi S 4700 field-emission scanning electron microscope.

## 2.6 Surface area measurement

Single-point Brunauer-Emmett-Teller (BET) surface area measurements were performed on electrode materials using a Micromeritics Flowsorb II 2300 surface area analyzer. The amount of  $N_2$  gas absorbed as a monolayer of atoms at 77K on the surface of the samples is a measure of its surface area. Before testing, the sample was placed in a U-shaped glass tube, weighed, and degassed at 150°C under a  $N_2/He$  mixture (3/7, v/v)

for about 1.5 hour. The glass tube was then immersed in liquid N<sub>2</sub> for adsorption and after that, in a beaker filled with tap water for desorption at room temperature. Both adsorption and desorption were considered complete when the change in the BET result was less than 0.02 m<sup>2</sup> g<sup>-1</sup>. The final surface area result was obtained from the desorption data of the single-point BET measurement.

### **2.7. Measurement of the solubility of NaPF<sub>6</sub> or NaF in different solvents**

Tests for the solubility of NaPF<sub>6</sub> or NaF in different solvents were made as described below: Twenty mL solvent was put into a vial and then a mass of salt corresponding to 0.05 or 0.2 M was added to the solvent and the vial was shaken for 5 min. If the solution became clear, another 0.05 or 0.2 M salt was added to the solution and shaken. These operations were repeated till the solution became and remained cloudy.

### **2.8 Automatic storage system.**

Figure 2.13 shows a home-made 190-channel storage system that was used in the automatic storage experiments in this thesis. The storage system has a Keithley Instruments model 2750 scanning voltmeter equipped with scanner cards with mechanical relays. The scanner cards connect the cells to the voltmeter only once every 6 hours for only 1 second. Additionally, the input impedance of the Keithley 2750 is > 10 GΩ, so the measurements were made at conditions which approximate true open circuit.

Petroleum coke (Conoco-Phillips)/Li half cells were assembled as described in section 2.3. The cells were discharged (lithiated), charged (delithiated) between 0.005 V and 1.5 V at C/10. Then the cells were discharged to the desired potential (0.005, 0.1, 0.2, 0.4, 0.6 or 0.8V) and held until the measured current decreased to C/100. Then the cells were transferred to the storage system. All the cells were stored in constant temperature boxes at 30.0 or 60.0°C which are stable to  $\pm 0.1^\circ\text{C}$ . The cells were stored for 500 hours while the open circuit potential was monitored. The entire system is controlled by a computer-running software developed in-house with VB.Net. This system is described in reference [59].



Figure 2.13. A picture of the 190-channel automated cell storage system

## 2.9 Symmetric cells.

Thin film electrodes and graphite/Li half cells were made following the procedure described in Sec. 2.3.1. These half cells were used to lithiate electrodes to pair with an identical delithiated (uncycled) electrode in the symmetric cell. The graphite half cells were discharged (lithiated), charged (delithiated) then discharged again between 5 mV and 1.2 V using a constant current corresponding to a charge or discharge in 20 hours (C/20) and held at 5 mV until the measured current decreased to the corresponding C/100 current. A Maccor series 4000 cycler was used for these steps.

After the half cells had completed the cycling described above, they were taken back into the argon-filled glove box with freshly punched 13 mm diameter graphite which had been dried under vacuum at 120°C for at least 6 hours. The half cells were carefully disassembled (making sure not to create a short across the cells) and the lithiated graphite was recovered. This lithiated electrode was then rebuilt in a new 2325 coin-type cell with a fresh electrode and fresh electrolyte of the same composition. A fresh electrode was used for the graphite/graphite symmetric cells to ensure that the amount of active Li in the electrodes was not larger than either electrode's capacity (due to the SEI formation on the fresh electrode) preventing possible lithium plating during cycling.

When constructing the symmetric cells, one polypropylene blown microfiber (BMF – available from 3M Co. 0.275 mm thickness, 3.2 mg/cm<sup>2</sup>) separator was used in

place of the 2 Celgard 2300 separators used in the half cells. The symmetric cells were then sealed with Torr Seal (Varian, USA) around the gasket between the can and cap in order to ensure virtually no electrolyte leakage during cycling at elevated temperatures. The symmetric cells were then cycled using a charger provided by E-One Moli Energy (Maple Ridge, BC, Canada) with a constant current between voltage limits of +/- 0.5 V. The details of construction and properties of a symmetric cell are described in ref [60]

### **2.10 Electrochemical impedance spectroscopy measurement.**

Electrochemical impedance spectroscopy (EIS) measurements were conducted on symmetric graphite/graphite cells after 20 cycles. The cells were cycled at  $30 \pm 0.1^\circ\text{C}$  with a rate of  $C/10$  between -0.5 and +0.5 V and then discharged to 0.0 V and held until the measured current dropped below  $C/100$  before impedance measurements were taken at room temperature ( $21 \pm 1^\circ\text{C}$ ) using a Maccor FRA 0356. AC impedance spectra were collected with ten points per decade from 10 kHz to 10 mHz with a signal amplitude of 10 mV.

### **2.11 Self-extinguishing time (SET) tests**

Self-extinguishing time tests were carried out following the procedure described by Xu *et al* [41]. However, two similar methods were employed to study the method-dependence of these results. In the first method, the cotton tip end of a cotton swab (Life Brand, Canada) having an ellipsoidal shape about 0.4 cm in diameter and



about 0.8 cm long was used. The cotton swab was placed in a watch glass as shown in the left panel of Figure 2.14. Figure 2.14 shows two cotton swab tips although only one was used in the SET test. The cotton swab tips had 100 mg of electrolyte added with a syringe. In the second method, a small sphere of glass wool was placed on aluminum foil as shown in the right panel of Figure 2.14. Figure 2.14 shows two glass wool spheres although only one was used in the SET test. These glass wool spheres had 100 mg of electrolyte added with a syringe. In both methods 1 and 2, the balls were ignited using a barbeque lighter and the time that it took for the flame to extinguish was recorded. The SET was obtained by dividing the time the flame burned by the electrolyte mass according to the procedure in the literature [41].



**Q-tip cotton balls on  
a watch glass**

**Glass wool on Al foil**

Figure 2.14 Illustration of the two different SET test methods used in this work: (right panel) Method 1: Cotton swab tip on a watch glass; (left panel); Method 2: glass wool on Al foil.

## **CHAPTER 3 STUDIES OF THE REACTIVITY OF NEGATIVE ELECTRODE MATERIALS FOR SODIUM-ION BATTERIES IN SOLVENTS AND ELECTROLYTES.**

### **3.1 Hard carbon**

#### **3.1.1 Sample preparation**

Please refer to Section 2.1 for the synthesis of the hard carbon sample used. This sample will be called “HC” for compactness.

#### **3.1.2 Electrochemical performance of hard carbon**

Figure 3.1 shows the first discharge curve of a Na/HC cell. The electrolyte was 1M NaClO<sub>4</sub>/PC and the discharge rate was C/80. The cells with pellet electrodes destined for ARC experiments were not charged so the irreversible capacity could not be checked in these cells. However, the inset in the lower panel of Figure 3.1 shows the discharge-charge curve of a Na/HC cell with a typical film electrode showing that the irreversible capacity is around 90 mAh/g. The hard carbon sample can deliver a capacity of about 320 ± 10 mAh/g during the first discharge. The curve can be divided into two parts: the sloping region, which is related to sodium inserting between the parallel graphene layers and the long plateau at very low potential which is related to sodium inserting into the pores of hard carbon [30]. These features agree well with reference [30].

The first discharge curve of Li/HC cells is also shown in Figure 3.1. The nanoporous carbon delivers a capacity of about  $405 \pm 10$  mAh/g during the first discharge.

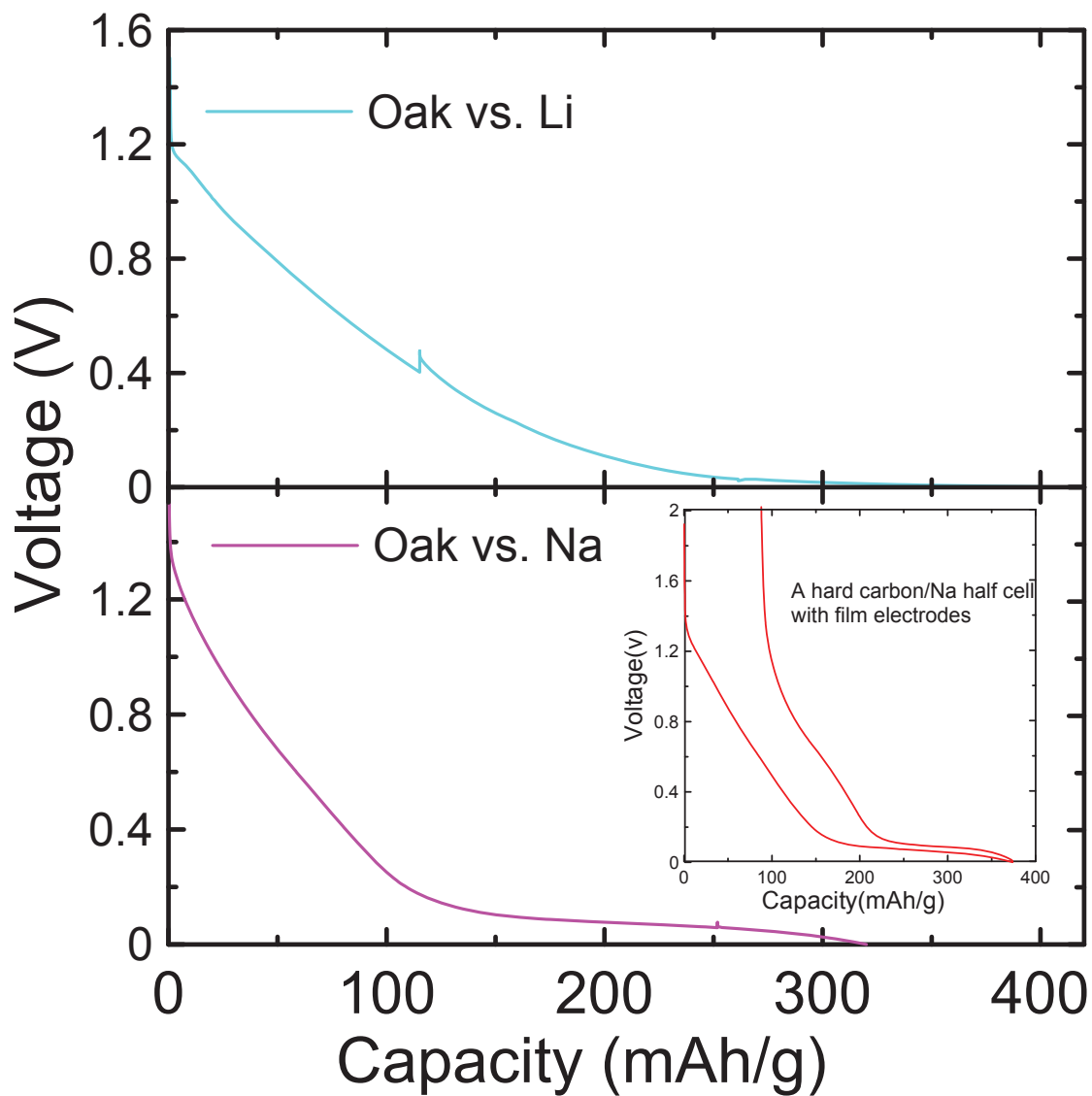


Figure 3.1 Potential versus specific capacity of Na/HC and Li/HC cells measured during the first discharge. The first cycle of a Na/HC half cell with a typical film electrode is shown as an inset in the bottom panel.

### 3.1.3 Reactivity of sodium-inserted hard carbon (Na:HC) in different solvents and electrolytes

Figure 3.2 shows the self-heating rate vs. T of 70 mg Li:HC or 70 mg Na:HC in the same mass of solvent or electrolytes (The notation Li:HC or Na:HC is used to represent hard carbon loaded with as much as Li or Na as possible in a room temperature electrochemical cell. The samples do not contain plated Li or Na). Li:HC shows much better thermal stability than Na:HC in both solvent and electrolytes. The onset temperature of the reactions between Li:HC and solvent or electrolyte is around 160°C, and the both reactions do not exceed the maximum heating rate of the ARC, 20°C/min in the test temperature range. Na:HC, on the other hand, has an onset temperature of 150°C in solvent and 130°C in NaPF<sub>6</sub>/EC:DEC electrolyte. The reactions involving Na:HC exceed the maximum tracking rate of the ARC before 270°C. Na:HC reacting with NaPF<sub>6</sub>/EC:DEC electrolyte exceeds the tracking rate of the ARC below 200°C. The reactivity of Na:HC in 1M NaClO<sub>4</sub>/PC is also shown in Figure 3.2. This experiment shows an even lower onset temperature (around 70°C) than NaPF<sub>6</sub>-based electrolyte. Even though Na:HC in NaClO<sub>4</sub>/PC electrolyte did not reach the maximum tracking rate of the ARC, as did Na:HC in NaPF<sub>6</sub>/EC:DEC, it appears that NaClO<sub>4</sub>/PC is probably not suitable for Na:HC electrodes in sodium-ion batteries because it reacts at a detectable rate with Na:HC at a relatively low temperature.

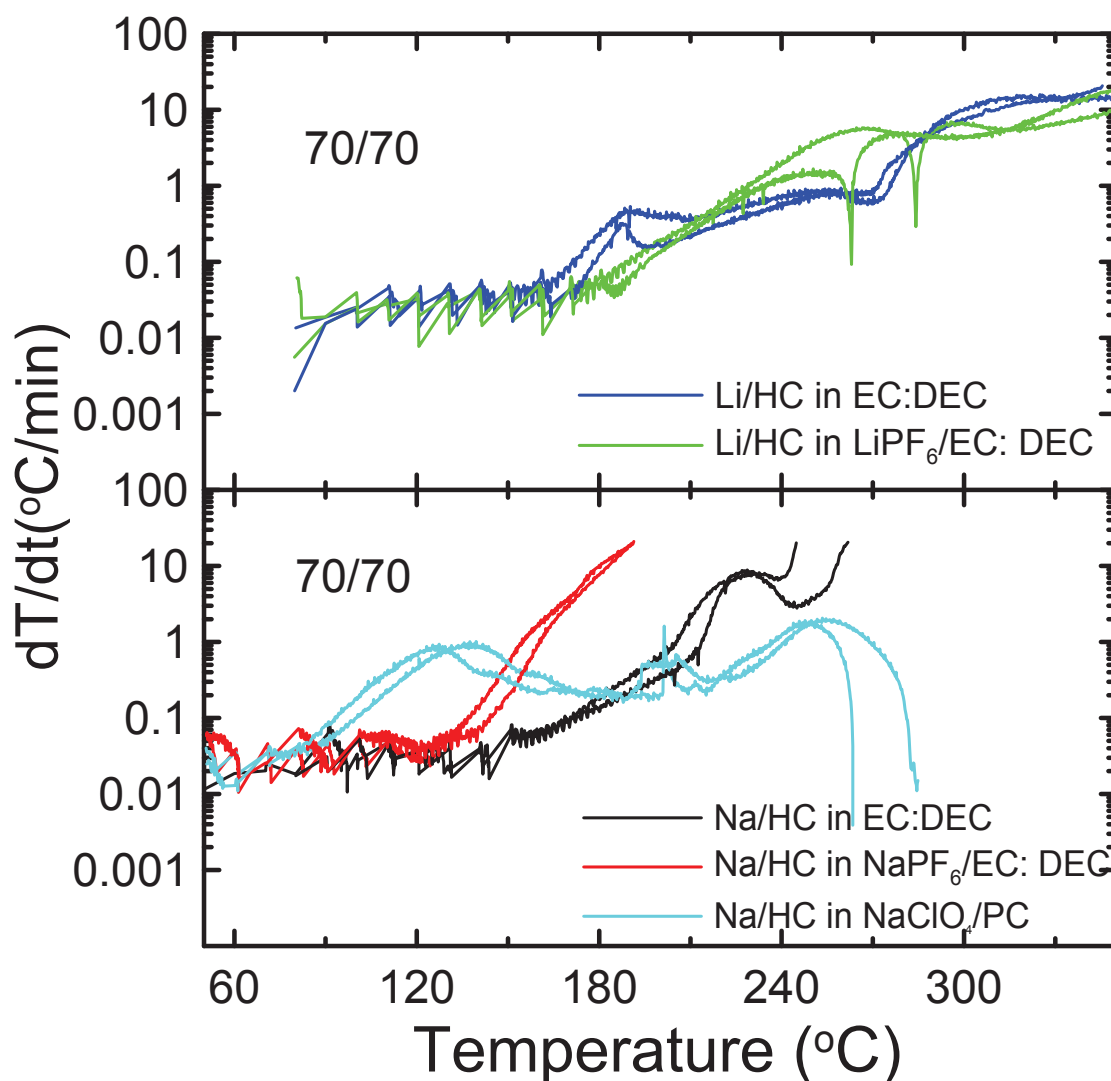


Figure 3.2 Self heating rate (SHR) vs. temperature of 70 mg Li:HC or 70 mg Na:HC reacting with 70 mg of electrolyte or solvent. Li:HC with EC:DEC (1:2 v/v) (Blue); Na:HC with EC:DEC (1:2 v/v) (Black); Li:HC with 1M LiPF<sub>6</sub> in EC:DEC (1:2 v/v) (Green); Na:HC with 1M NaPF<sub>6</sub> in EC:DEC (1:2 v/v) (Red); and Na:HC with 1M NaClO<sub>4</sub> in PC (Cyan), as indicated by the legend in the Figure.

Figure 3.3 shows the self-heating rate vs. T of 70 mg Na:HC in the same mass of EC, DEC and DMC in the left panels, and shows the XRD patterns of the products of the reactions after the ARC tests in the right panels. For DMC and DEC, there are

exothermic peaks at very low temperature (around 60°C to 70°C), which means that Na:HC reacts with DMC and DEC at this temperature. This could be problematic for the elevated temperature operation of Na-ion cells with nanoporous hard carbon electrodes that use large DEC or DMC fractions in their electrolytes. Each of EC, DMC and DEC react strongly with Na:HC once the temperature increases to near 150°C. DEC has the lowest onset temperature, followed by DMC and finally EC.

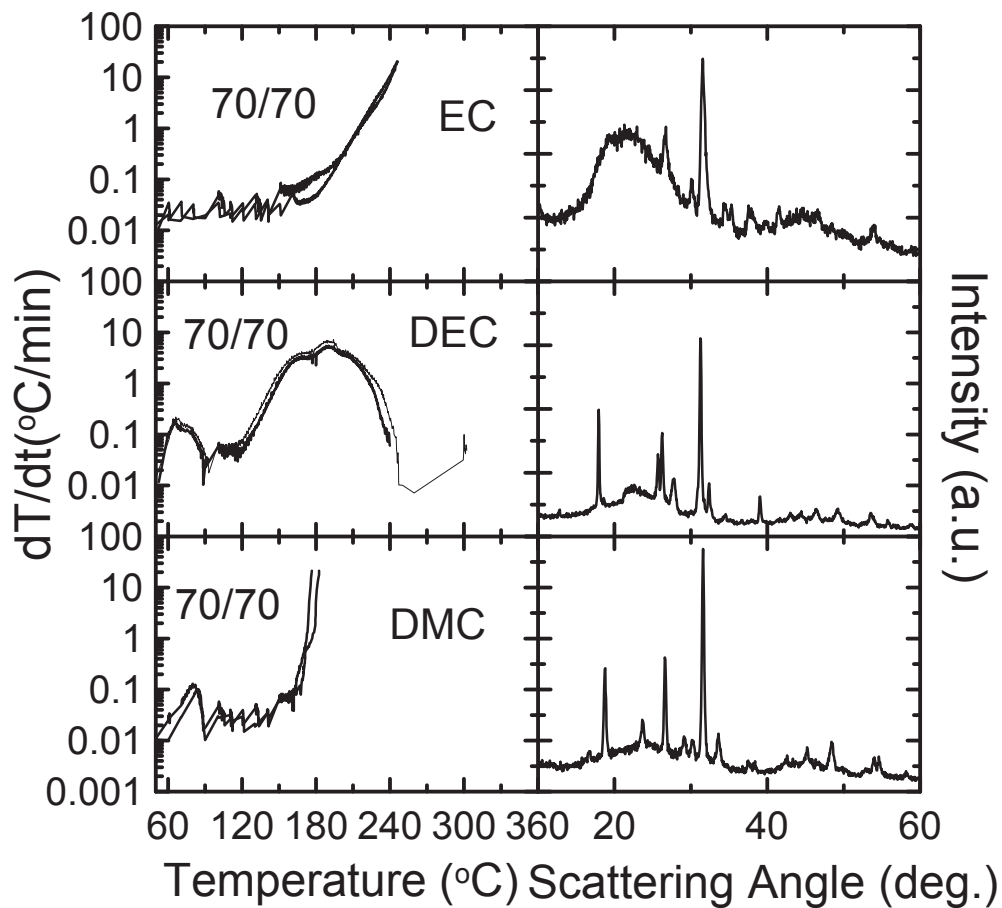
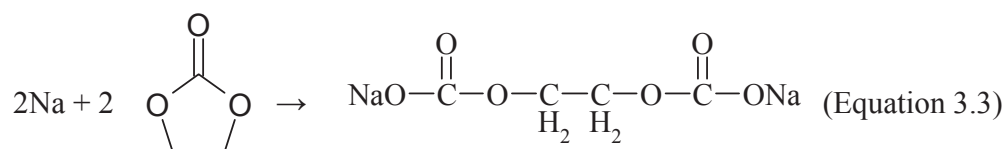
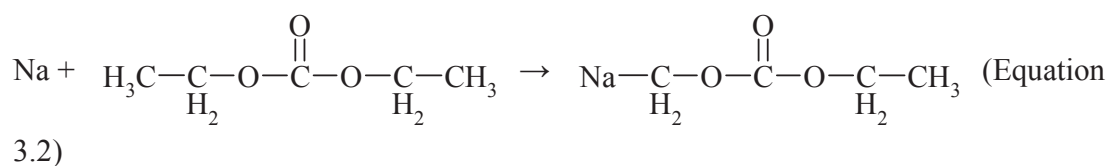
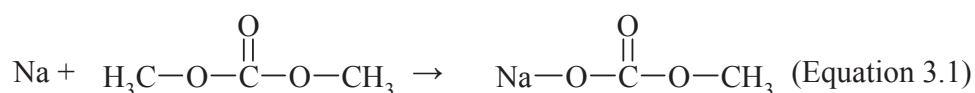


Figure 3.3 Self heating rate (SHR) vs. temperature of 70mg Na:HC in 70mg EC, 70mg DEC, 70mg DMC and the XRD patterns of the products after ARC tests, respectively.

The right panels of Figure 3.3 show that the XRD patterns of all these three products have similar Bragg peak positions, suggesting products with a similar crystal structure. As is well known, lithiated graphitized carbon reacts with EC, DEC and DMC to form lithium alkyl carbonates, among other products [12]. It is possible that Na:HC reacts with these solvents to give similar reaction products. Figure 3.4 shows the XRD pattern of product of the reaction of Na:HC with DMC, which is compared to a reference XRD pattern and a calculated (using Rietica) XRD pattern [61] (based on the crystal parameters given in ref. [62]) of sodium methyl carbonate. The experimental result agrees with the reference and calculated patterns very well, which shows that Na:HC reacted with DMC to form sodium methyl carbonate. By analogy, it can be proposed that Na:HC will react with solvents like EC, DEC or DMC at elevated temperature to produce sodium alkyl carbonates, as shown in the equations below:



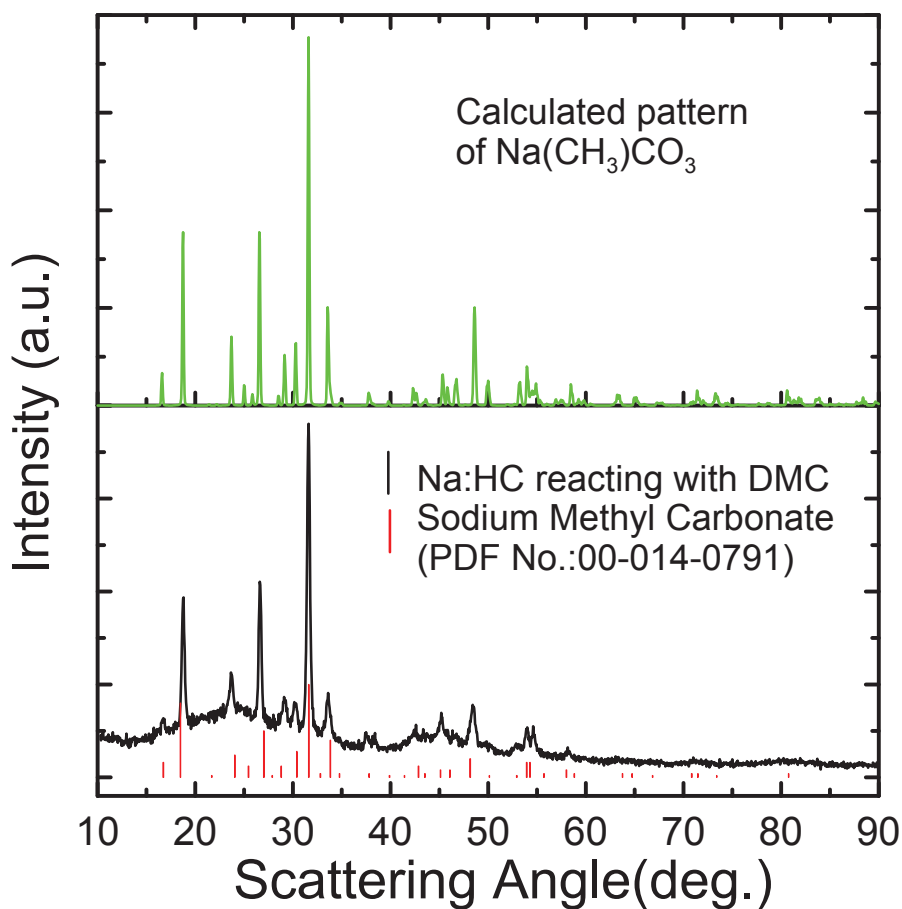


Figure 3.4 Reference, calculated and experimental XRD patterns of sodium methyl carbonate. The experimental pattern is the product of the reaction of Na:HC and DMC after the ARC experiment.

Figure 3.4 showed the product Na:HC reacting with DMC is sodium methyl carbonate. Similar statements cannot be conclusively made for the products of Na:HC reacting with DEC or EC because there are no reports of the structures of these compounds for comparison to the data in Figure 3.3. Sodium methyl carbonate is very stable in air, unlike lithium alkyl carbonate, which is very air-sensitive [12]. Assuming air-stable sodium alkyl carbonates are the main SEI components in sodium-ion batteries,



it may be possible to make the SEI of the negative electrode ahead of time. In this way no capacity loss to SEI formation will occur.

The left column in Figure 3.5 shows the self-heating rate vs. T of 70 mg Na:HC in the same mass of EC, DEC and EC:DEC (1:2 v/v), and the right column shows the XRD patterns of the products after the ARC tests. As described above, the reactions of Na:HC with EC and DEC occur in the same temperature range, so the products of the reaction of Na:HC with EC:DEC should come from both EC and DEC. Figure 3.6 shows an expanded view of the three XRD patterns from 10° to 40°. By comparison of the three patterns, the XRD pattern of the product of the reaction of Na:HC with EC:DEC (red line) has some peaks due to DEC reaction products (black line), such as the peaks at 18° and 28°, and some other peaks from EC reaction products (green line), such as peaks at 26.5° and 30.5°. Therefore, both EC and DEC contribute to the reaction of between Na:HC and EC:DEC.

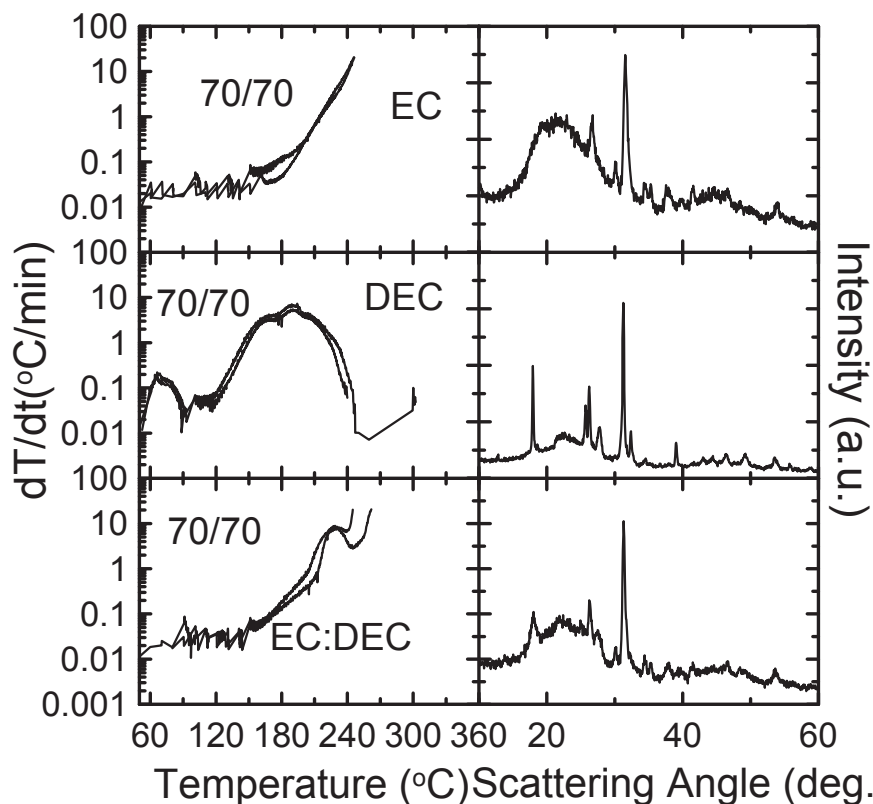


Figure 3.5 Self heating rate (SHR) vs. temperature of 70 mg Na:HC in 70 mg EC, 70 mg DEC or 70 mg EC:DEC (1:2 v/v) and the XRD patterns of the products after ARC tests, respectively.

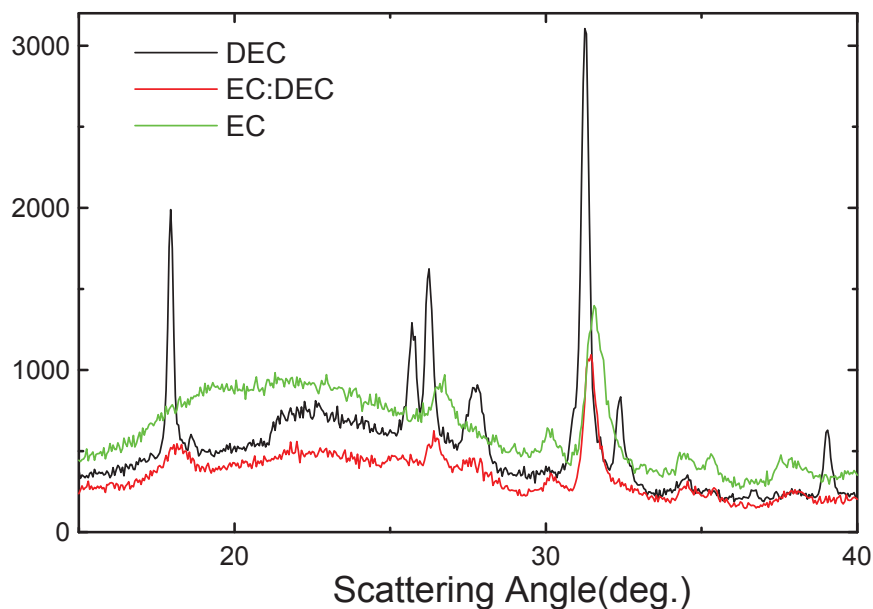


Figure 3.6 Expanded version of the XRD patterns (from 10° to 40°) of the products of Na:HC reacting with EC, DEC and EC:DEC, respectively.

The left column in Figure 3.7 shows the self-heating rate vs. T of 70 mg of Na:HC in the same mass of EC, DEC and 1M NaPF<sub>6</sub> in EC:DEC (1:2 v/v), and the right column shows the XRD patterns of the products after the ARC tests. Figure 3.8 shows an expanded view of the XRD patterns. The comparison of the three patterns shows almost all peaks from DEC reaction products appear in the product of the reaction with Na:HC and the electrolyte. There are also peaks that arise, especially the peak at around 38° from EC reaction products. It is not possible to state that the reaction products with electrolyte only arise from DEC, but it appears that the DEC products dominate the pattern which is different from the solvent case described by Figures 3.5 and 3.6.

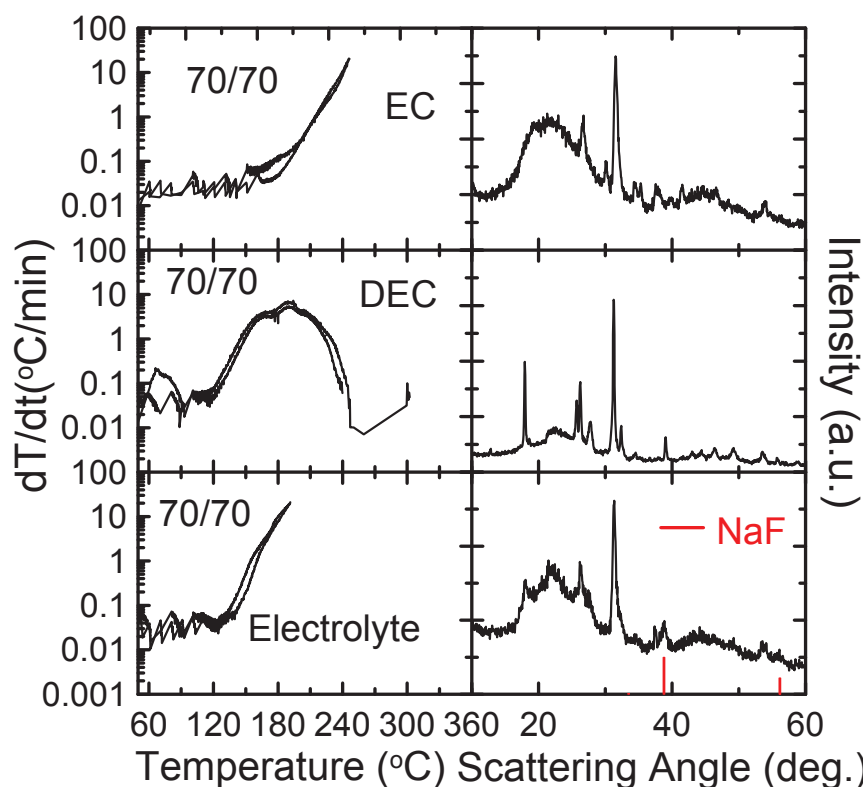


Figure 3.7 Self heating rate (SHR) vs. temperature of 70 mg Na:HC in 70 mg EC, 70 mg DEC or 70 mg 1M NaPF<sub>6</sub> in EC:DEC (1:2 v/v) and the XRD patterns of the products after ARC tests, respectively.

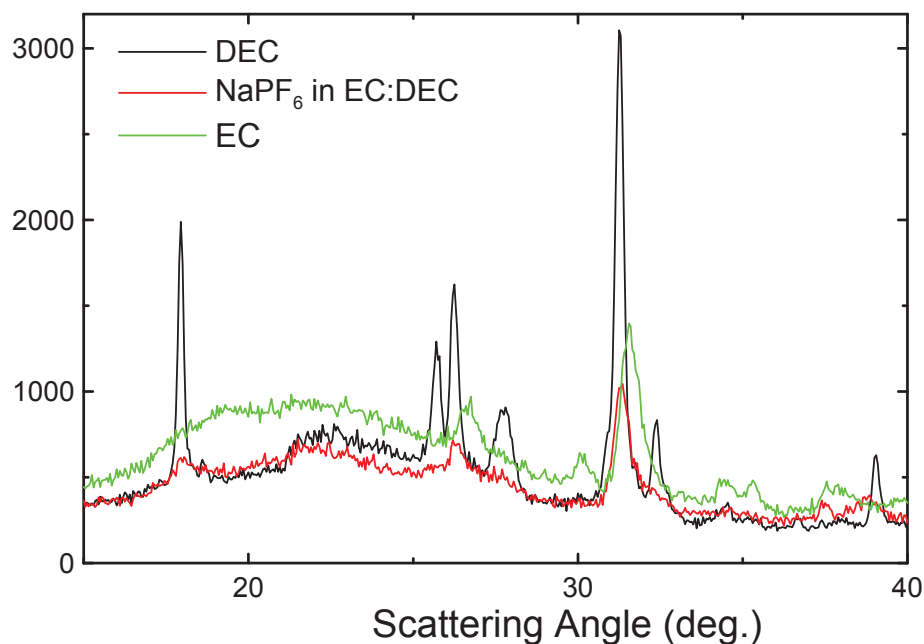


Figure 3.8 Expanded view of the XRD patterns (from  $10^{\circ}$  to  $40^{\circ}$ ) of the ARC products, of Na:HC reacting with EC, DEC and 1M NaPF<sub>6</sub> in EC:DEC (1:2 v/v), respectively.

Why are the reaction products different when NaPF<sub>6</sub> is present? First, there is very little, if any NaF observed (shown as red lines in Figure 3.7). Figure 3.9 shows the weight versus temperature as measured by TGA for NaPF<sub>6</sub> and LiPF<sub>6</sub>. NaPF<sub>6</sub> does not decompose significantly below 300°C which may explain why little NaF is observed in the XRD patterns of the Na:HC after heating with electrolyte. By contrast, LiPF<sub>6</sub> starts to decompose slowly to LiF and PF<sub>5</sub> [6, 63] below 100°C and the decomposition is completed by 200°C which helps explain why LiF is the majority product found after ARC experiments of LiC<sub>6</sub> in electrolyte.

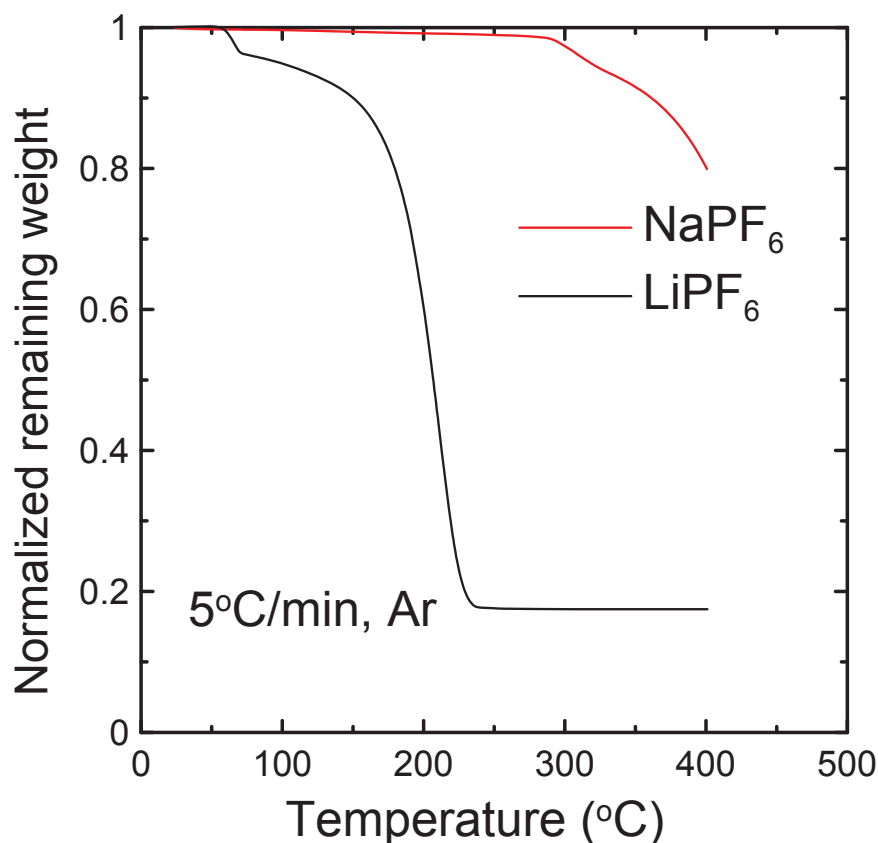


Figure 3.9 TGA experiments on NaPF<sub>6</sub> and LiPF<sub>6</sub>. The samples were heated at 5°C/min in argon gas.

One possible explanation for the different reactivity of Na:HC in electrolyte compared to in solvent might be strong “coordination” between NaPF<sub>6</sub> and EC. Preferential coordination of salts in mixed solvents does exist in lithium-ion battery systems, such as the case of LiPF<sub>6</sub> and EC, because LiPF<sub>6</sub> has the largest solubility in EC [12]. Such coordination could also affect the reactivity of mixed solvents and electrolytes with negative electrode materials loaded with lithium or sodium [12, 64]. This is because DEC and DMC are more reactive than EC and PC. If a thermally stable salt like NaPF<sub>6</sub> coordinates more strongly to a less reactive solvent in a solvent mixture, then the

reactivity of the solvent mixture with Na:HC will increase as salt is added because the more reactive component will not be coordinated to the salt and will be free to react. Table 3.1 shows the approximate solubility of NaPF<sub>6</sub> in different solvents as measured in this work. NaPF<sub>6</sub> has the largest solubility in EC, which probably means that NaPF<sub>6</sub> will coordinate most strongly to EC in a solvent mixture involving EC and DEC or DMC.

Table 3.1 Solubility of NaPF<sub>6</sub> in DMC, DEC, PC and EC

	Solvent			
	DMC	DEC	PC	EC
Dielectric constant (40°C)	3.12	2.82	64.4	89.6
Solubility (±0.2 M)	0.6	0.8	1.0	1.4

This may provide an explanation for the increased reactivity of Na:HC in electrolyte. As NaPF<sub>6</sub> is added, EC coordinates to the salt, leaving the more reactive DEC available to react with the Na:HC. Therefore the reaction of Na:HC in electrolyte is similar to that of Na:HC reacted with DEC, and the products come primarily from DEC. Since NaPF<sub>6</sub> does not decompose at low temperatures it apparently does not form NaF to cover the surface of the Na-containing carbon. The solubility of NaF in EC, DEC, PC and DMC was tested and found to be less than 0.05 M. Therefore, any formed NaF was not simply dissolved away.

Figure 3.10 shows the self-heating rate vs. T of 70 mg Na:HC in the same mass of EC:DEC, EC:DMC and in 1M NaPF<sub>6</sub> electrolytes of each solvent mixture. Figure 3.10

shows that adding NaPF<sub>6</sub> makes the Na:HC more reactive than it is in solvent alone. As discussed above, if NaPF<sub>6</sub> coordinates with EC, adding NaPF<sub>6</sub> reduces the contribution of EC to the thermal stability of Na:HC in electrolyte and the reaction of Na:HC in electrolyte is approximately the same as the reaction between Na:HC and DEC or DMC only. Figure 3.3 showed that DEC and DMC react with Na:HC at lower temperatures than EC. Therefore in NaPF<sub>6</sub>-containing electrolytes made of EC and DEC or DMC the reactivity of Na:HC is more severe than in the mixed solvent alone.

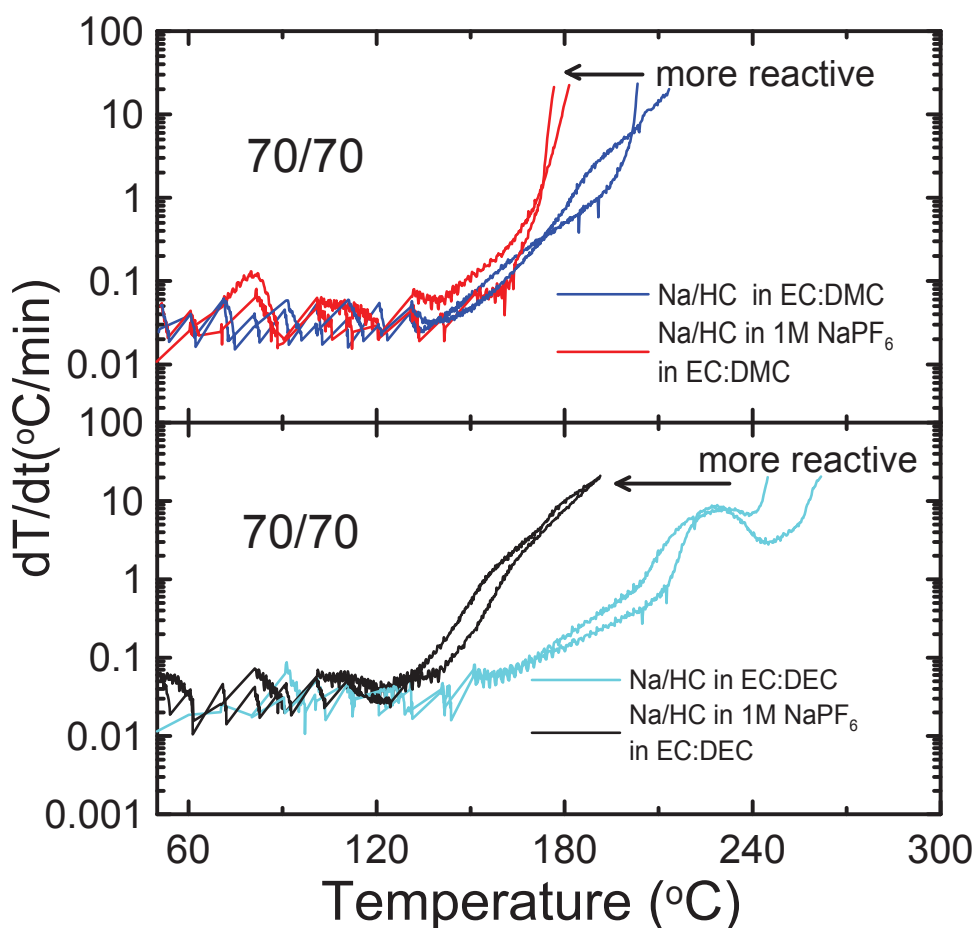


Figure 3.10 Self heating rate (SHR) vs. temperature of 70 mg Na:HC in 70 mg EC:DEC (1:2 v/v), 70 mg EC:DMC (1:2 v/v), 70 mg 1M NaPF<sub>6</sub> in EC:DEC (1:2 v/v) or 70 mg 1M NaPF<sub>6</sub> in EC:DMC (1:2 v/v).

Figure 3.11 shows the self-heating rate vs. T of 96 mg Na:HC in 40 mg of NaPF<sub>6</sub> in EC:DEC (1:2 v/v) electrolytes with different molarity. As the molarity of the electrolyte increases, the ARC samples showed increasing reactivity, because more NaPF<sub>6</sub> was added into the solvent and coordinated to EC, leaving the more reactive DEC available to react with the Na:HC. Assuming that each Na<sup>+</sup> and each PF<sub>6</sub><sup>-</sup> are coordinated by four EC molecules, a concentration of about 1.33 M would be required to exhaust all the EC molecules available in EC: DEC (1:2). Therefore it is possible that most of the EC molecules could be involved in the co-ordination at a concentration of 1.0 M. This speculation can explain why Na:HC is more reactive in NaPF<sub>6</sub> electrolyte than in EC:DEC solvent.

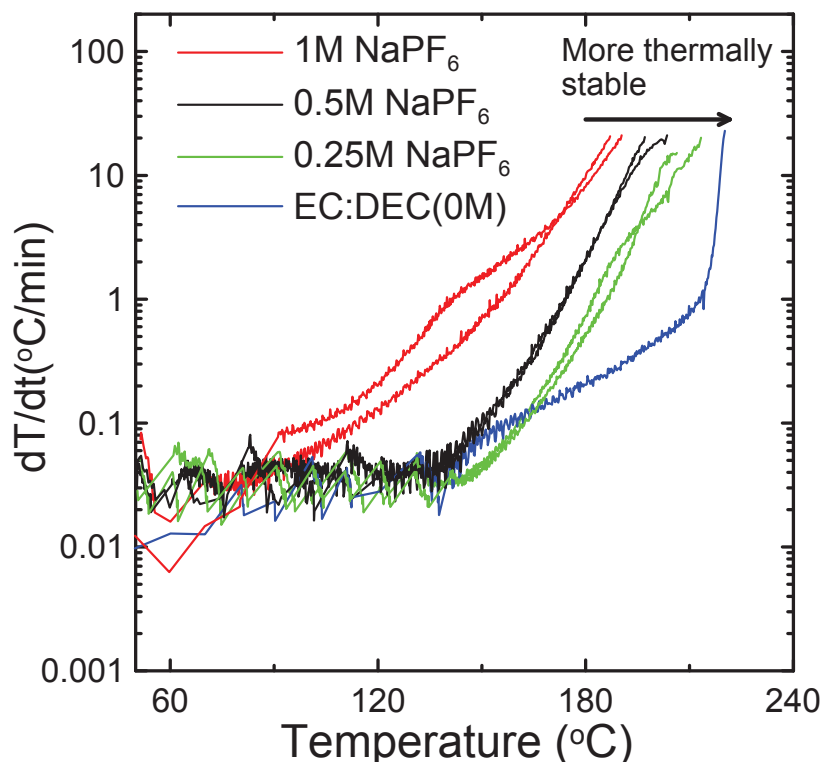


Figure 3.11 Self heating rate (SHR) vs. temperature of 96 mg Na:HC in 40 mg 1 M, 0.5 M, 0.25 M or 0 M (solvent only) NaPF<sub>6</sub> in EC:DEC (1:2 v/v).



### 3.1.4 Summary

The reactivity of Na:HC in different solvents and electrolytes was studied using ARC tests. Na:HC shows higher reactivity than Li:HC in solvent and electrolytes. The XRD results showed that Na:HC reacts with DMC to form sodium methyl carbonate. In EC:DEC solvent, Na:HC reacts with both EC and DEC and the products are derived from both EC and DEC. Adding NaPF<sub>6</sub> to make mixed electrolytes decreases the thermal stability of Na:HC probably because NaPF<sub>6</sub> coordinates more strongly with EC rendering it less reactive than the other solvent components. Therefore, the reaction of Na:HC with electrolyte is similar to the single reaction of Na:HC with DEC or Na:HC with DMC.

### 3.2. Comparison of the reactivity of Na<sub>x</sub>C<sub>6</sub> and Li<sub>x</sub>C<sub>6</sub> with non-aqueous solvents and electrolytes

Graphite and HC were made into Li/graphite and Na/HC electrochemical cells. The Li/Graphite cells reached a final capacity before disassembly of 320 ± 10 mAh/g and the Na/HC cells reached a specific capacity of 320 ± 10 mAh/g as shown in Figure 3.1. The specific surface areas of graphite and HC were measured to be 0.7 ± 0.1 m<sup>2</sup>/g and 2.1 ± 0.1 m<sup>2</sup>/g, respectively.

Figure 3.12 shows the self-heating rate vs. T of 70 mg Li:Graphite or 70 mg Na:HC in the same mass of solvent or electrolyte. Adding LiPF<sub>6</sub> to the solvent significantly reduces the reactivity of Li:Graphite, which agrees well with a previous report [6]. On the other hand, adding NaPF<sub>6</sub> increases the reactivity for Na:HC as evidenced by a reduction in the onset temperature for the self-heating exotherm and a

dramatic increase in self-heating rate compared to the salt-free solvent. The reason for the increasing reactivity of Na:HC in electrolyte has been investigated in the last section. The improved thermal stability of Li:Graphite in electrolyte has been attributed to the formation of LiF [6]. Since LiF is a stable inorganic solid, the formation of LiF improves the thermal stability of the layer of reaction products on the surface of the lithiated graphite and this is why the addition of LiPF<sub>6</sub> decreases the reactivity of LiC<sub>6</sub> with electrolyte [6].

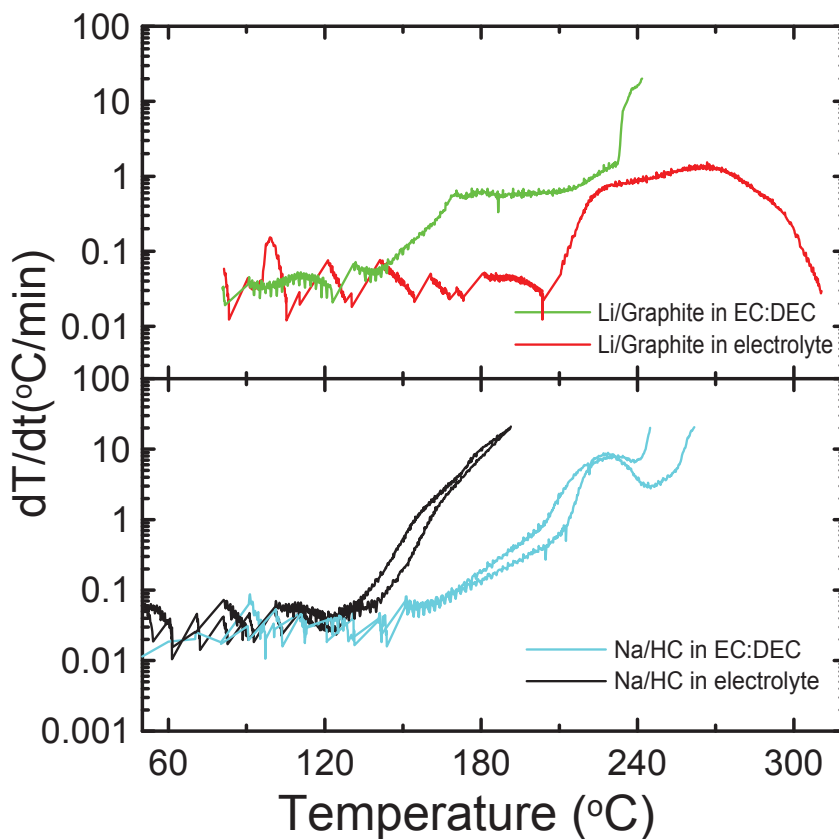


Figure 3.12 Self heating rate (SHR) vs. temperature of 70 mg LiC<sub>6</sub> or 70 mg Na:HC in 70 mg EC:DEC (1:2 v/v) (Li:MCMB: Green, Na:HC: Blue) or 70 mg 1M LiPF<sub>6</sub> in EC:DEC (1:2 v/v) (Red) or 1M NaPF<sub>6</sub> in EC:DEC (1:2 v/v) (Black), as indicated by the legend.

### 3.2.1 Summary

The reactivity of sodium intercalated hard carbon in EC:DEC solvent or in NaPF<sub>6</sub> EC:DEC electrolyte was studied by ARC and the results were compared to the reactivity of LiC<sub>6</sub> with solvent or LiPF<sub>6</sub> EC:DEC electrolyte. Adding NaPF<sub>6</sub> does not decrease the reactivity of Na:HC as adding LiPF<sub>6</sub> does for LiC<sub>6</sub>. This is because NaPF<sub>6</sub> is stable at elevated temperature (in the ARC test temperature range) and does not decompose to form stable inorganic salts, such as NaF, to decrease the reactivity. At the same time, NaPF<sub>6</sub> coordinates to EC and increases the reactivity of Na:HC in NaPF<sub>6</sub> EC:DEC electrolyte because the remaining DEC is more reactive than EC.

## CHAPTER 4 STUDIES OF THE REACTIVITY OF POSITIVE ELECTRODE MATERIALS FOR SODIUM-ION BATTERIES IN SOLVENTS AND ELECTROLYTES.

### 4.1 NaCrO<sub>2</sub>

#### 4.1.1 Synthesis of samples.

A NaCrO<sub>2</sub> sample was prepared by heat treatment of stoichiometric ratios of Na<sub>2</sub>CO<sub>3</sub> and Cr<sub>2</sub>O<sub>3</sub> at 900°C in argon for 5 h. The specific surface area of the sample was  $0.63 \pm 0.05 \text{ m}^2/\text{g}$  as measured by single point BET analysis. A LiCoO<sub>2</sub> sample was obtained from E-One Moli/Energy Canada Ltd. (Vancouver, BC) with a specific surface area of  $0.27 \text{ m}^2/\text{g}$ . A LiFePO<sub>4</sub> sample was obtained from Hydro-Québec, Canada with a specific surface area of  $23.9 \text{ m}^2/\text{g}$ .

#### 4.1.2 XRD and SEM

Figure 4.1 shows the powder XRD pattern of the NaCrO<sub>2</sub> sample. All the observed Bragg peaks matched the reference peak positions of NaCrO<sub>2</sub> (JCPDS # 250819, space group: R-3m). The lattice constants, atom positions and cation disorder were refined using the Rietveld method. The refined lattice constants of NaCrO<sub>2</sub> were found to be  $a = 2.976 \text{ \AA}$  and  $c = 15.969 \text{ \AA}$ . The Na/Cr cation disorder was less than 0.1%. Figure 4.1 also shows SEM images of the NaCrO<sub>2</sub> sample. The powder consisted of well-crystallized particles of 1~3  $\mu\text{m}$  diameter.

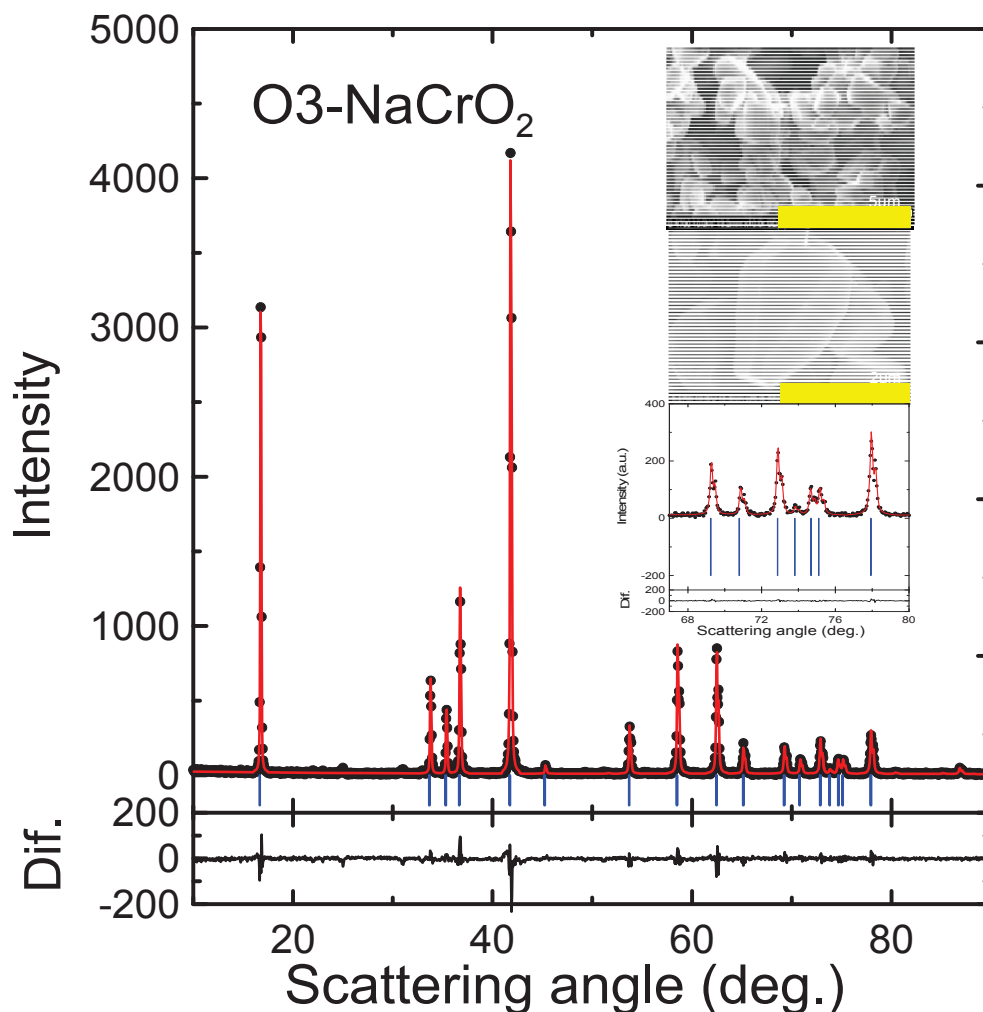


Figure 4.1 Diffraction pattern of synthesized  $\text{NaCrO}_2$  and Rietveld profile refinement. Circles and lines correspond, respectively, to the observed and calculated intensities. The differences between the observed and calculated patterns and the referenced peak positions of  $\text{NaCrO}_2$  corresponding to JCPDS # 250819 are also shown. SEM images of the  $\text{NaCrO}_2$  powder are shown in the inset. The inset also shows an expanded view of the region of the XRD pattern between  $67^\circ$  and  $80^\circ$  to demonstrate the quality of the fitted pattern to the data.

#### 4.1.3 Electrochemical performance of Na/ $\text{NaCrO}_2$ half cells

Figure 4.2 shows the initial potential versus specific capacity curve for the first charge and discharge of a Na/ $\text{NaCrO}_2$  coin cell cycling between 3.6 and 2.0 V. The cell

delivers a capacity of about 110 mAh/g during the first charge, indicating that  $\text{Na}_{0.5}\text{CrO}_2$  has formed at the end of charge. A couple of potential-capacity plateaus can be observed, which are related to the phase transitions: Hex. O3  $\rightarrow$  Mon. O3  $\rightarrow$  Mon. P3 [19]. The cycling performance is also shown as an inset. Only a few cycles are shown here, because two-electrode coin cells with a Na metal counter electrode are easily short-circuited due to very severe Na dendrites. This sample should have good cyclability according to Komaba's report [19]. Improvements focused at dendrite reduction in Na-metal containing coin-cells have been made through introducing polypropylene blown microfiber (BMF, 0.275 mm thickness, 3.2 mg/cm<sup>2</sup>, 3M Co.) as separators in the cells. Please refer to Figure 5.2 to find the improved cyclability of a Na/NaCrO<sub>2</sub> cell.

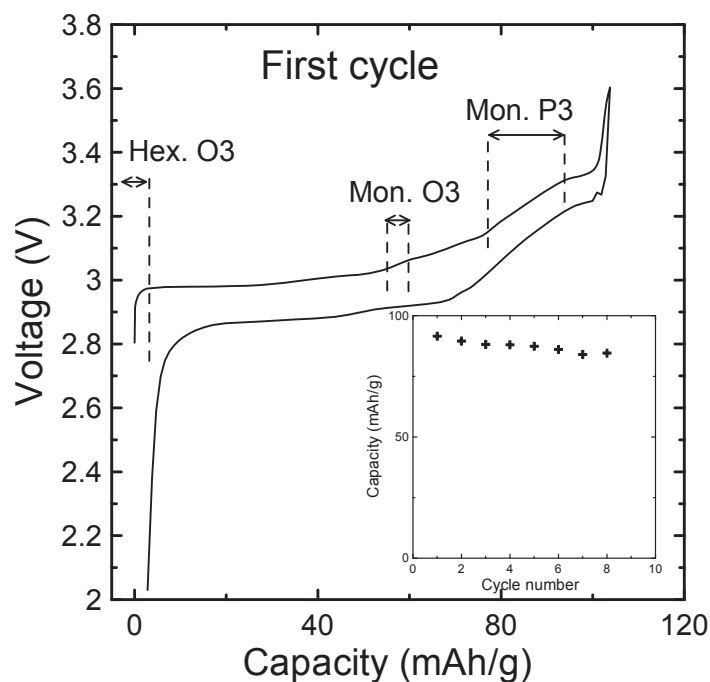


Figure 4.2 Potential versus specific capacity of a  $\text{NaCrO}_2$  electrode in a  $\text{Na}/\text{NaCrO}_2$  coin-type cell. The cell was charged and discharged between 3.6 and 2.0 V using a current corresponding to 25 mAh/g. Specific capacity versus cycle number is shown in the inset.

#### 4.1.4 Reactivity of deintercalated $\text{NaCrO}_2$ ( $\sim\text{Na}_{0.5}\text{CrO}_2$ ) in solvents and electrolytes

The bottom panel of Figure 4.3 shows the self-heating rate vs. temperature,  $T$ , of 100 mg of  $\text{Na}_{0.5}\text{CrO}_2$ ,  $\text{Li}_{0.5}\text{CoO}_2$  or  $\text{Li}_0\text{FePO}_4$  in the same mass of solvent (EC: DEC).  $\text{Na}_{0.5}\text{CrO}_2$  shows an initially unexpected lack of reactivity during the test temperature range ( $50^\circ\text{C}$  to  $350^\circ\text{C}$ ). There is no measurable heat released. On the other hand, the  $\text{Li}_{0.5}\text{CoO}_2$ : solvent sample started to react at around  $120^\circ\text{C}$  and exothermic behaviour occurs up to the end of the testing range.  $\text{Li}_0\text{FePO}_4$  shows low reactivity but eventually shows a brief exotherm beginning around  $300^\circ\text{C}$ .

As it is well-known, deintercalated  $\text{Li}_x\text{CoO}_2$  shows high reactivity in solvents due to the oxygen release from the decomposition of  $\text{Li}_{0.5}\text{CoO}_2$  at elevated temperature and subsequent solvent combustion [7]. Deintercalated  $\text{LiFePO}_4$  is very stable due to the strong bonding between  $\text{O}^{2-}$  and  $\text{P}^{5+}$  in  $(\text{PO}_4)^{3+}$  [65], but it still shows some limited reactivity in solvent at sufficiently high temperature [11].  $\text{Na}_{0.5}\text{CrO}_2$  shows even less reactivity than  $\text{Li}_0\text{FePO}_4$ , and to our knowledge, this is the first time a de-intercalated layered oxide has shown little exothermic behaviour during heating in non-aqueous solvent to  $350^\circ\text{C}$ .

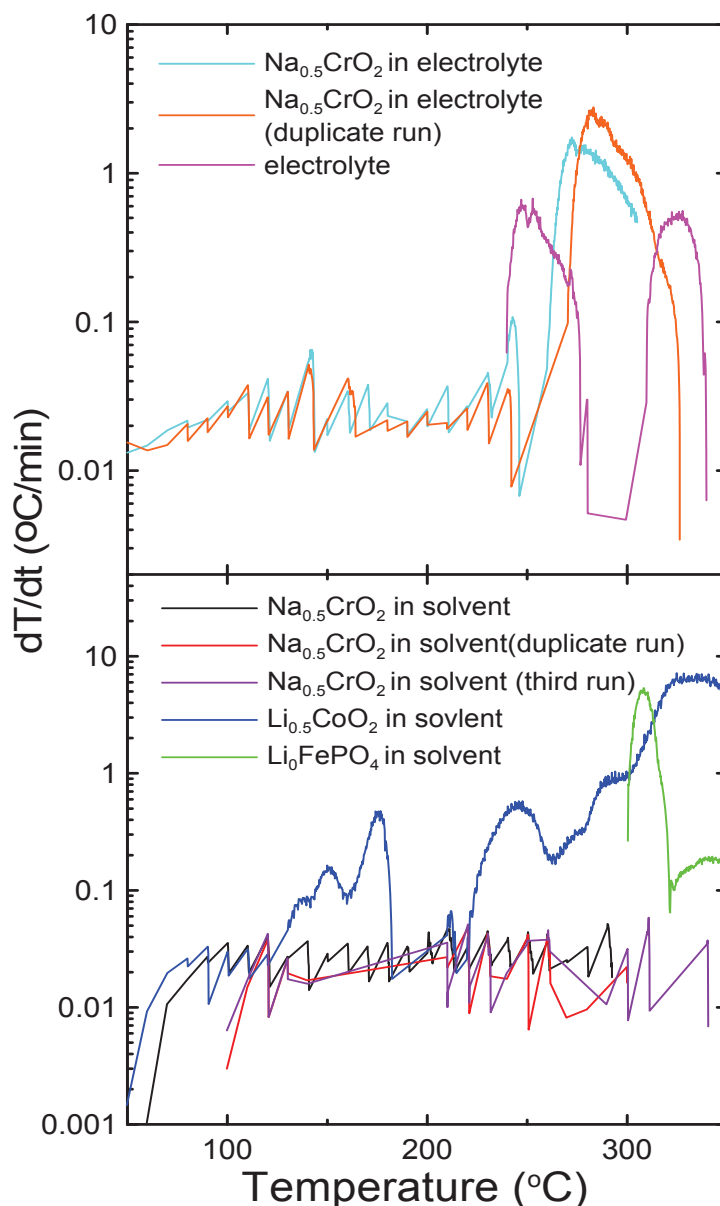


Figure 4.3 Self heating rate (SHR) vs. temperature of 100 mg  $\text{Na}_{0.5}\text{CrO}_2$ ,  $\text{Li}_{0.5}\text{CoO}_2$  or  $\text{Li}_0\text{FePO}_4$  in the same mass of EC: DEC (1:2 v/v) or 1M  $\text{NaPF}_6$  in EC: DEC (1:2 v/v), and the electrolyte itself. The legend indicates which curve corresponds to which sample. Some experiments on  $\text{Na}_{0.5}\text{CrO}_2$  were repeated three times as indicated.

The top panel of Figure 4.3 shows the self-heating rate vs. temperature of 100 mg of  $\text{Na}_{0.5}\text{CrO}_2$  in the same mass of 1M  $\text{NaPF}_6$ /EC: DEC electrolyte and the self-heating rate for 100 mg of the electrolyte itself.  $\text{Na}_{0.5}\text{CrO}_2$  also shows very high thermal stability



in electrolyte. There is no exothermic reaction until around 250°C and the total heat released is small. Given that the electrolyte itself shows a similar response, it is possible that much of the exothermic signal from the  $\text{Na}_{0.5}\text{CrO}_2$ /electrolyte sample comes from only the reaction of the electrolyte itself.  $\text{Na}_{0.5}\text{CrO}_2$  shows much better thermal stability than  $\text{Li}_{0.5}\text{CoO}_2$  and  $\text{Li}_x\text{Ni}_{1/3}\text{Mn}_{1/3}\text{Co}_{1/3}\text{O}_2$  in electrolyte [7, 11, 66].

Why does de-intercalated  $\text{NaCrO}_2$  have so little reactivity with non-aqueous solvent or electrolyte? One explanation could be the high stability of  $\text{Na}_{0.5}\text{CrO}_2$  at elevated temperature. Figure 4.4 shows the weight versus temperature as measured by TGA for  $\text{Na}_{0.5}\text{CrO}_2$ . The TGA result indicates that  $\text{Na}_{0.5}\text{CrO}_2$  loses less than 1% weight after heated to 350°C in argon, compared to more than 3% weight loss of  $\text{Li}_{0.5}\text{CoO}_2$  which decomposes to  $\text{LiCoO}_2$  and  $\text{Co}_3\text{O}_4$  [67] when heated to 350°C.

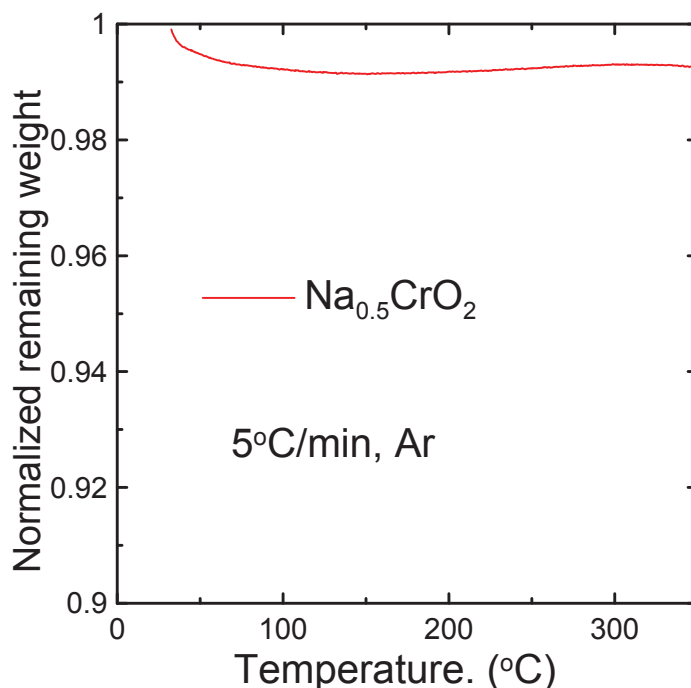
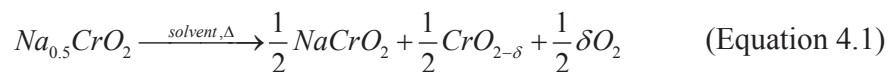


Figure 4.4 TGA experiments on  $\text{Na}_{0.5}\text{CrO}_2$ . The samples were heated at 5°C/min in argon gas

The left column of Figure 4.5 shows the XRD patterns of the products of heating  $\text{Na}_{0.5}\text{CrO}_2$  after ARC (with solvent) and TGA (dry  $\text{Na}_{0.5}\text{CrO}_2$ ). Figure 4.5 also shows the XRD patterns of fresh  $\text{Na}_{0.5}\text{CrO}_2$ , obtained directly from a charged coin cell, and pristine  $\text{NaCrO}_2$  for comparison. The XRD pattern of  $\text{Na}_{0.5}\text{CrO}_2$  after TGA shows the same peaks as fresh  $\text{Na}_{0.5}\text{CrO}_2$  which match the reference peak positions of  $\text{Na}_{0.52}\text{CrO}_2$  (JCPDS # 381205). Additionally, there are a weak set of other peaks that have appeared after the TGA experiment.

Figure 4.5 shows that the XRD pattern of the product of  $\text{Na}_{0.5}\text{CrO}_2$  reacting with solvent after ARC shows different peaks. Two phases can be identified from the XRD pattern. The first phase is O3- $\text{NaCrO}_2$  which matches the peak positions of pristine  $\text{NaCrO}_2$ . The XRD pattern of second phase, which matches the set of weak peaks from the TGA experiment on  $\text{Na}_{0.5}\text{CrO}_2$ , is more clearly observed by subtracting the  $\text{NaCrO}_2$  portion of the pattern from the initial data. The top panel in the right-hand column of Figure 4.5 shows the pattern of the second phase. Based on the lack of heat evolved in the ARC experiment and the little mass loss and few structural changes of  $\text{Na}_{0.5}\text{CrO}_2$  after TGA, which suggests little oxygen evolution from the solid, and the identification of one of the two phases as  $\text{NaCrO}_2$ , a scenario is proposed for the reaction occurring in the ARC experiment. The reaction between  $\text{Na}_{0.5}\text{CrO}_2$  and solvent in the ARC experiment is:



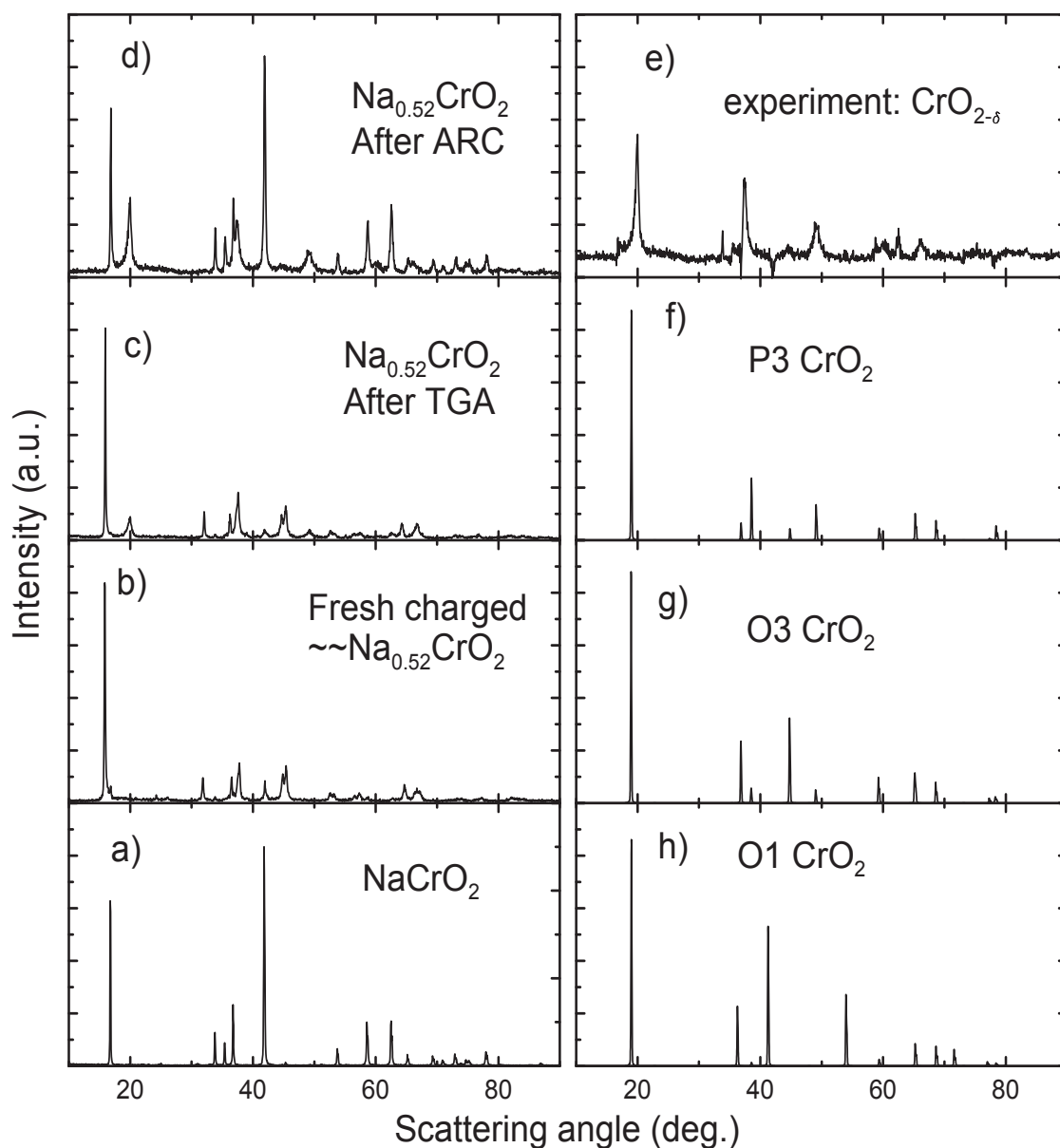


Figure 4.5 (left column) XRD patterns of a) pristine  $\text{NaCrO}_2$ , b)  $\text{Na}_{0.5}\text{CrO}_2$  prepared by charging an  $\text{Na}/\text{NaCrO}_2$  cell to 3.6 V, c) the product of  $\text{Na}_{0.5}\text{CrO}_2$  after a TGA experiment in argon, d) the product of  $\text{Na}_{0.5}\text{CrO}_2$  reacting with solvent in an ARC experiment to  $300^\circ\text{C}$ . (right column) XRD patterns of e) same as (a) with the  $\text{NaCrO}_2$  subtracted showing only the P3- $\text{CrO}_{2-\delta}$  f) calculated pattern of P3- $\text{CrO}_2$ , g) calculated pattern of O3- $\text{CrO}_2$  and h) calculated pattern of O1-  $\text{CrO}_2$ .

In Equation 4.1, only a small amount of oxygen,  $\delta$ , will be released, which can explain the low reactivity of  $\text{Na}_{0.5}\text{CrO}_2$  in solvent. The question now is whether the XRD pattern of the second phase is consistent with a layered  $\text{CrO}_{2-\delta}$  structure. Manthiram *et al.* reported the crystal structure of P3-structure  $\text{CoO}_{2-\delta}$  prepared by chemical oxidation of O3- $\text{LiCoO}_2$  [68]. Lattice constants of  $a = 2.8578 \text{ \AA}$  and  $c = 14.0019 \text{ \AA}$  and space group R3m were used to calculate the XRD pattern of P3- $\text{CrO}_2$  using Rietica. The result is shown in the second panel of the right column in Figure 4.5 which agrees fairly well with the experimental peaks from the second phase displayed in the panel above. For comparison, calculated XRD patterns of O3- $\text{CrO}_2$  and O1- $\text{CrO}_2$ , using appropriate lattice constants, are also shown. The experimental pattern agrees best with the calculated pattern of P3- $\text{CrO}_2$  and this supports our assumption about the reaction that occurred in the ARC (Reaction 4.1). Attempts to carefully refine the XRD pattern of P3- $\text{CrO}_{2-\delta}$  using Rietica failed, because the experimental peak positions are not exactly located at the calculated positions. This can be due to the presence of stacking faults as can be expected during the transition from the O3 to P3 structure. Work to determine these stacking faults using the DiFFaX program [69, 70] to obtain the best agreement with experiment will be discussed in next section. The XRD pattern of the product of  $\text{Na}_{0.5}\text{CrO}_2$  heated in electrolyte is not shown for brevity. That pattern also shows the  $\text{NaCrO}_2$  and  $\text{CoO}_{2-\delta}$  phases. This explains the high thermal stability of  $\text{Na}_{0.5}\text{CrO}_2$  in electrolyte and supports

the assumption that the small exothermic reaction in the ARC experiments on  $\text{Na}_{0.5}\text{CrO}_2/\text{electrolyte}$  originates from the decomposition of the electrolyte itself.

#### 4.1.5 Calculations of the XRD pattern P3-CrO<sub>2</sub> with different type of stacking faults

A stacking fault is a mistake in the stacking sequence of the layers in a layered crystal structure. Stacking faults occur in a number of crystal structures, but the most common example is in close-packed structures. Face-centered cubic (fcc) structures differ from hexagonal close packed (hcp) structures only in stacking order. When stacking one hexagonal close packed layer on top of another, the atoms are not directly on top of one another—the first two layers are identical for hcp and fcc, and labelled AB. If the third layer is placed so that its atoms are directly above those of the first layer, the stacking will be ABA—this is the hcp structure, and it continues ABABABAB. However, there is another possible location for the third layer, such that its atoms are not above the first layer. Instead, it is the atoms in the fourth layer that are directly above the first layer. This produces the stacking ABCABCABC, and is actually a cubic arrangement of the atoms. A stacking fault happens, for example, if the sequence ABCAB(stacking fault)ABCABC were found in an fcc structure.

In alkali transition-metal oxides, a stacking fault can be defined by the sequence of  $\text{MO}_2$  slabs. Figure 4.6 shows the crystal structure of P3 and O3 type layered-CrO<sub>2</sub> viewed in a 110 projection. The CrO<sub>2</sub> slabs in a unit cell are marked. In a P3-type structure, the stacking order of the CrO<sub>2</sub> is aB<sub>1</sub>BcA<sub>2</sub>AbC<sub>3</sub>Ca as shown in Figure 4.6 (“\_”

is prismatic site for alkali atoms), while in a O3-type structure, the stacking order of CrO<sub>2</sub> slabs is aB\_AbC\_BcA\_Ca (“\_” is octahedral site for alkali atoms). Hence, an O3-type stacking fault happens if the sequence aB\_BcA\_AbC\_CaB\_AbC\_AbC\_Ca is found in a P3 type structure.

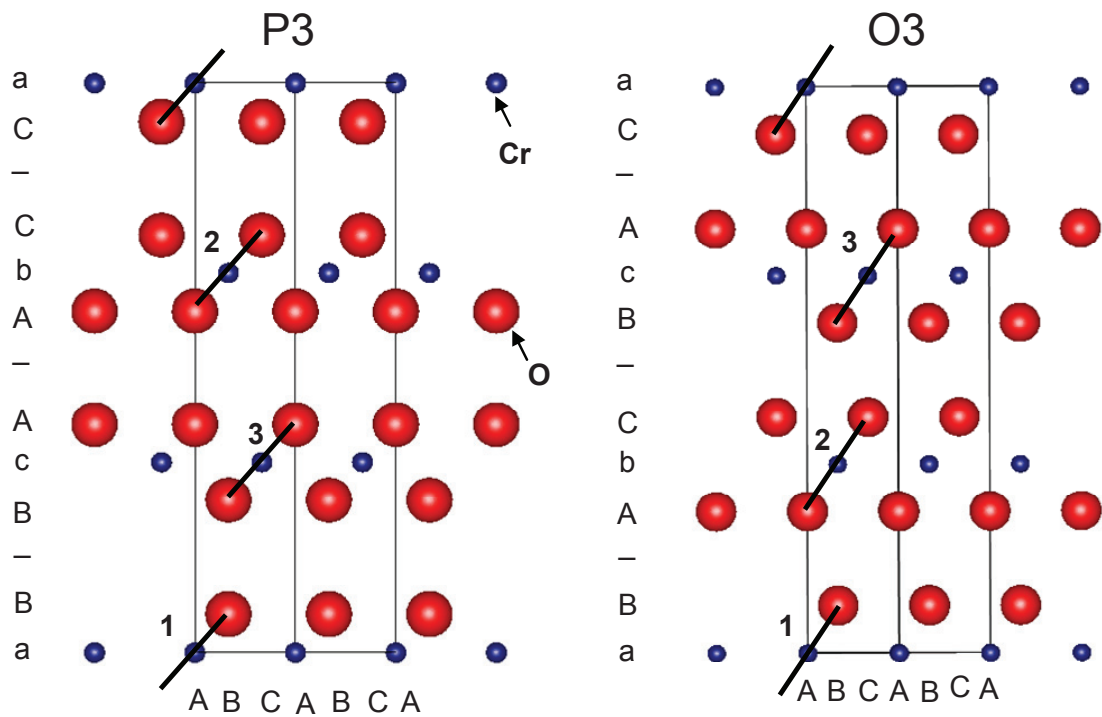


Figure 4.6 Crystal structure of P3 and O3 type layered-CrO<sub>2</sub> viewed in 110 projection

The program DIFFaX can be used to simulate powder X-ray diffraction patterns from crystals containing coherent planar stacking faults. This program exploits the recurring patterns found in randomized stacking sequences to compute the average interference wave function scattered from each layer type occurring in a faulted crystal. It has been used to simulate the nature of the stacking faults in T2, O2 and O6 type Li<sub>2/3</sub>(Co<sub>x</sub>Ni<sub>1/3-x</sub>Mn<sub>2/3</sub>)O<sub>2</sub> by Lu *et al.* as well as many other compounds [69].

To simulate the X-ray diffraction pattern of a stacking faulted structure using DIFFaX, one must specify the layers,  $i$ , that make up the structure as well as the probability,  $\alpha_{ij}$ , of finding layer  $j$  stacked after layer  $i$ . The interlayer translation vector,  $R_{ij}$ , must also be specified. In O3 and P3 type  $\text{CrO}_2$ , there are only 3 types of layers in one unit cell as indicated as 1, 2, 3 in Figure 4.6. Table 4.1 shows the layer stacking probabilities and stacking vectors in O3-P3 structure ( $x$  is a variable,  $0 \leq x \leq 1$ ). If  $x=1$ , the structure is O3 and if  $x=0$  the structure is P3.

Table 4.1 Layer stacking probabilities and stacking vectors

$i-j$	$\alpha_{ij}$ for O3-P3	$R_{xij}$	$R_{yij}$	$R_{zij}$
1----1	0	0	0	0
1----2	$x$	0.3333	0.6667	1
1----3	$1-x$	0.6667	0.3333	1
2----1	$1-x$	0.6667	0.3333	1
2----2	0	0	0	0
2----3	$x$	0.3333	0.6667	1
3---1	$x$	0.3333	0.6667	1
3----2	$1-x$	0.6667	0.3333	1
3----3	0	0	0	0

Figure 4.7 shows the simulated X-ray diffraction patterns for O3-P3 intergrowth structures of  $\text{CrO}_2$  sheets. Table 4.2 shows the layer structure factor and lattice constants used in calculations. These calculations were made by varying  $x$  from 0 to 1. The red

lines indicate the changes to the (012) and (104) peaks as the amount of stacking fault varies. Figure 4.8 shows the calculated XRD pattern of P3-type  $\text{CrO}_2$  with 10% O3-type stacking faults. It agrees quite well with the experimental results.

Table 4.2 Atomic coordinates of the  $\text{CrO}_2$  layer used for the calculation ( $a=b=2.859\text{\AA}$ ,  $C=4.6783\text{\AA}$ ,  $\gamma=120^\circ$ )

	x	y	z	Occupation
Cr	0	0	0	1
O1	1/3	2/3	0.25	1
O2	2/3	1/3	0.25	1

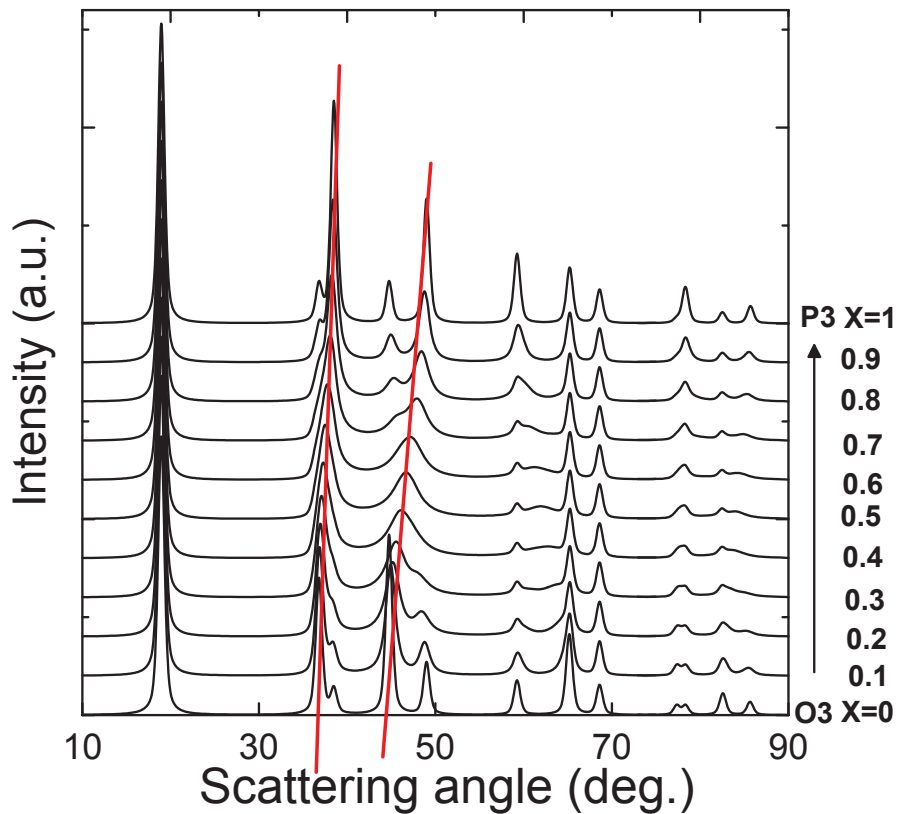


Figure 4.7 Simulations showing the effect of O3-P3 inter-growth. The calculations were made for  $0 < x < 1.0$



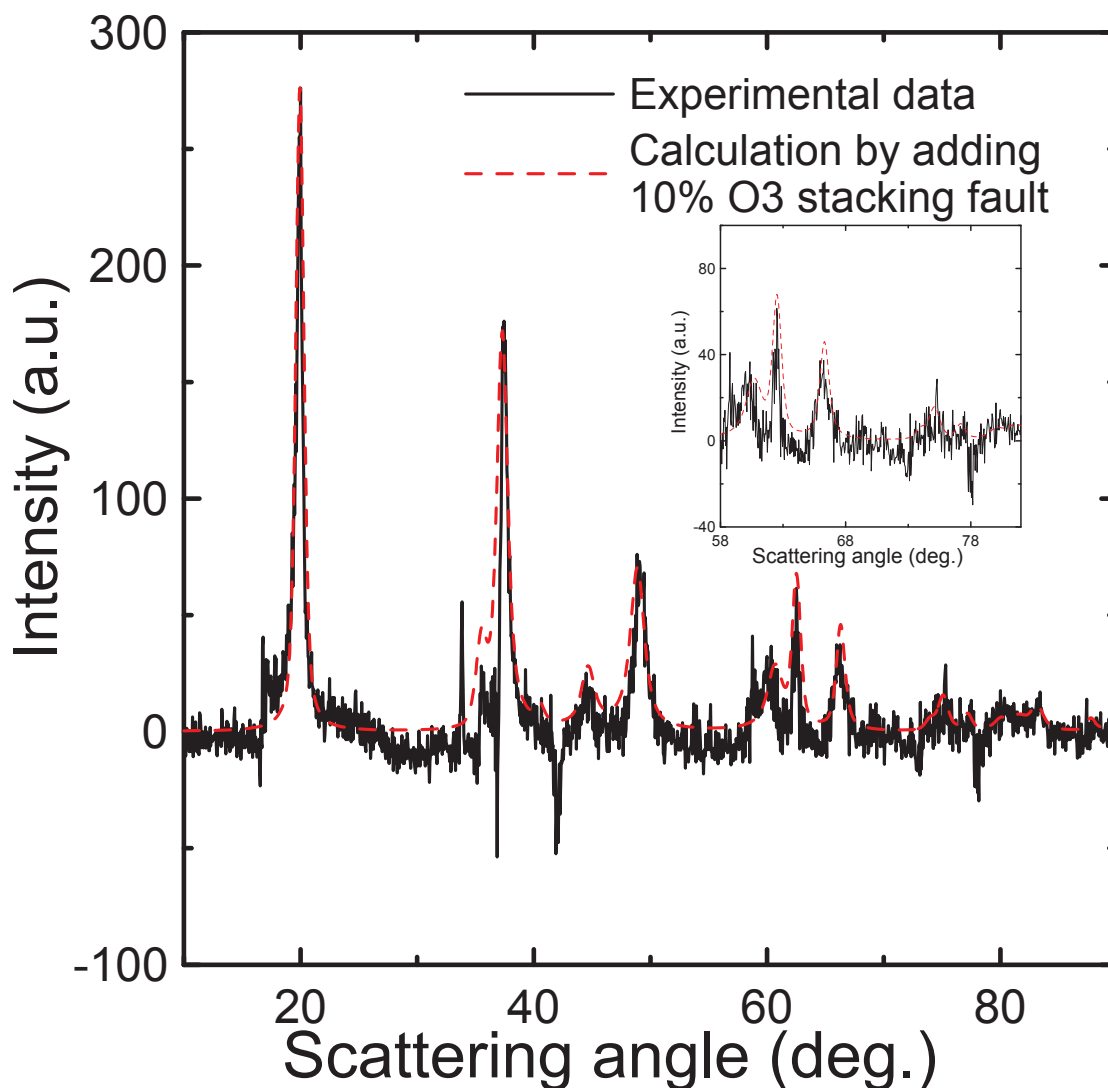


Figure 4.8 Calculated XRD pattern of P3-type CrO<sub>2</sub> with 10% O<sub>3</sub>-type stacking faults and the experimental result from Figure 4.5 (e). The inset shows an expanded view of the XRD pattern from 58° to 82°.

#### 4.1.6 Summary

In this section, O<sub>3</sub>-Type NaCrO<sub>2</sub> was successfully synthesized by solid state reaction and showed good electrochemical performance. The thermal stability of deintercalated Na<sub>0.5</sub>CrO<sub>2</sub> was studied by ARC and Na<sub>0.5</sub>CrO<sub>2</sub> shows virtually no reactivity with non-aqueous solvent between room temperature and 350°C. The reactivity

is even less than that of  $\text{Li}_0\text{FePO}_4$  in the same solvent.  $\text{Na}_{0.5}\text{CrO}_2$  also shows high thermal stability in  $\text{NaPF}_6$ -based electrolyte, better than that of  $\text{Li}_{0.5}\text{CoO}_2$  or  $\text{Li}_x\text{Ni}_{1/3}\text{Mn}_{1/3}\text{Co}_{1/3}\text{O}_2$  in electrolyte. Through an XRD investigation,  $\text{Na}_{0.5}\text{CrO}_2$  is believed to transform to  $\text{NaCrO}_2$  and  $\text{P3-CrO}_{2.8}$  during reaction with solvent or electrolyte. There is apparently minimal oxygen release and this is the reason for the high thermal stability of  $\text{Na}_{0.5}\text{CrO}_2$ . These findings could have profound implications for the safety of Na-ion batteries.

## 4.2 $\text{Na}_{0.65}\text{CoO}_2$

### 4.2.1 Synthesis of samples.

A  $\text{Na}_x\text{CoO}_2$  sample was prepared by heat treating a stoichiometric mixture of  $\text{Na}_2\text{CO}_3$  and  $\text{CoCO}_3$  at  $900^\circ\text{C}$  in air for 24 h. The composition,  $x$ , was determined to be  $x = 0.65 \pm 0.01$  by Atomic Absorption Spectroscopy using a Varian SpectrAA 55B. The specific surface area of the sample was  $0.99 \pm 0.05 \text{ m}^2/\text{g}$  as measured by single point BET analysis.

### 4.2.2 XRD and SEM

Figure 4.9 shows the powder XRD pattern of the initial  $\text{Na}_{0.65}\text{CoO}_2$  sample. All the observed Bragg peaks matched the reference peak positions of  $\text{P2-Na}_{0.71}\text{Co}_{0.96}\text{O}_2$  (JCPDS # 301182, space group:  $\text{P63}/\text{mmc}$ ) well and no impurity phases could be detected. The lattice constants, atom positions and cation disorder were refined using the Rietveld method. The calculated lattice constants of  $\text{Na}_{0.65}\text{CoO}_2$  were found to be  $a = 2.829 \text{ \AA}$  and

$c = 10.941 \text{ \AA}$ . Figure 4.9 also shows SEM images of the  $\text{Na}_{0.65}\text{CoO}_2$  sample. The powder consisted of well-crystallized particles of  $5 \sim 10 \text{ \mu m}$  diameter.

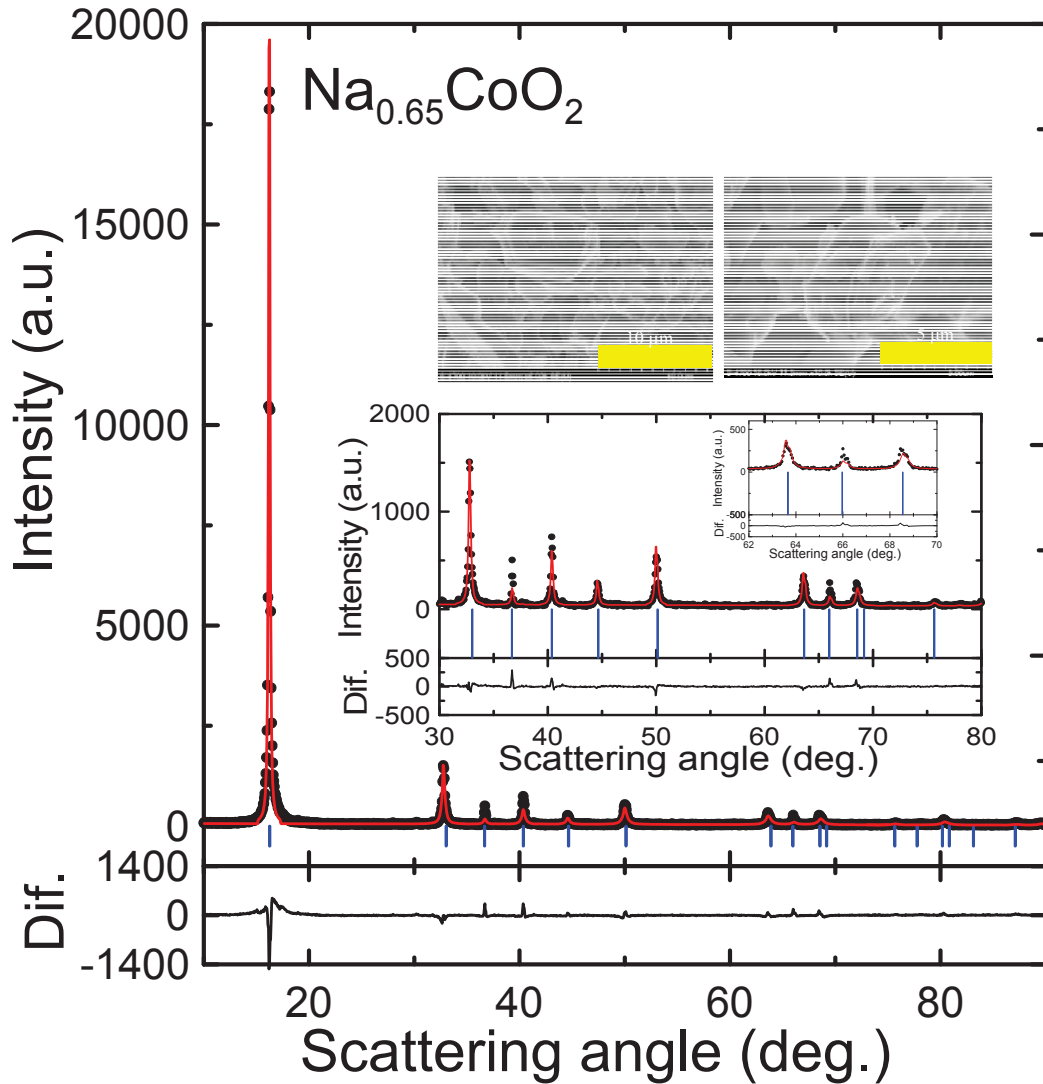


Figure 4.9 Diffraction pattern of synthesized  $\text{Na}_{0.65}\text{CoO}_2$  and Rietveld profile refinement. Circles and lines correspond, respectively, to the observed and calculated intensities. The differences between the observed and calculated patterns and the referenced peak positions of  $\text{Na}_{0.71}\text{Co}_{0.96}\text{O}_2$  corresponding to JCPDS # 301182 are also shown. Expanded version of XRD pattern (from  $30^\circ$  to  $80^\circ$ ) and SEM images of the  $\text{Na}_{0.65}\text{CoO}_2$  powder are shown in the inset. The inset in the inset also shows an expanded view of the data and calculation from  $62^\circ$  to  $70^\circ$

### 4.2.3 Electrochemical performance of $\text{Na}_{0.65}\text{CoO}_2/\text{Na}$ half cells

Figure 4.10 shows the potential versus  $x$  in  $\text{Na}_x\text{CoO}_2$  of a  $\text{Na}/\text{Na}_{0.65}\text{CoO}_2$  cell. The cell was first discharged to 2V versus Na and then charged to 4.3 V followed by a second discharge to 2 V. The curve shows many plateaus and steps, which are related to the existence of biphasic and single-phase domains [16]. The potential-composition behaviour in Figure 4.10 agrees quite well with the earlier work of Delmas *et al.* [16]. When charged from its initial composition of  $\text{Na}_{0.65}\text{CoO}_2$  to 4.3 V, the material delivers a capacity of 70 mAh/g, corresponding to the removal of about 0.3 mole of Na per mole of Co

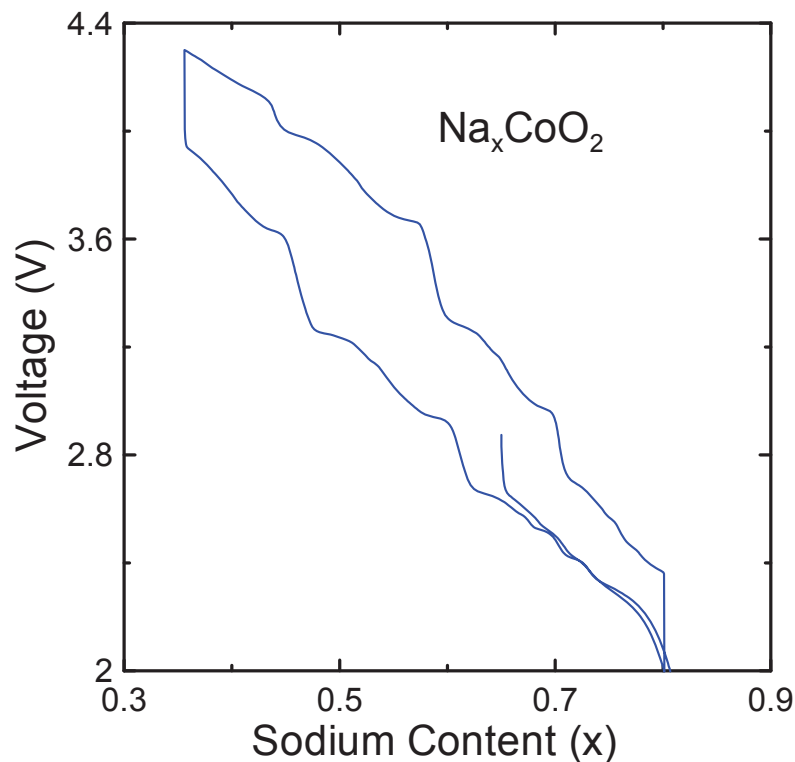


Figure 4.10 Potential versus specific capacity of a  $\text{Na}_{0.65}\text{CoO}_2$  electrode in a  $\text{Na}/\text{Na}_{0.65}\text{CoO}_2$  coin-type cell. The cell was charged and discharged between 4.3 and 2.0 V using a current corresponding to 5 mA/g.

#### 4.2.4 Reactivity of deintercalated $\text{Na}_{0.65}\text{CoO}_2$ ( $\sim\text{Na}_{0.3}\text{CoO}_2$ ) in solvents and electrolytes

The bottom panel of Figure 4.11 shows the self-heating rate versus temperature of 0.1 g  $\text{Na}_{0.35}\text{CoO}_2$  reacting with 0.1 g of EC:DEC. The experiment started at 50°C.  $\text{Na}_{0.35}\text{CoO}_2$  shows a relatively high reactivity in solvent. The onset temperature of the exothermic reaction is about 140°C (as given in the lower panel), and three significant exothermic peaks were observed till the end of the test (300°C). The top panel of Figure 4.11 shows the self-heating rate vs. temperature of 100 mg of  $\text{Na}_{0.35}\text{CoO}_2$  in the same mass of solvent EC:DEC, 0.5M  $\text{NaPF}_6$ /EC:DEC (1:2 v/v) and 1M  $\text{NaPF}_6$ /EC:DEC (1:2 v/v). In these experiments, the ARC was initially forced to 115°C at 5°C/min, before exotherm searching initiated. With salt added,  $\text{Na}_{0.35}\text{CoO}_2$  shows more reactivity at low temperature than in solvent alone. There is an exothermic reaction starting at around 115°C, and followed by another exothermic reaction starting at around 195°C in the samples containing  $\text{NaPF}_6$ . The total heat released by the first exothermic reaction, as measured by the temperature increase,  $\Delta T$ , indicated in Figure 4.11, seems to be roughly proportional to the molarity of the electrolyte.

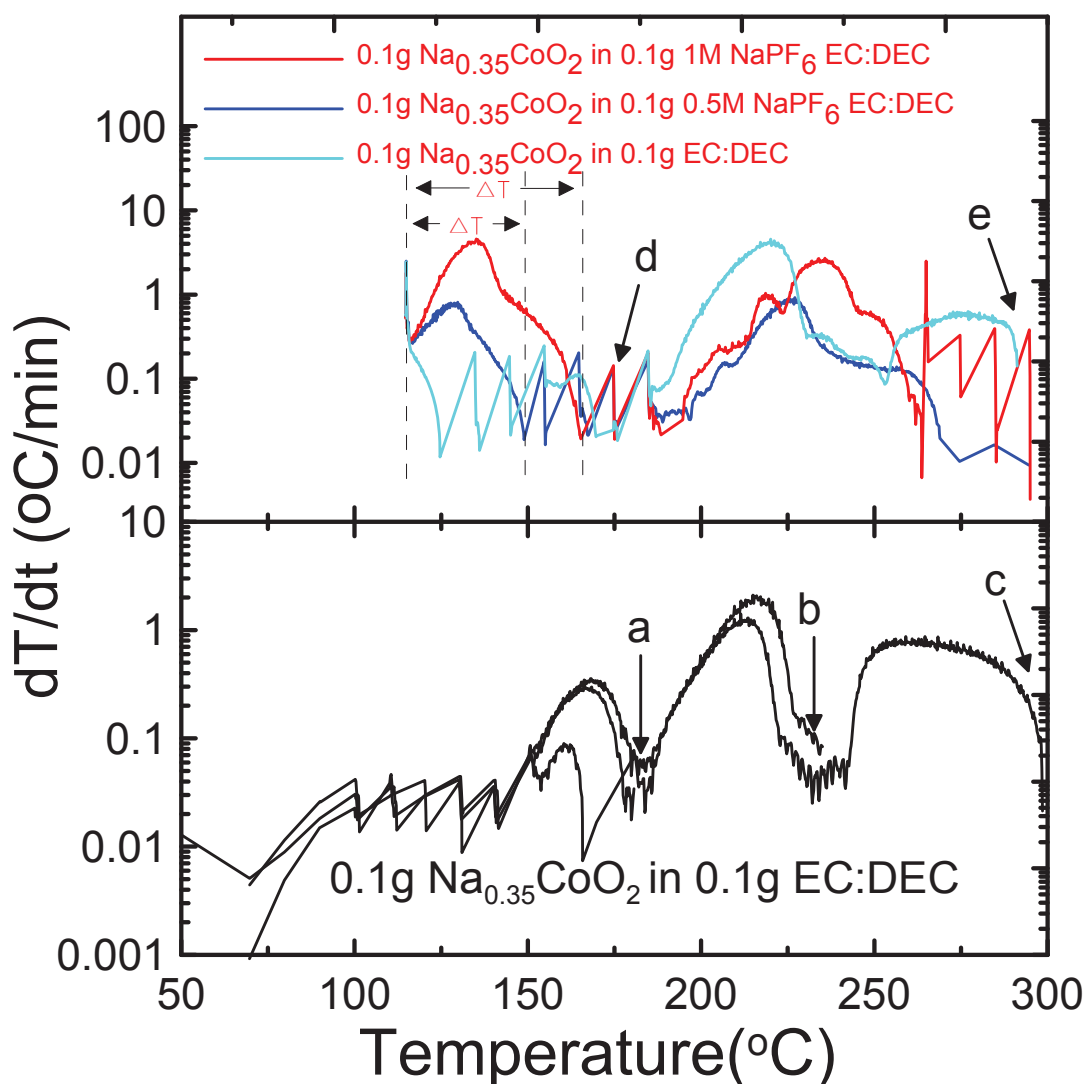
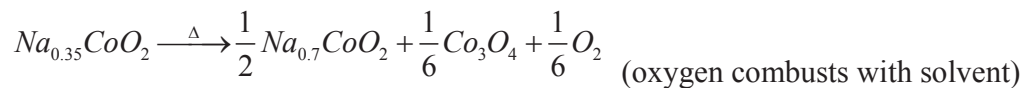


Figure 4.11 Self heating rate (SHR) vs. temperature of 100 mg  $\text{Na}_{0.35}\text{CoO}_2$  in the same mass of EC: DEC (1:2 v/v), 0.5M  $\text{NaPF}_6$  in EC: DEC (1:2 v/v) or 1M  $\text{NaPF}_6$  in EC: DEC (1:2 v/v). The starting temperature of ARC samples was set to  $50^\circ\text{C}$  (lower panel) or  $115^\circ\text{C}$  (upper panel) and the end temperature was set at  $180^\circ\text{C}$ ,  $230^\circ\text{C}$  or  $300^\circ\text{C}$ . The legend indicates which curve corresponds to which sample. The letters, a – f, indicate where samples were stopped for XRD experiments reported in Figures 4.11a – 4.11f, respectively.

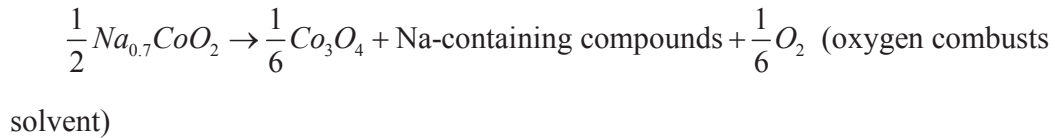
Figure 4.12a shows a XRD pattern of the products of heating  $\text{Na}_{0.35}\text{CoO}_2$  in solvent to  $180^\circ\text{C}$ , Figure 4.12b shows a XRD pattern of the products of heating  $\text{Na}_{0.35}\text{CoO}_2$  in solvent to  $230^\circ\text{C}$  and Figure 4.12c shows a XRD pattern of the same

reactants heated to 300°C.  $\text{Co}_3\text{O}_4$  can be identified in both Figures 4.12a and Figure 4.12b. A similar scenario to the reaction mechanism of  $\text{Li}_{0.5}\text{CoO}_2$  heated in solvent [7] is proposed for  $\text{Na}_{0.35}\text{CoO}_2$ .  $\text{Na}_{0.35}\text{CoO}_2$  decomposes to  $\text{Na}_x\text{CoO}_2$  (with  $x > 0.35$ ) and  $\text{Co}_3\text{O}_4$  and releases  $\text{O}_2$  to combust the solvent. In Figure 4.12a, some peaks can be identified as  $\text{Na}_x\text{CoO}_2$  ( $x \sim 0.7$ ) (the referenced peak positions of  $\text{Na}_{0.7}\text{CoO}_2$  are shown as blue lines). As the temperature increased, more  $\text{Co}_3\text{O}_4$  could be identified (shown in Figure 4.12b), while there is less peak intensity from  $\text{Na}_x\text{CoO}_2$ . In Figure 4.12c, only very well-crystallized  $\text{CoCO}_3$  can be identified. During the cooling process after the ARC test, cobalt oxide reacted with high pressure  $\text{CO}_2$ , originating from the combustion of solvent, to form  $\text{CoCO}_3$ . No Na-containing compound (such as  $\text{Na}_2\text{CO}_3$  or  $\text{NaHCO}_3$ ) can be observed in Figure 4.12c, perhaps to due to low crystallinity. The three steps of the reaction can be described as:

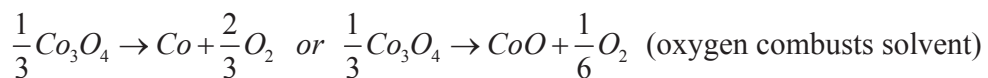
First exotherm;



Second exotherm;



Third Exotherm:



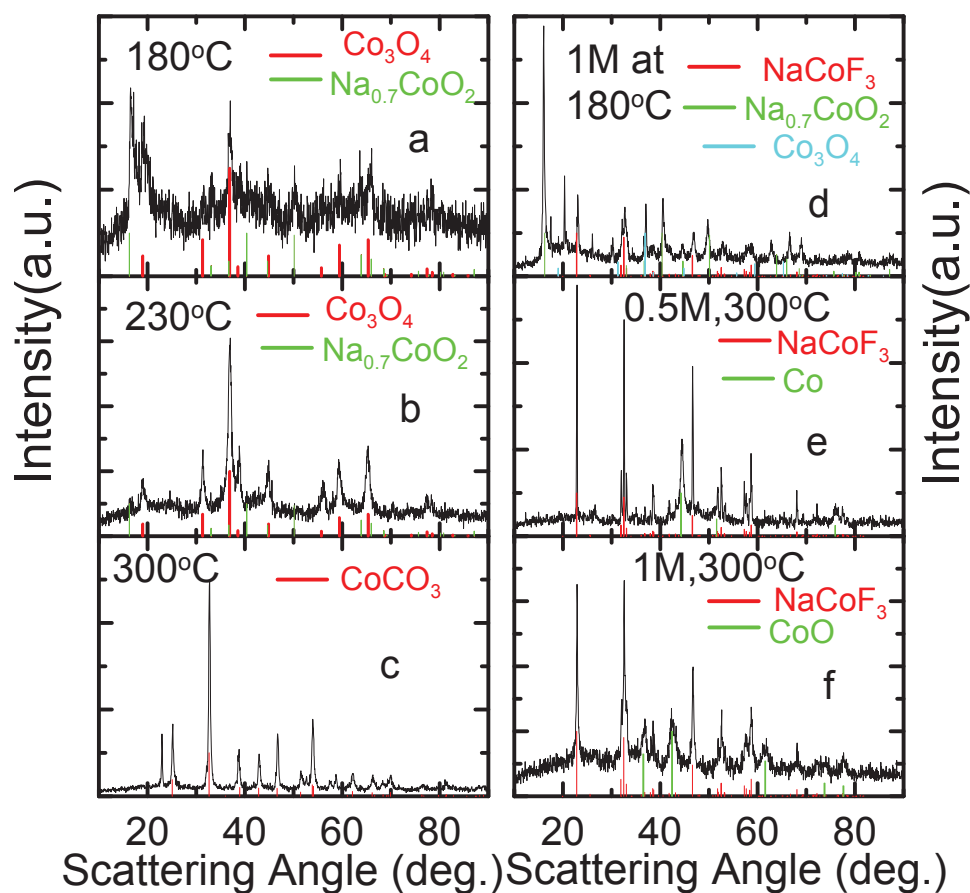


Figure 4.12 (left column) XRD patterns of a)  $\text{Na}_{0.35}\text{CoO}_2$  in solvent heated to  $180^\circ\text{C}$ , b)  $\text{Na}_{0.35}\text{CoO}_2$  in solvent heated to  $230^\circ\text{C}$ , c)  $\text{Na}_{0.35}\text{CoO}_2$  in solvent heated to  $300^\circ\text{C}$ ; (right column) XRD patterns of d)  $\text{Na}_{0.35}\text{CoO}_2$  in 1M  $\text{NaPF}_6$  based electrolyte heated to  $180^\circ\text{C}$ , e)  $\text{Na}_{0.35}\text{CoO}_2$  in 0.5 M  $\text{NaPF}_6$ -based electrolyte heated to  $300^\circ\text{C}$ , f)  $\text{Na}_{0.35}\text{CoO}_2$  in 1M  $\text{NaPF}_6$ -based electrolyte heated to  $300^\circ\text{C}$ . Reference peak positions of some compounds are shown by lines with different colors (indicated in the Figure)

In order to investigate what happened to the created  $\text{Na}_{0.7}\text{CoO}_2$  (Figure 4.12a) during the reaction, the reaction of as-synthesized  $\text{Na}_{0.65}\text{CoO}_2$  with solvent was also studied using ARC and the resulting reaction products were studied by XRD. Figure 4.13a shows the self-heating rate versus temperature of 0.1 g of  $\text{Na}_{0.35}\text{CoO}_2$  in 0.1 g EC:DEC and Figure 4.13d shows the XRD pattern of the products of the reaction after heating to  $300^\circ\text{C}$ . Figure 4.13a contains the same data set as the bottom panel of Figure



4.11 and Figure 4.13d contains the same data set as Figure 4.12c. Figures 4.13a and 4.13d have been included for comparison with the rest of the data in Figure 4.13. Figures 4.13b and 4.13c show the self-heating rate versus temperature of 0.1 g of as-synthesized  $\text{Na}_{0.65}\text{CoO}_2$  in 0.1 g EC:DEC where the experiments were terminated at 230°C and 300°C, respectively. Figure 4.13c also contains the data from Figure 4.13b so that the repeatability of the results to 230°C can be demonstrated. Figures 4.13e and 4.13f show the XRD patterns of the products of the reactions from the ARC experiments in Figures 4.13b and 4.13c, respectively.

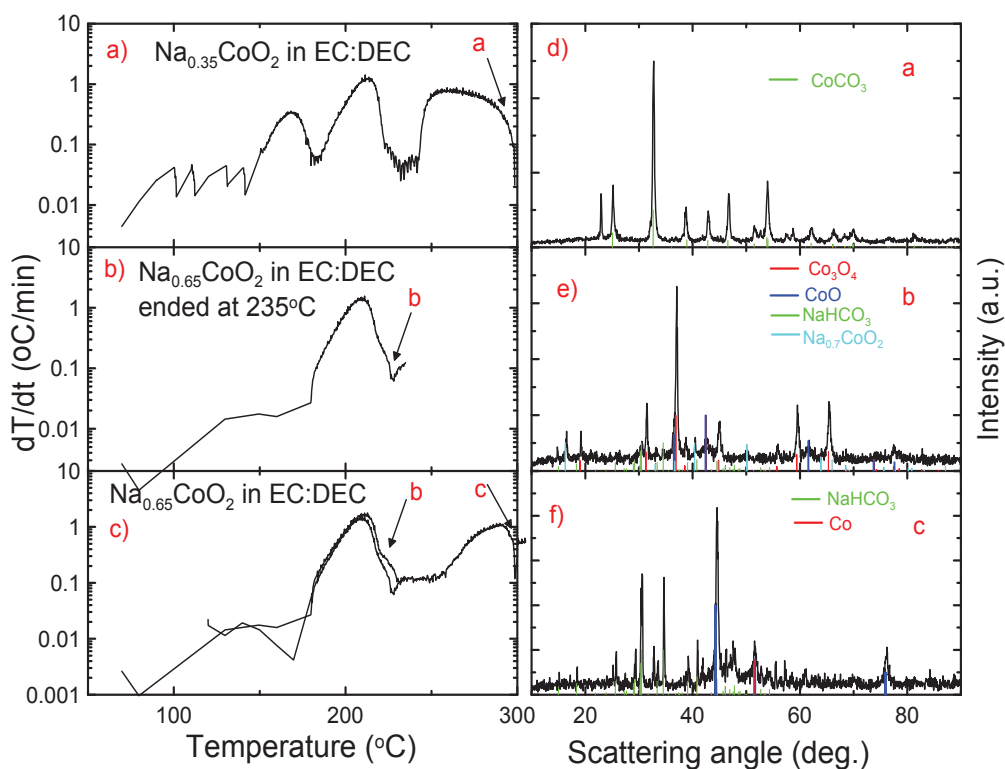


Figure 4.13 (left panel) Self heating rate (SHR) vs. temperature of a) 100 mg  $\text{Na}_{0.35}\text{CoO}_2$  in 100 mg EC: DEC (1:2 v/v) heated to 300°C, b)  $\text{Na}_{0.65}\text{CoO}_2$  in the 100 mg EC: DEC (1:2 v/v) heated to 230°C, c)  $\text{Na}_{0.65}\text{CoO}_2$  in the 100 mg EC: DEC (1:2 v/v) heated to 300°C. (right panel) XRD patterns of d)  $\text{Na}_{0.35}\text{CoO}_2$  in solvent heated to 300°C, e)  $\text{Na}_{0.65}\text{CoO}_2$  in solvent heated to 230°C, f)  $\text{Na}_{0.65}\text{CoO}_2$  in solvent heated to 300°C. Reference peak positions of some compounds are shown by lines with different colors.

Figure 4.13a shows that  $\text{Na}_{0.35}\text{CoO}_2$  shows three distinct exothermic peaks while Figure 4.13c shows that as-synthesized  $\text{Na}_{0.65}\text{CoO}_2$  shows two distinct exothermic peaks. Figure 4.12a demonstrated that the first exothermic peak of the reaction between  $\text{Na}_{0.35}\text{CoO}_2$  and solvent was the formation of  $\text{Na}_{0.7}\text{CoO}_2$  and  $\text{Co}_3\text{O}_4$ . The second exothermic peak in Figure 4.13a matches the exothermic peak in Figure 4.13b and the first exothermic peak in Figure 4.13c, strongly suggesting that this peak is caused by the same reaction process. Figure 4.13e shows that the reaction product after heating  $\text{Na}_{0.65}\text{CoO}_2$  in solvent to  $230^\circ\text{C}$  is mostly  $\text{Co}_3\text{O}_4$ , some remaining  $\text{Na}_{0.7}\text{CoO}_2$  and some  $\text{NaHCO}_3$ . These products, apart from the  $\text{NaHCO}_3$ , agree with the products observed in Figure 4.12b collected after the second exothermic peak in Figure 4.13a.

Figure 4.13f shows the XRD pattern of the reaction products after heating  $\text{Na}_{0.65}\text{CoO}_2$  and solvent to  $300^\circ\text{C}$ . This XRD pattern shows primarily Co and  $\text{NaHCO}_3$ . The XRD pattern in Figure 4.13d for the reaction products between  $\text{Na}_{0.35}\text{CoO}_2$  and solvent shows primarily  $\text{CoCO}_3$ , formed by the reaction of formed CoO and  $\text{CO}_2$  during cooling. The differences between the products in Figures 4.13d and 4.13f are caused by the increased amount of Na present in the experiment in Figure 4.13f, leading to the formation of  $\text{NaHCO}_3$ , the consumption of  $\text{CO}_2$  and oxygen, hence eliminating the formation of  $\text{CoCO}_3$ . Table 4.3 summarizes the results of the reactions between  $\text{Na}_{0.35}\text{CoO}_2$  or  $\text{Na}_{0.65}\text{CoO}_2$  and solvent or electrolytes.

The right column of Figure 4.12 shows the XRD patterns of products of heating  $\text{Na}_{0.35}\text{CoO}_2$  in electrolyte with different molarities to  $180^\circ\text{C}$  and  $300^\circ\text{C}$  (as indicated by positions d and e in Figure 4.11). By comparison with Figure 4.11,  $\text{Na}_{0.35}\text{CoO}_2$  shows quite different reactivity in electrolyte than in solvent. The XRD patterns help explain why this is the case as they show the presence of completely different compounds. In all three XRD patterns in the right column of Figure 4.12, a new phase,  $\text{NaCoF}_3$ , can be identified. The fluorine in this phase can only come from  $\text{NaPF}_6$ . This result means that  $\text{NaPF}_6$ , which is normally used as the salt in the electrolyte of sodium-ion batteries [24], can react with  $\text{Na}_{0.35}\text{CoO}_2$  at elevated temperature. The analogous reaction does not occur for  $\text{Li}_x\text{CoO}_2$  in  $\text{LiPF}_6$ -based electrolytes because  $\text{LiCoF}_3$  is not known. Additionally, the analogous reaction does not occur in  $\text{Na}_x\text{CrO}_2$  in  $\text{NaPF}_6$ -based electrolytes as discussed in section 4.1.4 because  $\text{NaCrF}_3$  does not exist. The presence of  $\text{NaCoF}_3$  also explains why the total heat released during the first exothermic reaction found in the in ARC trace of  $\text{Na}_{0.35}\text{CoO}_2/\text{electrolyte}$  is related to the concentration of  $\text{NaPF}_6$  in electrolyte as shown in the top panel of Figure 4.11.  $\text{NaCoF}_3$  is formed after the first exothermic reaction (at  $180^\circ\text{C}$ ), as shown in the top right panel in Figure 4.11. The reactions that occur at elevated temperatures in  $\text{Na}_{0.35}\text{CoO}_2/\text{electrolyte}$  mixtures in the ARC experiments are summarized in Table 4.3.

Table 4.3 Reaction products between  $\text{Na}_{0.65}\text{CoO}_2$  or  $\text{Na}_{0.35}\text{CoO}_2$  and solvent or electrolytes heated in ARC experiments to different temperatures.

Solid Reactant	Liquid Reactant	Final Temperature (°C)	Products observed by XRD experiments	Figure
$\text{Na}_{0.35}\text{CoO}_2$	EC:DEC	180	$\text{Co}_3\text{O}_4$ and $\text{Na}_{0.7}\text{CoO}_2$	4.12a
$\text{Na}_{0.35}\text{CoO}_2$	EC:DEC	230	Mostly $\text{Co}_3\text{O}_4$	4.12b
$\text{Na}_{0.35}\text{CoO}_2$	EC:DEC	300 (recall, XRD at room Temperature)	$\text{CoCO}_3$ (created during cooling)	4.12c
$\text{Na}_{0.65}\text{CoO}_2$	EC:DEC	230	$\text{Co}_3\text{O}_4$ , $\text{NaHCO}_3$ , small $\text{Na}_{0.7}\text{CoO}_2$	4.13e
$\text{Na}_{0.65}\text{CoO}_2$	EC:DEC	300	Co and $\text{NaHCO}_3$	4.13f
$\text{Na}_{0.35}\text{CoO}_2$	1M $\text{NaPF}_6$ EC:DEC	180	$\text{NaCoF}_3$ , $\text{Na}_{0.7}\text{CoO}_2$ and $\text{Co}_3\text{O}_4$	4.12d
$\text{Na}_{0.35}\text{CoO}_2$	1M $\text{NaPF}_6$ EC:DEC	300	$\text{NaCoF}_3$ and CoO	4.12f
$\text{Na}_{0.35}\text{CoO}_2$	0.5 M $\text{NaPF}_6$ EC:DEC	300	$\text{NaCoF}_3$ and Co	4.12e

#### 4.2.5 Summary

In this section, P2-type  $\text{Na}_{0.65}\text{CoO}_2$  was successfully synthesized by solid state reaction and showed good electrochemical performance. The thermal stability of deintercalated  $\text{Na}_{0.65}\text{CoO}_2$  ( $\sim\text{Na}_{0.35}\text{CoO}_2$ ) was studied by ARC and  $\text{Na}_{0.35}\text{CoO}_2$  shows relatively high reactivity in solvent and in  $\text{NaPF}_6$ -based electrolyte. Through an XRD investigation, the reaction mechanism of  $\text{Na}_{0.35}\text{CoO}_2$  in solvent is believed to be similar

to  $\text{Li}_{0.5}\text{CoO}_2$  in solvent.  $\text{Na}_{0.35}\text{CoO}_2$  decomposes to  $\text{Na}_{0.7}\text{CoO}_2$  and  $\text{Co}_3\text{O}_4$ , and releases  $\text{O}_2$  at the same time, which combusts the solvent, generating heat.  $\text{Na}_{0.7}\text{CoO}_2$  is also not stable at elevated temperature in solvent as it reacts to form  $\text{NaHCO}_3$  and cobalt oxides or cobalt metal releasing more  $\text{O}_2$  to combust more solvent. In electrolyte,  $\text{NaPF}_6$  rapidly reacts with  $\text{Na}_{0.35}\text{CoO}_2$  to form  $\text{NaCoF}_3$  and  $\text{CoO/Co}$  at elevated temperature. Additionally, this reaction to form  $\text{NaCoF}_3$  may proceed slowly at the temperatures of battery operation. These results are instructive for the future design of electrolytes and electrodes to be used in sodium-ion batteries.

### **4.3 $\text{NaNi}_{0.5}\text{Mn}_{0.5}\text{O}_2$**

#### **4.3.1 Synthesis of the sample.**

$\text{Ni}_{0.5}\text{Mn}_{0.5}(\text{OH})_2$  was prepared by a coprecipitation synthesis that was described in Section 2.2.2. Then  $\text{Ni}_{0.5}\text{Mn}_{0.5}(\text{OH})_2$  was mixed with a stoichiometric amount of  $\text{Na}_2\text{CO}_3$  and grinding in an automatic grinder. A  $\text{NaNi}_{0.5}\text{Mn}_{0.5}\text{O}_2$  sample was obtained by heat treating the mixture at  $900^\circ\text{C}$  in air for 24 h. The specific surface area of the sample was  $0.62 \pm 0.05 \text{ m}^2/\text{g}$  as measured by single point BET analysis.

#### **4.3.2 XRD and SEM**

Figure 4.14 shows the powder XRD pattern of the initial  $\text{NaNi}_{0.5}\text{Mn}_{0.5}\text{O}_2$  sample. All the observed Bragg peaks matched those reported in the literature quite well [19]. The lattice constants, atom positions and cation disorder were refined using the Rietveld

method. The calculated lattice constants of  $\text{NaNi}_{0.5}\text{Mn}_{0.5}\text{O}_2$  were found to be  $a = 2.968 \text{ \AA}$  and  $c = 15.909 \text{ \AA}$ . The Na/Ni cation disorder was less than 2% based on the refinement. Figure 4.14 also shows SEM images of the  $\text{NaNi}_{0.5}\text{Mn}_{0.5}\text{O}_2$  sample. The powder consisted of well-crystallized particles of  $3 \sim 5 \mu\text{m}$  in diameter.

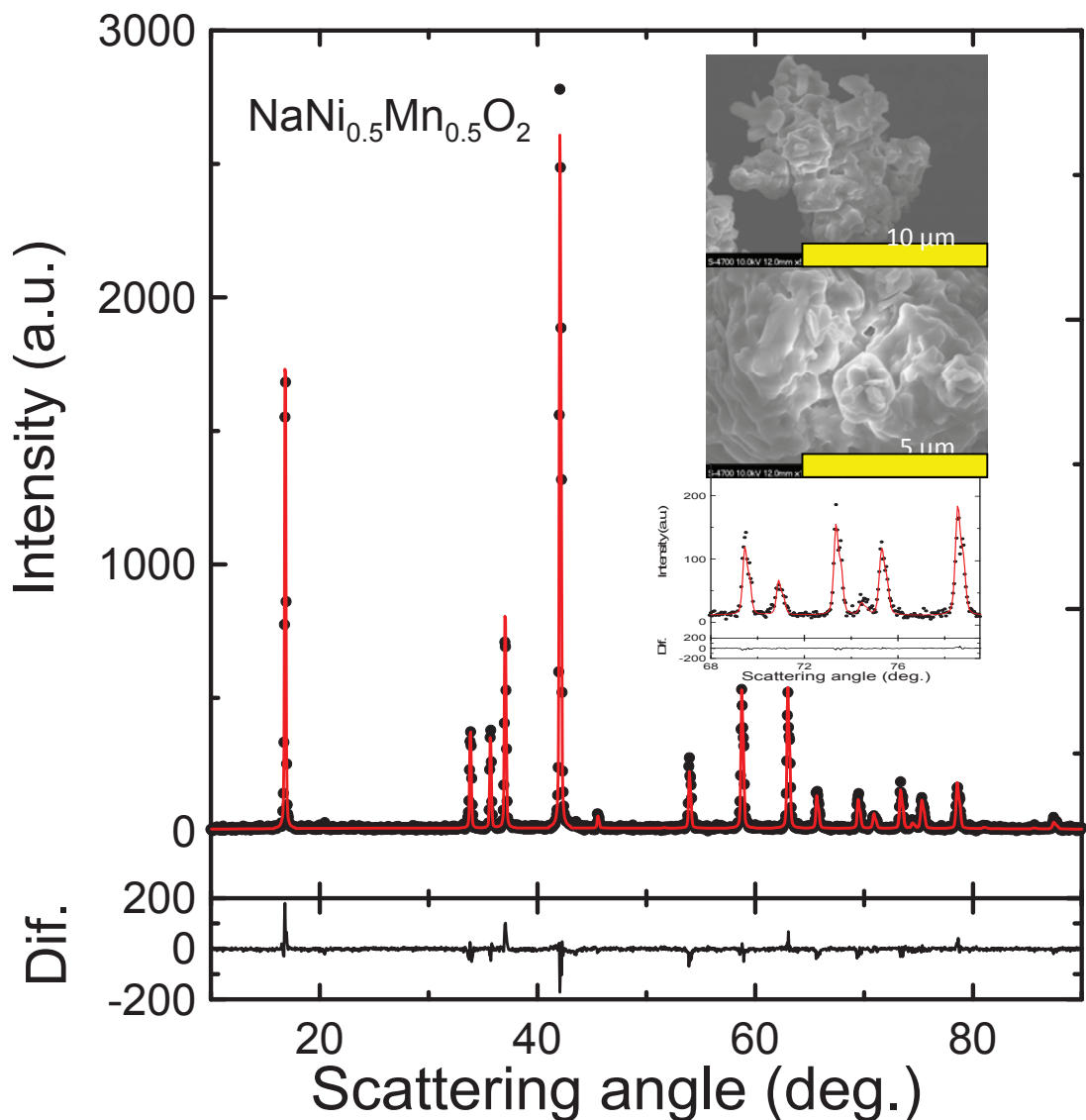


Figure 4.14 Diffraction pattern of synthesized  $\text{NaNi}_{0.5}\text{Mn}_{0.5}\text{O}_2$  and Rietveld profile refinement. Circles and lines correspond, respectively, to the observed and calculated intensities. The differences between the observed and calculated patterns are also shown. SEM images of the  $\text{NaNi}_{0.5}\text{Mn}_{0.5}\text{O}_2$  powder are shown in the inset. An inset showing an expanded view of the XRD pattern between  $68^\circ$  and  $79^\circ$  is also shown

### 4.3.3 Electrochemical performance of Na/ $\text{NaNi}_{0.5}\text{Mn}_{0.5}\text{O}_2$ half cells

Figure 4.15 shows the initial potential, V, versus specific capacity, Q, curve for the first charge and discharge of a Na/ $\text{NaNi}_{0.5}\text{Mn}_{0.5}\text{O}_2$  coin cell cycling between 3.8 and 2.0 V. The cell delivers a capacity of about 125 mAh/g during the first charge, indicating that  $\text{Na}_{0.5}\text{Ni}_{0.5}\text{Mn}_{0.5}\text{O}_2$  has formed at the end of charge at 3.8 V. A number of potential-capacity plateaus can be observed, which are related to the phase transitions: Hex. O3  $\rightarrow$  Mon. O3  $\rightarrow$  Hex. P3  $\rightarrow$  Mon. P3 [19]. The  $dQ/dV$  versus V curve is also shown as an inset, which clearly shows the plateaus observed in the charge-discharge curve as peaks in  $dQ/dV$  vs. V.

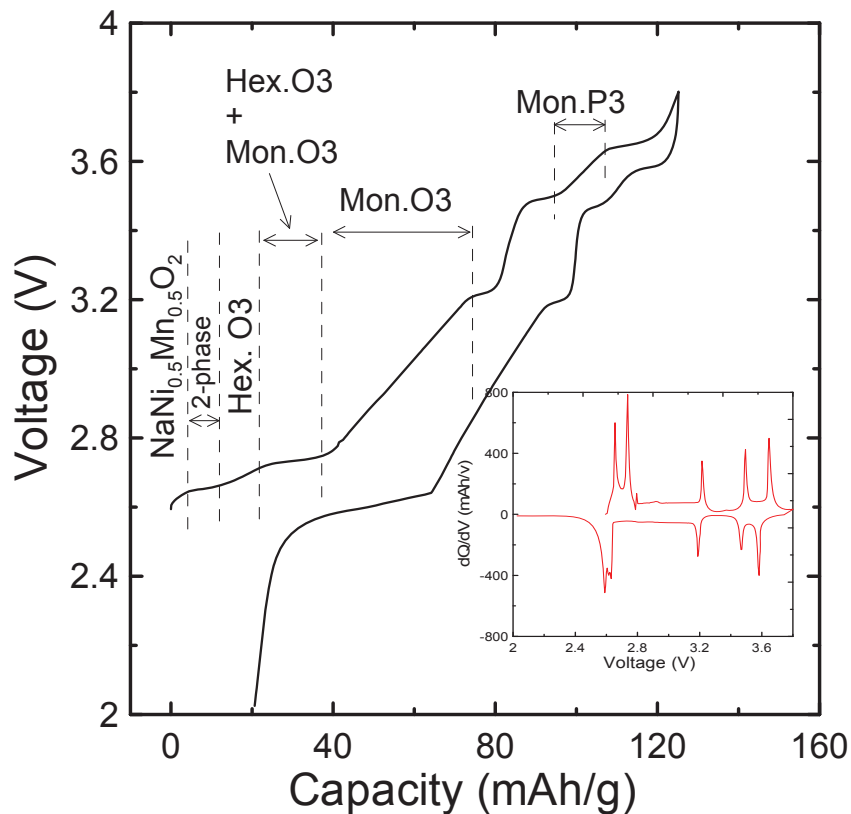


Figure 4.15 Potential versus specific capacity of a  $\text{NaNi}_{0.5}\text{Mn}_{0.5}\text{O}_2$  electrode in a Na/ $\text{NaNi}_{0.5}\text{Mn}_{0.5}\text{O}_2$  coin-type cell. The cell was charged and discharged between 3.8 V and

2.0 V using a current corresponding to 10 mA/g.

#### **4.3.4 Reactivity of deintercalated $\text{NaNi}_{0.5}\text{Mn}_{0.5}\text{O}_2$ ( $\sim\text{Na}_{0.5}\text{Ni}_{0.5}\text{Mn}_{0.5}\text{O}_2$ ) in solvents and electrolytes**

Figure 4.16 shows the self-heating rate versus temperature of 0.1 g  $\text{Na}_{0.5}\text{Ni}_{0.5}\text{Mn}_{0.5}\text{O}_2$  reacting with 0.1 g of EC: DEC, 0.1 g 1M  $\text{NaPF}_6$  in EC: DEC (1:2 v/v). The experiment started at 50°C.  $\text{Na}_{0.5}\text{Ni}_{0.5}\text{Mn}_{0.5}\text{O}_2$  shows a relatively high reactivity in both solvent and electrolyte. The onset temperature of the exothermic reaction is at about 175°C in solvent, and the exothermic reaction continues until the experiment end temperature (300°C). The  $\text{Na}_{0.5}\text{Ni}_{0.5}\text{Mn}_{0.5}\text{O}_2$ /electrolyte case shows quite different exothermic behaviour. The first exothermic peak starts at around 120°C and ends at around 160°C. Then there is another exothermic reaction beginning at 225°C (for  $\text{NaPF}_6$  in EC: DEC)/ 240 °C (for  $\text{NaPF}_6$  in PC), which lasts till the experiment end temperature. The ARC result for 0.1 g  $\text{Na}_{0.5}\text{Ni}_{0.5}\text{Mn}_{0.5}\text{O}_2$  heated in 0.1 g 1 M  $\text{NaPF}_6$ /PC electrolyte is also shown in Figure 4.16 for comparison.  $\text{Na}_{0.5}\text{Ni}_{0.5}\text{Mn}_{0.5}\text{O}_2$  shows a very similar reactivity in  $\text{NaPF}_6$ /PC as it does in  $\text{NaPF}_6$ /EC:DEC apart from the second exotherm occurring at 240°C instead of 215°C. It is believed that  $\text{Na}_{0.5}\text{Ni}_{0.5}\text{Mn}_{0.5}\text{O}_2$  has the same reaction mechanism in  $\text{NaPF}_6$ /PC as in  $\text{NaPF}_6$ /EC:DEC at elevated temperature.



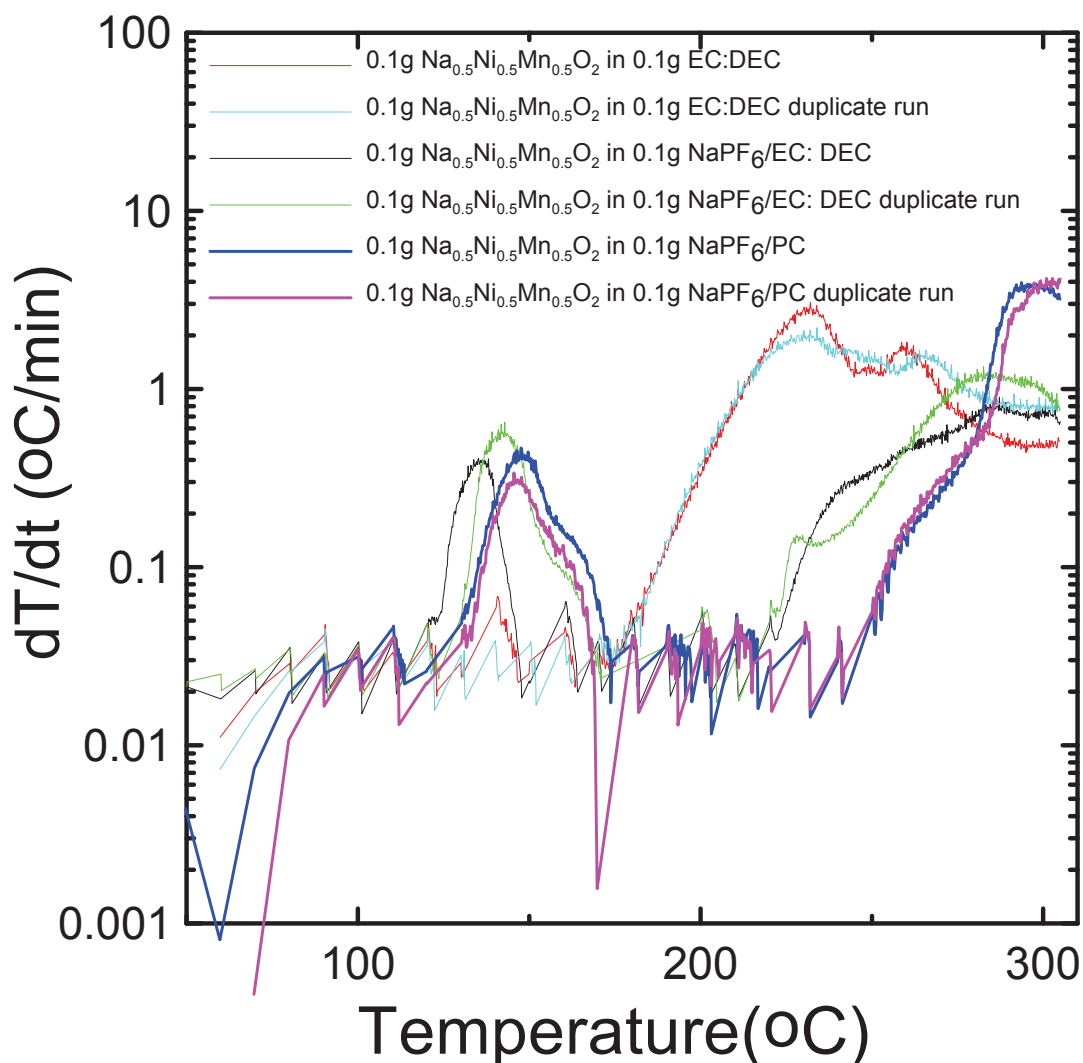


Figure 4.16 Self heating rate (SHR) vs. temperature of 100 mg Na<sub>0.5</sub>Ni<sub>0.5</sub>Mn<sub>0.5</sub>O<sub>2</sub> in the same mass of EC: DEC (1:2 v/v), 1M NaPF<sub>6</sub> in EC: DEC (1:2 v/v) and 1M NaPF<sub>6</sub> in PC. The legend indicates which curve corresponds to which sample.

There are few reports which study the details of the reaction mechanism between charged Li<sub>0.5</sub>Ni<sub>0.5</sub>MnO<sub>2</sub> and solvent or electrolyte at elevated temperature, even though its reactivity has been reported [71, 72]. Based on TGA experiments on charged LiMnO<sub>2</sub> and LiNiO<sub>2</sub> [67], it is expected that Na<sub>0.5</sub>Ni<sub>0.5</sub>Mn<sub>0.5</sub>O<sub>2</sub> will decompose at elevated temperature, liberating oxygen. In the presence of solvent or electrolyte the

decomposition will occur at a lower temperature since the liberated oxygen can combust the solvent.

In order to probe the expected the reaction mechanism, XRD tests were carried out to investigate the products of heating  $\text{Na}_{0.5}\text{Ni}_{0.5}\text{Mn}_{0.5}\text{O}_2$  in solvent and electrolyte. Figure 4.17 shows the XRD patterns of the products after heating  $\text{Na}_{0.5}\text{Ni}_{0.5}\text{Mn}_{0.5}\text{O}_2$  with electrolyte (4.17c) or solvent (4.17d) to  $300^\circ\text{C}$ , and all the products have been identified by the position of their Bragg peaks as indicated in Figure 4.17. The reaction of  $\text{Na}_{0.5}\text{Ni}_{0.5}\text{Mn}_{0.5}\text{O}_2$  heated with solvent gives products of nickel manganese oxide and Ni metal.  $\text{MnCO}_3$  is believed to form due to the reaction of manganese oxide and  $\text{CO}_2$  during the cooling process, similar to formation of  $\text{CoCO}_3$  when  $\text{Na}_x\text{CoO}_2$  was heated in solvent as discussed in section 4.2.4.

Figure 4.16c shows that  $\text{NaMnF}_3$ ,  $\text{NaNiF}_3$  or  $\text{Na}(\text{Ni},\text{Mn})\text{F}_3$  were identified as products when  $\text{Na}_{0.5}\text{Ni}_{0.5}\text{Mn}_{0.5}\text{O}_2$  was heated in electrolyte, which is similar to the case when  $\text{Na}_x\text{CoO}_2$  reacts with  $\text{NaPF}_6$ -containing electrolyte which was discussed in section 4.2.4. There is a Bragg peak at  $19^\circ$  which is not labeled in Figure 4.17c. This peak is thought to arise from  $\text{Na}_3\text{MnF}_6$ ,  $\text{Na}_3\text{NiF}_6$  or  $\text{Na}_3(\text{Ni},\text{Mn})\text{F}_6$  as will be discussed further below.

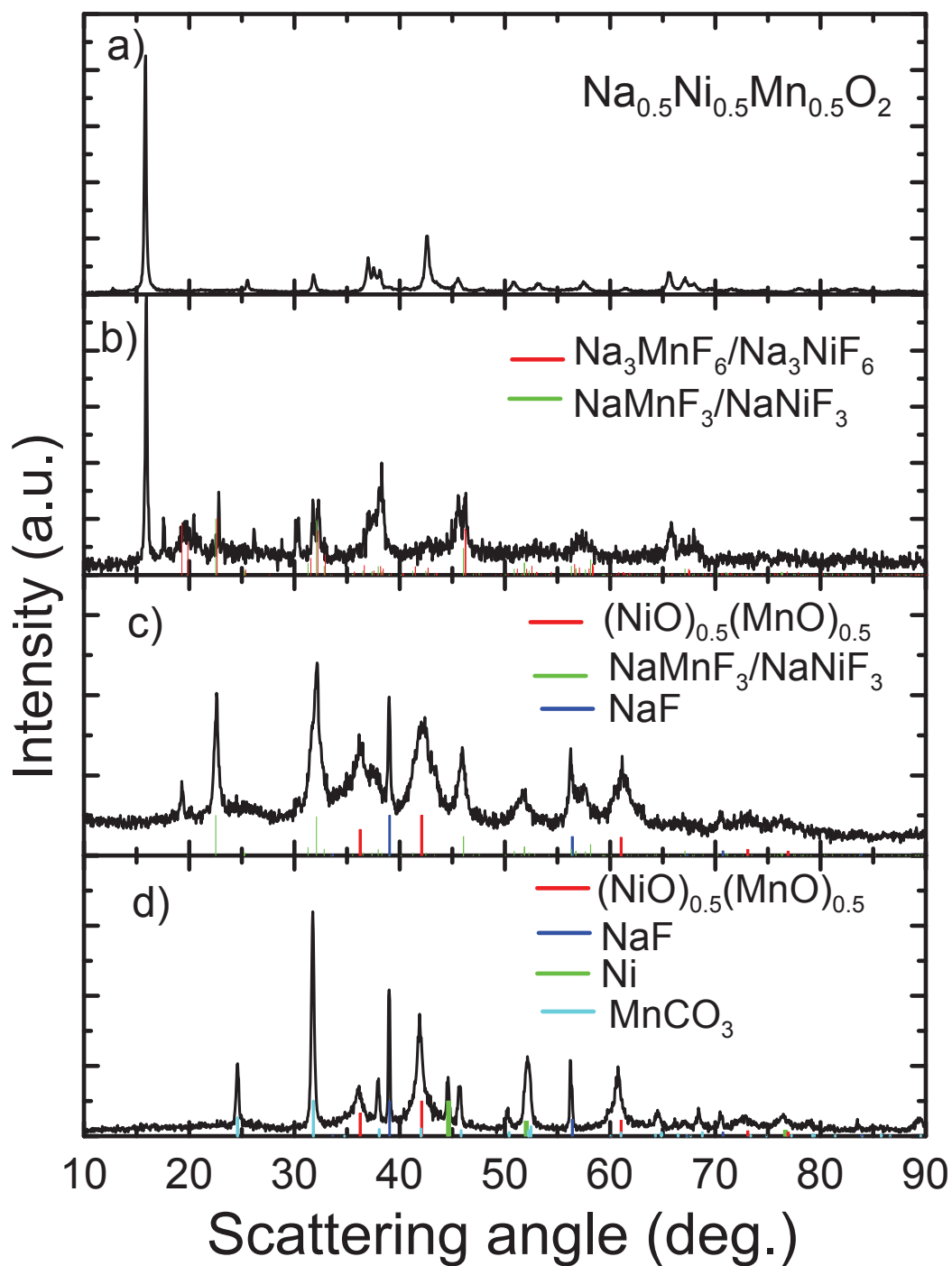


Figure 4.17 XRD patterns of a) dry, unheated  $\text{Na}_{0.5}\text{Ni}_{0.5}\text{Mn}_{0.5}\text{O}_2$ , b)  $\text{Na}_{0.5}\text{Ni}_{0.5}\text{Mn}_{0.5}\text{O}_2$  heated to 175°C in electrolyte, c)  $\text{Na}_{0.5}\text{Ni}_{0.5}\text{Mn}_{0.5}\text{O}_2$  heated to 300°C in electrolyte and d)  $\text{Na}_{0.5}\text{Ni}_{0.5}\text{Mn}_{0.5}\text{O}_2$  heated to 300°C in solvent after the ARC tests. Reference peak positions of some compounds are shown by lines with different colors (indicated in the Figure)

Figure 4.17b shows an X-ray diffraction (XRD) pattern of the product of heating  $\text{Na}_{0.5}\text{Ni}_{0.5}\text{Mn}_{0.5}\text{O}_2$  with electrolyte to  $175^\circ\text{C}$  (right after the first exothermic reaction of  $\text{Na}_{0.5}\text{Ni}_{0.5}\text{Mn}_{0.5}\text{O}_2/\text{electrolyte}$  in Figure 4.16). Figure 4.17a shows the XRD pattern of fresh  $\text{Na}_{0.5}\text{Ni}_{0.5}\text{Mn}_{0.5}\text{O}_2$  for comparison. In Figure 4.17b, besides unreacted  $\text{Na}_{0.5}\text{Ni}_{0.5}\text{Mn}_{0.5}\text{O}_2$ , the isostructural compounds  $\text{Na}_3\text{MnF}_6$ ,  $\text{Na}_3\text{NiF}_6$  or  $\text{Na}_3(\text{Ni,Mn})\text{F}_6$  and the isostructural compounds  $\text{NaMnF}_3$ ,  $\text{NaNiF}_3$  or  $\text{Na}(\text{Ni,Mn})\text{F}_3$  could be both identified. Therefore, the first exothermic peak in Figure 4.16 is related to  $\text{Na}_{0.5}\text{Ni}_{0.5}\text{Mn}_{0.5}\text{O}_2$  reacting with  $\text{NaPF}_6$  to form sodium manganese/nickel fluorides. Considering the very small amounts of  $\text{Na}_3\text{MnF}_6$ ,  $\text{Na}_3\text{NiF}_6$  or  $\text{Na}_3(\text{Ni,Mn})\text{F}_6$  that could be found after heating to  $300^\circ\text{C}$ , it is reasonable to believe that  $\text{Na}_3\text{MnF}_6$ ,  $\text{Na}_3\text{NiF}_6$  or  $\text{Na}_3(\text{Ni,Mn})\text{F}_6$  formed at lower temperature and transformed to  $\text{NaMnF}_3$ ,  $\text{NaNiF}_3$  or  $\text{Na}(\text{Ni,Mn})\text{F}_3$  at higher temperature. It is believed that the first exothermic reaction in Figure 4.16 stops when the  $\text{NaPF}_6$  in the electrolyte is used up. That is why there is still unreacted  $\text{Na}_{0.5}\text{Ni}_{0.5}\text{Mn}_{0.5}\text{O}_2$  remaining in the XRD pattern in Figure 4.17b. Table 4.4 summarizes the results in Figure 4.17.

Table 4.4 Reactants and reaction products found after the ARC experiments of Figure 4.16 as described by Figure 4.17. Products of the reaction of  $\text{Na}_x\text{Ni}_{0.5}\text{Mn}_{0.5}\text{O}_2$  with PVDF as detailed in Figure 4.18 are also listed

Reactants	Final Temp. (°C)	Products Found by XRD	Figure
$\text{NaNi}_{0.5}\text{Mn}_{0.5}\text{O}_2$	300	$\text{NaNi}_{0.5}\text{Mn}_{0.5}\text{O}_2$	4.18d
$\text{NaNi}_{0.5}\text{Mn}_{0.5}\text{O}_2$ + 10% PVDF + 10% Super S	300	$\text{NiMnO}_3$ + NaF	4.18b
$\text{Na}_{0.5}\text{Ni}_{0.5}\text{Mn}_{0.5}\text{O}_2$ + 10% PVDF + 10% Super S	300	$\text{NiMn}_2\text{O}_4$ + (Ni,Mn)O + NaF	4.18a
$\text{Na}_{0.5}\text{Ni}_{0.5}\text{Mn}_{0.5}\text{O}_2$ + 10% PVDF + 10% Super S + EC:DEC solvent	300	(Ni,Mn)O + $\text{MnCO}_3$ (on cooling) + Ni + NaF	4.18c + 4.17d
$\text{Na}_{0.5}\text{Ni}_{0.5}\text{Mn}_{0.5}\text{O}_2$ + 10% PVDF + 10% Super S + 1M $\text{NaPF}_6$ EC:DEC electrolyte	175	$\text{Na}(\text{Ni,Mn})\text{F}_3$ + $\text{Na}_3(\text{Ni,Mn})\text{F}_6$ + unreacted $\text{Na}_{0.5}\text{Ni}_{0.5}\text{Mn}_{0.5}\text{O}_2$	4.17b
$\text{Na}_{0.5}\text{Ni}_{0.5}\text{Mn}_{0.5}\text{O}_2$ + 10% PVDF + 10% Super S + 1M $\text{NaPF}_6$ EC:DEC electrolyte	300	(Ni,Mn)O + $\text{Na}(\text{Ni,Mn})\text{F}_3$ + NaF	4.17c

Figures 4.17c and 4.17d show that NaF was identified as a reaction product even when  $\text{Na}_{0.5}\text{Ni}_{0.5}\text{Mn}_{0.5}\text{O}_2$  reacted with solvent where no  $\text{NaPF}_6$  was present. The only source of fluorine in  $\text{Na}_{0.5}\text{Ni}_{0.5}\text{Mn}_{0.5}\text{O}_2$ /solvent reaction is the binder, polyvinylidene fluoride (PVDF).

A series of experiments were designed to investigate the possible reaction between  $\text{Na}_{0.5}\text{Ni}_{0.5}\text{Mn}_{0.5}\text{O}_2$  and PVDF. Figure 4.18a shows the XRD patterns of the products of heating dry  $\text{Na}_{0.5}\text{Ni}_{0.5}\text{Mn}_{0.5}\text{O}_2$  electrode powder (containing 10% by weight of PVDF) to  $300^\circ\text{C}$  in the ARC. Figure 4.18b shows the XRD pattern of the reaction products after heating dry fresh  $\text{NaNi}_{0.5}\text{Mn}_{0.5}\text{O}_2$  electrode powder (containing 10% PVDF) to  $300^\circ$  in the ARC. Figures 4.18c and 4.18d show the XRD patterns of the products of  $\text{Na}_{0.5}\text{Ni}_{0.5}\text{Mn}_{0.5}\text{O}_2$  (with 10% PVDF) reacting with solvent and fresh  $\text{NaNi}_{0.5}\text{Mn}_{0.5}\text{O}_2$  (No PVDF) alone, respectively, after heating to  $300^\circ\text{C}$  in the ARC. Figure 4.18d shows that fresh  $\text{NaNi}_{0.5}\text{Mn}_{0.5}\text{O}_2$  did not show any structural change when heated to  $300^\circ\text{C}$ , however, when it was mixed with PVDF and then was heated. Figure 4.18b shows that a significant change structural change occurred due to the formation of NaF and  $\text{NiMnO}_3$ . Therefore, even uncharged fresh  $\text{NaNi}_{0.5}\text{Mn}_{0.5}\text{O}_2$  can react with PVDF at elevated temperature. This could be a concern if  $\text{NaNi}_{0.5}\text{Mn}_{0.5}\text{O}_2$  is used as positive electrode material in a sodium ion battery with PVDF as the binder. Figure 4.18a shows that dry charged  $\text{Na}_{0.5}\text{Ni}_{0.5}\text{Mn}_{0.5}\text{O}_2$  and PVDF show similar reaction products to fresh  $\text{NaNi}_{0.5}\text{Mn}_{0.5}\text{O}_2$  and PVDF except for the formation of more complicated Ni and Mn oxides. NaF is also a product. The results in Figure 4.18 explain how NaF was formed when  $\text{Na}_{0.5}\text{Ni}_{0.5}\text{Mn}_{0.5}\text{O}_2$ , with PVDF was heated in solvent. It is also reasonable to believe that NaF appears as one product of heating  $\text{Na}_{0.5}\text{Ni}_{0.5}\text{Mn}_{0.5}\text{O}_2$  in electrolyte due to the reaction of  $\text{Na}_{0.5}\text{Ni}_{0.5}\text{Mn}_{0.5}\text{O}_2$  with PVDF, not from any reaction with  $\text{NaPF}_6$ . The reactants and

reaction products found at 175°C and at 300°C in the experiments of this study are also summarized in Table 4.4.

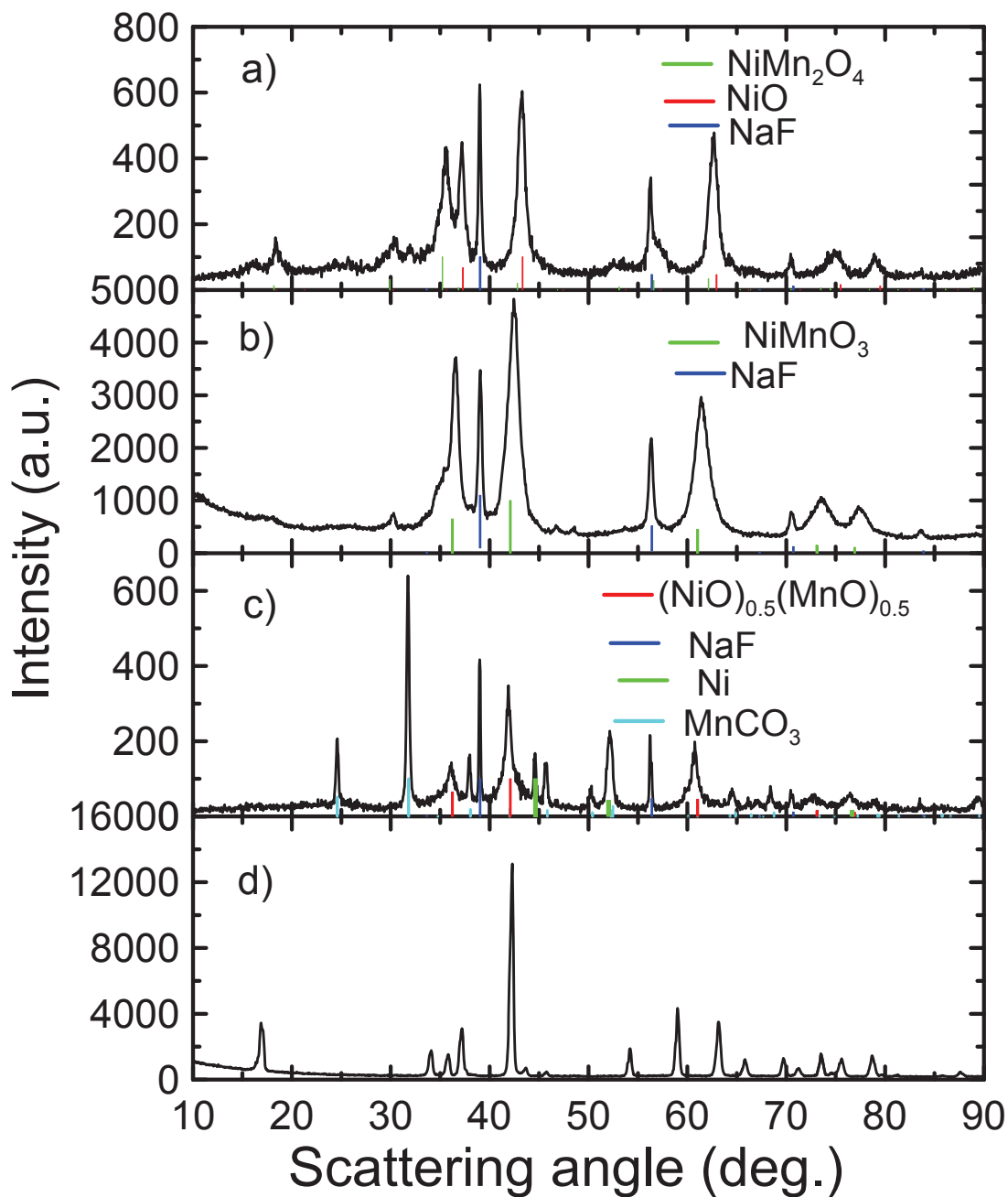


Figure 4.18 XRD patterns of a)  $\text{Na}_{0.5}\text{Ni}_{0.5}\text{Mn}_{0.5}\text{O}_2$  electrode powder (containing PVDF), b) dry  $\text{NaNi}_{0.5}\text{Mn}_{0.5}\text{O}_2$  electrode powder (containing PVDF), c)  $\text{Na}_{0.5}\text{Ni}_{0.5}\text{Mn}_{0.5}\text{O}_2$  with solvent and d) fresh  $\text{NaNi}_{0.5}\text{Mn}_{0.5}\text{O}_2$  after heating to 300°C in the ARC. Reference peak positions of some compounds are shown by lines with different colors.

#### 4.3.5 Summary

In this section, O3-Type  $\text{NaNi}_{0.5}\text{Mn}_{0.5}\text{O}_2$  was successfully synthesized by solid state reaction and showed good electrochemical performance. The reactivity of deintercalated  $\text{NaNi}_{0.5}\text{Mn}_{0.5}\text{O}_2$  ( $\sim\text{Na}_{0.5}\text{Ni}_{0.5}\text{Mn}_{0.5}\text{O}_2$ ) was studied by ARC and it was found that  $\text{Na}_{0.5}\text{Ni}_{0.5}\text{Mn}_{0.5}\text{O}_2$  shows relatively high reactivity in solvent and in  $\text{NaPF}_6$ -based electrolyte. An XRD investigation of the products of the reactions between  $\text{Na}_x\text{Ni}_{0.5}\text{Mn}_{0.5}\text{O}_2$  ( $x = 0.5$  and  $x = 1$ ) allowed the exotherms observed in the ARC experiments to be understood. A summary of the reaction products observed for the various experiments is given in Table 4.4.

Briefly: 1)  $\text{Na}_x\text{Ni}_{0.5}\text{Mn}_{0.5}\text{O}_2$  reacts with PVDF to form  $\text{NaF}$  and transition metal oxides at temperatures above  $175^\circ\text{C}$ ; 2)  $\text{Na}_{0.5}\text{Ni}_{0.5}\text{Mn}_{0.5}\text{O}_2$  reacts with EC:DEC solvent to form  $(\text{Ni},\text{Mn})\text{O}$ ,  $\text{Ni}$  and  $\text{MnCO}_3$  (on cooling) and 3)  $\text{Na}_{0.5}\text{Ni}_{0.5}\text{Mn}_{0.5}\text{O}_2$  reacts with 1M  $\text{NaPF}_6$  EC:DEC to produce the additional products  $\text{Na}_3(\text{Ni},\text{Mn})\text{F}_6$  and  $\text{Na}(\text{Ni},\text{Mn})\text{F}_3$ . The  $\text{Na}_3(\text{Ni},\text{Mn})\text{F}_6$  converts to  $\text{Na}(\text{Ni},\text{Mn})\text{F}_3$  at higher temperature. The reaction between  $\text{Na}_{0.5}\text{Ni}_{0.5}\text{Mn}_{0.5}\text{O}_2$  and  $\text{NaPF}_6$  occurs at the lowest temperature, creating a new exotherm in the ARC traces, not observed when  $\text{NaPF}_6$  is not included in the reaction. These results are instructive for those concerned with the design of electrolytes, binder and electrodes to be used in sodium-ion batteries.



# CHAPTER 5 THE REACTIVITY OF CHARGED ELECTRODE MATERIALS WITH SODIUM BIS(TRIFLUOROMETHANESULFONYL)IMIDE (NaTFSI) BASED-ELECTROLYTE AT ELEVATED TEMPERATURES

## 5.1 Thermal stability of NaTFSI

$\text{NaN}(\text{CF}_3\text{SO}_2)_2$ , called NaTFSI, is a useful salt for the electrolyte of Na-ion batteries. Figure 5.1 shows the fractional remaining weight versus temperature as measured by TGA for NaTFSI and  $\text{NaPF}_6$ .  $\text{NaPF}_6$  does not decompose significantly below  $300^\circ\text{C}$  while NaTFSI does not decompose until about  $400^\circ\text{C}$ . Figure 5.1 also shows that  $\text{NaClO}_4$  does not decompose till more than  $500^\circ\text{C}$ . This results indicates that  $\text{NaClO}_4$  has the best thermal stability of the three pure salts and that NaTFSI is more stable than  $\text{NaPF}_6$ .

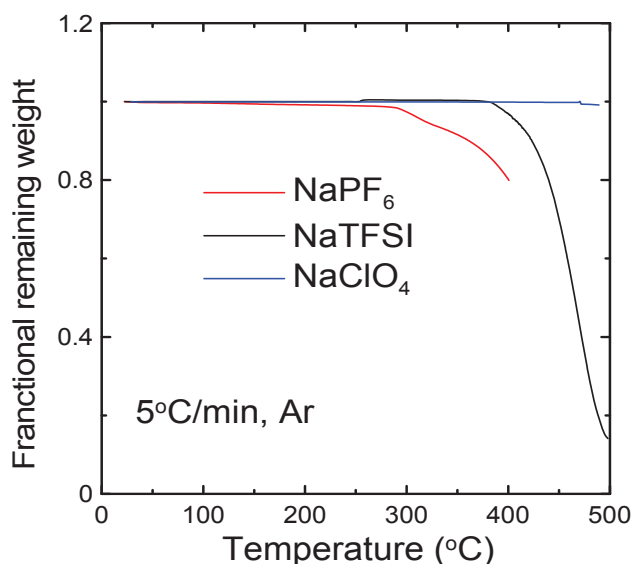


Figure 5.1 Fractional remaining weight versus temperature in TGA experiments on  $\text{NaPF}_6$  and NaTFSI. The samples were heated at  $5^\circ\text{C}/\text{min}$  in argon gas.

## 5.2 Electrochemical performance of NaCrO<sub>2</sub> and hard carbon in NaTFSI based-electrolyte

Figure 5.2 shows the potential versus specific capacity curve for the first charge and discharge of a Na/NaCrO<sub>2</sub> coin cell cycling between 2.0 and 3.6 V. The cell delivers a capacity of about 120 mAh/g during the first charge, indicating that Na<sub>0.5</sub>CrO<sub>2</sub> has formed at the end of charge. A couple of potential-capacity plateaus can be observed, which are related to the phase transitions: Hex. O3 → Mon. O3 → Mon. P3 (this has been discussed in section 4.1.3 and indicated in Figure 4.2). The initial capacity is slightly higher than in Figure 4.2 where NaClO<sub>4</sub>/PC electrolyte was used. The cycling performance is also shown as an inset. The cell shows good capacity retention over the 30 tested cycles. The cycling performance of a cell using NaClO<sub>4</sub>/PC electrolyte is shown for comparison. There is an odd “dip” in the capacity cycle number curve near cycle 5. The origin of this dip is unknown, but it might be caused by initially poor wetting of the polypropylene BMF separator by the PC-based electrolyte. The same feature is observed in the hard carbon cells as will be discussed below. Based on the results in Figure 5.2, NaTFSI shows good compatibility with the NaCrO<sub>2</sub> positive electrode in sodium-ion batteries.

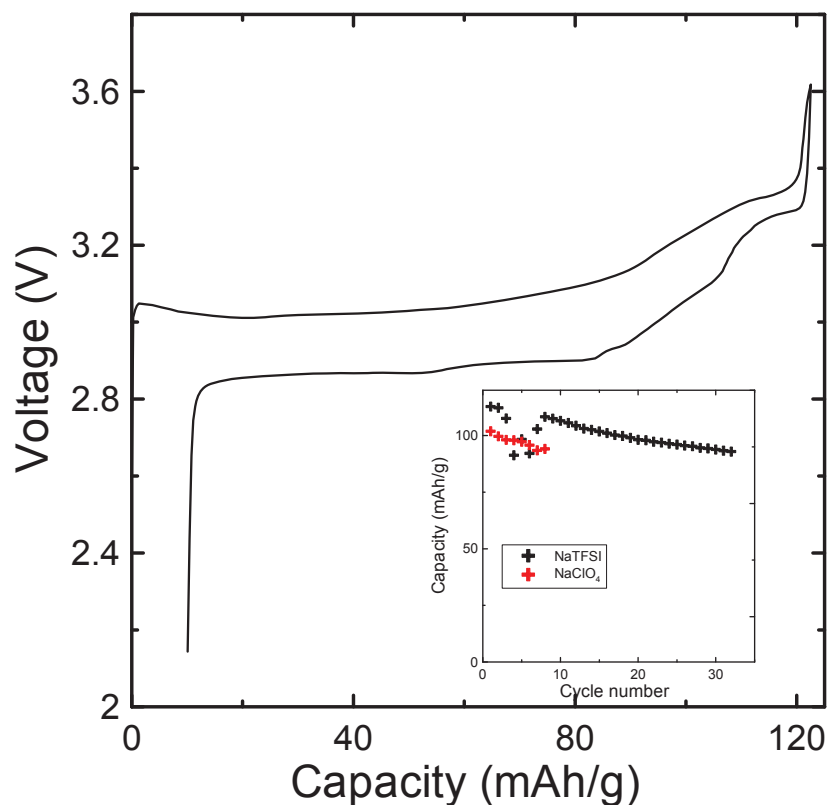


Figure 5.2 Potential versus specific capacity of a  $\text{NaCrO}_2$  electrode in a  $\text{Na}/\text{NaCrO}_2$  coin-type cell using  $\text{NaTFSI}/\text{PC}$  electrolyte. The cell was charged and discharged between 3.6 and 2.0 V using a current corresponding to 25 mA/g. Specific capacity versus cycle number is shown in the inset.

Figure 5.3 shows the potential versus specific capacity curve for the first 10 cycles of a  $\text{Na}/\text{hard carbon}$  coin cell, cycling between 2.0 and 0.005 V, with  $\text{NaTFSI}/\text{PC}$  electrolyte. The cell shows a capacity of around 300 mAh/g during the first discharge. The reversible capacity is around 200 mAh/g. The cycling performance is also shown as an inset. Except for the “dip” discussed above, the  $\text{Na}/\text{hard carbon}$  half cells show good cycling performance using  $\text{NaTFSI}/\text{PC}$  electrolyte. The reversible capacity of hard carbon in  $\text{NaTFSI}/\text{PC}$  electrolyte ( $\sim 200$  mAh/g) is lower than it was in  $\text{NaClO}_4/\text{PC}$  electrolyte ( $\sim 240$  mAh/g) [20]. This may be an effect of different impedance between the

two cells, causing the former to reach the lower cutoff potential too early. Based on Figure 5.3, it appears that NaTFSI is compatible with the negative electrode material.

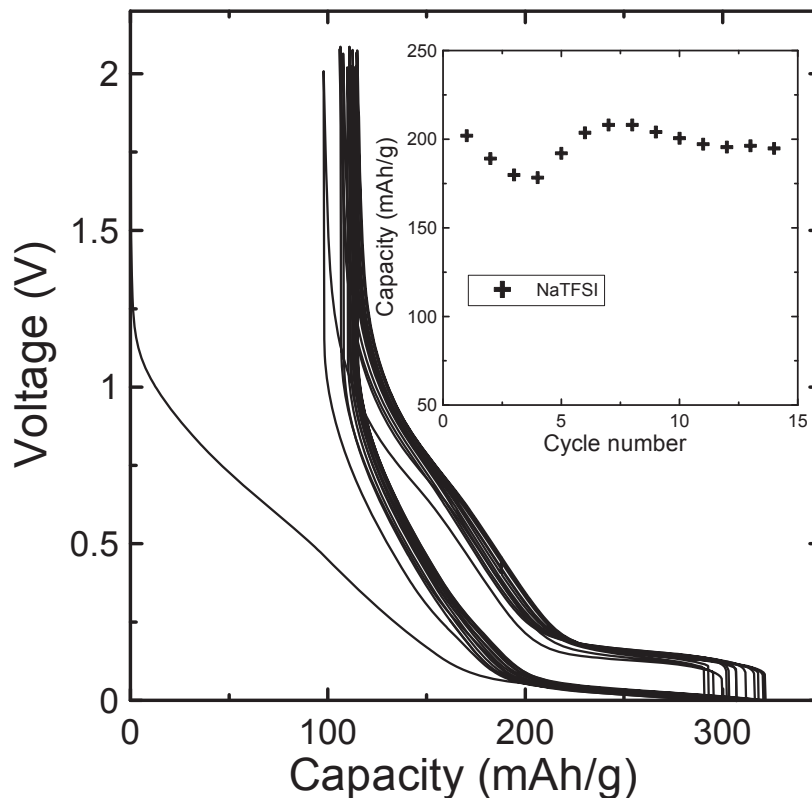


Figure 5.3 Potential versus specific capacity of a hard carbon electrode in a hard carbon/Na coin-type cell. The cell was charged and discharged between 2 and 0.005 V using a current corresponding to 25 mA/g. Specific capacity versus cycle number is shown in the inset.

### 5.3 The reactivity of charged electrode materials with NaTFSI-based electrolyte

Since NaTFSI in PC shows a good compatibility with both positive and negative electrode materials, it is important to investigate the reactivity of charged electrode materials in NaTFSI/PC electrolyte. Figure 5.4 shows the self-heating rate vs. temperature,  $T$ , of 100 mg of  $\text{Na}_{0.5}\text{CrO}_2$  in the same mass of solvent (EC:DEC or PC) and

electrolyte (NaPF<sub>6</sub>/EC:DEC or NaTFSI/PC). Chapter 4 showed that Na<sub>0.5</sub>CrO<sub>2</sub> has a surprisingly low reactivity in EC:DEC because Na<sub>0.5</sub>CrO<sub>2</sub> decomposes to NaCrO<sub>2</sub> and layered-structure CrO<sub>2-δ</sub> with a very small amount of O<sub>2</sub> release. Na<sub>0.5</sub>CrO<sub>2</sub> also had very low reactivity in electrolyte as shown in section 4.1.4. Here, Na<sub>0.5</sub>CrO<sub>2</sub> also shows a similar negligible reactivity in PC and there is almost no measurable heat released during the test temperature range (50°C - 350°C). The mechanism for the low reactivity should be the same as it is in EC:DEC. Na<sub>0.5</sub>CrO<sub>2</sub> has a lower reactivity in NaTFSI/PC electrolyte than it does in NaPF<sub>6</sub>/EC:DEC, which may result from the higher thermal stability of the salt itself (Figure 5.1).

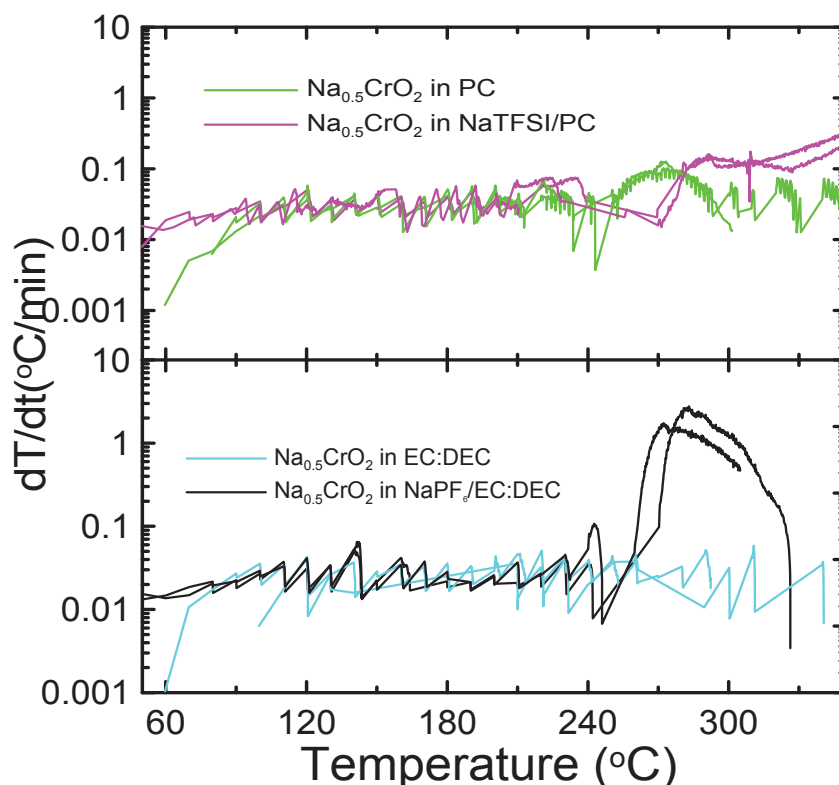


Figure 5.4 Self heating rate (SHR) vs. temperature for 100 mg Na<sub>0.5</sub>CrO<sub>2</sub> in the same mass of EC:DEC, PC, NaPF<sub>6</sub>/EC:EDC and NaTFSI/PC. The legend indicates which curve corresponds to which sample.

Figure 5.5 shows the self-heating rate vs. temperature,  $T$ , of 70 mg of Na:HC in the same mass of solvent (EC:DEC or PC) or electrolyte (NaPF<sub>6</sub>/EC:DEC or NaTFSI/PC). The results of Na:HC reacting in NaClO<sub>4</sub>/PC and NaPF<sub>6</sub>/PC are also shown for comparison. Na/HC shows a high reactivity in EC:DEC and an even higher reactivity in NaPF<sub>6</sub>/EC:DEC due to the coordination between NaPF<sub>6</sub> and EC as described in Section 3.1. Na:HC shows a slightly lower reactivity in PC than in EC:DEC. The starting temperature of the exothermic reaction is 180°C in PC compared to 150°C in EC:DEC and the maximum self heating rate (SHR) is smaller in the PC case. However, Na:HC shows different reactivity in PC based electrolytes. A strong exothermic peak was observed starting from 90°C when Na:HC was heated in NaClO<sub>4</sub>/PC electrolyte. When NaPF<sub>6</sub> or NaTFSI are used instead of NaClO<sub>4</sub>, then the reaction between electrolyte and Na:HC does not onset until about 140 or 150°C, compared to 120°C in NaPF<sub>6</sub>/EC:DEC.

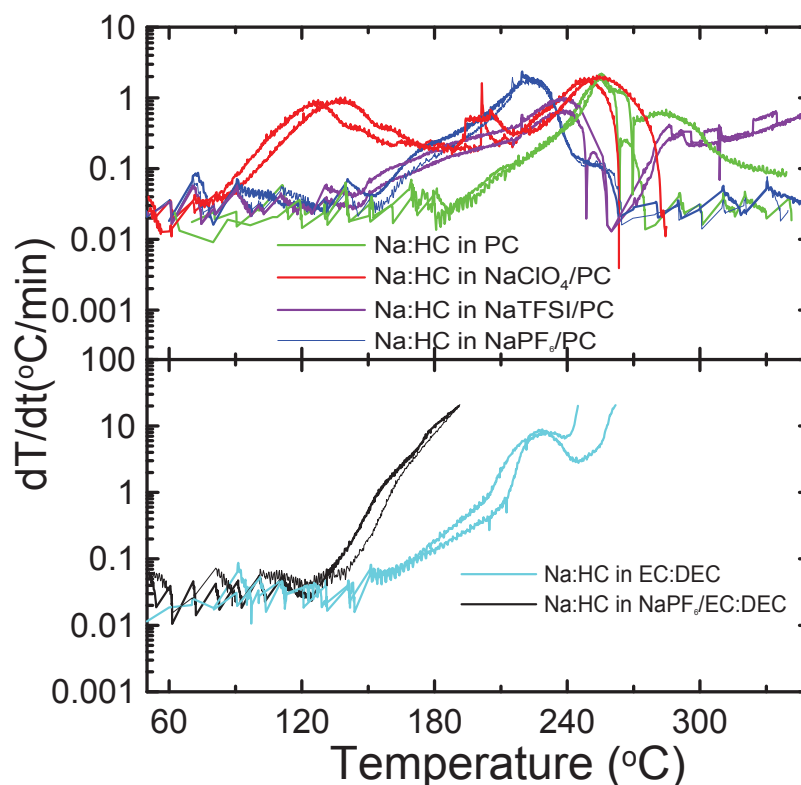


Figure 5.5 Self heating rate (SHR) vs. temperature of 70 mg sodium inserted hard carbon (Na:HC) in the same mass of EC:DEC, PC, NaPF<sub>6</sub>/EC:EDC, NaPF<sub>6</sub>/PC, NaClO<sub>4</sub>/PC or NaTFSI/PC. The legend indicates which curve corresponds to which sample.

Based on the ARC results for Na<sub>0.5</sub>CrO<sub>2</sub> and hard carbon in different electrolytes, it can be concluded that NaTFSI in PC will not increase the reactivity of charged electrode materials with electrolytes at elevated temperature compared to other electrolytes that have been studied. In fact, the use of NaTFSI may even lower the reactivity of the charged negative electrode material to some extent.

#### 5.4 Al-corrosion of NaTFSI

Pure LiTFSI is not currently used in Li-ion batteries because it causes corrosion of the Al positive electrode current collector. By analogy, it is interesting to see the

impact of NaTFSI on the Al current collector. Figure 5.6 shows the cyclic voltammogram of an Al/Na cell tested at room temperature. During the first anodic sweep, the current increased abruptly around 4.15 V vs. Na/Na<sup>+</sup> and persisted during the cathodic sweep until 3.5 V. During the next cycles, Figure 5.6 shows that the current increase occurred near 3.9 V during the anodic sweep and again persisted during the cathodic sweep until 3.5 V. This hysteresis and the persistent current over many cycles indicate Al-electrode corrosion [73]. Such Al-electrode corrosion may block the application of NaTFSI for high voltage positive electrode materials of Na-ion batteries.

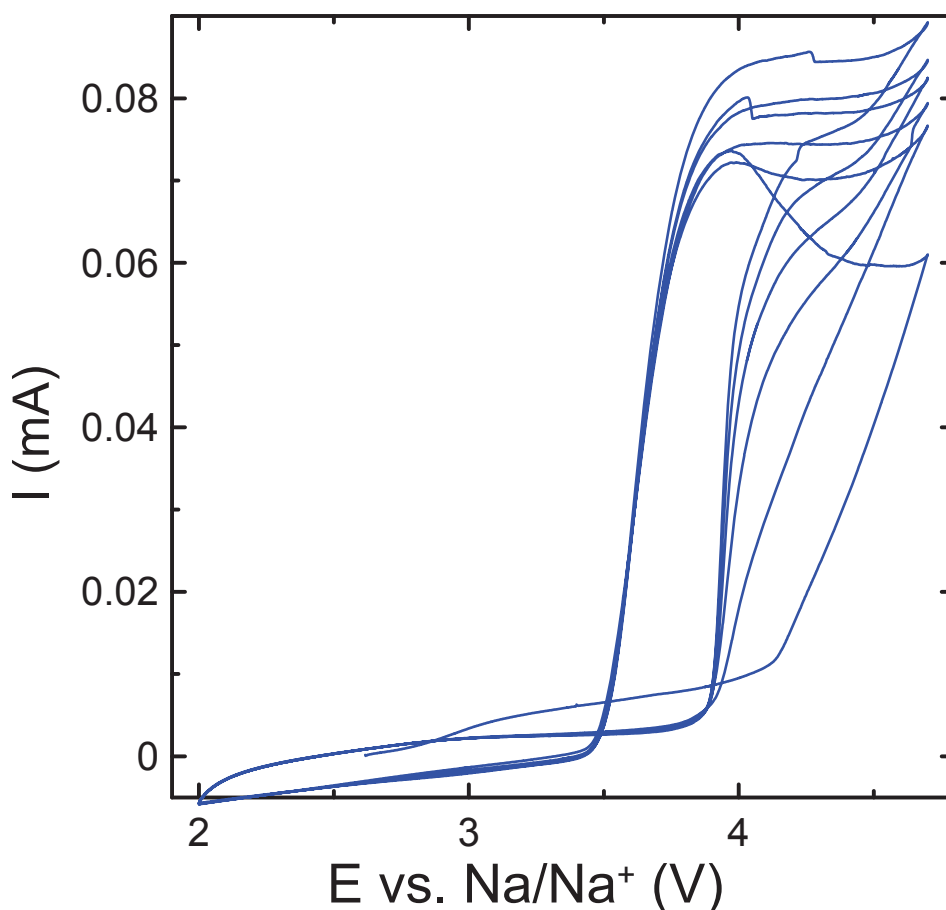


Figure 5.6 Cyclic voltammogram of an Al/Na cell using NaTFSI/PC electrolyte at a sweep rate of 10 mV/s.



## 5.5 Summary

In this chapter, sodium bis(trifluoromethanesulfonyl)imide (NaTFSI) was studied as a salt for the electrolyte of sodium-ion batteries, mainly with respect to safety. It shows higher thermal stability than NaPF<sub>6</sub> when heated in inert gas. Na/NaCrO<sub>2</sub> and Na/hard carbon half cells achieve good electrochemical performance using NaTFSI/PC electrolyte, which indicates NaTFSI has good compatibility with both positive and negative electrode materials. Deintercalated NaCrO<sub>2</sub> (~ Na<sub>0.5</sub>CrO<sub>2</sub>) and sodium-inserted hard carbon show similar or even slightly lower reactivity in NaTFSI/PC electrolyte at elevated temperature when compared to other known electrolytes (NaPF<sub>6</sub>/EC:DEC, NaClO<sub>4</sub>/PC, etc). However, the pure NaTFSI-based electrolyte causes Al corrosion at high potential. These results demonstrate that NaTFSI is a good candidate for the electrolyte salt of sodium-ion batteries, at least in situations where the positive electrode potential is not so high as to cause Al corrosion,

## **CHAPTER 6 TRIPHENYL PHOSPHATE AS A FLAME RETARDANT ADDITIVE FOR LITHIUM-ION BATTERIES**

### **6.1 The impact of TPP on electrochemical performance of negative electrode materials**

#### **6.1.1 Electrochemical performance of petroleum coke/Li cells with different electrolytes**

Figure 6.1 shows the potential versus specific capacity curve for the initial cycles of coke/Li half cells using control electrolyte and electrolyte with 40% TPP. Cells with 40% TPP show smaller capacity than the control cells at 30°C due to increased impedance as can be observed from the voltage step at the discharge-charge switch point. At 60°C, adding TPP does not impact the capacity due to higher electrolyte conductivity. Figure 6.2 shows the irreversible capacity versus TPP content during the first cycle of coke/Li cells. The irreversible capacity corresponds to irreversible lithium consumption in SEI growth. Figure 6.2 shows that there is no large impact on the irreversible capacity due to the addition of TPP. All cells at a given temperature have almost the same irreversible capacity showing that adding TPP, even at concentrations as high as 40%, does not increase the lithium consumption during SEI growth. Table 6.1 lists the specific capacity for the first discharge, first charge and the irreversible capacity of cells with 0, 5, 10, 20 and 40% TPP tested at 30°C. Table 6.2 lists similar information for cells tested at 60°C. Tables 6.1 and 6.2 show that TPP has little impact on the irreversible capacity.

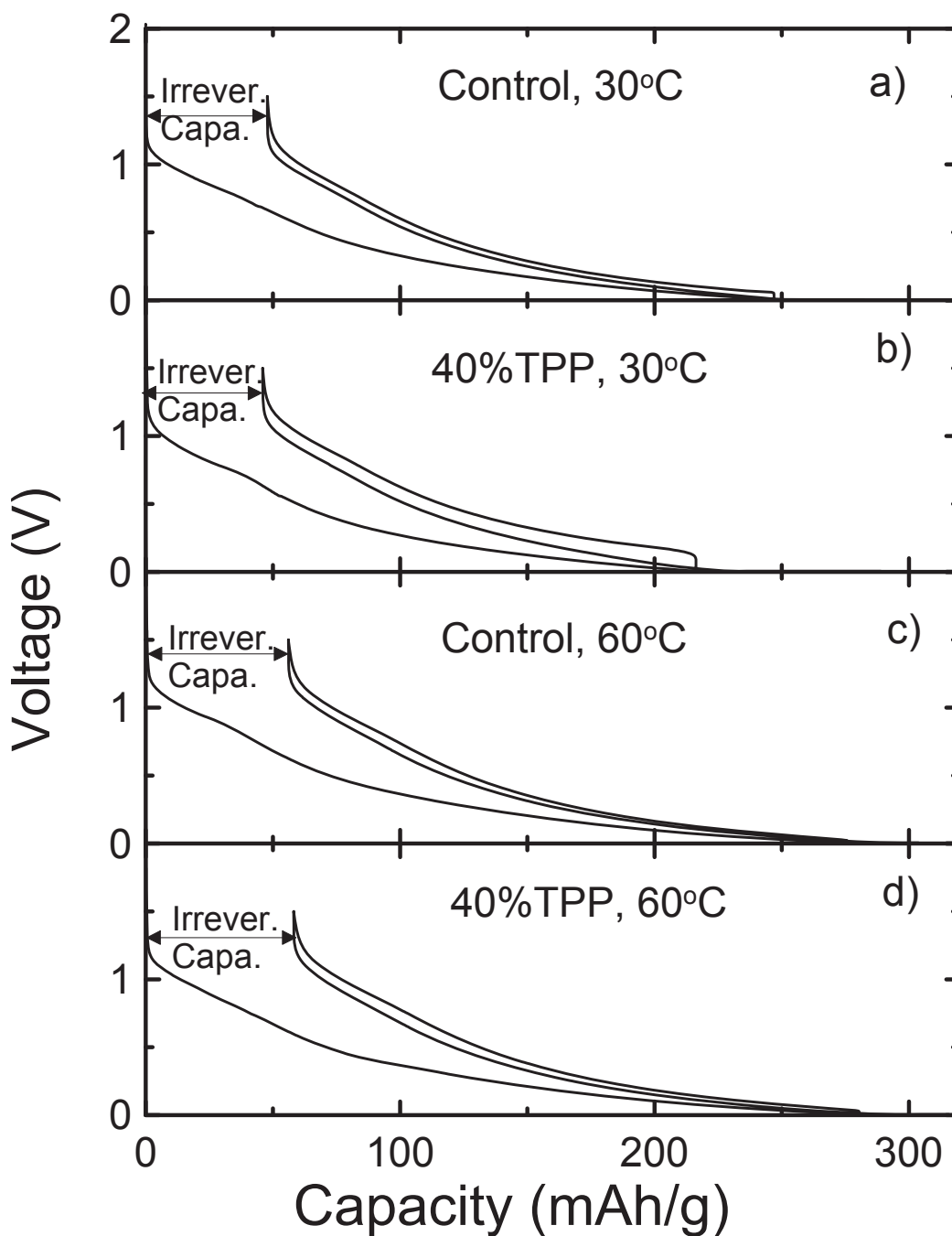


Figure 6.1 Potential versus specific capacity for the first discharge-charge cycle of coke/Li half cells using control electrolyte and electrolyte with 40% TPP. Temperatures are indicated in the various panels

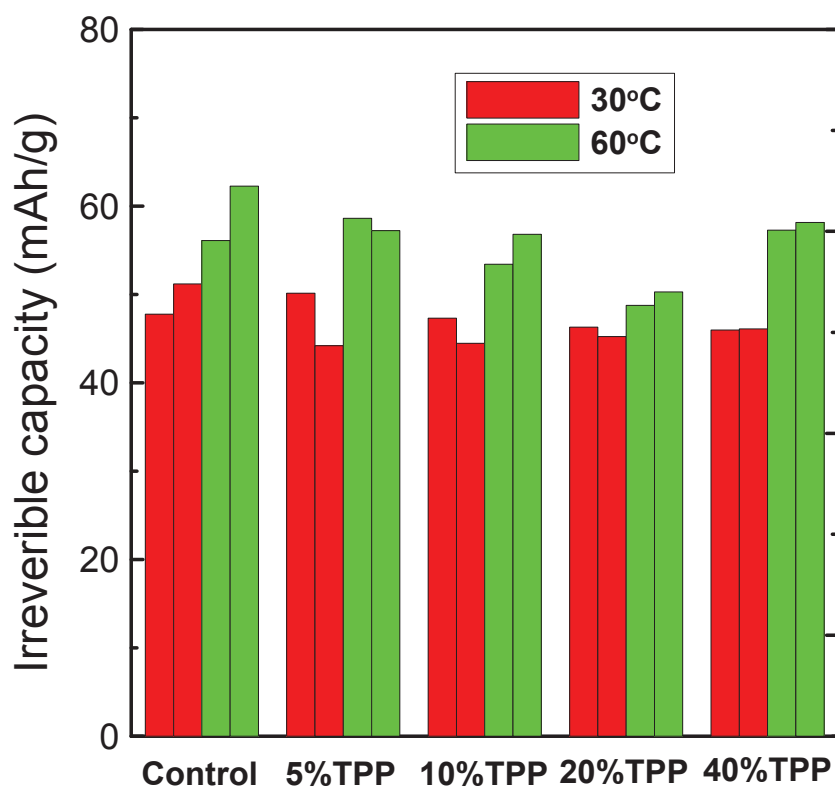


Figure 6.2 The irreversible capacity measured during the first cycle of coke/Li cells with different concentrations of TPP at 30°C and 60°C (results for duplicate cells are shown).

Table 6.1 First discharge specific capacity, first charge specific capacity and irreversible capacity for coke/Li cells tested at 30°C with different amounts of TPP in the electrolyte.

Concentration. of TPP (%)	1 <sup>st</sup> discharge capacity (mAh/g)	1 <sup>st</sup> charge capacity (mAh/g)	Irreversible capacity (mAh/g)
0 (control)	247	199	48
0 (control)	246	195	51
5	254	210	44
5	257	206	51
10	243	199	44
10	248	201	47
20	233	188	45
20	239	193	46
40	223	177	46
40	216	170	46

Table 6.2 First discharge specific capacity, first charge specific capacity and irreversible capacity for coke/Li cells tested at 60°C with different amounts of TPP in the electrolyte.

Concentration. of TPP (%)	1 <sup>st</sup> discharge capacity (mAh/g)	1 <sup>st</sup> charge capacity (mAh/g)	Irreversible capacity (mAh/g)
0 (control)	273	211	62
0 (control)	276	220	56
5	290	233	57
5	283	224	59
10	275	218	57
10	269	216	53
20	265	215	50
20	253	204	49
40	280	222	58
40	277	220	57

Figure 6.3 shows the open-circuit voltage (OCV) versus time curves from the storage experiments at 30°C and 60°C on coke/Li half cells stored at 0.005 V (left panels) and at 0.4 V (right panels). The cells contained different concentrations of TPP, as indicated in the different panels of Figure 6.3. Figure 6.3 shows that all cells with TPP show similar OCV increase at 30°C compared to the controls, no matter if the cells were stored at 0.005 V or at 0.4 V. At 60°C, all cells with TPP show smaller OCV increase with time, especially cells having 40% TPP.

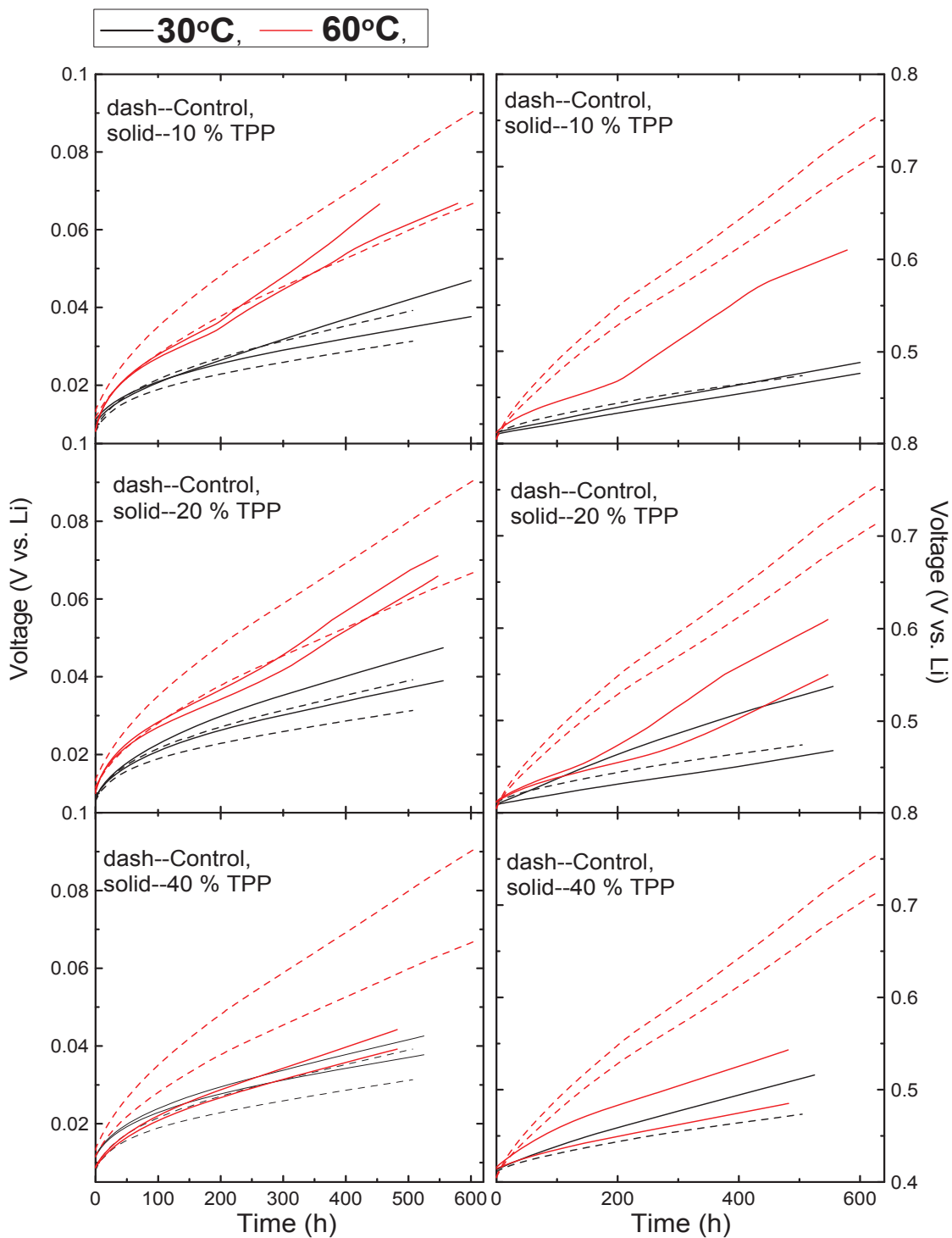


Figure 6.3 The open-circuit voltage (OCV) versus time of coke/Li cells at 30°C and 60°C stored at 0.005 V (left panel) and 0.4 V (right panel) with different concentrations of TPP as indicated in the Figure. Results for duplicate cells are shown.

The OCV increase can be converted to an amount of lithium extracted through reaction with electrolyte during the 500 hour storage period [74]. This is done by noting that:

$$dQ = \int dQ/dV dV. \quad \text{Equation 6.1}$$

The differential capacity,  $dQ/dV$  vs.  $V$  for a coke/Li cell was measured and shown in Figure 3 in ref. [75]. Then it was used to convert the potential changes during storage to capacity changes in stored charge using Eqn. 6.1. Figure 6.4 shows the results for the cells stored at 30°C. Figure 6.4 shows that the amount of Li converted to SEI during storage decreased with increasing potential but was not strongly affected by TPP content. Figure 6.5 shows the results for the cells stored at 60°C. Figure 6.5 shows that the amount of Li converted to SEI during storage decreased with increasing potential and also decreased strongly with TPP content. Therefore, it appears that in the presence of TPP at 60°C, a more stable SEI film is formed that limits reactions with intercalated lithium. If this more stable film has lower impedance than the standard SEI (formed in standard electrolyte), it will be a better SEI. However, as shown below, it has higher impedance.

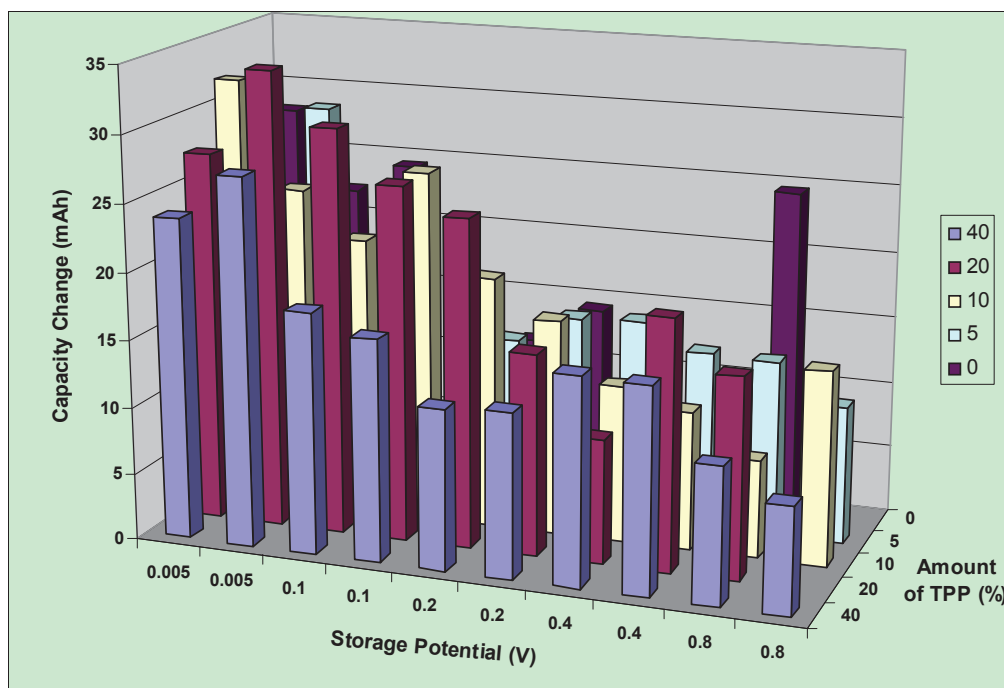


Figure 6.4 Amount of Li in mAh/g removed from  $\text{Li}_x\text{C}_6$  during storage at 30°C plotted as a function of the storage potential and the amount of TPP in the electrolyte.

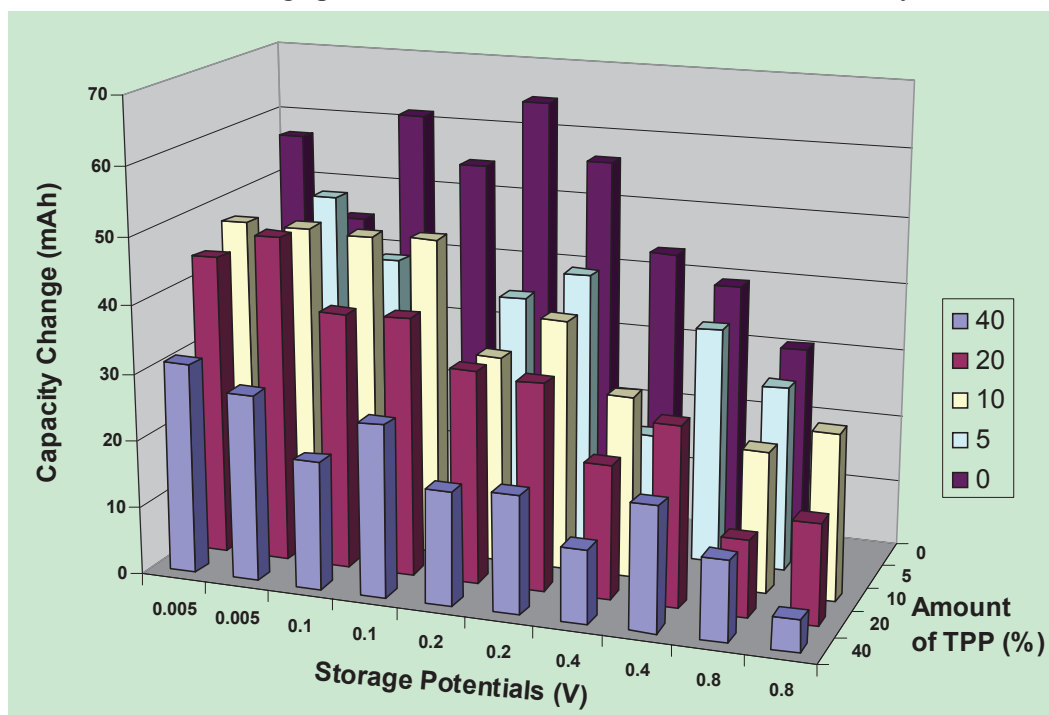


Figure 6.5 Amount of Li in mAh/g removed from  $\text{Li}_x\text{C}_6$  during storage at 60°C plotted as a function of the storage potential and the amount of TPP in the electrolyte.



### 6.1.2 Electrochemical performance of graphite/graphite symmetric cells with different electrolytes

Graphite/graphite symmetric cells were described in section 2.9 in this thesis. Figure 6.6 shows the voltage versus specific capacity for the first 20 cycles of graphite/graphite symmetric cells with different concentrations of TPP cycled using currents corresponding to C/10 at a temperature of  $30.0 \pm 0.1^\circ\text{C}$ . Graphite/graphite symmetric cells show similar performance to the controls until greater than 20% TPP is added to the electrolyte. Cells with 30 or 40% TPP show evidence for increased capacity loss during the first 20 cycles and also for increased impedance as can be discerned by the “gap” or polarization between the charge and discharge curves.

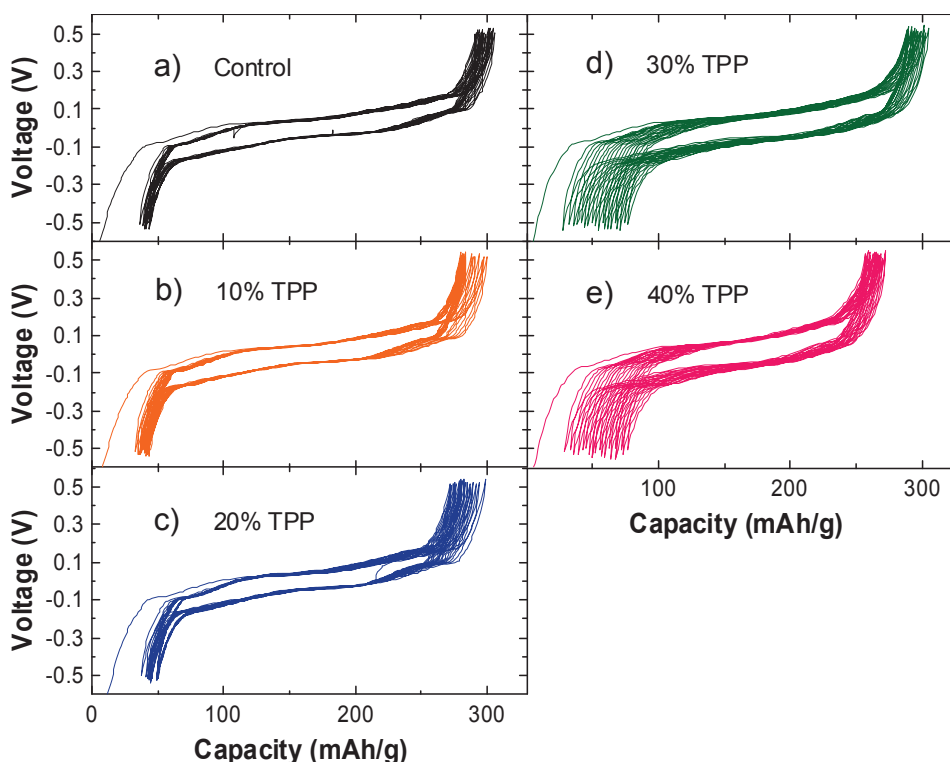


Figure 6.6 Voltage versus specific capacity for a graphite/graphite symmetric cells with different concentrations of TPP cycled at C/10 and at a temperature of  $30.0 \pm 0.1^\circ\text{C}$ . Only the first 20 cycles are shown.

Figure 6.7 shows the specific capacity versus cycle number for the graphite/graphite symmetric cells with different concentrations of TPP cycling at  $30^{\circ}\text{C} \pm 0.1^{\circ}\text{C}$  (duplicate cells are shown). The reader is directed to reference [60] to review the expected behaviour for graphite/graphite symmetric cells. One expects capacity loss with cycling even in the control cells due to continual SEI growth and the lack of excess Li atoms in the cell. Figure 6.7 shows that the TPP-containing cells show progressively smaller capacity with TPP content compared to the control cells. Based on the results for petroleum coke, adding TPP does not cause excessive consumption of lithium at the graphite electrode. Therefore the capacity reduction in Figure 6.7 with TPP content is an impedance effect as discussed further below. Figure 6.7 also shows that in all cases, by 70 cycles, the rate of capacity loss of the TPP-containing cells approximately matches that of the control cells.

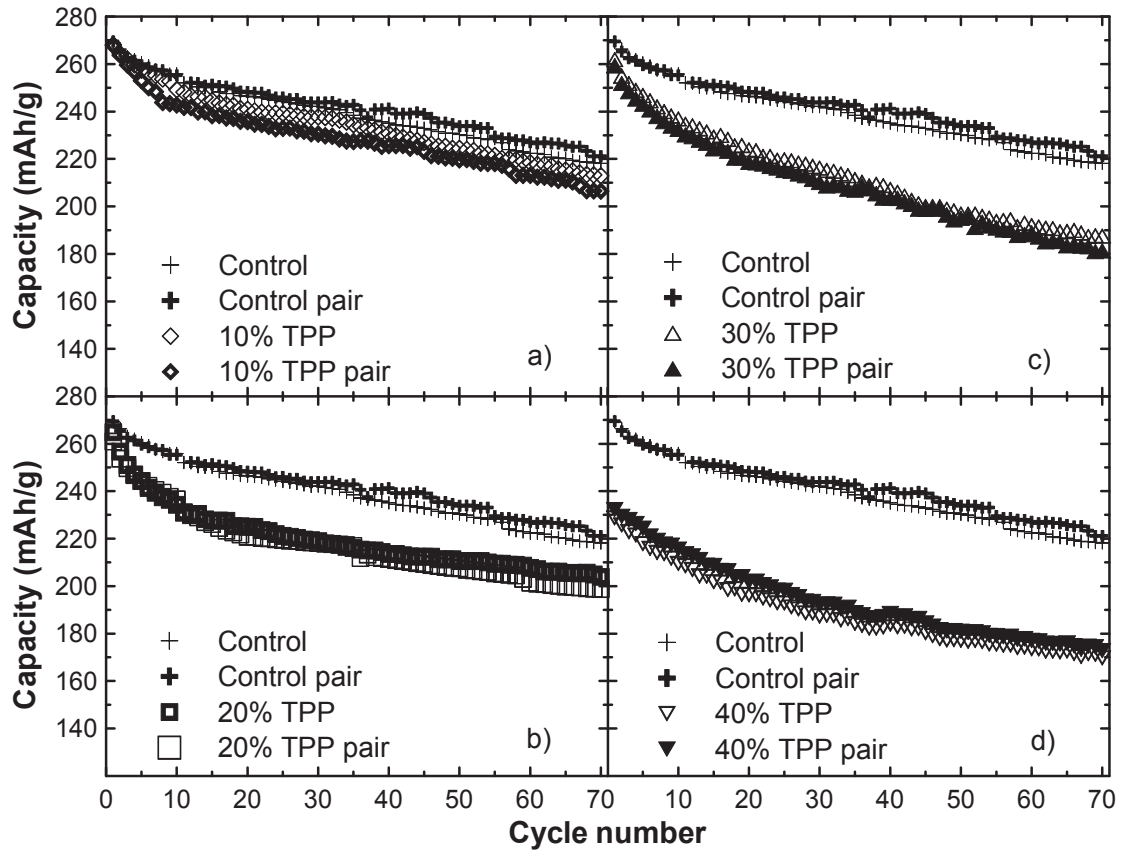


Figure 6.7 The specific capacity versus cycle number of graphite/graphite symmetric cells with different concentrations of TPP cycled at  $C/10$  at a temperature of  $30.0 \pm 0.1^\circ\text{C}$ .

Figure 6.8 shows the charge/discharge voltage polarization measured during the cycling of the graphite/graphite symmetric cells containing different amounts of TPP.

Here, the polarization is taken to be the difference between the average charge and discharge voltage calculated using the following equation,

$$\Delta V = \left( \frac{\int_{\text{Charge}} V(q) dq}{Q_{\text{Charge}}} \right) - \left( \frac{\int_{\text{Discharge}} V(q) dq}{Q_{\text{Discharge}}} \right) \quad \text{Equation 6.2}$$

In all cases, the polarization increases with cycle number, with the rate of increase becoming more severe for the cells with higher TPP contents. Figure 6.8 suggests that there is some issue with TPP in the graphite/graphite cells that leads to ever-growing cell impedance. The TPP content in the electrolyte reaches 1M at 27% TPP. If TPP co-ordinates very strongly to  $\text{Li}^+$ , then the desolvation of the  $\text{Li}^+$  at the electrode surfaces could lead to an increased charge transfer resistance with TPP content. This could explain the offset in the initial values of  $\Delta V$  with TPP-content observed in Figure 6.8, but not the increased rate of impedance growth with cycle number for cells with higher TPP contents.

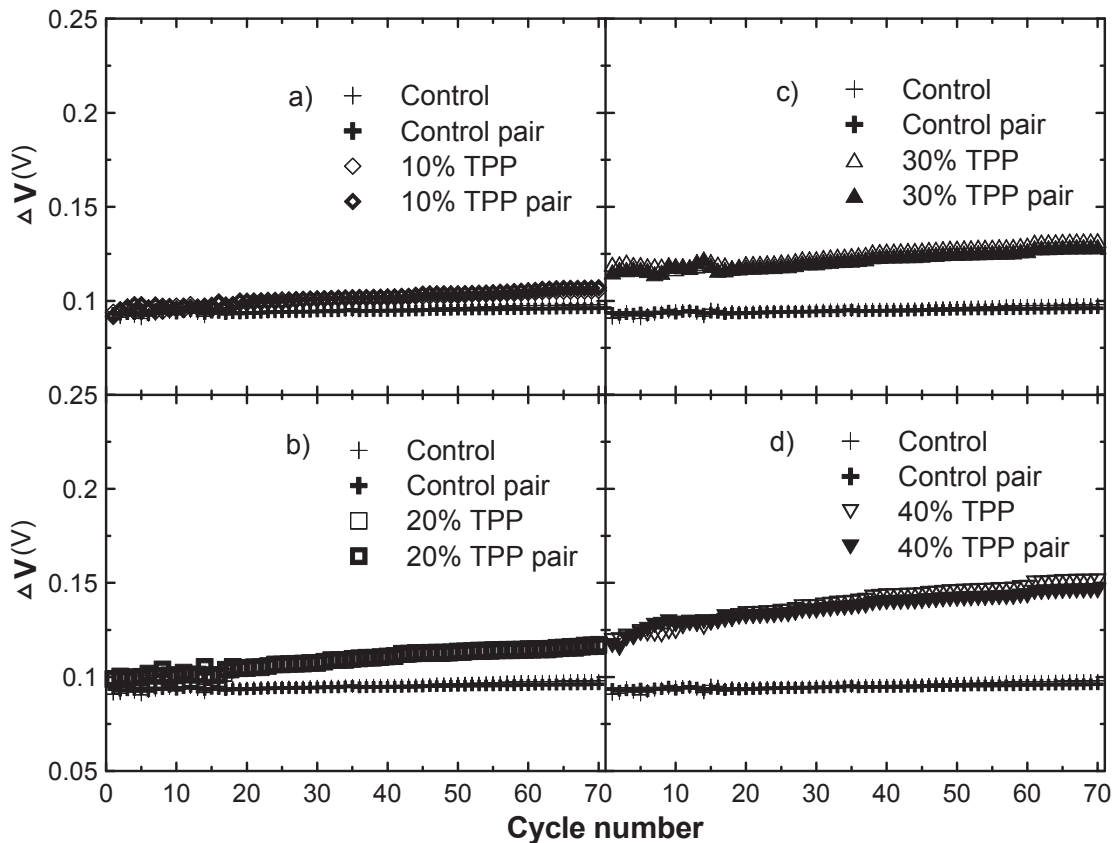


Figure 6.8 Charge-discharge potential polarizations,  $\Delta V$ , in units of volts, plotted versus cycle number for the cells described by Figure 6.7.

Figure 6.9 shows the AC impedance results for the graphite/graphite symmetric cells with different TPP contents after 20 cycles. The AC impedance spectra were collected at 30°C. To aid in the discussion of these spectra, quantities  $R_1$ ,  $R_2$  and  $R_3$  are defined in Figure 6.9 for the green data points, corresponding to 30% TPP. The resistance  $R_1$ , which is the high frequency intercept on the real axis, can be associated with the electrolyte resistance. For the cells with 0, 10 and 20% TPP,  $R_2$  and  $R_3$  are not distinguishable. However, for TPP contents of 30 and 40%, a new semicircle in the AC impedance spectrum appears and the locations on the real axis where there are minima in the imaginary impedance have been labelled as  $R_2$  and  $R_3$ . Further experiments are required to correlate the differences  $R_2 - R_1$  and  $R_3 - R_2$  to physically meaningful impedances in the cell like the charge-transfer resistance and the current collector/electrode interface, for example. Therefore, simply the variations of  $R_2 - R_1$  and  $R_3 - R_2$  with TPP content are tabulated in Table 6.3. Table 6.3 shows that the initial high frequency impedance,  $R_1$ , which corresponds to the electrolyte resistance, increases from about 4  $\Omega$  to about 11  $\Omega$  as the concentration of TPP in electrolyte increases. Table 6.3 also shows that the diameters of the lower frequency semicircles,  $R_2 - R_1$  and  $R_3 - R_2$  also increase with TPP content. This agrees with the results in Figure 6.9 which implied a larger low frequency impedance for cells with larger TPP content. The origin of the impedance increase with TPP content is not understood at this time.

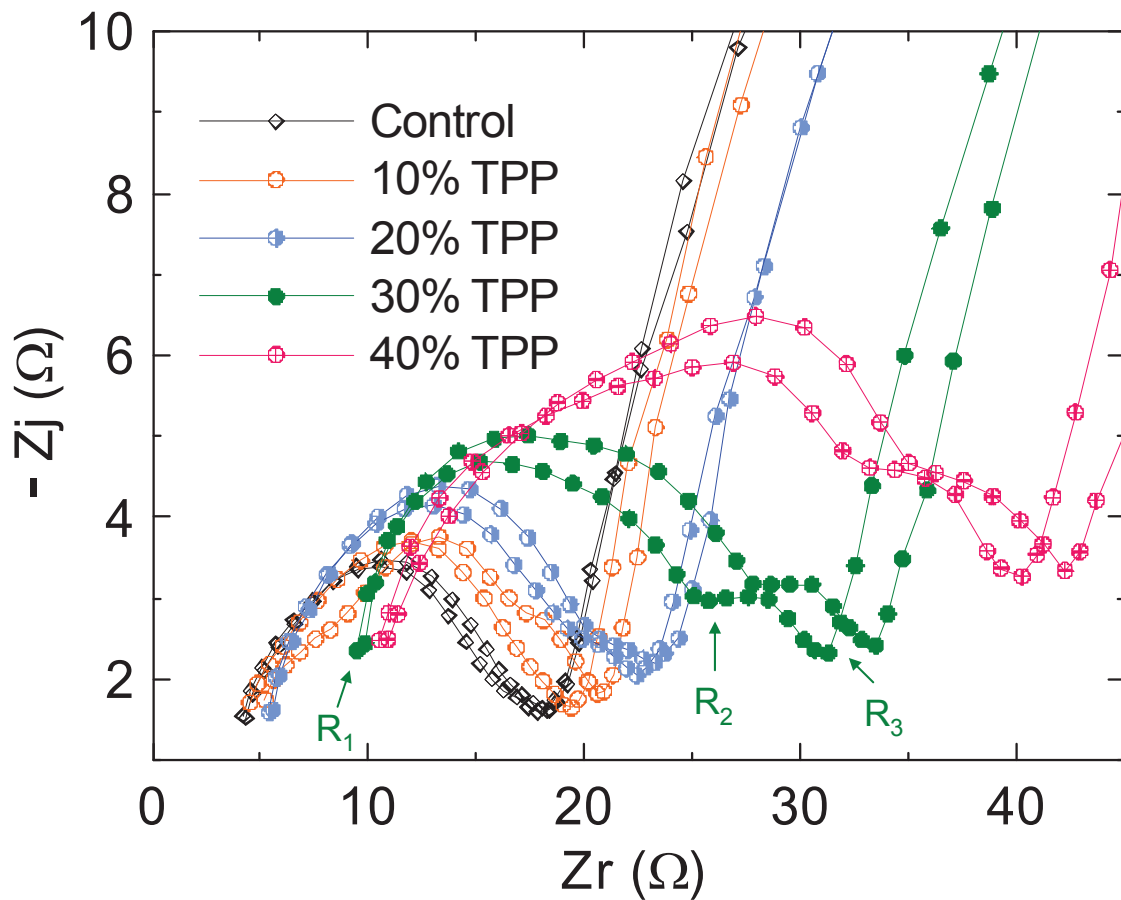


Figure 6.9 The negative imaginary impedance plotted versus the real impedance for graphite/graphite symmetric cells with different concentrations of TPP. The results were obtained for the cells described in Figures 6.6, 6.7 and 6.8, after 20 cycles. The frequency range extended from 0.01Hz to 100 kHz and the data were collected at 30°C

Table 6.3 Measured impedance results for graphite/graphite symmetric cells with different concentration of TPP after 40 cycles.

electrolyte	$R_1$ ( $\Omega$ )	$R_2-R_1$ ( $\Omega$ )	$R_3-R_2$ ( $\Omega$ )
control	4.2	13.6	
10% TPP	5.2	15.4	
20% TPP	5.4	17	
30% TPP	9.8	18	5.7
40% TPP	10.9	24	7.3

### 6.1.3 Summary

The effect of TPP on the electrochemical performance of negative electrode materials was studied using coke/Li half cells with automated storage and with graphite/graphite symmetric cells. The studies on the coke/Li cells showed that increased TPP concentrations did not increase irreversible capacity during the first cycle at either 30 or 60°C. The storage experiments showed that Li was not extracted from  $\text{Li}_x\text{C}_6$  more rapidly in the presence of TPP, in fact, the rate of extraction was reduced at 60°C for cells containing TPP compared to control cells. These experiments suggest that TPP does not accelerate SEI growth, but, instead leads to a more stable SEI. This does not mean a better SEI.

Graphite/graphite symmetric cells with TPP were studied in cycling and AC impedance studies. The cycling studies showed lower capacity for cells with higher TPP contents and a greater rate of increase of charge-discharge polarization with cycling for cells with higher TPP content. Both of these observations are consistent with higher impedance for cells with higher TPP content. The continual increase in the charge-discharge polarization is troublesome and suggests that whatever SEI is formed in the presence of high TPP content has components that lead to high impedance. Impedance reducing additives should be tried in the presence of TPP to see if this effect can be mitigated. Some initial results of such efforts will be reported in section 7.2.2.

These results show that when high concentrations of TPP are used, high enough to perhaps impart some reasonable flame retardant properties, there are impedance related problems that develop at the negative electrode. These are not related to an unstable SEI, but instead to a SEI that appears to have impeded Li transport.

## **6.2 The reactivity of charged electrode materials with electrolytes containing TPP**

In the previous section, the impact of triphenyl phosphate (TPP) as a flame retardant additive on the electrochemical performance of negative electrode materials was studied using studies involving symmetric cells, automated storage tests and AC impedance spectroscopy. The impact of TPP on positive electrode materials has been reported as well [76]. It was found that a more stable SEI on the negative electrode material was formed in the presence of TPP but that this film had larger impedance. Similarly the presence of TPP was found to strongly increase the impedance of positive electrode symmetric cells with either  $\text{Li}[\text{Ni}_{0.8}\text{Co}_{0.15}\text{Al}_{0.05}]\text{O}_2$  (NCA) or NMC electrodes [76]. In the case of graphite/graphite and NCA/NCA symmetric cells, charge-discharge capacity retention in the presence of TPP equivalent to that in the absence of TPP was observed. In the case of the NCA/NCA symmetric cells, 2% vinylene carbonate, was required to achieve acceptable performance of cells with 30 or 40% TPP by volume [76]. The NMC/NMC symmetric cells showed inferior performance compared to the



NCA/NCA cells in the absence and presence of TPP for reasons that we do not yet understand.

These results suggest that it may be possible to make Li-ion cells with up to 40% TPP that function adequately. The major remaining question is whether such cells would provide a safety advantage over cells without TPP. The answer to such a question must involve studies of the reactivity between the charged electrode materials and TPP-containing electrolyte and studies to determine if TPP does impart flame retardant properties to the electrolyte.

In this section, the performances of NMC/NMC symmetric cells containing TPP previously published are first summarized. The reactivity of lithiated graphite and deintercalated NMC and NCA in electrolytes containing different amounts of TPP were studied using ARC. The flame retardant properties of electrolytes containing TPP was judged by self-extinguishing time (SET) tests. These results are an appropriate supplement and continuation of our previous work on the impact of TPP on the electrochemical properties of both positive and negative electrode materials.

### **6.2.1 Impact of TPP on the electrochemical performance of NMC/NMC and graphite/graphite symmetric cells.**

Figure 6.10 shows the specific capacity versus cycle number for the NMC/NMC symmetric cells with 0 (control), 10% and 40% TPP cycling at  $30^{\circ}\text{C} \pm 0.1^{\circ}\text{C}$  (duplicate cells are shown). TPP increases the capacity fading of NMC/NMC symmetric cells compared to control cells. The impact of TPP on graphite/graphite symmetric cells was

shown in Figure 6.7. The capacity fading of NMC/NMC symmetric cells (Figure 6.10) and the reduction of the initial capacity of graphite/graphite symmetric cells (Figure 6.7) became more significant as the TPP content increased. These changes are caused primarily by the increased impedance of the surface films caused by the TPP containing electrolyte [76], which was discussed in section 6.1.2 as well.

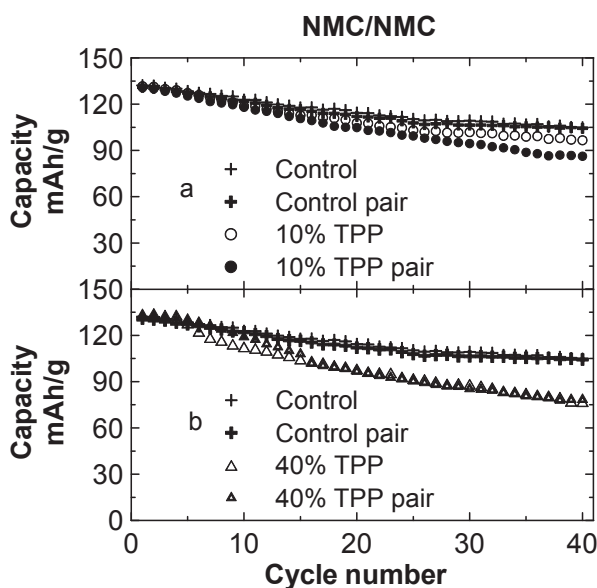


Figure 6.10 The specific capacity versus cycle number of NMC/NMC symmetric cells with different concentrations of TPP in their electrolytes as indicated. The cells were cycled at C/10 at a temperature of  $30.0 \pm 0.1^\circ\text{C}$ . Results for two cells are shown for each TPP concentration and results for control cells are included in each panel for comparison.

### 6.2.2 Impact of TPP on the reactivity of NMC and graphite in electrolytes

Figure 6.11 shows the self-heating rate vs. temperature, T, as measured by accelerating rate calorimetry, of 70 mg of  $\text{LiC}_6$  in the same mass of various electrolytes with different concentrations of TPP.  $\text{LiC}_6$  shows less reactivity in electrolytes containing 10% TPP or 40% TPP than it does in the control electrolyte in the temperature range

between 100 and 200°C. The LiC<sub>6</sub> samples with 40% TPP show similar reactivity to the control sample above 200°C as well. This result indicates that adding TPP does not intensify the reactivity of lithiated graphite in electrolyte at elevated temperature.

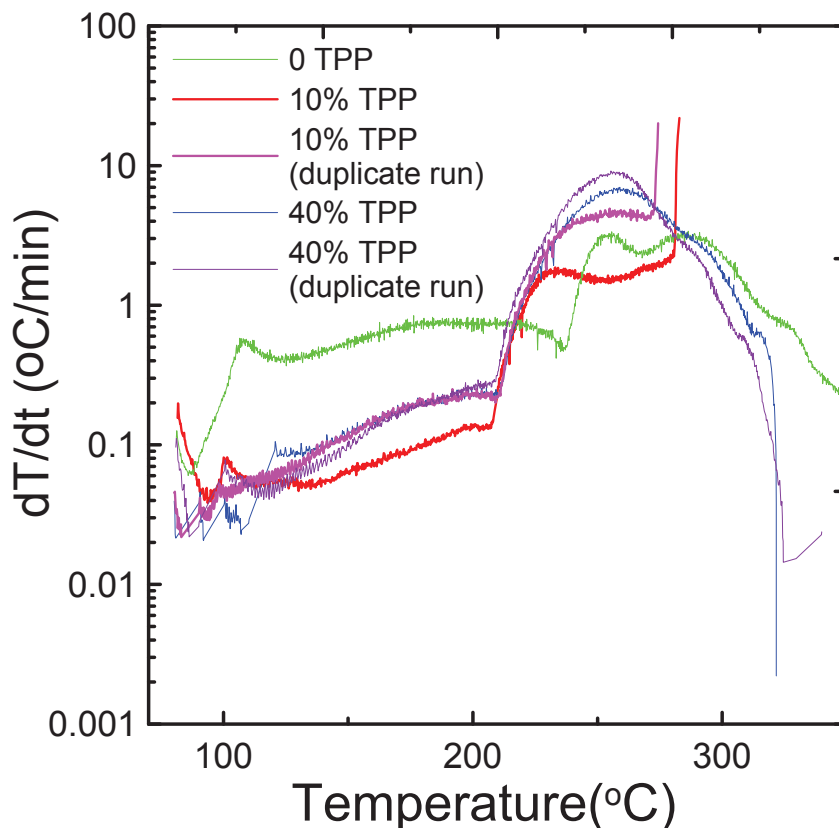


Figure 6.11 Self heating rate (SHR) vs. temperature for 70 mg lithiated graphite (LiC<sub>6</sub>), in the same mass of electrolytes containing different amounts of TPP. The legend indicates which curve corresponds to which sample.

Figure 6.12 shows the self-heating rate vs. temperature,  $T$ , of 94 mg of deintercalated NMC in 30 mg of electrolytes with different concentrations of TPP. Unlike lithiated graphite, charged NMC shows quite different reactivity in electrolyte containing TPP compared to control electrolyte at elevated temperature. A new exothermic peak at around 200°C can be observed in all experiments with TPP-containing electrolytes and

the maximum self heating rate of this peak increases with the content of TPP. This indicates a higher reactivity of charged NMC in the presence of TPP. Even though charged NMC does not reach thermal runaway in these experiments with electrolyte containing 40% TPP, the higher reactivity at lower temperature is a serious concern. This means TPP may lead to increased reactivity at the positive electrode side in cells under conditions of electrical or mechanical abuse. Ideally, the addition of a flame retardant would not impact, or would even reduce, the electrode/electrolyte reactivity.

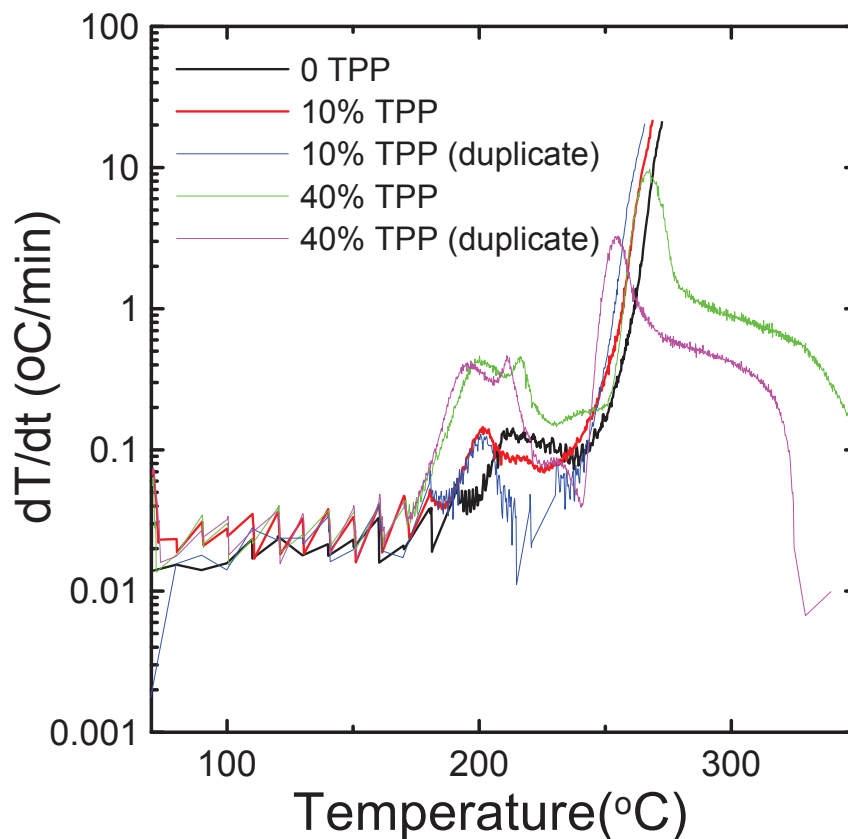


Figure 6.12 Self heating rate (SHR) vs. temperature of 94 mg of charged NMC (4.2 V vs.  $\text{Li}/\text{Li}^+$ ), in 30 mg of electrolytes containing different amounts of TPP. The legend indicates which curve corresponds to which sample.

Figure 6.13 shows the self-heating rate vs. temperature,  $T$ , of 70 mg of deintercalated NCA in 30 mg of electrolyte with different concentrations of TPP. Charged NCA shows higher reactivity than deintercalated NMC in control electrolyte, which agrees well with previous reports [77]. Unlike NMC, NCA shows lower reactivity in electrolytes containing 40% TPP during the whole temperature range of the ARC test. It does not reach thermal runaway as in control electrolyte, where thermal runaway is reached at around 225°C. The reason for the difference between NMC and NCA is not understood. Future work should explain how TPP impact the reactivity of different cathode materials.

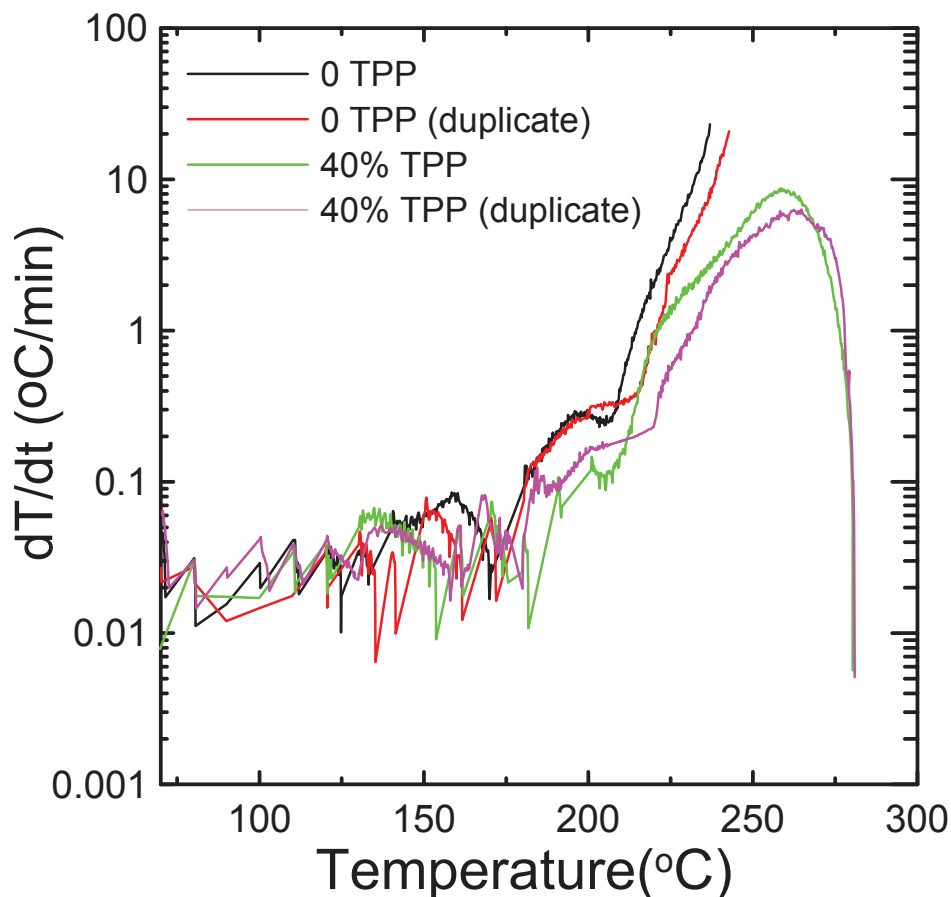


Figure 6.13 Self heating rate (SHR) vs. temperature of 94 mg of charged NCA (4.2 V vs.  $\text{Li/Li}^+$ ), in 30 mg of electrolyte containing different amounts of TPP. The legend indicates which curve corresponds to which sample.

### 6.2.3 Impact of TPP on the flammability of electrolyte

Figure 6.14 shows the SET plotted vs. the concentration of TPP in electrolytes that use EC:DEC or EC:DMC as solvents. Results from the test methods 1 and 2 described in the section 2.11 are shown. In each case the SET was calculated by the average of 8 measurements and the error is less than 10% of the plotted value. There are clear differences between the results measured using cotton swab tips in a watch glass and glass wool spheres on Al foil. Which of these methods indicates results relevant to the events that occur in a burning Li-ion battery? The answer is unknown. It is worth noting that cotton balls and glass wool were both used in the reported references [41, 47]. Those references do not report how the cotton balls or glass wool spheres were supported. The SET result in Figure 6.13 using cotton swab tips on a watch glass shows a nearly linear relationship between the SET and TPP concentration, suggesting that 40% TPP would be very effective as a flame retardant. However, the SET results in Figure 6.13 measured using glass wool on Al foil give an entirely different conclusion. There is virtually no effect of TPP in reducing the SET. The disagreement between the results measured by methods 1 and 2 strongly suggest that it cannot be guaranteed that TPP will have any flame retardant effect in burning Li-ion batteries.

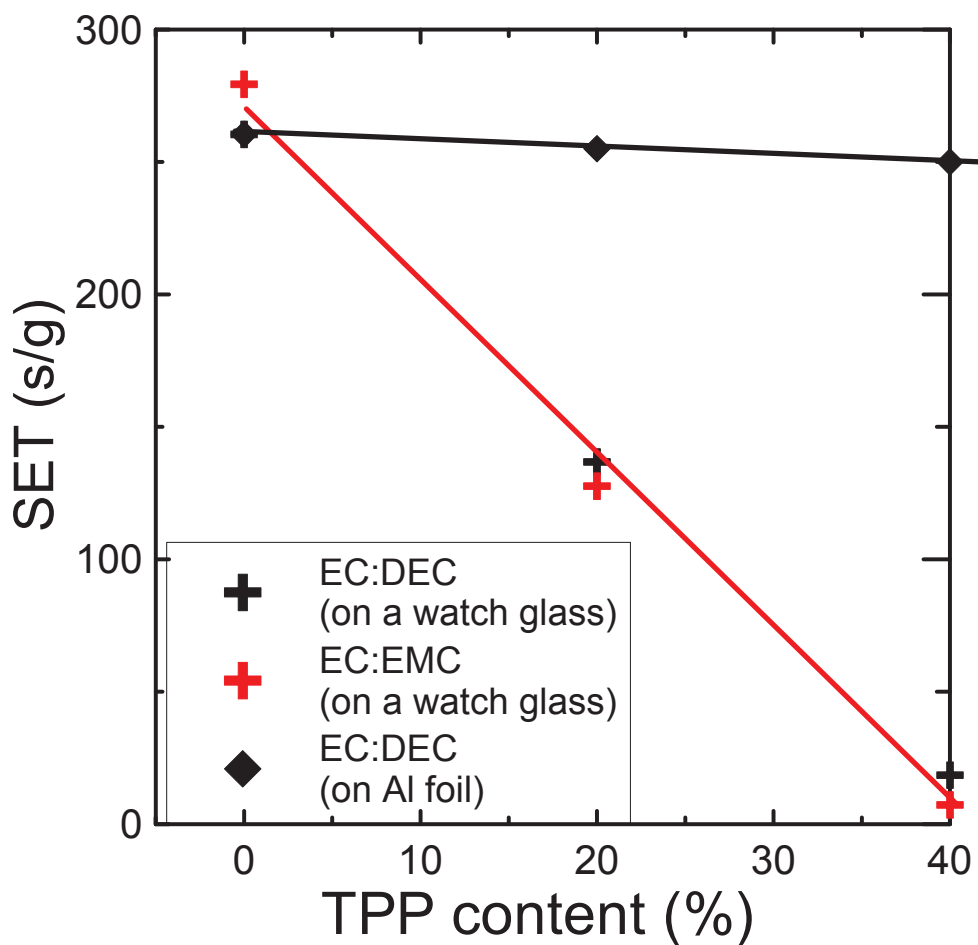


Figure 6.14 Self-extinguishing time (SET) for electrolytes containing various concentrations of TPP. Results using the two test methods are shown. The solid lines are guides for the eye.

Due to the differences between SET results from methods 1 and 2, small pools of electrolyte on flat surfaces were ignited with the barbecue lighter. The results were not measured quantitatively, but mirrored the results found for the glass wool on Al foil (method 2) where additions of TPP had virtually no effect on the SET. This research on TPP began due to convincing, but apparently incomplete (based on Figure 6.14), reports that TPP imparts flame retardant properties to the electrolyte. It is extremely clear that a

standard test method to judge the flame retarding effect of electrolytes containing flame retardants needs to be developed and that whatever method is developed must actually have relevance to events that occur in the abuse of Li-ion batteries.

#### **6.2.4 Summary**

Studies with graphite/graphite, NCA/NCA, NMC/NMC symmetric cells suggest it may be possible to develop electrolytes containing up to 40% TPP that allow adequately functioning Li-ion cells to be made. The reactivity between lithiated graphite and electrolyte at elevated temperature, as measured by ARC, is no worse in the presence of TPP. By contrast, charged NMC shows a distinctly higher reactivity at temperatures between 180 and 220°C in electrolytes containing TPP than in control electrolyte. However, TPP improves the thermal stability of charged NCA. The reason for the different performance of NMC and NCA in electrolytes containing TPP is not understood. These results indicate that adding TPP would not intensify the reactivity of negative electrode material but would make an NMC positive electrode more reactive at lower temperature. TPP may not be an ideal flame retardant additive.

SET results suggest that TPP is an effective flame retardant using one method and that it is not using another method. The SET test is clearly very method-dependent and almost certainly will not give a valid indication of how a proposed flame retardant will behave in a Li-ion battery abuse scenario. Researchers need to develop methods relevant to Li-ion battery abuse scenarios to judge the impact of proposed flame retardants.



## CHAPTER 7 CONCLUSIONS AND FUTURE WORK

### 7.1 Conclusions

#### 7.1.1 Thermal Stability of sodium-ion battery materials

The thermal stability of sodium-ion battery materials were studied in this thesis using accelerating rate calorimetry.

Hard carbon was studied as a negative electrode material. The reactions between Na:HC and different solvents and electrolytes were investigated. Na:HC reacted with carbonate solvents (EC, DEC, DMC) to form sodium alkyl carbonates. Na: HC showed lower reactivity in solvents (EC:DEC and EC:DMC) than in NaPF<sub>6</sub>-based electrolytes. This was due to the coordination between NaPF<sub>6</sub> and EC, which left more reactive DEC and DMC free to react with Na:HC. Na:HC also showed higher reactivity in both solvent and electrolyte than lithiated graphite.

NaCrO<sub>2</sub>, Na<sub>0.65</sub>CoO<sub>2</sub> and NaNi<sub>0.5</sub>Mn<sub>0.5</sub>O<sub>2</sub> were studied as positive electrode materials for sodium-ion batteries. NaCrO<sub>2</sub> showed good electrochemical performance and deintercalated NaCrO<sub>2</sub> (~ Na<sub>0.5</sub>CrO<sub>2</sub>) showed superior thermal stability in both solvent and electrolyte. Na<sub>0.5</sub>CrO<sub>2</sub> was found to decompose to NaCrO<sub>2</sub> and P3-type CrO<sub>2-δ</sub> at elevated temperature, where a tiny amount of O<sub>2</sub> was released to, causing the extremely low reactivity of Na<sub>0.5</sub>CrO<sub>2</sub>. The DIFFaX program was used to model O3-type stacking faults in P3-type CrO<sub>2-δ</sub>. About 10% O3-type stacking faults were discovered in

the  $\text{CrO}_{2.8}$  sample.  $\text{Na}_{0.65}\text{CoO}_2$  showed acceptable electrochemical performance as a positive electrode material for sodium-ion batteries. However, deintercalated  $\text{Na}_{0.65}\text{CoO}_2$  ( $\sim \text{Na}_{0.35}\text{CoO}_2$ ) showed high reactivity in both solvent and electrolyte.  $\text{Na}_{0.35}\text{CoO}_2$  decomposed to  $\text{Na}_{0.7}\text{CoO}_2$  and  $\text{Co}_3\text{O}_4$ , and released  $\text{O}_2$  at the same time, which combusted the solvent, generating heat.  $\text{Na}_{0.7}\text{CoO}_2$  was also not stable at elevated temperature in solvent as it reacted to form  $\text{NaHCO}_3$  and cobalt oxides or cobalt metal releasing more  $\text{O}_2$  to combust more solvent. In electrolyte,  $\text{NaPF}_6$  rapidly reacts with  $\text{Na}_{0.35}\text{CoO}_2$  to form  $\text{NaCoF}_3$  and  $\text{CoO/Co}$  at elevated temperature.  $\text{NaNi}_{0.5}\text{Mn}_{0.5}\text{O}_2$  had good electrochemical performance when tested in a  $\text{NaNi}_{0.5}\text{Mn}_{0.5}\text{O}_2/\text{Na}$  half cell. Deintercalated  $\text{NaNi}_{0.5}\text{Mn}_{0.5}\text{O}_2$  ( $\sim \text{Na}_{0.5}\text{Ni}_{0.5}\text{Mn}_{0.5}\text{O}_2$ ) showed high reactivity in both solvent and electrolyte. It was found that  $\text{Na}_{0.5}\text{Ni}_{0.5}\text{Mn}_{0.5}\text{O}_2$  decomposed to  $(\text{Ni,Mn})\text{O}$ ,  $\text{Ni}$  and  $\text{MnCO}_3$  (on cooling) and released  $\text{O}_2$  to combust the solvent.  $\text{Na}_{0.5}\text{Ni}_{0.5}\text{Mn}_{0.5}\text{O}_2$  reacted with 1M  $\text{NaPF}_6$  EC:DEC to produce the additional products  $\text{Na}_3(\text{Ni,Mn})\text{F}_6$  and  $\text{Na}(\text{Ni,Mn})\text{F}_3$ .  $\text{Na}_{0.5}\text{Ni}_{0.5}\text{Mn}_{0.5}\text{O}_2$  and even uncharged  $\text{NaNi}_{0.5}\text{Mn}_{0.5}\text{O}_2$  reacted with PVDF to form  $\text{NaF}$  at low temperature.

Sodium bis(trifluoromethanesulfonyl)imide ( $\text{NaTFSI}$ ) was studied as a salt for the electrolyte of sodium-ion batteries.  $\text{Na/NaCrO}_2$  and  $\text{Na/hard carbon}$  half cells all showed good electrochemical performance using  $\text{NaTFSI/PC}$  electrolyte. Deintercalated  $\text{NaCrO}_2$  ( $\sim \text{Na}_{0.5}\text{CrO}_2$ ) and  $\text{Na:HC}$  showed similar or even slightly lower reactivity in  $\text{NaTFSI/PC}$  electrolyte at elevated temperature when compared to other known

electrolytes (NaPF<sub>6</sub>/EC:DEC, NaClO<sub>4</sub>/PC, etc). However, the pure NaTFSI-based electrolyte caused Al corrosion at high potential.

These studies aim to investigate the advantage/disadvantage of sodium-ion batteries from the point of view of thermal stability. From the study of hard carbon as negative electrode material, sodium-ion batteries that include hard carbons as negative electrodes would likely show a higher tendency to self-heat than lithium-ion batteries in both solvent and electrolyte. NaCrO<sub>2</sub> shows very good thermal stability in both solvent and electrolyte, which is better than any known lithium layered transition metal oxide and even LiFePO<sub>4</sub>. However, both Na<sub>0.65</sub>CoO<sub>2</sub> and NaNi<sub>0.5</sub>Mn<sub>0.5</sub>O<sub>2</sub> show new thermal stability concerns which were not discovered in related lithium systems (LiCoO<sub>2</sub> and LiNi<sub>0.5</sub>Mn<sub>0.5</sub>O<sub>2</sub>) before, like the reactions between electrode materials and electrolyte salt and reactions between the electrode material and binder. All these results are instructive for those concerned with the design of electrolytes, binder and electrodes to be used in sodium-ion batteries. NaTFSi is a good candidate for the electrolyte salt of sodium-ion batteries; however its application is limited to situations where the positive electrode potential is not so high as to cause Al corrosion or when corrosion inhibiting additives are used.

### **7.2.2 Triphenyl phosphate (TPP) as a flame retardant additive for lithium-ion battery**

The impact of triphenyl phosphate (TPP) on the electrochemical performance, reactivity of lithium-ion battery materials and the flammability of electrolytes were

comprehensively studied. TPP negatively impacted the electrochemical performance of both negative electrode and positive electrode sides, which was due to the high impedance caused by TPP. TPP also increased the reactivity of deintercalated  $\text{LiNi}_{1/3}\text{Mn}_{1/3}\text{Co}_{1/3}$  at high temperature while it did not change the reactivity of lithiated graphite much. Adding 40% TPP to electrolyte could make the electrolyte non-flammable as determined by a Self-Extinguishing Time (SET) test. However, SET test results strongly depended on the experimental method used.

## **7.2 Future work**

### **7.2.1 Study of the reactivity of new sodium intercalated compounds for sodium-ion batteries**

. Recently, different types of new sodium compounds were synthesized and studied for potential use in sodium-ion batteries. As discussed in Chapter 1,  $\text{Na}_2\text{MPO}_4\text{F}$  (M= Fe, Mn, Co, Ni) and  $\text{NaFeSO}_4\text{F}$  were studied by Nazar *et al* [25, 27]. Based on the experience in lithium-ion batteries, fluorides and phosphates all have very good thermal stability, such as  $\text{LiFePO}_4$  and  $\text{LiVPO}_4\text{F}$  [78]. So it is possible that  $\text{Na}_2\text{MPO}_4\text{F}$  (M= Fe, Mn, Co, Ni) and  $\text{NaFeSO}_4\text{F}$  will have very good thermal stability and they could be good choices for positive electrode materials of sodium-ion batteries based on safety considerations. Additionally, some new sodium intercalation compounds were studied as negative electrode materials for sodium-ion batteries.  $\text{Na}_2\text{Ti}_3\text{O}_7$ , studied by Senguttuvan *et al.*, showed a capacity of around 200 mAh/g at an average voltage of 0.3 V [32]. The

electrochemistry of Sn-based alloy negative electrode materials were also studied [33]. The reactivity of these compounds should be studied by ARC and compared to results of known electrode materials, such as NaCrO<sub>2</sub> and hard carbon.

### **7.2.2 Improvement of the performance of TPP-based electrolytes for lithium-ion batteries**

The negative impact of TPP on the electrochemical performance of lithium-ion batteries was the high impedance caused by TPP. Recently, Burns *et al.* studied the effect of trimethoxyboroxine (TMOBX) on the impedance of LiCoO<sub>2</sub>/graphite and LiNi<sub>1/3</sub>Mn<sub>1/3</sub>Co<sub>1/3</sub>O<sub>2</sub>/graphite wound cells. It was found that TMOBX significantly reduced the impedance of the full cells without impacting the capacity retention or columbic efficiency much [79]. It was also found that the combination of vinylene carbonate (VC) and TMOBX gave the best cell performance over all, considering impedance, capacity retention and columbic efficiency [79]. Hence, it is reasonable to introduce TMOBX and VC into the electrolytes containing TPP. It is expected that the impedance of the cells could be reduced by the function of TMOBX and VC, while the non-flammability of the electrolyte could be retained.

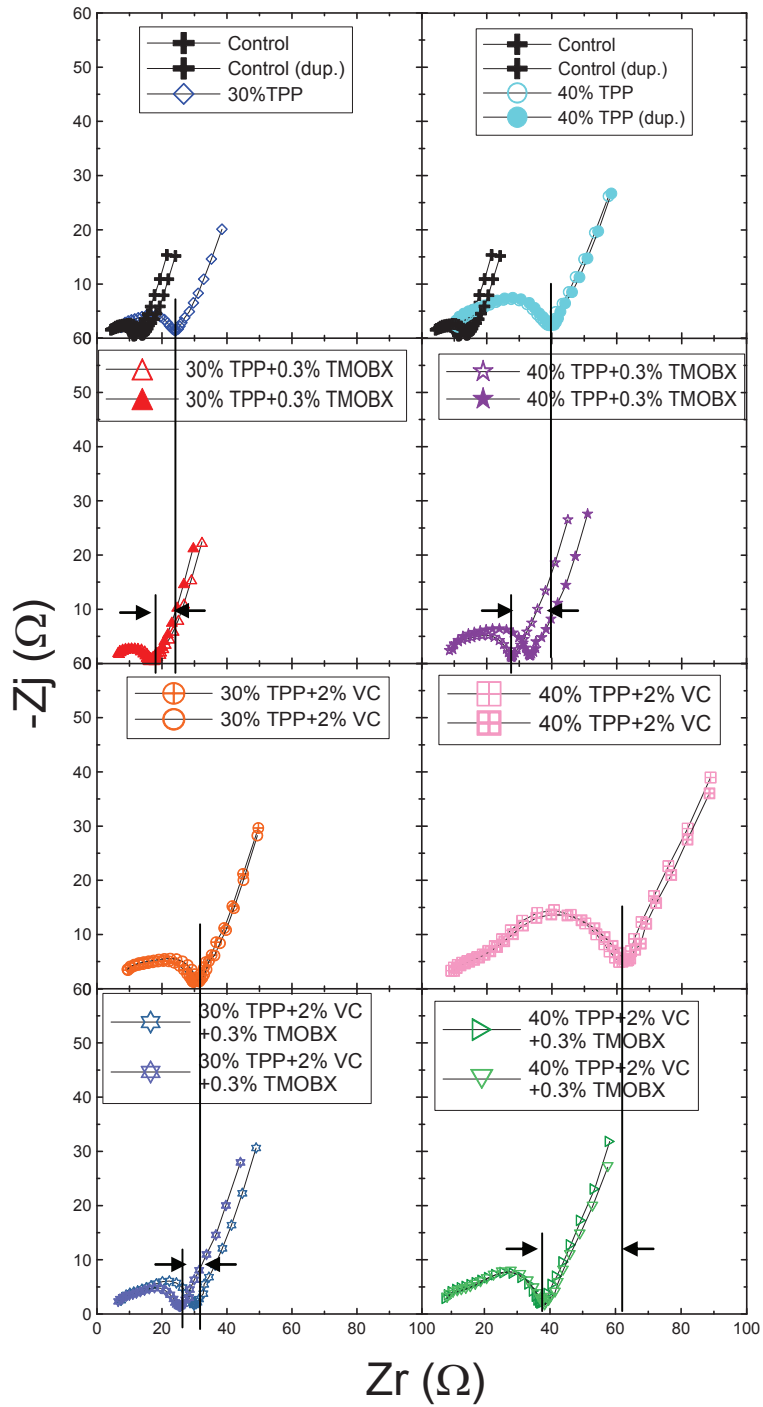


Figure 7.1 The negative imaginary impedance plotted versus the real impedance for coke/coke symmetric cells with different electrolytes.

Figure 7.1 shows the initial results of the impact of TMOBX and VC on the impedance of petroleum coke/ petroleum coke symmetric cells containing 30% and 40% TPP. It is clear that TMOBX could reduce the impedance of cells significantly. Other work on this issue is in process.

### **7.2.3 Study of other flame retardants as additives for lithium-ion batteries.**

Recently, more and more attention has been paid on the studies of flame retardant additives for lithium-ion batteries. However, most studies are lacking systematic investigation of the impacts of FRs on the different properties of lithium-ion batteries. Hence, more comprehensive understandings of known FRs, such as TMP, TEP, DMMP and etc, are needed through work similar to that described in Chapter 6.

Furthermore, based on our studies and other reports [41, 43], more than 20% FRs are needed to reduce the electrolyte flammability. This could increase the cost of electrolytes and increase the cost of lithium-ion batteries. Considering the negative impact of such high concentration of FRs in the electrolyte on the electrochemical performance of lithium-ion batteries, it is necessary to develop new types of FRs, which are not limited to organophosphorus or organohalogen compounds. It is also valuable to develop solvents with low flammability as described in ref. [49].

#### **7.2.4 Fundamental understanding of function of additives on the electrochemical performance of lithium-ion batteries.**

A small amount of additives could improve the performance of lithium-ion batteries significantly [75, 79]. Additives are very economical and effective. However, most of the reports about additives focus on the results that can be observed. More fundamental understanding of the function of additives in lithium-ion batteries are lacking. For example, TMOBX was proved to reduce cell impedance significantly, but the reason for the impedance reduction is unknown [79].

It is believed that many additives function by modifying the properties of passivation films on the surface of the negative electrode or the positive electrode. It is necessary to apply more characterization methods, like Raman spectroscopy, infrared spectroscopy, X-ray photoelectron spectroscopy and etc., in such studies to understand how additives modify the surface films on electrodes.

#### **7.2.5 Studies the reactivity of other layered-structure sodium transition metal oxides as positive electrode materials for Na-ion batteries**

In Chapter 1, some other layered-structure sodium transition metal oxides, such as  $\text{Na}_x\text{Fe}_{0.5}\text{Mn}_{0.5}\text{O}_2$  and  $\text{Na}_{2/3}\text{Mn}_{2/3}\text{Ni}_{1/3}\text{O}_2$  were discussed as positive electrode materials for Na-ion batteries. Their structural and electrochemical performance have been reported [21, 24]. However, it is also important to investigate the reactivity of such materials in solvents and electrolytes at elevated temperature through ARC. Their reactivity will be an important consideration for their potential application in Na-ion batteries.



Recently, Sathiya *et al.* reported the structural and electrochemical performance of  $\text{NaNi}_{1/3}\text{Mn}_{1/3}\text{Co}_{1/3}\text{O}_2$  as a positive electrode material for Na-ion batteries [80]. It is also valuable to study the reactivity of such material. Furthermore, different Na-NMC ( $\text{NaNi}_x\text{Mn}_y\text{Co}_z\text{O}_2$ ) composites could be synthesized and studied.

#### **7.2.6 Can Na-ion batteries work in aqueous electrolytes?**

There have been research works about lithium-ion batteries in aqueous electrolytes [81, 82]. Aqueous electrolytes can provide extremely high conductivity and extremely low cost, even though the voltage of cells is relatively low. Recently, Aquion Energy has announced sodium-ion batteries with aqueous electrolyte. They use  $\text{NaMnO}_2$  as the positive electrode, activated carbon as the negative electrode and  $\text{Na}_2\text{SO}_4$  in water as the electrolyte. The batteries show excellent electrochemical performance. Even though these batteries do not have competitive volumetric energy densities with lithium-ion batteries, they are quite suitable for energy storage. The company announced full scale production of such batteries in 2013 [83]. Future work should be carried out to study the impact of additives in aqueous electrolyte on the electrochemical performance of sodium-ion batteries. It is also interesting to try other positive electrode materials in aqueous electrolyte system.

## REFERENCES:

- [1] “Lithium Ion Battery SAFETY”, *The Electrochemical Society’s Interface*, 2, **21** (2012)
- [2] Thomas B. Reddy, *Linden’s Handbook of Batteries* (fourth edition), McGraw-Hill, U. S. (2010)
- [3] M. N. Richard, J. R. Dahn, *J. Electrochem. Soc.* **146**, 2068 (1999)
- [4] M. N. Richard, J. R. Dahn, *J. Electrochem. Soc.* **146**, 2078 (1999)
- [5] D. D. MacNeil, D. Larcher, J. R. Dahn, *J. Electrochem. Soc.* **146**, 3596 (1999)
- [6] J. Jiang, J. R. Dahn, *Electrochim. Acta*, **49**, 4599 (2004)
- [7] D. D. MacNeil, J. R. Dahn, *J. Electrochem. Soc.* **149**, A912 (2002)
- [8] J. Jiang, K. W. Eberman, L. J. Krause, J. R. Dahn, *J. Electrochem. Soc.* **152**, A566 (2005)
- [9] F. Zhou, X. M. Zhao, J. R. Dahn, *J. Electrochem. Soc.* **156**, A343 (2009)
- [10] “Batteries in Electric Cars Examined After Chevy Volt Fire”  
<http://www.nytimes.com/2011/11/12/business/energy-environment/regulators-examine-electric-car-batteries-after-fire.html> (accessed Jan.18<sup>th</sup>, 2013)
- [11] J. Jiang, J. R. Dahn, *Electrochem. Commun.* **6**, 724 (2004).
- [12] K. Xu, *Chem. Rev.* **104**, 4303 (2004)
- [13] M. N. Obrovac, *13th Advanced Automotive Battery Conference*, Pasadena, U. S., 2013
- [14] “In Bolivia, Untapped Bounty Meets Nationalism”  
[http://www.nytimes.com/2009/02/03/world/americas/03lithium.html?ref=world&\\_r=0](http://www.nytimes.com/2009/02/03/world/americas/03lithium.html?ref=world&_r=0)  
(accessed Feb.18<sup>th</sup>, 2013)
- [15] C. Delmas, J. J. Braconnier, C. Fouassier, P. Hagenmuller, *Solid State Ionics*, **3-4**, 165 (1981)

- [16] R. Berthelot, D. Carlier, C. Delmas, *Nature Mater.* **10**, 74 (2011)
- [17] J.J. Braconnier, C. Delmas, P. Hagenmuller, *Mat. Res. Bull.*, **17**, 993 (1982).
- [18] S. Komaba, C. Takei, T. Nakayama, A. Ogata, N. Yabuuchi, *Electrochem. Commun.* **12**, 355 (2010).
- [19] S. Komaba, T. Nakayama, A. Ogata, T. Shimizu, C. Takei, S. Takada, A. Hokura, I. Nakai, *ECS Trans.* **16**, 43 (2009).
- [20] S. Komaba, W. Murata, T. Ishikawa, N. Yabuuchi, T. Ozeki, T. Nakayama, A. Ogata, K. Gotoh, K. Fujiwara, *Adv. Func. Mater.* **21**, 3859 (2011).
- [21] N. Yabuuchi, M. Kajiyama, J. Iwatate, H. Nishikawa, S. Hitomi, R. Okuyama, R. Usui, Y. Yamada, S. Komaba, *Nature Mater.* **11**, 512 (2012)
- [22] X. Ma, H. Chen, G. Ceder, *J. Electrochem. Soc.* **158**, A1307 (2011)
- [23] M. M. Doeff, M.Y. Peng, Y. Ma, L. C. De Jonghe, *J. Electrochem. Soc.* **141**, L145 (1994)
- [24] Z. H. Lu, J. R. Dahn, *J. Electrochem. Soc.* **148**, A1225 (2001)
- [25] B. L. Ellis, W. R. Makahnouk, W. N. Rowen-Weetaluktuk, D. H. Ryan, L. F. Nazar, *Chem. Mater.* **22**, 1059 (2010)
- [26] Y. Kawabe, N. Yabuuchi, M. Kajiyama, N. Fukuhara, T. Inamasu, R. Okuyama, I. Nakai, S. Komaba, *Electrochemistry*, **80**, 80 (2012)
- [27] R. Tripathi, T. N. Ramesh, B. L. Ellis, L. F. Nazar, *Ange. Chem. Edition* **49**, 8737 (2010)
- [28] "Abundance in Earth's crust"  
[http://www.webelements.com/periodicity/abundance\\_crust/](http://www.webelements.com/periodicity/abundance_crust/) (accessed Feb. 18<sup>th</sup>, 2013)
- [29] D. A. Stevens, J. R. Dahn, *J. Electrochem. Soc.* **147**, 4428 (2000)
- [30] D. A. Stevens, J. R. Dahn, *J. Electrochem. Soc.* **148**, A803 (2001)
- [31] S. Komaba, T. Mikumo, N. Yabuuchi, A. Ogata, H. Yoshida, Y. Yamada, *J. Electrochem. Soc.* **157**, A60 (2010)

- [32] P. Senguttuvan, G. Rousse, V. Seznec, J. M. Tarascon, M.R. Palacín, *Chem. Mater.* **23**, 4109 (2011)
- [33] L. D. Ellis, T. D. Hatchard, M. N. Obrovac, *J. Electrochem. Soc.* **159**, A1801 (2012)
- [34] V.L. Chevrier, G. Ceder, *J. Electrochem. Soc.* **158**, A1011 (2011)
- [35] A. Ponrouch, E. Marchante, M. Courty, J. M. Tarascon, M.R. Palacín, *Energy & Environ. Sci.* **5**, 8572 (2012)
- [36] A. R. Horrocks, *Advances in fire retardant materials*, Cambridge, (2008)
- [37] L A Hollingbery, T R Hull, *Polymer Degradation and Stability* **97**, 504(2012)
- [38] J. W. Hastie, *J. Res. Natl. Bur. Stand., Sect. A*, **77A**, 733 (1973)
- [39] C. W. Lee, R. Venkatachalapathy, J. Prakash, *Electrochem. Solid-State Lett.* **3**, 63 (2000)
- [40] X.Wang, E. Yasukawa, S. Kasuya, *J. Electrochem. Soc.* **148**, A1058 (2001)
- [41] K. Xu, M.S. Ding, S.S. Zhang, J.L. Allen, T.R. Jow, *J. Electrochem. Soc.* **149**, A622 (2002).
- [42] K. Xu, M.S. Ding, S.S. Zhang, J.L. Allen , T.R. Jow, *J. Electrochem. Soc.* **150**, A161 (2003).
- [43] K. Xu, S.S. Zhang, J.L. Allen, T.R. Jow, *J. Electrochem. Soc.* **150**, A170 (2003).
- [44] M. C. Smart, F.C. Krause, C. Hwang, Meeting Abstract, *219<sup>th</sup> ECS Meeting*, Montreal, Canada, May (2011)
- [45] Y. Hyung, D. R. Vissers, K. Amine, *J. Power Sources*, **119-121**, 383 (2003)
- [46] H. F. Xiang, H.Y. Xu, Z.Z. Wang, C.H. Chen, *J. Power Sources*, **173**, 562 (2007)
- [47] J. Hu, Z.Jin, H. Zhong, H. Zhan, Y. Zhou, Z. Li, *J. Power Sources*, **197**, 297 (2012)
- [48] J.Arai, *J. Electrochem. Soc.* **150**, A219 (2003).

- [49] J. Arai, *J. Power Sources*, **119-121**, 388 (2003)
- [50] P. Isken, C. Dippel, R. Schmitz, R.W. Schmitz, M. Kunze, S. Passerini, M. Winter, A. Lex-Balducci, *Electrochimica Acta*, **56**, 7530 (2011)
- [51] W. B. Xing, J. S. Xue, T. Zheng, A. Gibaud, J. R. Dahn, *J. Electrochem. Soc.* **143**, 3482 (1996)
- [52] W. B. Xing, J. R. Dahn, *J. Electrochem. Soc.* **144**, 1195 (1997)
- [53] A. van Bommel, Ph.D. Thesis, Dalhousie University (2011)
- [54] R.A. Dunlap, D.A. Small, D.D. MacNeil, M.N. Obrovac, J. R. Dahn, *J. Alloys Compounds*, **289**, 135 (1999)
- [55] M. Doyle, J. Newman, J. Reimers, *J. Power. Sources*, **52**, 221 (1994)
- [56] P.W. Atkins, *Physical Chemistry*, 5<sup>th</sup> Ed. Freeman, New York (1994)
- [57] W. E. Brown, D. Dollimore, A. K. Galway, *Comprehensive Chemical Kinetics*, **22**, 91 (1980)
- [58] D. D. Macneil, S. Trussler, H. Fortier, J. R. Dahn, *Thermochemica Acta* **386**, 153 (2002)
- [59] X. Xia, P. Ping. J. R. Dahn, *J. Electrochem. Soc.* **159**, A1460 (2012)
- [60] J. C. Burns, L. J. Krause, Dinh-Ba Le, L. D. Jensen, A. J. Smith, D. J. Xiong, J. R. Dahn, *J. Electrochem. Soc.* **158**, A1417 (2011).
- [61] B.A. Hunter, C.J. Howard, "CCP14", <http://www.ccp14.ac.uk/>. (accessed Jan 16<sup>th</sup>, 2013)
- [62] M. Kunert, P. Wiegeleben, H. Gorls, E. Dinjus, *Inorg. Chem. Commun.* **1**, 131 (1998)
- [63] S. E. Sloop, J. K. Pugh, S. Wang, J. B. Kerr, K. Kinoshita, *Electrochem. Solid-State Lett.* **4**, A42 (2001).
- [64] K. Matsubara, R. Kaneuchi, N. Maekita, *J. Chem. Soc., Faraday Trans.* **94**, 3601 (1998)

- [65] A. Yamada, S. C. Chung, K. Hinokuma, *J. Electrochem. Soc.*, **148**, A224 (2001).
- [66] J. Jiang, K. W. Eberman, L. J. Krause, J. R. Dahn, *J. Electrochem. Soc.* **152**, A556 (2005).
- [67] J. R. Dahn, E. W. Fuller, M. Obrovac, U. von Sacken, *Solid State Ionics.* **69**, 565 (1994).
- [68] S. Venkatraman, A. Manthiram, *Chem. Mater.* **14**, 3907 (2002).
- [69] Z. Lu, J. R. Dahn, *Chem. Mater.* **13**, 2078 (2001).
- [70] M. M. J. Treacy, J. M. Newsam, M. W. Deem, *Proc. R. Soc. London A*, **433**, 499 (1999).
- [71] T. Ohzuku, Y. Makimura, *Chem. Lett.* 744 (2001)
- [72] F. Zhou, X. M. Zhao, Z. H. Lu, J. W. Jiang, J. R. Dahn, *Electrochem. Solid-State Lett.* **11**, A155 (2008).
- [73] H. Yang, K. Kwon, T. M. Devine, J. W. Evans, *J. Electrochem. Soc.* **147**, 4399 (2000)
- [74] N. N. Sinha, J. C. Burns, R. J. Sanderson, J. R. Dahn, *J. Electrochem. Soc.* **158**, A1400 (2011).
- [75] N. N. Sinha, T. H. Marks, H. M. Dahn, A. J. Smith, J. C. Burns, D. J. Coyle, J. J. Dahn, J. R. Dahn, *J. Electrochem. Soc.* **159**, A1672 (2012).
- [76] P. Ping, Q. S. Wang, J.H. Sun, X. Xia, J. R. Dahn, *J. Electrochem. Soc.* **159**, A1467 (2012)
- [77] Y. Wang, J. Jiang, J.R. Dahn, *Electrochem. Commun.* **9**, 2534 (2007).
- [78] F. Zhou, X. M. Zhao, J. R. Dahn, *Electrochem. Commun.* **11**, 589 (2009).
- [79] J.C. Burns, N.N. Sinha, G.Jain, C. M. VanElzen, W.M. Lamanna, A. Xiao, E. Scott, J. Choi, J.R. Dahn, *J. Electrochem. Soc.* **159**, A1105 (2012).

[80] M. Sathiya, K. Hemalatha, K. Ramesha, J.-M. Tarascon, A. S. Prakash, *Chem. Mater.* **24**, 1846 (2012).

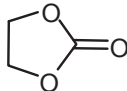
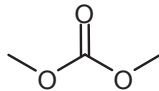
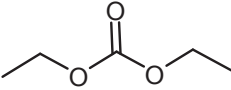
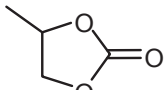
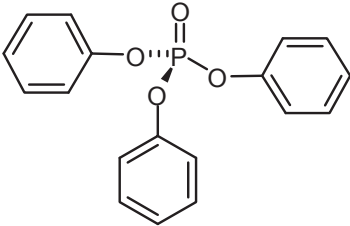
[81] W, Li, J. R. Dahn, D. S. Wainwright, *Science*, **264**, 1115 (1994)

[82] P. He, J. H. Liu, W. J. Cui, J. Y. Luo, Y. Y. Xia, *J. Power Sources*, **56**, 2351 (2011)

[83]“Aquion Technical Presentation”,  
<http://www.aquionenergy.com/thank-you---jays-presentation/>(accessed Jan. 20<sup>th</sup>, 2013)

## APPENDIX A

### Structure of some organic molecules in this thesis

Solvents	Structure
EC	
DMC	
DEC	
PC	
TPP	



## **APPENDIX B**

### **Copyright Information**

The copyright information is outlined in this section, with the permissions granted for contents use in this thesis.

## Copyright permission for Figure 1.5

---

---

### NATURE PUBLISHING GROUP LICENSE TERMS AND CONDITIONS

Nov 26, 2012

---

---

This is a License Agreement between Xin Xia ("You") and Nature Publishing Group ("Nature Publishing Group") provided by Copyright Clearance Center ("CCC"). The license consists of your order details, the terms and conditions provided by Nature Publishing Group, and the payment terms and conditions.

**All payments must be made in full to CCC. For payment instructions, please see information listed at the bottom of this form.**

License Number	3036631151877
License date	Nov 26, 2012
Licensed content publisher	Nature Publishing Group
Licensed content publication	Nature Materials
Licensed content title	Electrochemical investigation of the P2-Na <sub>x</sub> CoO <sub>2</sub> phase diagram
Licensed content author	R. Berthelot, D. Carlier, C. Delmas
Licensed content date	Dec 12, 2010
Volume number	10
Issue number	1
Type of Use	reuse in a thesis/dissertation
Requestor type	non-commercial (non-profit)
Format	print
Portion	figures/tables/illustrations
Number of figures/tables/illustrations	1
High-res required	no
Figures	Potential versus specific capacity of a Na <sub>0.7</sub> CoO <sub>2</sub> electrode in a Na/Na <sub>0.7</sub> CoO <sub>2</sub> cell
Author of this NPG article	no
Your reference number	
Title of your thesis / dissertation	Study of the safety of metal-ion batteries
Expected completion date	Jan 2013
Estimated size (number of pages)	170
Total	0.00 USD
Terms and Conditions	

---

---

## Terms and Conditions for Permissions

Nature Publishing Group hereby grants you a non-exclusive license to reproduce this material for this purpose, and for no other use, subject to the conditions below:

1. NPG warrants that it has, to the best of its knowledge, the rights to license reuse of this material. However, you should ensure that the material you are requesting is original to Nature Publishing Group and does not carry the copyright of another entity (as credited in the published version). If the credit line on any part of the material you have requested indicates that it was reprinted or adapted by NPG with permission from another source, then you should also seek permission from that source to reuse the material.
2. Permission granted free of charge for material in print is also usually granted for any electronic version of that work, provided that the material is incidental to the work as a whole and that the electronic version is essentially equivalent to, or substitutes for, the print version. Where print permission has been granted for a fee, separate permission must be obtained for any additional, electronic re-use (unless, as in the case of a full paper, this has already been accounted for during your initial request in the calculation of a print run). NB: In all cases, web-based use of full-text articles must be authorized separately through the 'Use on a Web Site' option when requesting permission.
3. Permission granted for a first edition does not apply to second and subsequent editions and for editions in other languages (except for signatories to the STM Permissions Guidelines, or where the first edition permission was granted for free).
4. Nature Publishing Group's permission must be acknowledged next to the figure, table or abstract in print. In electronic form, this acknowledgement must be visible at the same time as the figure/table/abstract, and must be hyperlinked to the journal's homepage.
5. The credit line should read:  
Reprinted by permission from Macmillan Publishers Ltd: [JOURNAL NAME] (reference citation), copyright (year of publication)  
For AOP papers, the credit line should read:  
Reprinted by permission from Macmillan Publishers Ltd: [JOURNAL NAME], advance online publication, day month year (doi: 10.1038/sj.[JOURNAL ACRONYM].XXXXX)

**Note: For republication from the *British Journal of Cancer*, the following credit lines apply.**

Reprinted by permission from Macmillan Publishers Ltd on behalf of Cancer Research UK: [JOURNAL NAME] (reference citation), copyright (year of publication) For AOP papers, the credit line should read:

Reprinted by permission from Macmillan Publishers Ltd on behalf of Cancer Research UK: [JOURNAL NAME], advance online publication, day month year (doi: 10.1038/sj.[JOURNAL ACRONYM].XXXXX)

6. Adaptations of single figures do not require NPG approval. However, the adaptation should be credited as follows:

Adapted by permission from Macmillan Publishers Ltd: [JOURNAL NAME] (reference citation), copyright (year of publication)

**Note: For adaptation from the *British Journal of Cancer*, the following credit line applies.**

Adapted by permission from Macmillan Publishers Ltd on behalf of Cancer Research UK: [JOURNAL NAME] (reference citation), copyright (year of publication)

7. Translations of 401 words up to a whole article require NPG approval. Please visit <http://www.macmillanmedicalcommunications.com> for more information. Translations of up to a 400 words do not require NPG approval. The translation should be credited as follows:

Translated by permission from Macmillan Publishers Ltd: [JOURNAL NAME] (reference citation), copyright (year of publication).

**Note: For translation from the *British Journal of Cancer*, the following credit line applies.**

Translated by permission from Macmillan Publishers Ltd on behalf of Cancer Research UK: [JOURNAL NAME] (reference citation), copyright (year of publication)

We are certain that all parties will benefit from this agreement and wish you the best in the use of this material. Thank you.

Special Terms:

v1.1

**If you would like to pay for this license now, please remit this license along with your payment made payable to "COPYRIGHT CLEARANCE CENTER" otherwise you will be invoiced within 48 hours of the license date. Payment should be in the form of a check or money order referencing your account number and this invoice number RLNK500904689. Once you receive your invoice for this order, you may pay your invoice by credit card. Please follow instructions provided at that time.**

**Make Payment To:  
Copyright Clearance Center  
Dept 001  
P.O. Box 843006  
Boston, MA 02284-3006**

**For suggestions or comments regarding this order, contact RightsLink Customer Support: [customercare@copyright.com](mailto:customercare@copyright.com) or +1-877-622-5543 (toll free in the US) or +1-978-646-2777.**

**Gratis licenses (referencing \$0 in the Total field) are free. Please retain this printable license for your reference. No payment is required.**

---

---

## Copyright permission for Figure 1.7

---

### ELSEVIER LICENSE TERMS AND CONDITIONS

Nov 26, 2012

---

This is a License Agreement between Xin Xia ("You") and Elsevier ("Elsevier") provided by Copyright Clearance Center ("CCC"). The license consists of your order details, the terms and conditions provided by Elsevier, and the payment terms and conditions.

**All payments must be made in full to CCC. For payment instructions, please see information listed at the bottom of this form.**

Supplier	Elsevier Limited The Boulevard, Langford Lane Kidlington, Oxford, OX5 1GB, UK
Registered Company Number	1982084
Customer name	Xin Xia
Customer address	Rm 1108, 2060 Quingate place, Halifax, NS b3l4p7
License number	3036650549670
License date	Nov 26, 2012
Licensed content publisher	Elsevier
Licensed content publication	Materials Research Bulletin
Licensed content title	Etude par desintercalation electrochimique des systemes NaxCrO2et NaxNiO2
Licensed content author	J.J. Braconnier, C. Delmas, P. Hagenmuller
Licensed content date	August 1982
Licensed content volume number	17
Licensed content issue number	8
Number of pages	8
Start Page	993
End Page	1000
Type of Use	reuse in a thesis/dissertation
Intended publisher of new work	other
Portion	figures/tables/illustrations
Number of figures/tables/illustrations	1
Format	both print and electronic

---

Are you the author of this Elsevier article?	No
Will you be translating?	No
Order reference number	
Title of your thesis/dissertation	Study of the safety of metal-ion batteries
Expected completion date	Jan 2013
Estimated size (number of pages)	170
Elsevier VAT number	GB 494 6272 12
Permissions price	0.00 USD
VAT/Local Sales Tax	0.0 USD / 0.0 GBP
Total	0.00 USD
Terms and Conditions	

### INTRODUCTION

1. The publisher for this copyrighted material is Elsevier. By clicking "accept" in connection with completing this licensing transaction, you agree that the following terms and conditions apply to this transaction (along with the Billing and Payment terms and conditions established by Copyright Clearance Center, Inc. ("CCC"), at the time that you opened your Rightslink account and that are available at any time at <http://myaccount.copyright.com>).

### GENERAL TERMS

2. Elsevier hereby grants you permission to reproduce the aforementioned material subject to the terms and conditions indicated.

3. Acknowledgement: If any part of the material to be used (for example, figures) has appeared in our publication with credit or acknowledgement to another source, permission must also be sought from that source. If such permission is not obtained then that material may not be included in your publication/copies. Suitable acknowledgement to the source must be made, either as a footnote or in a reference list at the end of your publication, as follows:

“Reprinted from Publication title, Vol/edition number, Author(s), Title of article / title of chapter, Pages No., Copyright (Year), with permission from Elsevier [OR APPLICABLE SOCIETY COPYRIGHT OWNER].” Also Lancet special credit - “Reprinted from The Lancet, Vol. number, Author(s), Title of article, Pages No., Copyright (Year), with permission from Elsevier.”

4. Reproduction of this material is confined to the purpose and/or media for which permission is hereby given.

5. Altering/Modifying Material: Not Permitted. However figures and illustrations may be altered/adapted minimally to serve your work. Any other abbreviations, additions, deletions and/or any other alterations shall be made only with prior written authorization of Elsevier Ltd. (Please contact Elsevier at [permissions@elsevier.com](mailto:permissions@elsevier.com))

6. If the permission fee for the requested use of our material is waived in this instance, please be advised that your future requests for Elsevier materials may attract a fee.

7. Reservation of Rights: Publisher reserves all rights not specifically granted in the combination of (i) the license details provided by you and accepted in the course of this licensing transaction, (ii) these terms and conditions and (iii) CCC's Billing and Payment terms and conditions.

8. License Contingent Upon Payment: While you may exercise the rights licensed immediately upon issuance of the license at the end of the licensing process for the transaction, provided that you have disclosed complete and accurate details of your proposed use, no license is finally effective unless and until full payment is received from you (either by publisher or by CCC) as provided in CCC's Billing and Payment terms and conditions. If full payment is not received on a timely basis, then any license preliminarily granted shall be deemed automatically revoked and shall be void as if never granted. Further, in the event that you breach any of these terms and conditions or any of CCC's Billing and Payment terms and conditions, the license is automatically revoked and shall be void as if never granted. Use of materials as described in a revoked license, as well as any use of the materials beyond the scope of an unrevoked license, may constitute copyright infringement and publisher reserves the right to take any and all action to protect its copyright in the materials.

9. Warranties: Publisher makes no representations or warranties with respect to the licensed material.

10. Indemnity: You hereby indemnify and agree to hold harmless publisher and CCC, and their respective officers, directors, employees and agents, from and against any and all claims arising out of your use of the licensed material other than as specifically authorized pursuant to this license.

11. No Transfer of License: This license is personal to you and may not be sublicensed, assigned, or transferred by you to any other person without publisher's written permission.

12. No Amendment Except in Writing: This license may not be amended except in a writing signed by both parties (or, in the case of publisher, by CCC on publisher's behalf).

13. Objection to Contrary Terms: Publisher hereby objects to any terms contained in any purchase order, acknowledgment, check endorsement or other writing prepared by you, which terms are inconsistent with these terms and conditions or CCC's Billing and Payment terms and conditions. These terms and conditions, together with CCC's Billing and Payment terms and conditions (which are incorporated herein), comprise the entire agreement between you and publisher (and CCC) concerning this licensing transaction. In the event of any conflict between your obligations established by these terms and conditions and those established by CCC's Billing and Payment terms and conditions, these terms and conditions shall control.

14. Revocation: Elsevier or Copyright Clearance Center may deny the permissions described in this License at their sole discretion, for any reason or no reason, with a full refund payable to you. Notice of such denial will be made using the contact information provided by you. Failure to receive such notice will not alter or invalidate the denial. In no event will Elsevier or Copyright Clearance Center be responsible or liable for any costs, expenses or damage incurred by you as a result of a denial of your permission request, other than a refund of the amount(s) paid by you to

posted to the web site must maintain the copyright information line on the bottom of each image. You are not allowed to download and post the published electronic version of your chapter, nor may you scan the printed edition to create an electronic version.

Central Storage: This license does not include permission for a scanned version of the material to be stored in a central repository such as that provided by Heron/XanEdu.

19. **Website** (regular and for author): A hyper-text must be included to the Homepage of the journal from which you are licensing at <http://www.sciencedirect.com/science/journal/xxxxx>, or for books to the Elsevier homepage at <http://www.elsevier.com>

20. **Thesis/Dissertation**: If your license is for use in a thesis/dissertation your thesis may be submitted to your institution in either print or electronic form. Should your thesis be published commercially, please reapply for permission. These requirements include permission for the Library and Archives of Canada to supply single copies, on demand, of the complete thesis and include permission for UMI to supply single copies, on demand, of the complete thesis. Should your thesis be published commercially, please reapply for permission.

21. **Other Conditions**:

v1.6

**If you would like to pay for this license now, please remit this license along with your payment made payable to "COPYRIGHT CLEARANCE CENTER" otherwise you will be invoiced within 48 hours of the license date. Payment should be in the form of a check or money order referencing your account number and this invoice number RLNK500904742. Once you receive your invoice for this order, you may pay your invoice by credit card. Please follow instructions provided at that time.**

**Make Payment To:  
Copyright Clearance Center  
Dept 001  
P.O. Box 843006  
Boston, MA 02284-3006**

**For suggestions or comments regarding this order, contact RightsLink Customer Support: [customercare@copyright.com](mailto:customercare@copyright.com) or +1-877-622-5543 (toll free in the US) or +1-978-646-2777.**

**Gratis licenses (referencing \$0 in the Total field) are free. Please retain this printable license for your reference. No payment is required.**

---



posted to the web site must maintain the copyright information line on the bottom of each image. You are not allowed to download and post the published electronic version of your chapter, nor may you scan the printed edition to create an electronic version.

Central Storage: This license does not include permission for a scanned version of the material to be stored in a central repository such as that provided by Heron/XanEdu.

19. **Website** (regular and for author): A hyper-text must be included to the Homepage of the journal from which you are licensing at <http://www.sciencedirect.com/science/journal/xxxxx>, or for books to the Elsevier homepage at <http://www.elsevier.com>

20. **Thesis/Dissertation**: If your license is for use in a thesis/dissertation your thesis may be submitted to your institution in either print or electronic form. Should your thesis be published commercially, please reapply for permission. These requirements include permission for the Library and Archives of Canada to supply single copies, on demand, of the complete thesis and include permission for UMI to supply single copies, on demand, of the complete thesis. Should your thesis be published commercially, please reapply for permission.

21. **Other Conditions**:

v1.6

**If you would like to pay for this license now, please remit this license along with your payment made payable to "COPYRIGHT CLEARANCE CENTER" otherwise you will be invoiced within 48 hours of the license date. Payment should be in the form of a check or money order referencing your account number and this invoice number RLNK500904742. Once you receive your invoice for this order, you may pay your invoice by credit card. Please follow instructions provided at that time.**

**Make Payment To:**  
Copyright Clearance Center  
Dept 001  
P.O. Box 843006  
Boston, MA 02284-3006

**For suggestions or comments regarding this order, contact RightsLink Customer Support: [customer@copyright.com](mailto:customer@copyright.com) or +1-877-622-5543 (toll free in the US) or +1-978-646-2777.**

**Gratis licenses (referencing \$0 in the Total field) are free. Please retain this printable license for your reference. No payment is required.**

---

---

## Copyright permission for Figure 1.8

### ELSEVIER LICENSE TERMS AND CONDITIONS

Nov 26, 2012

This is a License Agreement between Xin Xia ("You") and Elsevier ("Elsevier") provided by Copyright Clearance Center ("CCC"). The license consists of your order details, the terms and conditions provided by Elsevier, and the payment terms and conditions.

**All payments must be made in full to CCC. For payment instructions, please see information listed at the bottom of this form.**

Supplier	Elsevier Limited The Boulevard, Langford Lane Kidlington, Oxford, OX5 1GB, UK
Registered Company Number	1982084
Customer name	Xin Xia
Customer address	Rm 1108, 2060 Quingate place, Halifax, NS b3l4p7
License number	3036650448947
License date	Nov 26, 2012
Licensed content publisher	Elsevier
Licensed content publication	Electrochemistry Communications
Licensed content title	Electrochemical intercalation activity of layered NaCrO <sub>2</sub> vs. LiCrO <sub>2</sub>
Licensed content author	Shinichi Komaba, Chikara Takei, Tetsuri Nakayama, Atsushi Ogata, Naoaki Yabuuchi
Licensed content date	March 2010
Licensed content volume number	12
Licensed content issue number	3
Number of pages	4
Start Page	355
End Page	358
Type of Use	reuse in a thesis/dissertation
Portion	figures/tables/illustrations
Number of figures/tables/illustrations	1
Format	both print and electronic
Are you the author of this Elsevier article?	No

Will you be translating?	No
Order reference number	
Title of your thesis/dissertation	Study of the safety of metal-ion batteries
Expected completion date	Jan 2013
Estimated size (number of pages)	170
Elsevier VAT number	GB 494 6272 12
Permissions price	0.00 USD
VAT/Local Sales Tax	0.0 USD / 0.0 GBP
Total	0.00 USD
Terms and Conditions	

### INTRODUCTION

1. The publisher for this copyrighted material is Elsevier. By clicking "accept" in connection with completing this licensing transaction, you agree that the following terms and conditions apply to this transaction (along with the Billing and Payment terms and conditions established by Copyright Clearance Center, Inc. ("CCC"), at the time that you opened your Rightslink account and that are available at any time at <http://myaccount.copyright.com>).

### GENERAL TERMS

2. Elsevier hereby grants you permission to reproduce the aforementioned material subject to the terms and conditions indicated.
3. Acknowledgement: If any part of the material to be used (for example, figures) has appeared in our publication with credit or acknowledgement to another source, permission must also be sought from that source. If such permission is not obtained then that material may not be included in your publication/copies. Suitable acknowledgement to the source must be made, either as a footnote or in a reference list at the end of your publication, as follows:  
  
 "Reprinted from Publication title, Vol /edition number, Author(s), Title of article / title of chapter, Pages No., Copyright (Year), with permission from Elsevier [OR APPLICABLE SOCIETY COPYRIGHT OWNER]." Also Lancet special credit - "Reprinted from The Lancet, Vol. number, Author(s), Title of article, Pages No., Copyright (Year), with permission from Elsevier."
4. Reproduction of this material is confined to the purpose and/or media for which permission is hereby given.
5. Altering/Modifying Material: Not Permitted. However figures and illustrations may be altered/adapted minimally to serve your work. Any other abbreviations, additions, deletions and/or any other alterations shall be made only with prior written authorization of Elsevier Ltd. (Please contact Elsevier at [permissions@elsevier.com](mailto:permissions@elsevier.com))
6. If the permission fee for the requested use of our material is waived in this instance, please be advised that your future requests for Elsevier materials may attract a fee.

## Copyright permission for Figure 1.10

### JOHN WILEY AND SONS LICENSE TERMS AND CONDITIONS

Dec 06, 2012

This is a License Agreement between Xin Xia ("You") and John Wiley and Sons ("John Wiley and Sons") provided by Copyright Clearance Center ("CCC"). The license consists of your order details, the terms and conditions provided by John Wiley and Sons, and the payment terms and conditions.

**All payments must be made in full to CCC. For payment instructions, please see information listed at the bottom of this form.**

License Number	3043210850788
License date	Dec 06, 2012
Licensed content publisher	John Wiley and Sons
Licensed content publication	Advanced Functional Materials
Book title	
Licensed content author	Shinichi Komaba,Wataru Murata,Toru Ishikawa,Naoaki Yabuuchi,Tomoaki Ozeki,Tetsuri Nakayama,Atsushi Ogata,Kazuma Gotoh,Kazuya Fujiwara
Licensed content date	Aug 11, 2011
Start page	3859
End page	3867
Type of use	Dissertation/Thesis
Requestor type	University/Academic
Format	Print and electronic
Portion	Figure/table
Number of figures/tables	1
Number of extracts	
Original Wiley figure/table number(s)	Figure 11
Will you be translating?	No
Order reference number	
Total	0.00 USD
Terms and Conditions	

#### TERMS AND CONDITIONS

This copyrighted material is owned by or exclusively licensed to John Wiley & Sons, Inc. or one of its group companies (each a "Wiley Company") or a society for whom a Wiley Company has

exclusive publishing rights in relation to a particular journal (collectively WILEY"). By clicking "accept" in connection with completing this licensing transaction, you agree that the following terms and conditions apply to this transaction (along with the billing and payment terms and conditions established by the Copyright Clearance Center Inc., ("CCC's Billing and Payment terms and conditions"), at the time that you opened your Rightslink account (these are available at any time at <http://myaccount.copyright.com>)

#### Terms and Conditions

1. The materials you have requested permission to reproduce (the "Materials") are protected by copyright.
2. You are hereby granted a personal, non-exclusive, non-sublicensable, non-transferable, worldwide, limited license to reproduce the Materials for the purpose specified in the licensing process. This license is for a one-time use only with a maximum distribution equal to the number that you identified in the licensing process. Any form of republication granted by this licence must be completed within two years of the date of the grant of this licence (although copies prepared before may be distributed thereafter). The Materials shall not be used in any other manner or for any other purpose. Permission is granted subject to an appropriate acknowledgement given to the author, title of the material/book/journal and the publisher. You shall also duplicate the copyright notice that appears in the Wiley publication in your use of the Material. Permission is also granted on the understanding that nowhere in the text is a previously published source acknowledged for all or part of this Material. Any third party material is expressly excluded from this permission.
3. With respect to the Materials, all rights are reserved. Except as expressly granted by the terms of the license, no part of the Materials may be copied, modified, adapted (except for minor reformatting required by the new Publication), translated, reproduced, transferred or distributed, in any form or by any means, and no derivative works may be made based on the Materials without the prior permission of the respective copyright owner. You may not alter, remove or suppress in any manner any copyright, trademark or other notices displayed by the Materials. You may not license, rent, sell, loan, lease, pledge, offer as security, transfer or assign the Materials, or any of the rights granted to you hereunder to any other person.
4. The Materials and all of the intellectual property rights therein shall at all times remain the exclusive property of John Wiley & Sons Inc or one of its related companies (WILEY) or their respective licensors, and your interest therein is only that of having possession of and the right to reproduce the Materials pursuant to Section 2 herein during the continuance of this Agreement. You agree that you own no right, title or interest in or to the Materials or any of the intellectual property rights therein. You shall have no rights hereunder other than the license as provided for above in Section 2. No right, license or interest to any trademark, trade name, service mark or other branding ("Marks") of WILEY or its licensors is granted hereunder, and you agree that you shall not assert any such right, license or interest with respect thereto.
5. NEITHER WILEY NOR ITS LICENSORS MAKES ANY WARRANTY OR REPRESENTATION OF ANY KIND TO YOU OR ANY THIRD PARTY, EXPRESS, IMPLIED OR STATUTORY, WITH RESPECT TO THE MATERIALS OR THE ACCURACY OF ANY INFORMATION CONTAINED IN THE MATERIALS, INCLUDING, WITHOUT LIMITATION, ANY IMPLIED WARRANTY OF MERCHANTABILITY, ACCURACY, SATISFACTORY QUALITY, FITNESS FOR A PARTICULAR PURPOSE, USABILITY, INTEGRATION OR NON-INFRINGEMENT AND ALL SUCH WARRANTIES ARE HEREBY EXCLUDED BY WILEY AND ITS LICENSORS AND WAIVED BY YOU.
6. WILEY shall have the right to terminate this Agreement immediately upon breach of this Agreement by you.
7. You shall indemnify, defend and hold harmless WILEY, its Licensors and their respective directors, officers, agents and employees, from and against any actual or threatened claims, demands, causes of action or proceedings arising from any breach of this Agreement by you.
8. IN NO EVENT SHALL WILEY OR ITS LICENSORS BE LIABLE TO YOU OR ANY OTHER PARTY OR ANY OTHER PERSON OR ENTITY FOR ANY SPECIAL, CONSEQUENTIAL, INCIDENTAL, INDIRECT, EXEMPLARY OR PUNITIVE DAMAGES, HOWEVER CAUSED, ARISING OUT OF OR IN CONNECTION WITH THE DOWNLOADING, PROVISIONING, VIEWING OR USE OF THE MATERIALS REGARDLESS OF THE FORM OF ACTION, WHETHER FOR BREACH OF CONTRACT, BREACH OF WARRANTY,

TORT, NEGLIGENCE, INFRINGEMENT OR OTHERWISE (INCLUDING, WITHOUT LIMITATION, DAMAGES BASED ON LOSS OF PROFITS, DATA, FILES, USE, BUSINESS OPPORTUNITY OR CLAIMS OF THIRD PARTIES), AND WHETHER OR NOT THE PARTY HAS BEEN ADVISED OF THE POSSIBILITY OF SUCH DAMAGES. THIS LIMITATION SHALL APPLY NOTWITHSTANDING ANY FAILURE OF ESSENTIAL PURPOSE OF ANY LIMITED REMEDY PROVIDED HEREIN.

9. Should any provision of this Agreement be held by a court of competent jurisdiction to be illegal, invalid, or unenforceable, that provision shall be deemed amended to achieve as nearly as possible the same economic effect as the original provision, and the legality, validity and enforceability of the remaining provisions of this Agreement shall not be affected or impaired thereby.

10. The failure of either party to enforce any term or condition of this Agreement shall not constitute a waiver of either party's right to enforce each and every term and condition of this Agreement. No breach under this agreement shall be deemed waived or excused by either party unless such waiver or consent is in writing signed by the party granting such waiver or consent. The waiver by or consent of a party to a breach of any provision of this Agreement shall not operate or be construed as a waiver of or consent to any other or subsequent breach by such other party.

11. This Agreement may not be assigned (including by operation of law or otherwise) by you without WILEY's prior written consent.

12. Any fee required for this permission shall be non-refundable after thirty (30) days from receipt.

13. These terms and conditions together with CCC's Billing and Payment terms and conditions (which are incorporated herein) form the entire agreement between you and WILEY concerning this licensing transaction and (in the absence of fraud) supersedes all prior agreements and representations of the parties, oral or written. This Agreement may not be amended except in writing signed by both parties. This Agreement shall be binding upon and inure to the benefit of the parties' successors, legal representatives, and authorized assigns.

14. In the event of any conflict between your obligations established by these terms and conditions and those established by CCC's Billing and Payment terms and conditions, these terms and conditions shall prevail.

15. WILEY expressly reserves all rights not specifically granted in the combination of (i) the license details provided by you and accepted in the course of this licensing transaction, (ii) these terms and conditions and (iii) CCC's Billing and Payment terms and conditions.

16. This Agreement will be void if the Type of Use, Format, Circulation, or Requestor Type was misrepresented during the licensing process.

17. This Agreement shall be governed by and construed in accordance with the laws of the State of New York, USA, without regards to such state's conflict of law rules. Any legal action, suit or proceeding arising out of or relating to these Terms and Conditions or the breach thereof shall be instituted in a court of competent jurisdiction in New York County in the State of New York in the United States of America and each party hereby consents and submits to the personal jurisdiction of such court, waives any objection to venue in such court and consents to service of process by registered or certified mail, return receipt requested, at the last known address of such party.

#### **Wiley Open Access Terms and Conditions**

All research articles published in Wiley Open Access journals are fully open access: immediately freely available to read, download and share. Articles are published under the terms of the [Creative Commons Attribution Non Commercial License](#), which permits use, distribution and reproduction in any medium, provided the original work is properly cited and is not used for commercial purposes. The license is subject to the Wiley Open Access terms and conditions:

Wiley Open Access articles are protected by copyright and are posted to repositories and websites in accordance with the terms of the [Creative Commons Attribution Non Commercial License](#). At the time of deposit, Wiley Open Access articles include all changes made during peer review, copyediting, and publishing. Repositories and websites that host the article are

responsible for incorporating any publisher-supplied amendments or retractions issued subsequently.  
Wiley Open Access articles are also available without charge on Wiley's publishing platform, **Wiley Online Library** or any successor sites.

#### **Use by non-commercial users**

For non-commercial and non-promotional purposes individual users may access, download, copy, display and redistribute to colleagues Wiley Open Access articles, as well as adapt, translate, text- and data-mine the content subject to the following conditions:

- The authors' moral rights are not compromised. These rights include the right of "paternity" (also known as "attribution" - the right for the author to be identified as such) and "integrity" (the right for the author not to have the work altered in such a way that the author's reputation or integrity may be impugned).
- Where content in the article is identified as belonging to a third party, it is the obligation of the user to ensure that any reuse complies with the copyright policies of the owner of that content.
- If article content is copied, downloaded or otherwise reused for non-commercial research and education purposes, a link to the appropriate bibliographic citation (authors, journal, article title, volume, issue, page numbers, DOI and the link to the definitive published version on Wiley Online Library) should be maintained. Copyright notices and disclaimers must not be deleted.
- Any translations, for which a prior translation agreement with Wiley has not been agreed, must prominently display the statement: "This is an unofficial translation of an article that appeared in a Wiley publication. The publisher has not endorsed this translation."

#### **Use by commercial "for-profit" organisations**

Use of Wiley Open Access articles for commercial, promotional, or marketing purposes requires further explicit permission from Wiley and will be subject to a fee. Commercial purposes include:

- Copying or downloading of articles, or linking to such articles for further redistribution, sale or licensing;
- Copying, downloading or posting by a site or service that incorporates advertising with such content;
- The inclusion or incorporation of article content in other works or services (other than normal quotations with an appropriate citation) that is then available for sale or licensing, for a fee (for example, a compilation produced for marketing purposes, inclusion in a sales pack)
- Use of article content (other than normal quotations with appropriate citation) by for-profit organisations for promotional purposes
- Linking to article content in e-mails redistributed for promotional, marketing or educational purposes;
- Use for the purposes of monetary reward by means of sale, resale, licence, loan, transfer or other form of commercial exploitation such as marketing products
- Print reprints of Wiley Open Access articles can be purchased from: [corporatesales@wiley.com](mailto:corporatesales@wiley.com)

Other Terms and Conditions:

BY CLICKING ON THE "I AGREE..." BOX, YOU ACKNOWLEDGE THAT YOU HAVE READ AND FULLY UNDERSTAND EACH OF THE SECTIONS OF AND PROVISIONS SET FORTH IN THIS AGREEMENT AND THAT YOU ARE IN AGREEMENT WITH AND ARE WILLING TO ACCEPT ALL OF YOUR OBLIGATIONS AS SET FORTH IN THIS AGREEMENT.

v1.7

**If you would like to pay for this license now, please remit this license along with your payment made payable to "COPYRIGHT CLEARANCE CENTER" otherwise you will be invoiced within 48 hours of the license date. Payment should be in the form of a check or money order referencing your account number and this invoice number RLNK500912474. Once you receive your invoice for this order, you may pay your invoice by credit card. Please follow instructions provided at that time.**

**Make Payment To:  
Copyright Clearance Center  
Dept 001  
P.O. Box 843006  
Boston, MA 02284-3006**

**For suggestions or comments regarding this order, contact RightsLink Customer Support: [customercare@copyright.com](mailto:customercare@copyright.com) or +1-877-622-5543 (toll free in the US) or +1-978-646-2777.**

**Gratis licenses (referencing \$0 in the Total field) are free. Please retain this printable license for your reference. No payment is required.**

---



## Copyright permission for Figure 1.11

### NATURE PUBLISHING GROUP LICENSE TERMS AND CONDITIONS

Dec 04, 2012

This is a License Agreement between Xin Xia ("You") and Nature Publishing Group ("Nature Publishing Group") provided by Copyright Clearance Center ("CCC"). The license consists of your order details, the terms and conditions provided by Nature Publishing Group, and the payment terms and conditions.

**All payments must be made in full to CCC. For payment instructions, please see information listed at the bottom of this form.**

License Number	3042070003129
License date	Dec 04, 2012
Licensed content publisher	Nature Publishing Group
Licensed content publication	Nature Materials
Licensed content title	P2-type $\text{Na}_x[\text{Fe}_{1/2}\text{Mn}_{1/2}]\text{O}_2$ made from earth-abundant elements for rechargeable Na batteries
Licensed content author	Naoaki Yabuuchi, Masataka Kajiyama, Junichi Iwatate, Heisuke Nishikawa, Shuji Hitomi, Ryoichi Okuyama
Licensed content date	Apr 29, 2012
Volume number	11
Issue number	6
Type of Use	reuse in a thesis/dissertation
Requestor type	non-commercial (non-profit)
Format	print and electronic
Portion	figures/tables/illustrations
Number of figures/tables/illustrations	1
High-res required	no
Figures	Charge/discharge curve and cycle performance of $\text{Na}_2/3\text{Fe}_{0.5}\text{Mn}_{0.5}\text{O}_2/\text{Na}$ half cells cycled between 1.5 and 4.3 V
Author of this NPG article	no
Your reference number	
Title of your thesis / dissertation	Study of the safety of metal-ion batteries
Expected completion date	Jan 2013
Estimated size (number of pages)	170
Total	0.00 USD

Copyright permission for Figure 1.9, 1.12, 1.13, 1.14, 1.15, 1.16, 1.17, 1.18, 1.19, 1.20,  
1.21, Table 2.1 and other contents

Jan. 15. 2013 2:57 PM

No. 0659 p. 1

**Request for Permission to Reproduce or Re-Publish ECS Material**

Please fax (this form to: The Electrochemical Society (ECS), Attn: Permissions Requests, 1.609.730.0629.  
You may also e-mail your request to: [copyright@electrochem.org](mailto:copyright@electrochem.org). Include all the information as required on this  
form. Please allow 3-7 days for your request to be processed.

I am preparing a (choose one):  paper  chapter  book  thesis

entitled: Studies of the safety of metal-ion batteries

to be published by: Dalhousie University

in an upcoming publication entitled: N/A

I request permission to use the following material in the publication noted above, and request nonexclusive  
rights for all subsequent editions and in all foreign language translations for distribution throughout the world.

Description of material to be used—indicate what material you wish to use (figures, tables, text, etc.) and give  
the full bibliographic reference for the source publication. You may attach a separate list, organized by ECS title.

See separate list

Signature: \_\_\_\_\_ Date: Jan. 16th 2013

Name: XIN XIA

Address: Department of Physics, Dalhousie University  
6210 Lehigh Rd Halifax NS B3H 3J5

Telephone: 902-494-2991 Fax: 902-494-2791

E-mail: xinxia@dal.ca

Permission is granted to reproduce the above-referenced material. Please acknowledge the author(s) and  
publication data of the original material, and include the words: "Reproduced by permission of The  
Electrochemical Society."

Jan. 17, 2013 \_\_\_\_\_  
Date Ann F. Goedkoop, Director of Publications

## 1. Figure 4 on Page 46

From Paper:

S. Komaba, T. Nakayama, A. Ogata, T. Shimizu, C. Takei, S. Takada, A. Hokura, I. Nakai

Electrochemically Reversible Sodium Intercalation of Layered  $\text{NaNi}_{0.5}\text{Mn}_{0.5}\text{O}_2$  and  $\text{NaCrO}_2$ 

Vol. 16, Issue 42 (2009) 43-55

ECS Transactions

## 2. Figure 1 and Figure 2 on Page 1272

From Paper:

D. A. Stevens, J. R. Dahn

High Capacity Anode Materials for Rechargeable Sodium-Ion Batteries

Vol. 147, Issue 4 (2000) 1271-1273

Journal of The Electrochemical Society

## 3. Figure 5 and Figure 6 on Page 65

From Paper:

C. W. Lee, R. Venkatachalapathy, J. Prakash

A Novel Flame-Retardant Additive for Lithium Batteries

Vol. 3, Issue 2 (2000) 63-65

Electrochemical and Solid-State Letters

## 4. Figure 2 on Page A1059, Figure 3 on Page A1060 and Figure 14 on Page A1064

From Paper:

X. Wang, E. Yasukawa, S. Kasuya

Nonflammable Trimethyl Phosphate Solvent-Containing Electrolytes for Lithium-Ion Batteries: I. Fundamental Properties

Vol. 148, Issue 10 (2001) A1058-A1065

Journal of The Electrochemical Society

## 5. Figure 1 on Page A623, Figure 2 on Page A624 and Figure 5 on Page A626

From Paper:

K. Xu, M.S. Ding, S.S. Zhang, J.L. Allen, T.R. Jow

An Attempt to Formulate Nonflammable Lithium Ion Electrolytes with Alkyl Phosphates and Phosphazenes

Vol. 149, Issue 5 (2002) A622-A626

Journal of The Electrochemical Society

## 6. Figure 1 on Page A163

From Paper:

K. Xu, M.S. Ding, S.S. Zhang, J.L. Allen, T.R. Jow

Evaluation of Fluorinated Alkyl Phosphates as Flame Retardants in Electrolytes for Li-Ion Batteries: I. Physical and Electrochemical Properties

Vol. 150, Issue 2 (2003) A161-A169

Journal of The Electrochemical Society

6. Figure 4 on Page A173

From Paper:

K. Xu, S.S. Zhang, J.L. Allen, T.R. Jow  
Evaluation of Fluorinated Alkyl Phosphates as Flame Retardants in Electrolytes for Li-Ion Batteries:II. Performance in Cell  
Vol. 150, Issue 2 (2003) A170-A175  
Journal of The Electrochemical Society

7. Texts and Figures

From Papers listed below:

Xin Xia, P. Ping, J. R. Dahn

The Reactivity of Charged Electrode Materials with Electrolytes Containing the Flame Retardant, Triphenyl Phosphate  
Vol.159, Issue 11 (2012) A1834-A1837  
Journal of The Electrochemical Society

Xin Xia, P. Ping, J. R. Dahn

Studies of the effect of Triphenyl Phosphate on the Negative Electrode of Li-ion cells  
Vol.159, Issue 9 (2012) A1460-A1466  
Journal of The Electrochemical Society

Xin Xia, J. R. Dahn

A study of the reactivity of de-intercalated  $\text{NaNi}_{0.5}\text{Mn}_{0.5}\text{O}_2$  with non-aqueous solvent and electrolyte by Accelerating Rate Calorimetry  
Vol.159, Issue 7 (2012) A1048-A051  
Journal of The Electrochemical Society

Xin Xia, J. R. Dahn

Study of the Reactivity of Na/Hard Carbon with Different Solvents and Electrolytes  
Vol.159, Issue 5 (2012) A515-A519  
Journal of The Electrochemical Society

Xin Xia, J. R. Dahn

A Study of the Reactivity of De-Intercalated  $\text{P2-Na}_x\text{CoO}_2$  with Non-Aqueous Solvent and Electrolyte by Accelerating Rate Calorimetry  
Vol.159, Issue 5 (2012) A647-A650  
Journal of The Electrochemical Society

Xin Xia, J. R. Dahn

" $\text{NaCrO}_2$  is a Fundamentally Safe Positive Electrode Material for Sodium-Ion Batteries with Liquid Electrolytes"  
Vol.15, Issue 1 (2012) A1-A4  
Electrochemical and Solid-State Letters

Xin Xia, M. N. Obrovac, J. R. Dahn  
Comparison of the Reactivity of  $\text{Na}_x\text{C}_6$  and  $\text{Li}_x\text{C}_6$  with Non-Aqueous Solvents and  
Electrolytes  
Vol.14, Issue 9 (2011) A130-A3  
Electrochemical and Solid-State Letters

✓